In vivo Evaluation of Nanodimensional Drug Delivery Systems via Positron Emission Tomography

Dissertation

zur Erlangung des Grades
„Doktor der Naturwissenschaften (Dr. rer. nat.)“
im Promotionsfach Chemie

Am Fachbereich Chemie, Pharmazie und Geowissenschaften
der Johannes Gutenberg-Universität Mainz
vorgelegt von

Karolin Wagener

Mainz, im Juni 2018

Dekan:

Erster Berichterstatter: Univ.-Prof. Dr. Frank Rösch

Zweiter Berichterstatter:

Tag der mündlichen Prüfung: 19. Juli 2018

Die vorliegende Arbeit wurde unter der Betreuung von Prof. Dr. Frank Rösch in der Zeit von 2015 bis 2018 am Institut für Kernchemie der Johannes Gutenberg-Universität Mainz angefertigt.

“I hereby declare that I wrote the dissertation submitted without any unauthorized external assistance and used only sources acknowledged in the work. All textual passages which are appropriated verbatim or paraphrased from published and unpublished texts as well as all information obtained from oral sources are duly indicated and listed in accordance with bibliographical rules. In carrying out this research, I complied with the rules of standard scientific practice as formulated in the statutes of Johannes Gutenberg-University Mainz to insure standard scientific practice.”

Mainz, Juni 2018

Abstract

In vivo tracking is crucial for the pre-clinical evaluation of drug delivery systems (DDSs), in order to understand structure-property relationships of the DDSs and their resulting pharmacokinetic profile. Among nuclear medical imaging tools, positron emission tomography (PET) is a powerful and noninvasive technique, allowing for quantification and providing an excellent spatial and temporal resolution. Because of these advantages, PET bears great potential in the evaluation of DDSs. In the herein presented work, different nanodimensional DDSs were evaluated via positron emission tomography and/or biodistribution studies in mice and rats. By the utilization of the radionuclides ^{18}F, ^{131}I and ^{64}Cu, various research questions could be answered.

First, random (*ran*) copolymers consisting of *N*-(2-hydroxypropyl)methacrylamide (HMPA) and lauryl methacrylate (LMA), which had shown favorable short-term *in vivo* characteristics in former studies, were radiolabeled with ^{131}I. The longer-lived radioisotope ^{131}I enabled tracking of their pharmacokinetics in tumor-bearing rats over three days. Despite a polymer clearance from the blood within this time span, there was an increase in tumor uptake observable over time, which strongly emphasizes the enhanced permeability and retention (EPR) effect. Regarding the stability of the ^{131}I-label, *ex vivo* biodistribution experiments, considering the uptake in the thyroid, indicated low metabolism rates.

Another part of this work focused on the *in vivo* evaluation of stealth liposomes. These spherical vesicles exhibit an excellent biocompatibility as well as a low toxicity since phospholipids as their main components are also the building blocks of cellular membranes. A polymer shell prevents them from being detected by the mononuclear phagocyte system (MPS). For this purpose, one needs to ensure a stable anchorage into the lipid bilayer, ideally paired with multifunctionality, which enables the linkage of different modalities (e.g. radiolabel and targeting vector). Thus, different multifunctional hyperbranched polyglycerols (*hb*PG) with a dialkyl anchor and their respective liposomal formulations were investigated in PET and biodistribution studies in mice, with respect to liposome stability. To compare *hb*PG and the gold standard PEG regarding their shielding properties, also a PEG lipid was examined. The polyether lipids were rapidly cleared via the renal system, whereas the corresponding liposomes circulated in the blood stream over the period of investigation. Overall, liposomes shielded by the *hb*PG lipids exhibited a favorable biodistribution, rendering them promising novel nanovesicles for drug transport and targeting.

Radiolabeling of the polyether lipids was carried out prior to the liposome formation via copper-catalyzed alkyne-azide cycloaddition (CuAAC) using 1-azido-2-(2-(2-[^{18}F]fluoroethoxy)ethoxy)ethane ([^{18}F]F-TEG-N_3). This approach ensured the separation of cytotoxic copper, but entailed a time-

consuming radiosynthesis on the other hand. Thus, a direct radiolabeling of preformed liposomes was tested. Herein, a main emphasis lay on the quantification of the retained amount of copper upon purification. For this purpose, ^{64}Cu, produced at the TRIGA Mark II research reactor Mainz, was utilized as catalyst for the CuAAC between liposomes and non-radioactive F-TEG-N_3. In this way, the final copper content of the liposomes could straightforwardly be quantified by gamma spectrometry, revealing that only 0.018 % of the added radioactivity was still associated with the liposome after purification. The ration of retained copper is so low, that an *in vivo* application of the liposomes is absolutely reasonable.

In the last part of this work, *hb*PG-shielded liposomes, bearing multiple carbohydratic trimannose molecules on their surface, were investigated, regarding their potential to address dendritic cells (DCs) *in vivo*. DCs are professional antigen-presenting cells, which initialize all antigen-specific immune responses. Thus, they are a compelling target in cancer immunotherapy. The *in vivo* fate of the trimannosylated liposomes was evaluated via *in vivo* PET and *ex vivo* biodistribution studies in mice and the results were compared to similar liposomes bearing no trimannose on their surface. Here, the multifunctionality of *hb*PG was beneficial, as the ^{18}F-label for tracking and the trimannose-label for DC-targeting could be implemented on the same molecule. It was found that the mannosylated liposomes highly accumulated in liver, spleen and bone marrow, compared to their non-mannosylated counterparts. These findings suggest, that the mannosylated liposomes were recognized by DCs, expressed in the mentioned organs. However, it cannot be excluded that other antigen-presenting cells, besides DCs, have also be targeted. Future cell studies on murine splenic immune cells have to elucidate which cell types are addressed in particular and to which extent. For this purpose, Oregon Green 488-labeled polyether lipids and respective liposomal formulations have already been synthesized.

Zusammenfassung

Für die Entwicklung von Wirkstofftransportsystemen ist eine präklinische *in vivo* Evaluierung unerlässlich, um Informationen über deren Struktur-Wirkungsbeziehungen und die daraus resultierende Pharmakokinetik zu erhalten. Die Positronen-Emissions-Tomographie (PET) ist ein leistungsfähiges und nichtinvasives bildgebendes Verfahren, das die Möglichkeit der Quantifizierung und eine ausgezeichnete räumliche und zeitliche Auflösung bietet. Aufgrund dieser Vorteile birgt die PET für die Evaluierung von Wirkstofftransportsystemen ein großes Potential. In der hier vorgestellten Arbeit wurden verschiedene nanodimensionale Wirkstofftransportsysteme mittels Positronen-Emissions-Tomographie und/oder Biodistributionsstudien an Mäusen und Ratten evaluiert. Durch den Einsatz der Radionuklide ^{18}F, ^{131}I und ^{64}Cu konnten verschiedene Fragestellungen beantwortet werden.

Zunächst wurden statistische Copolymere aus N-(2-Hydroxypropyl)methacrylamid (HMPA) und Laurylmethacrylat (LMA), die in früheren Studien über einen kurzen Zeitraum gute *in vivo*-Eigenschaften gezeigt hatten, mit ^{131}I radioaktiv markiert. Das längerlebige Radioisotop ^{131}I ermöglichte die Untersuchung ihrer Pharmakokinetik in tumortragenden Ratten über drei Tage. Trotz einer vollständigen Clearance des Poylmers aus dem Blut innerhalb dieser Zeitspanne war eine Zunahme der Tumoraufnahme zu beobachten, was sich mit dem sogenannten EPR-Effekt (engl. *enhanced permeability and retention*) erklären lässt. Untersuchungen zur Stabilität des ^{131}I-Labels, mittels Quantifizierung der Anreicherung der applizierten Radioaktivität in der Schilddrüse, zeigten niedrige Metabolisierungsraten.

Ein weiterer Teil dieser Arbeit konzentrierte sich auf die *in vivo*-Evaluierung von Stealth-Liposomen. Diese kugelförmigen Vesikel weisen eine ausgezeichnete Biokompatibilität sowie eine geringe Toxizität auf, da Phospholipide, als deren Hauptbestandteile, auch als Bausteine für Zellmembranen fungieren. Eine Polymerhülle um das Stealth-Liposom verhindert dessen Erkennung durch das mononukleäre Phagozytensystem (MPS). Dazu muss eine stabile Verankerung der Polymere in der Lipid-Doppelschicht der Liposomen gewährleistet sein, idealerweise gepaart mit einer Multifunktionalität der Polymere, welche die Anbindung verschiedener Modalitäten (z.B. Radiolabel und Targeting-Vektor) ermöglicht. Daher wurden unterschiedliche multifunktionale hyperverzweigte Polyglycerine (*hb*PG) mit einem Dialkylanker und ihre jeweiligen liposomalen Formulierungen in PET- und Biodistributionsstudien an Mäusen untersucht. Dies geschah mit Fokus auf die *in vivo*-Stabilität der Liposomen. Um *hb*PG und den Goldstandard zur Abschirmung von Liposomen, PEG, hinsichtlich ihrer Eigenschaften zu vergleichen, wurde auch ein PEG-Lipid untersucht. Die reinen Polyetherlipide unterlagen einer schnellen renalen Ausscheidung. Ihre entsprechenden liposomalen Formulierungen dagegen zirkulierten über den Untersuchungszeitraum in der Blutbahn. Insgesamt zeigten Liposomen, die durch die neuartigen *hb*PG-

Lipide abgeschirmt waren, eine günstige Biodistribution, so dass sie vielversprechende Kandidaten für Medikamententransport und aktives Targeting darstellen.

Die Radiomarkierung der Polyetherlipide mit 1-Azido-2-(2-(2-[^{18}F]fluorethoxy)ethoxy)ethan ([^{18}F]F-TEG-N_3) erfolgte, vor der Liposomenbildung, über eine kupferkatalysierte Alkin-Azid-Cycloaddition (CuAAC). Dieser Ansatz stellte die Abtrennung von zytotoxischem Kupfer sicher, erforderte aber auf der anderen Seite eine zeitaufwändige Radiosynthese. Daher wurde eine direkte Radiomarkierung von vorgeformten Liposomen getestet. Dabei lag der Schwerpunkt auf der Quantifizierung der nach der Reinigung der Liposomen noch vorhandenen Kupfermenge. Dazu wurde ^{64}Cu, hergestellt am TRIGA Mark II Forschungsreaktor Mainz, als Katalysator für die CuAAC zwischen Liposomen und nicht-radioaktivem F-TEG-N_3 eingesetzt. Auf diese Weise ließ sich der finale Kupfergehalt der Liposomen mittels Gammaspektrometrie quantifizieren. Es zeigte sich, dass nach der Reinigung nur noch 0,018 % der zugeführten ^{64}Cu-Radioaktivität mit den Liposomen assoziiert waren. Der Anteil an zurückgehaltenem Kupfer ist demnach so gering, dass eine *in vivo*-Applikation der Liposomen absolut vertretbar ist.

Im letzten Teil dieser Arbeit wurden *hb*PG-abgeschirmte Liposomen, die mehrere Moleküle des Kohlenhydrats Trimannose auf ihrer Oberfläche trugen, hinsichtlich ihres Potenzials, dendritische Zellen (DCs) *in vivo* zu targetieren, untersucht. DCs sind professionelle antigenpräsentierende Zellen, welche alle antigenspezifischen Immunantworten initialisieren. Damit sind sie ein vielversprechender Ansatzpunkt für eine aktive Krebsimmuntherapie. Die Pharmakokinetik der trimannosylierten Liposomen wurde mittels *in vivo* PET und *ex vivo* Biodistributionsstudien an Mäusen untersucht und die Ergebnisse mit Liposomen verglichen, die keine Trimannose auf ihrer Oberfläche trugen, sich aber ansonsten nicht unterschieden. Hier war die Multifunktionalität von *hb*PG von Vorteil, da das ^{18}F-Label, für Imaging-Zwecke, und das Trimannose-Label, für die Targetierung von DCs, an ein und das selbe Molekül angebunden werden konnten. Es zeigte sich, dass sich die mannosylierten Liposomen, im Vergleich zu ihren nicht mannosylierten Pendants, stark in Leber, Milz und Knochenmark akkumulierten. Diese Ergebnisse deuten darauf hin, dass die mannosylierten Liposomen von DCs, die in den genannten Organen exprimiert werden, erkannt wurden. Es kann jedoch nicht ausgeschlossen werden, dass neben DCs auch andere antigenpräsentierende Zellen targetiert wurden. Zukünftige Zellstudien an murinen Milz-Immunzellen müssen daher klären, welche Zelltypen adressiert werden und in welchem Ausmaß. Zu diesem Zweck wurden bereits Oregon Green 488-markierte Polyetherlipide und entsprechende liposomale Formulierungen synthetisiert.

Graphical Abstract

HPMA-*ran*-LMA copolymers – short and long term *in vivo* fate (see chapter 3.1).

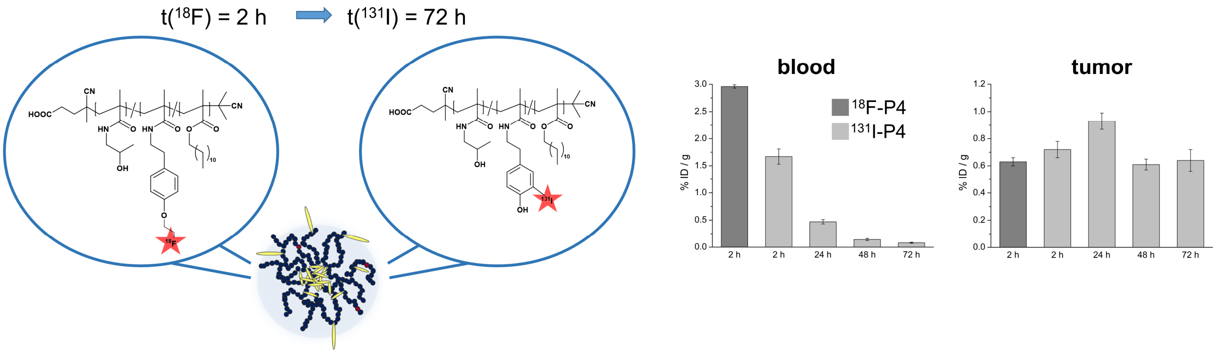

Linear and hyperbranched polyether lipids for liposome shielding: synthesis, characterization, liposome preparation and *in vivo* studies (see chapter 3.2).

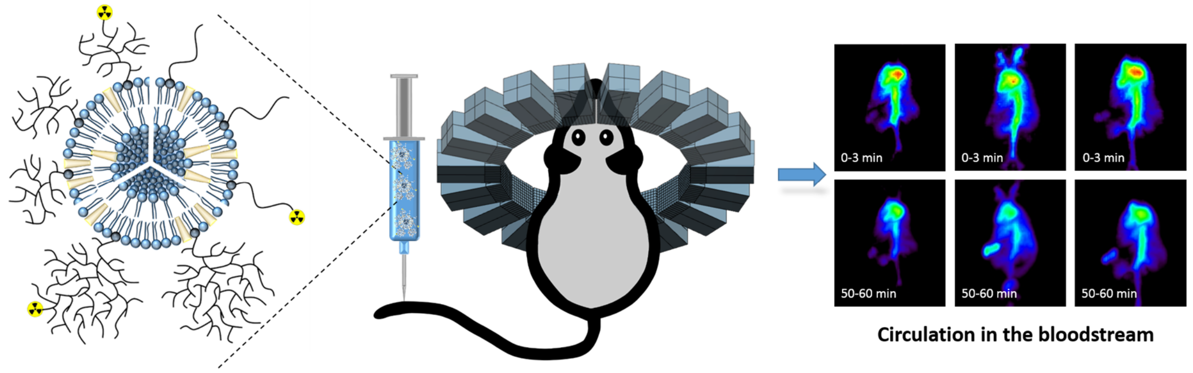

0-3 min
0-3 min
0-3 min
50-60 min
50-60 min
50-60 min
Circulation in the bloodstream

CuAAC on liposomes: Quantification of retained copper using ^{64}Cu-spiked Cu(I) (see chapter 3.3).

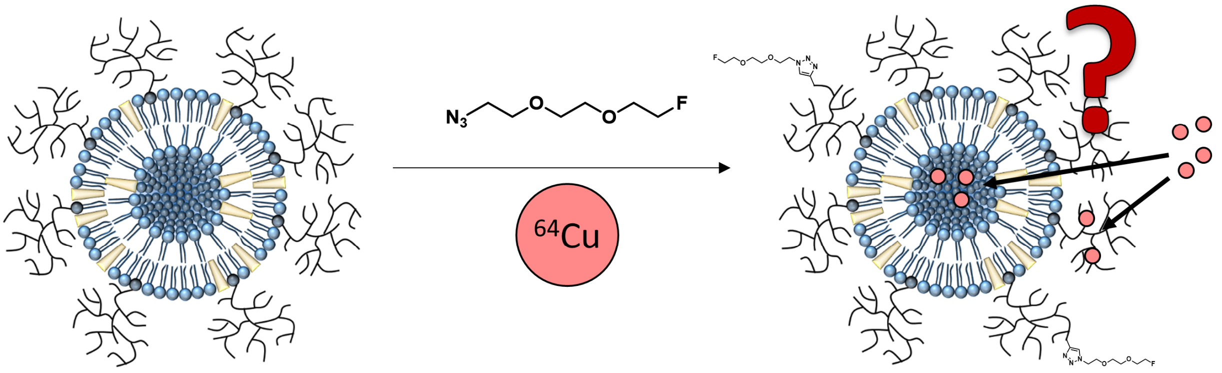

Targeting of immune cells with trimannosylated liposomes (see chapter 3.4).

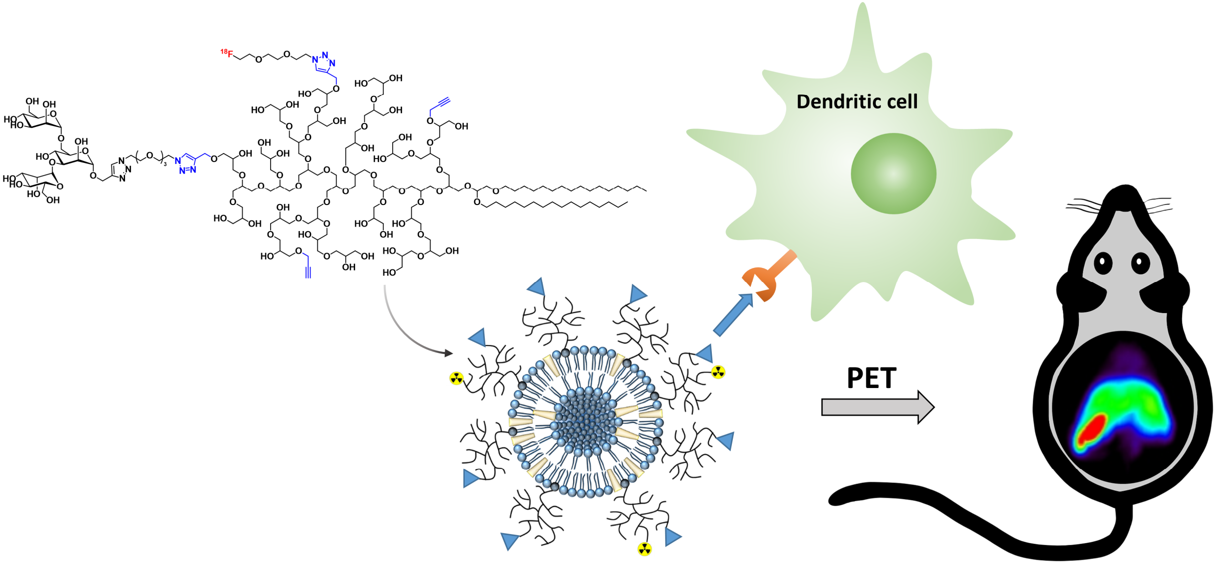
^{18}F
Dendritic cell
PET

Für meine Eltern

Table of contents

1 Introduction 1

1.1 PET 1

1.1.1 PET radionuclides 4

1.2 Radiofluorination with ^{18}F 6

1.3 Radioiodination 9

1.4 Nanoparticulate and polymeric drug delivery systems 10

1.4.1 Liposomes 12

1.4.2 HPMA-based polymers 14

1.4.3 Imaging of drug delivery (systems) 16

1.5 References 18

2 Motivation and Objectives 29

3 Manuscripts 35

3.1 Long-term biodistribution study of HPMA-*ran*-LMA copolymers *in vivo* by means of ^{131}I-labeling 37

3.2 Comparison of Linear and Hyperbranched Polyether Lipids for Liposome Shielding by ^{18}F-Radiolabeling and Positron Emission Tomography 69

3.3 Copper-catalyzed click reactions: Quantification of retained copper using ^{64}Cu-spiked Cu(I), exemplified for CuAAC reactions on liposomes 111

3.4 Targeting of Immune Cells with Trimannosylated Liposomes 131

4 Summary and Outlook 187

4.1 References 193

5 Appendix 197

5.1 List of abbreviations 197

5.2 List of publications 201

5.3 Acknowledgment 203

5.4 Curriculum Vitae 205

1 Introduction

1 Introduction

15 years after the discovery of radioactivity by Henri Becquerel (1896), Ernest Rutherford asked George de Hevesy in 1911 to isolate radium D from a sample of lead chloride. De Hevesy failed, but took advantage of the inseparability by mixing lead with radium D of known radioactivity. In this way, he was able to trace the path of the lead during chemical reactions.[1] The radiotracer method was born. Besides, de Hevesy recognized the opportunity to trace metabolic processes *in vivo* using this method. In 1923 he studied the absorption and the transportation of lead in plants.[2] He used very small amounts of the radioactive substance in order to not cause a pharmacological interaction. In 1943 de Hevesy received the Nobel Prize in Chemistry "*for his work on the use of isotopes as tracers in the study of chemical processes*". The radiotracer method, discovered by de Hevesy, provides the basis for the modern nuclear medicine.[3]

1.1 PET

Another breakthrough enroute to modern nuclear medicine was the development of the positron emission tomography (PET) by Ter-Pogossian, Phelps und Hoffman.[4] PET is a non-invasive, functional imaging technique, by which it is possible to trace biochemical and metabolic processes *in vivo*.[5] Both, a qualitative and a quantitative analysis of the acquired data is possible.[6] To perform a PET scan, it is necessary to apply a radioisotope or a radioactively labeled pharmaceutical, which, according to the respective question, either binds to a specific target or passively traverses or accumulates at the target side. PET-radiopharmaceuticals utilize a positron-emitting radionuclide, whose proton-rich nucleus stabilizes via a β^+-conversion. In this process, a proton is transformed into a neutron, whereas a positron and an electron neutrino are emitted. Formula 1 shows the general equation of a β^+-conversion.

$$ {}^{A}_{Z}X_{N} \rightarrow {}_{Z-1}^{A}X_{N+1} + {}^{0}_{1}\mathrm{e}^{+} + {}^{0}_{0}\nu_{\mathrm{e}} + \Delta E \tag{1} $$

The energy, released during the conversion, is distributed randomly between positron and electron neutrino. The emitted positrons therefore have energies between 0 and a maximum β^+-energy ($E_{\beta+,\max}$), which differs for different positron-emitting radionuclides. Once emitted, the positron travels through the surrounding medium and continuously loses energy via elastic and inelastic collisions. After it has lost almost all its kinetic energy, it annihilates with a nearby electron under the emission of their rest energy of 1022 keV (corresponds to 2 x 511 keV = rest energy of the electron + rest energy of the positron) (see Figure 1) in the form of γ-radiation.[7] The distance traveled by the positron depends on its kinetic energy. The higher this energy the larger is the distance between the place of origin and the place of annihilation of the positron.

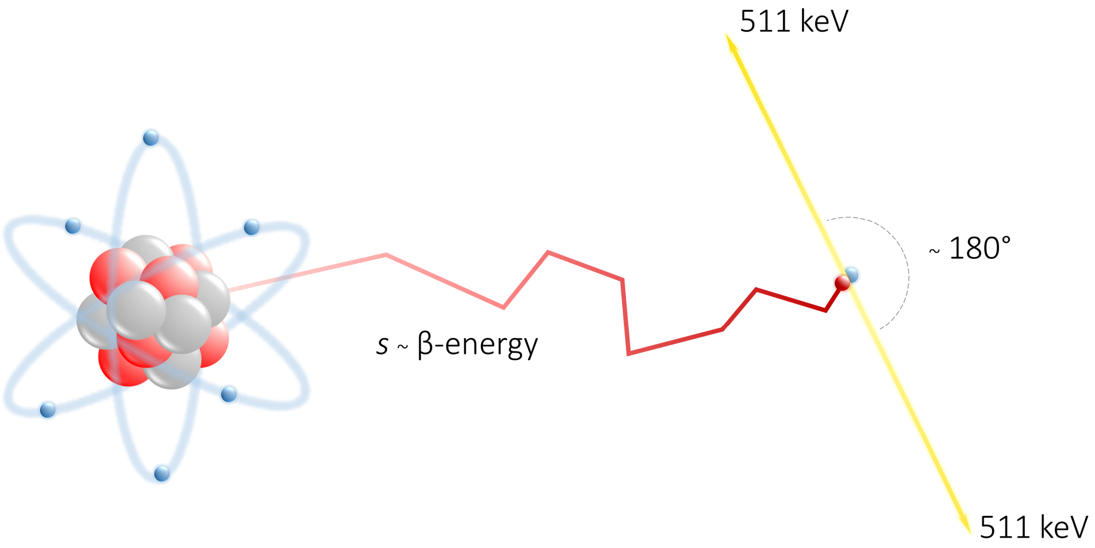

Figure 1. Schematic figure of a β^+-conversion and subsequent annihilation of a *para*-positronium (not true to scale).

There are several possibilities for the annihilation to occur which have been described in detail by Ache.[8] In the following, two of these possibilities will be highlighted. One possibility is a direct annihilation of a “free” positron with an electron. This can happen for both “in flight” positrons as well as for thermalized ones. Here, the spins of positron and electron can be parallel or antiparallel at the time of annihilation. An antiparallel orientation results in the release of two photons with 511 keV each at an angle of approximately 180°. With parallel alignment of the spins, an odd number of photons (usually three) is emitted. Angular and energy distribution between the photons is more complex than for the two-photon-annihilation. The ratio of the cross sections σ of parallel to antiparallel orientation of the spins upon the meeting of electron and positron is 1:372.[8] A second possibility is the formation of a positronium prior to the annihilation. A positronium can be considered as analogue of a hydrogen atom in which the proton is replaced by a positron. Its formation takes place in a small energy range of the positron of only a few eV, the so called Ore gap. The Ore gap is the energy range between the first excited state (E^*) of a substrate molecule and the difference between its ionization potential (V) and the binding energy of the positronium which is 6.8 eV (see Formula 2).[8] Above the ore range, competitive processes such as ionization and electronical excitation of the substrate molecules dominate the formation of a positronium. Below the Ore range, the positron does not have enough energy to form a positronium with an electron of a substrate molecule.

$$\Delta_O = E^* - (V - 6.8\ \mathrm{eV}) \tag{2}$$

The positronium can exist in two possible configurations, which differ in the orientation of their spins. The configuration with antiparallel spins, called *para*-positronium, forms with a probability of 25 %. Annihilation occurs with the emission of two γ-quants with 511 keV respectively at an angle of almost 180° (Figure 1). The mean lifetime τ of a free *para*-positronium is $1.25 \cdot 10^{-10}$ s.[8] In case the positronium exhibits parallel spins, the configuration is known as *ortho*-positronium and forms with a probability of 75 %. Annihilation leads to the emission of three γ-quants with a summed energy of 1022 keV, but neither with a defined angular nor energy distribution. τ of free *para*-positronium is $1.4 \cdot 10^{-7}$ s.[8] Of these two, only the annihilation of the *para*-positronium which forms in just 25 % of all cases can be used for PET measurements. However, through interaction with a paramagnetic surrounding, a spin conversion between the two states is possible. The much longer lifetime of the *ortho*-positronium results then in a higher amount of *para*-positronium annihilations. However, spin conversion is only one mechanism that decreases the rate of three-photon-annihilations and ultimately <1 % of the positrons annihilate into three photons.[9]

The objective of PET is the detection of the point of origin of an annihilation. In order to do so, one makes use of the coincidence and of the emission angle of approximately 180° of the two γ-quants derived from of a two-photon-annihilation. A PET scanner consists of multiple circularly arranged scintillation detectors coupled to photomultipliers (Figure 2). To date, bismuth germanate (BGO) and lutetium based scintillators like lutetium oxyorthosilicate (LSO) are the most common detector materials.[10] In case that opposing detectors recognize two γ-quants in a timeframe of approximately 6-12 ns[11] (depending on the detector material), the event is recorded in a data set as so called “Line of Response” (LOR). A LOR is an imaginary line between the two detectors, on which the annihilation did occur somewhere. Using a reconstruction algorithm, a computer can generate an activity profile by superposing the LORs and accomplishing a variety of other corrections to e.g. eliminate random coincidences. Common reconstruction algorithms are for example filtered back projection (FBP) and ordered subsets expectation maximization (OSEM).[12]

In order to quantify a PET measurement, it is necessary to conduct a transmission scan with an external radiation source prior or after the emission scan. In this way it is possible to calculate the attenuation of the photon radiation by the body.[13] More recent combined systems, like PET/computed tomography[14] (CT) scanners or PET/magnetic resonance tomography[15] (MRT) scanners allow for a calculation of the attenuation using the CT[16] or MRT[17] data, which is relatively easy in case of PET/CT but still challenging for PET/MRT.

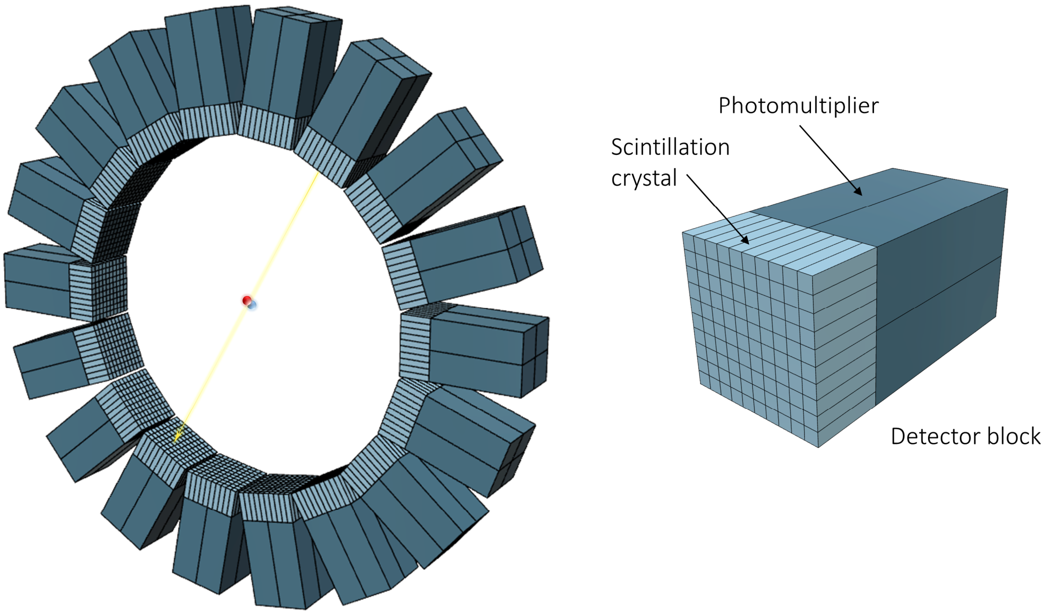

Figure 2. PET detection ring with indicated annihilation of a positronium (left) and single detector block from close up (right).

1.1.1 PET radionuclides

There are numerous radionuclides which are positron emitters. Not all of them are suitable as PET radionuclides. Besides the essential property of β^+-conversion, other nuclear aspects like half-life, β^+-conversion ratio and $E_{\beta+,\mathrm{max}}$ are of major importance. Moreover, it is necessary to consider parameters like specific activity (A_s) and availability of the radionuclides. Table 1 summarizes nuclear properties and production routes of some frequently used positron emitters for PET.

Table 1. Nuclear properties and production routes of some important PET nuclides.[18–23]

Nuclide	Half-life	$E_{\beta+,\mathrm{max}}$ [MeV]	β^+-ratio [%]	Exemplary production route
^{11}C	20.37 min	0.96	99.8	$^{14}N(p,\alpha)^{11}C$
^{13}N	9.967 min	1.20	99.8	$^{16}O(p,\alpha)^{13}N$
^{15}O	2.041 min	1.74	99.9	$^{14}N(d,n)^{15}O$
^{18}F	109.7 min	0.63	96.9	$^{18}O(p,n)^{18}F$
^{44}Sc	3.97 h	1.47	94.3	$^{44}Ti/^{44}Sc$ generator
^{64}Cu	12.7 h	0.65	17.9	$^{63}Cu(p,n)^{64}Cu$
^{68}Ga	67.71 min	1.90	89.1	$^{68}Ge/^{68}Ga$ generator
^{82}Rb	1.273 min	3.38	95.5	$^{82}Sr/^{82}Rb$ generator
^{89}Zr	78.41 h	0.90	22.3	$^{89}Y(p,n)^{89}Zr$

The half-life significantly determines the radiation exposure of the patient, the window for *in vivo* imaging and the duration of the radiosynthesis. Short-lived radionuclides like ^{13}N and ^{15}O render it impossible to perform a time-consuming radiosynthesis. Furthermore, they are unsuitable to be used with a radiotracer which needs an extended amount of time to accumulate at the target side. That is why they are predominantly used as perfusion tracers in the form of $[^{13}N]NH_3$ and $[^{15}O]H_2O$.[24] Advantageous is the low radiation exposure of the patient because of the short half-life of these positron emitters. However, radionuclides with longer half-lives, like ^{68}Ga and ^{18}F, enable sophisticated radiosyntheses and feature even after a certain amount of time a sufficient activity for PET measurements. Besides a longer half-life allows for an investigation of slower biochemical processes, which causes a slower accumulation at the target side.

Since exclusively β^+-conversions can be used for PET, a high ratio of β^+-conversions is desirable. Concomitant gamma radiation, e.g. emitted from an excited daughter nucleus derived from an electron capture (EC), can interfere with the measurement, if it is detected within the coincidence energy window of the scanner.[25] Moreover, unusable concomitant radiation means a higher radiation burden for the patient.

Only if the point of origin and the point of annihilation are close to each other, a good spatial resolution can be achieved. As the travel distance correlates with $E_{\beta+\max}$, this should be low.

Another important point is the availability of the radionuclide. Many PET nuclides are cyclotron-produced, limiting their utilization to clinics and research centers with associated or nearby cyclotron, especially when it comes to short-lived radionuclides like ^{13}N, ^{15}O or ^{11}C. A few PET nuclides can be produced by a radionuclide generator in which a mother nuclide exhibits a longer half-life than its daughter nuclide. The mother is immobilized on a stationary phase whereas the daughter, which accumulates over time, can be separated and utilized as PET nuclide. A radionuclide generator enables the independent production of PET nuclides at a comparatively cheap rate. The most important generator system for PET is the ^{68}Ge/^{68}Ga generator.

The specific activity of a radionuclide must be considered as well. It is defined as the activity divided by the mass of the sum of all radioactive and stable isotopes of the element involved.[26] The unit of the A_s is $Bq \cdot mol^{-1}$ or $Bq \cdot kg^{-1}$. When the A_s is low, the patient inevitably obtains a high amount of non-radioactive but still pharmacologically active substance in order to reach a reasonable amount of radioactivity for a PET scan. This is particularly an issue, when the tracers are toxic or highly potent. Highest A_s can be reached under carrier free conditions (*c.f.*). Carrier free conditions relate to a radioisotope, which is free of other radioactive or stable isotopes of the same element, so called carriers. This can only be accomplished, when the radionuclide does not have any naturally-occurring isotopes. During the production and further processing of nuclides with naturally-occurring isotopes, the sample is inevitably contaminated with these isotopes, although they are not added on purpose. These conditions are called no carrier added (*n.c.a.*). In an *n.c.a.* production or synthesis the A_s strongly depends on the abundance of the naturally-occurring isotopes. For example, it is challenging to reach a high A_s working with ^{11}C, since ^{12}C occurs ubiquitously. Under specific circumstances it can be necessary to add carriers on purpose, which is called carrier added (*c.a.*). A *c.a.* production (e.g. (n,γ)-production pathways) or a *c.a.* synthesis leads to a very low A_s.

1.2 Radiofluorination with ^{18}F

From Table 1 it can be seen, that ^{18}F prohibits excellent properties for a usage as PET nuclide. A disadvantage is though, that fluorine in contrast to carbon, nitrogen and oxygen occurs rather rarely in biomolecules. This means, that introducing ^{18}F almost always causes a structural alteration of the underlying biomolecule, which potentially affect its chemical properties, biological function, selectivity, affinity and metabolism.[27] As a result, every new ^{18}F-labeled radiotracer needs to be evaluated thoroughly.

In many cases, ^{18}F can successfully introduced in a biomolecule by substituting either a hydrogen or a hydroxyl group. A hydrogen-fluorine exchange is possible since the van der Waals radii of both elements are comparable (r_W(fluorine)=1.47 Å; r_W(hydrogen)=1.2 Å), causing only slight structural alterations to the molecule.[27] However, hydrogen and fluorine strongly differ in their electronical properties, why an exchange leads to a major shift in the polarity of the chemical bond. A hydroxyl-fluorine exchange is feasible because of the similarity of their electronical properties. Besides, both can function as hydrogen bond acceptors and the bond length of the hydroxyl-carbon bond (1.43 Å) is comparable to the bond length of the fluorine-carbon bond (1.39 Å).[27]

Production of ^{18}F

Historically produced at a nuclear reactor[28], nowadays ^{18}F is produced at a cyclotron. Table 2 provides an overview of important production routes of ^{18}F. Depending on the target, two different chemical forms can be obtained. The usage of a water target ($[^{18}O]H_2O$ or $[^{16}O]H_2O$) leads to the formation of $[^{18}F]F^-_{aq}$ (*n.c.a.*). In order to produce $[^{18}F]F_2$, gas targets with for example ^{20}Ne filling are used. Here, ^{18}F radicals, formed during irradiation, firstly adsorb on the surface of the target. The release is then effected by the addition of $[^{19}F]F_2$ gas. This is why $[^{18}F]F_2$ comes *c.a.*, resulting in a low A_s.

Table 2. Important production routes of ^{18}F.[29]

Nuclear reaction	Target	Chemical form of ^{18}F
$^{18}O(p,n)^{18}F$	$[^{18}O]H_2O$	$[^{18}F]F^-_{aq}$
$^{16}O(^3He,p)^{18}F$	$[^{16}O]H_2O$	$[^{18}F]F^-_{aq}$
$^{20}Ne(d,\alpha)^{18}F$	^{20}Ne (0.1-0.2 % F_2)	$[^{18}F]F_2$
$^{18}O(p,n)^{18}F$	$[^{18}O]O_2$, Kr (1 % F_2)	$[^{18}F]F_2$

Methods for ^{18}F-labeling

Biomolecules can be radiolabeled with ^{18}F in three different ways: electrophilic fluorination, nucleophilic fluorination or indirect fluorination using a synthon.

In an electrophilic fluorination *c.a.* $[^{18}F]F_2$ is used. Therefore, the A_s of the fluorinated molecules is low and it is necessary to use high concentrations in order to reach a sufficient signal. Though, the electrophilic fluorination is limited to molecules which are non-toxic and do not affect the investigated biochemical process even at a high concentration. Another disadvantage is the low selectivity of the reaction caused by the high reactivity of the $[^{18}F]F_2$ gas. To overcome this problem silyl or stannyl compounds are used as precursors to introduce ^{18}F in a defined position by demetallization. Aromatic amino acids such as 6-L-$[^{18}F]$Fluordopa or 6-$[^{18}F]$Fluorotyrosine are prominent examples for clinically used radiotracers which are routinely produced via an electrophilic fluorination.[30]

Nucleophilic fluorination with $[^{18}F]F^-$ is the most common method to introduce ^{18}F into molecules.[31] Advantages over electrophilic fluorination are a better A_s, because $[^{18}F]F^-_{aq}$ can be produced *n.c.a.* and the greater selectivity of the nucleophilic fluorination. Due to the manufacturing process, $[^{18}F]F^-$ comes in water, where it exhibits a large hydrate shell. This makes it inactive for a nucleophilic substitution. Therefore, it must be dried prior to the actual labeling reaction. For drying purposes, the $[^{18}F]F^-$ is fixed on an anion exchange cartridge and then eluted with a suitable mixture of base and typically acetonitrile (MeCN). If necessary, a phase transfer catalyst is added, too. Small amounts of remaining water are removed by repeated azeotropic distillation with MeCN. For labeling purposes, the dry $[^{18}F]F^-$ is redissolved usually in a dipolar, aprotic solvent which can dissolve both non-polar and polar compounds. The absence of acidic protons suppresses the formation of hydrofluoric acid. Common solvents are MeCN, dimethyl sulfoxide (DMSO) and dimethylformamide (DMF).[32] The added base should be non-nucleophilic, but capable of trapping free protons which would otherwise lead to the formation of hydrofluoric acid. Potassium carbonate is usually used as base. The addition of phase transfer catalyst causes a complexation of the base cation (potassium if potassium carbonate is used). This "enlarges" the cation, which makes it softer, according to the Pearson acid base concept (HSAB concept). Consequently, the nucleophilia and solubility of $[^{18}F]F^-$, which is small and hard according to the HSAB concept, increases. 4,7,13,16,21,24-Hexaoxa-1,10-diazabicyclo[8.8.8]hexacosane (Kryptofix®222) is a frequently used phase transfer catalyst in radiofluorination reactions.[33] Instead of “enlarging” the counter ion of $[^{18}F]F^-$ by complexation, it is also possible to use large base cations like tetrabutylammonium or caesium cations directly. Lastly, if the precursor has acidic protons they must be protected prior to the labeling reaction and deprotected afterwards. When the fluorination reaction is carried out on aromatic compounds, it follows an S_NAr mechanism. The introduction of fluorine into an alkyl chain is carried out according to an S_N2 mechanism, which is why a Walden inversion occurs during the fluorination of chiral centers. In order to fluorinate alkyl chains, halogens (Br, I) and sulfonic acid esters (triflates, tosylates, mesylates) are used as nucleofugues, while nitro or trialkyl ammonium groups are often substituted when fluorine is introduced in aromatic compounds.[32]

In some cases, it is not possible to fluorinate a precursor molecule directly. For example, if base labile or temperature sensitive precursors like proteins are used. In these instances, fluorination can be performed with the help of a synthon, which usually is a small and easy to radiolabel molecule. For radiofluorination it is labeled with [^{18}F]F$^-$ in a first step and linked to the precursor in a second step. Through this two-step process, it is possible to circumvent the harsh reaction conditions (high temperature, basic conditions) of a direct fluorination, as the ^{18}F-synthon can be attached to the sensitive precursor molecule under mild conditions. Besides mild reaction conditions, the second reaction should be fast and tolerate several functional groups. A prominent class of reactions that meets all these criteria are click reactions. This term refers to a set of powerful, highly reliable and selective reactions which allow for a rapid synthesis in high yields.[34] One of them is the Cu(I)-catalyzed azide-alkyne cycloaddition (CuAAC) whose scope was firstly recognized by Huisgen in 1961.[35] In this reaction, a terminal azide is coupled to a terminal alkyne with the aid of a Cu(I) catalyst to form a 1,2,3-triazole. A mechanism proposed by Worrell *et al.* in 2013 is shown in Figure 3.[36] They assume that the reaction starts with the formation of a π-complex between Cu(I) and the acetylide species. Subsequently a σ-bound copper acetylide is formed enabling the coordination of a second copper atom to the triple bond. This compound then reversibly coordinates the azide species, followed by a nucleophilic attack of the β-carbon of the acetylide at terminal nitrogen of the azide forming a covalent C-N bond. The ring closure occurs after a second C-N bond is formed, resulting in a triazolide ring. Protonation then yields the 1,2,3-triazole.

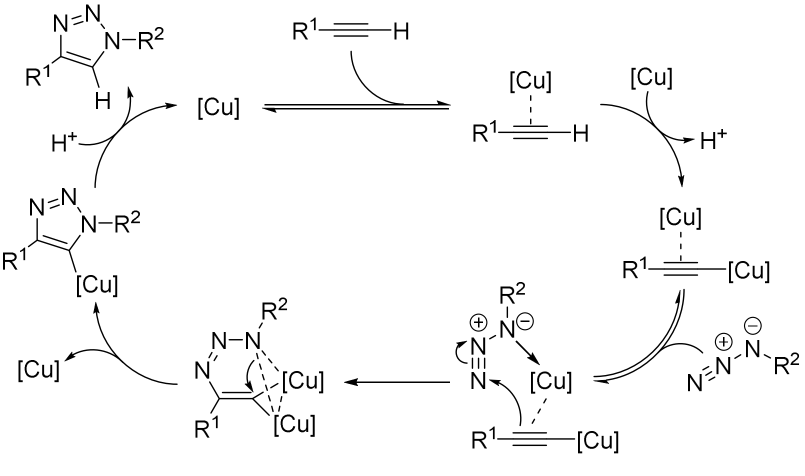

Figure 3. Proposed mechanism for the CuAAC involving two Cu atoms.[36]

The outstanding advantages of the CuAAC are its great efficiency, its regiospecificity and its rapidity even at ambient temperatures which is particularly useful if sensitive biomolecules are involved.[37] It is orthogonal with most organic functional groups and works with a great variety of both azide and alkyne reactants. Furthermore, it tolerates many different solvents and a wide range of pH values.[38] Besides that, the resulting 1,2,3-triazole structure exhibits excellent biological properties since it mimics a peptide bond.[39] If an ^{18}F-containing terminal azide or alkyne is used as a prosthetic group, it can be coupled to a biomolecule via a CuAAC in high yields and under mild reaction conditions.[37,39] This approach has been published in 2006 by Marik and Sutcliffe for the first time.[40]

The Cu(I) species can be added directly as Cu(I) salt, most commonly copper iodide, or it can be generated *in situ* by comproportionation of Cu(0) and Cu(II) or by reduction of a Cu (II) salt.[38] Here Cu(II) sulfate together with sodium ascorbate as reducing agent is a widely used system.[37] Problematic with the usage of copper is its cytotoxicity.[41] This requires a complete removal of the copper prior to an application. An alternative is the strain-promoted alkyne-azide cycloaddition (SPAAC), which makes use of strained, cyclic alkynes, whose ring strain drive the reaction and obviates the usage of the copper catalyst.[42]

1.3 Radioiodination

The half-life of ^{18}F limits the detection window of ^{18}F-fluorinated compounds to a few hours. Longer-lived radioisotopes can be advantageous over ^{18}F to image slower physiological processes or to investigate the long term fate of new chemical entities (NCEs). With the PET isotope ^{124}I ($t_{1/2}$ = 4.15 d), the γ-emitters ^{123}I ($t_{1/2}$ = 13.2 h) and ^{125}I ($t_{1/2}$ = 59.41 d) and the β^--emitter ^{131}I ($t_{1/2}$ = 8.02 d)[43], iodine offers a whole series of longer-lived radioisotopes suitable for imaging, therapy or *in vitro* studies.

The introduction of radioiodine into molecules is mainly accomplished either by electrophilic demetalation, e.g. radioiodo-destannylation, or by direct electrophilic aromatic substitution. In both cases it is necessary to generate a reactive electrophilic iodine species, since radioactive iodine is usually available as sodium iodide. This is accomplished *in situ* by the addition of oxidants, most commonly chloramine-T (CAT; *N*-chloro tosylamide sodium salt) and Iodogen™ (1,3,4,6-tetrachloro-3α,6α-diphenyl glycoluril) (Figure 4).[44] CAT is soluble in water. Thus, precursor molecules are exposed to relatively harsh oxidizing conditions, which promotes the formation of byproducts. The usage of insoluble oxidants like Iodogen™ or Iodobeads, which consist of CAT immobilized on spherical polystyrene particles, can prevent byproduct formation since the oxidants have less contact with the precursor molecules and can be removed more quickly. In comparison to a direct electrophilic radioiodination as depicted in Figure 4, electrophilic demetalation allows for a radioiodination of less reactive precursor molecules and provides a greater regioselectivity.[45] On the other hand, the synthesis of the precursors might be challenging and the inherent toxicity of many organometallic species urges a careful purification of the final product.

In general, the aliphatic carbon-iodine bond is relatively weak (D^{o}_{298}(CH_3-I)=238.9 kJ/mol)[46] and *in vivo* deiodination occurs fairly easy. Although, the bonding of iodine to aromatic carbon atoms is stronger (D^{o}_{298}(C_6H_5-I)=272.0 kJ/mol)[46], *in vivo* deiodination must always be taken into account, making an investigation of the released iodine, e.g. by measuring the thyroid uptake, inevitable.

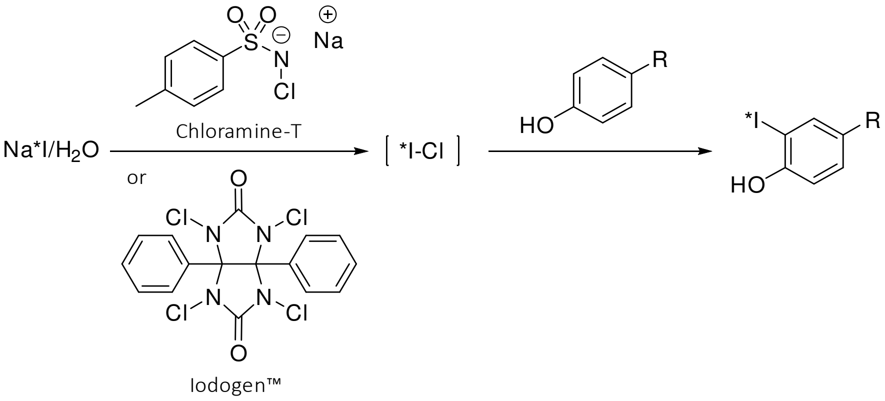
Chloramine-T
Na*I/H2O
or
[*I-Cl]
Iodogen™
HO
R
*I
HO
R

Figure 4. Direct radioiodination via electrophilic aromatic substitution. The reactive electrophilic iodine species is generated *in situ* via an oxidant like CAT or Iodogen™. Asteriks indicates a radioactive isotope.

1.4 Nanoparticulate and polymeric drug delivery systems

Many highly effective NCEs fail during development since they exhibit a poor bioavailability, short circulation times or a lack of selectivity leading to an unwanted systemic effect.[47] To achieve the required effect the dose has to be heightened resulting in an increase of undesirable side effects. In other words they have a low therapeutic index (TI). The TI is the ratio between the dose of a therapeutic that induces adverse effects that are intolerable relative to the indication and the dose that leads to the desired pharmacological effect.[48] To overcome this disadvantage, various drug delivery systems (DDS) which can improve the pharmacological properties of therapeutics have been developed during the last decades (see Figure 5).[47,49–52]

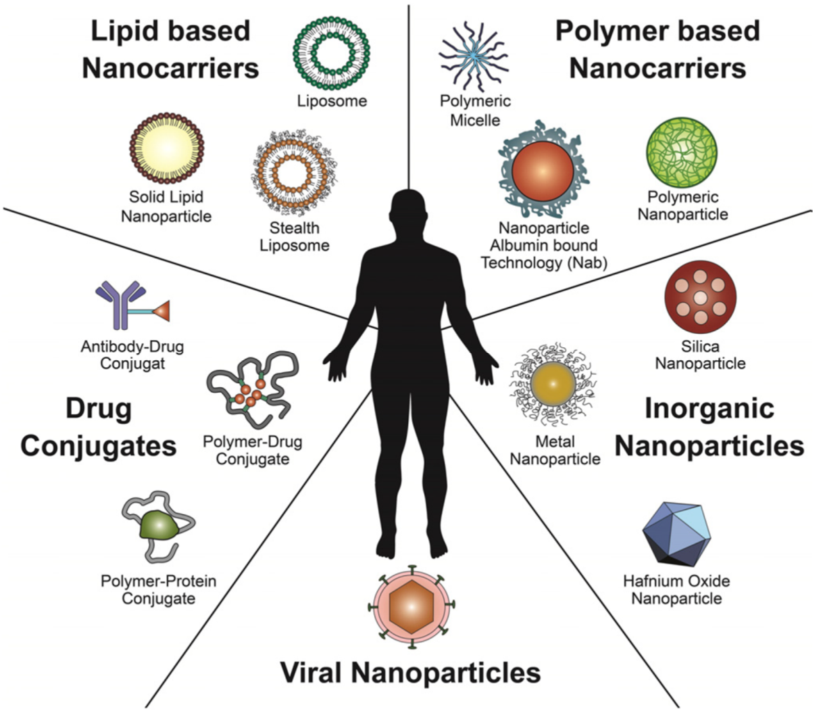
Lipid based Nanocarriers
Liposome
Solid Lipid Nanoparticle
Stealth Liposome
Polymer based Nanocarriers
Polymeric Micelle
Nanoparticle Albumin bound Technology (Nab)
Polymeric Nanoparticle
Antibody-Drug Conjugat
Drug Conjugates
Polymer-Drug Conjugate
Polymer-Protein Conjugate
Silica Nanoparticle
Metal Nanoparticle
Inorganic Nanoparticles
Hafnium Oxide Nanoparticle
Viral Nanoparticles

Figure 5. Drug delivery systems which are of importance in nanomedicine.[53]

According to the database clinicaltrials.gov, 808 nanomedicine formulations (search terms ‘liposome’, ‘nanoparticle’, ‘micelle’) were registered for clinical trials by February 2018. They exist in various shapes, such as spheres, rods, discs, filaments, cylinders, tubes, cubes, etc.[54,55] and can consist of lipids, polymers, carbon or a great variety of inorganic compounds.[56] Although they are quite different in structure and components, they all serve one or more of the following purposes: 1. Dispersibility and protection *in vivo*, 2. Targeted delivery, 3. Controlled release.

1. Dispersibility and protection *in vivo*: Therapeutics that exhibit a low water solubility can be transferred in a stable aqueous dispersion prior to injection with the help of a DDS. This improves their bioavailability and thus enhances their efficacy. After the injection the therapeutic is exposed to enzymatic degradation, excretion and uptake by the immune system. A suitable DDS can prevent or at least delay this processes.

2. Targeted delivery: The encapsulation of a therapeutic can increase its concentration at the target side. There are two different mechanisms by which the targeting can proceed, passively and actively. Passive targeting relates to the enhanced permeability and retention (EPR) effect associated with tumor tissue. It was firstly described by Matsumura and Maeda in 1986.[57] The EPR effect refers to the phenomenon that macromolecules of a sufficient size and circulation time accumulate at much higher concentrations in tumor tissues than in normal tissues or organs.[58] This is caused by pathological alterations of tumorous tissue. Due to the rapid growth of tumors, the endothelial cell layer that normally separates the bloodstream from the surrounding tissue has fenestrations that allow macromolecules and nanoparticles to penetrate into the tumor tissue without hindrance. Once inside the tumor, a reduced or completely missing lymph drainage causes that they are not removed and accumulate in the tumor tissue. Active targeting relies on specific targeting vectors crafted on the surface of the DDSs, which bind to receptors expressed on targeted cells or tissues. This method is not limited to tumor tissue but enables the targeting of all types of cells.

3. Controlled release: Controlled release is an umbrella term for any type of effect DDSs have on the release of a cargo. Principal forms are sustained release, internal or external stimuli-sensitive release.[56] Sustained release means that the encapsulated drugs are released successively from the nanoparticle over an extended period of time. For this purpose the nanoparticle must be biodegradable, so that they are degraded over time. If they are non-biodegradable, they must be permeable, so that a slow diffusion of the cargo can occur. In this way it is possible to maintain a constant plasma level of the drug without multiple administrations. Furthermore it enables the administration of lower doses for therapeutics with a high initial excretion or metabolization rate. However, a substantial deficit of sustained release

systems is that they are not specific to a target site. To overcome this drawback, stimulus responsive DDSs have been developed.[59,60] Here, the stimulus can be internal, like a change in pH in pathological areas or an increase in temperature caused by an inflammation. A second approach is the usage of an external stimulus. Magnetic fields can concentrate magneto-sensitive DDSs in desired areas for instance or exposure to ultrasound can facilitate the penetration of DDSs into cells and releases the cargo of ultrasound-sensitive DDSs.[59]

1.4.1 Liposomes

One prominent class of DDSs are liposomes, which have been first described in 1965 by Bangham *et al*.[61] Since then they have been actively investigated with success. In the 1970s pioneers as Gregory Gregoriadis understood their potential as drug delivery systems.[62–65] In 1995 Doxil®, liposome-encapsulated doxorubicin, became the first FDA-approved nano-drug.[66] Others like DaunoXome® (1996) and Depocyt® (1999) followed.[67] In 2017 there have been 15 liposomal drugs on the market.[67] Liposomes are spherical vesicles which mainly consist of phospholipids. Phospholipids are amphiphilic molecules with a hydrophilic head and two hydrophobic tails. In an aqueous environment they arrange in such way, that the hydrophilic heads are exposed to the aqueous surrounding whereas the lipophilic tails interact with one another. To “avoid edges”[68] they tend to form closed structures such as liposomes (Figure 6) which can vary in size and lamellarity. Because of the hydrophilic core and the lipophilic bilayer they enable both the transportation of hydrophilic and lipophilic drugs. Besides that and the afore mentioned advantages of DDSs in general, liposomes additionally are biodegradable and have an excellent biocompatibility as well as a low toxicity since phospholipids as their main components are also the building blocks of cellular membranes.[69] To modulate the stability of a liposome, the composition and the phase transition temperature (T_M) of the phospholipids are especially important. Below their T_M phospholipids exist in the gel state, which makes the liposomes more stable and less leaky for encapsulated therapeutics. Above their T_M phospholipids are in the fluid state. This means for an increased water permeability and more leaky liposomes.[70] The stability can be further enhanced by adding cholesterol, which increases the packing of phospholipid molecules, making the liposomes less permeable.[71,72] Moreover, the tendency to aggregate is reduced in cholesterol-containing liposomes[73] and they better withstand severe shear stress.[74] Frequently used phospholipid/cholesterol ratios are 1:1 ore 2:1.[75] Another important issue affecting the behavior of liposomes is their size. For a utilization as drug delivery system an elongated circulation time is favorable. A lower size limit for maximization of the circulation time is the renal filtration cutoff size. Particles with an hydrodynamic radius (R_h)<5.5 nm are rapidly cleared via the renal pathway.[76] A second lower size limit is given by the vascular fenestration of the liver. Here the filtration cutoff is 50-100 nm, thus particles smaller than 50 nm will interact with hepatocytes.[77] The upper limit of particle size is determined by splenic filtration. Particles exceeding

200 nm tend to accumulate in the spleen.[78] Liposome fate is not only affected by size and composition but also by charge. Depending on the composition, liposomes can be positively, negatively or neutrally charged. Positively charged liposomes interact well with negatively charged cell membranes and DNA, which is why these types of liposomes are used in gene therapy. A negative charge in many cases leads to a much more rapid clearance from the blood.[79–81]

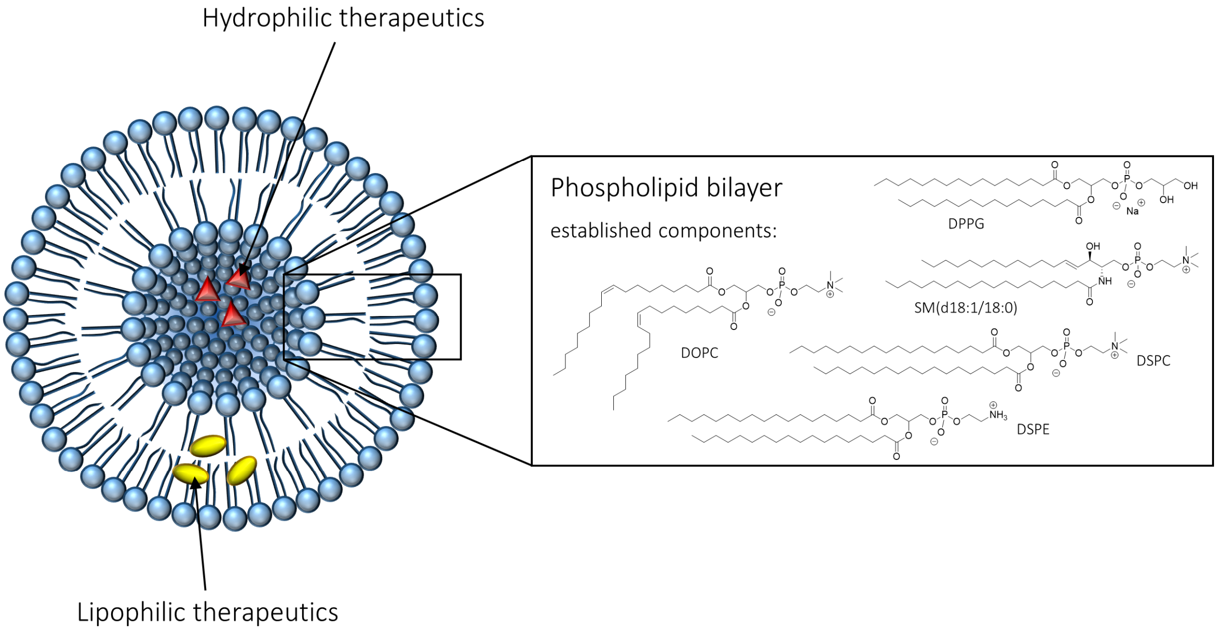

Figure 6. Schematic cross section of a unilamellar liposome with encapsulated therapeutics. DOPC: 1,2-dioleoyl-*sn*-glycero-3-phosphocholine, DPPG: 1,2-dipalmitoyl-*sn*-glycero-3-phosphoglycerol, SM(d18:1/18:0): *N*-stearoyl sphingomyelin, DSPC: 1,2-distearoyl-*sn*-glycero-3-phosphocholine, DSPE: 1,2-distearoyl-*sn*-glycero-3-phosphoethanolamine.

Although liposomes are made from phospholipids and mimic biomembranes, they are still foreign to the body. On intravenous injection, conventional liposomes are rapidly detected by the mononuclear phagocyte system (MPS) and are taken up in liver and spleen.[82] As a result, the *in vivo* circulation time is minimized which is unfavorable if the MPS is not the target site.[83] A breakthrough was achieved by using poly(ethylene glycol) (PEG) chains as a stabilizing polymer shell (stealth liposomes) (Figure 7B).[84,85] In this approach PEG is linked covalently to cholesterol or phospholipids to ensure anchoring in the lipid bilayer. The hydrophilic polymer layer of the stealth liposomes prevents detection by the MPS via steric repulsion, resulting in prolonged retention in the blood, reduced MPS uptake and reduced aggregation in serum. First described in the early 1990s[86–88], stealth liposomes are now an established system used in clinical practice.[89] Current research aims to make the PEG shell cleavable upon a stimulus thus facilitating the release of the cargo at the target site (Figure 7C).[90–93] Additionally, effort is put into the development of other shielding polymers advantageous over PEG (Figure 7A). For example, Frey and coworker reported the synthesis of different branched polyether lipids based on polyglycerol (PG) for liposome preparation.[94] Romberg *et al.* evaluated poly(amino acid)s as coating polymers for stealth liposomes[95] and Whiteman *et al*. successfully tested poly(*N*-(2-hydroxypropyl)methacrylamide) (HPMA) for steric protection of liposomes.[96]

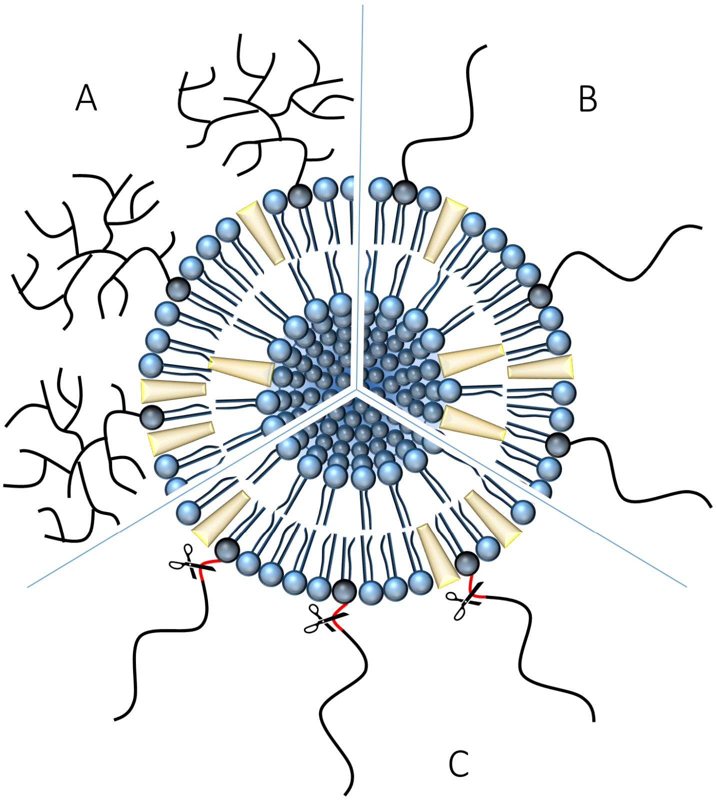

Figure 7. Schematic cross section of stealth liposomes consisting of phospholipids and cholesterol (in yellow), shielded by hyperbranched PG (A), shielded by linear PEG (B) and shielded by cleavable PEG (C).

1.4.2 HPMA-based polymers

Shielding of liposomes is not the only scope of HPMA polymers. They can also be utilized as DDSs by themselves. By binding a therapeutic covalently on a synthetic polymer backbone, it is possible to improve the pharmacological properties of a drug. This concept was firstly proposed by Helmut Ringsdorf in 1975.[97] He elaborated a polymer therapeutic consisting of at least three different units. One area serves the solubility of the whole macromolecule. Hereby, the solubility can either be mediated by possible side chains or by the polymeric backbone itself. The second area is the region where the therapeutic is bound. Here either a cleavable or firm bond is possible. The third area includes the targeting moiety, which can either be an attached molecule or a non-specific resorption enhancer like a polycationic structure or just an increased molecular weight for the exploitation of the EPR effect. Figure 8 shows the conceptual design of such a polymer therapeutic. In this regard, poly(HPMA) and PEG are up to now the most widely investigated polymeric backbones.[98]

Poly(HPMA) satisfies major requirements for utilization in the clinical. It is non-toxic, non-immunogenic and highly water soluble.[99] In comparison to PEG, which is most commonly functionalized at the end groups only, poly(HPMA) has the advantage of multifunctionality holding a high drug-carrying capacity.

Poly(HPMA) was initially investigated as plasma expander in the 1970s.[100] Subsequently, collaborative research of Duncan and colleagues in the 1980s resulted in two HPMA copolymer-doxorubicin conjugates (PK1 and PK2).[101] PK1 (Figure 9) became the first polymer-anticancer drug conjugate to enter clinical trials in 1994.[102]

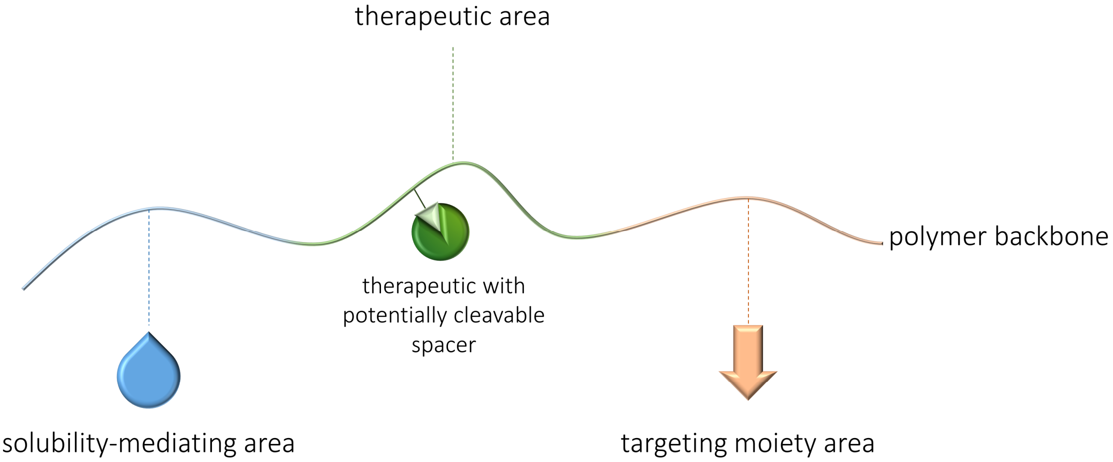
therapeutic area
polymer backbone
therapeutic with potentially cleavable spacer
solubility-mediating area
targeting moiety area

Figure 8. Conceptual design of a polymer therapeutic conceived by H. Ringsdorf.

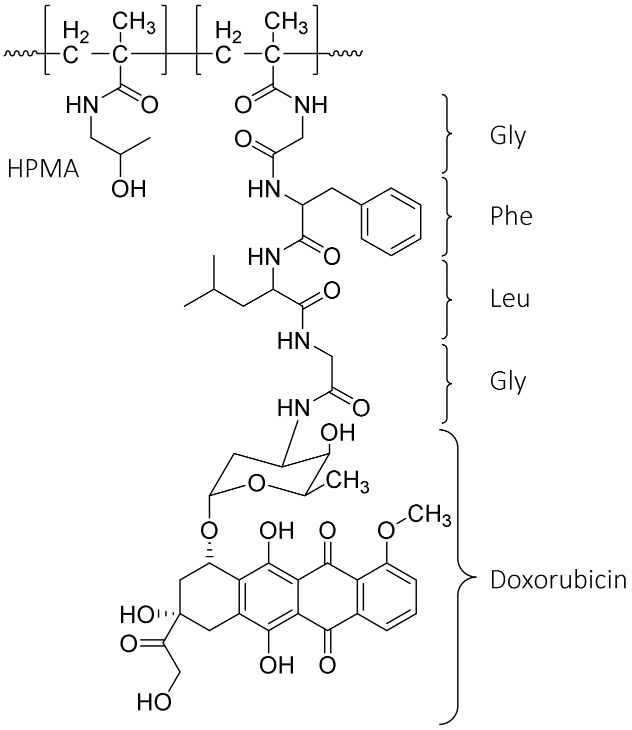
HPMA
Gly
Phe
Leu
Gly
Doxorubicin

Figure 9. Molecular structure of the HPMA copolymer-doxorubicin conjugates PK1 (molecular weight: ~30,000 Da, doxorubicin content: ~8 wt%) with peptidyl Gly-Phe-Leu-Gly side-chains which are amenable to degradation by lysosomal enzymes.[103]

Despite the various advantageous properties of HPMA as backbone for polymer therapeutics and several HPMA drug conjugates entered clinical trials, there is no HPMA-based polymer therapeutics on the market up till now. One reason for this is, that poly(HPMA) is not inherently biodegradable. Thus, the molecular weight of first generation HPMA-based polymer-drug conjugates was limited to 45 kDa (limit for renal excretion).[104] The application of molecular weights above 45 kDa leads to an accumulation of the polymer in the body whereas a lower molecular weight by implication lowers the circulation time of the polymer conjugate, which simultaneously decreases its pharmaceutical efficiency. In conclusion, the lack of biodegradability confined the molecular weight of first generation HPMA-based polymer-drug conjugates to suboptimal molecular weights. A second reason is the broad distribution of molecular weight during synthesis of poly(HPMA) via free radical polymerization, which was applied for the production of the clinically tested HPMA therapeutics.[105] From the clinical standpoint, polymer therapeutics are NCEs that must be well characterized and whose production and purification must be reproducible to guarantee homogeneity of the final conjugates. To archive narrow molecular weight distributed HPMA copolymer precursors, further fractionation methods were applied.[105] However, advances in polymer chemistry opened the doors for a second generation of HPMA polymers. The introduction of controlled radical polymerization techniques like atom transfer radical polymerization (ATRP)[106] or reversible addition-fragmentation chain transfer (RAFT) polymerization[107,108] enabled the synthesis of well-defined HPMA-based polymers with a narrow molecular weight distribution.[109,110] The combination of RAFT polymerization with reactive ester chemistry by using functional reactive ester monomers allowed for the straightforward introduction of multiple functionalities.[111] Here, a precursor polymer is synthesized via RAFT polymerization and the desired functionalities are introduced afterwards via polymeranalogous reaction (Figure 10). RAFT polymerization followed by polymer coupling with a biodegradable coupling agent allowed for the synthesis of well-defined backbone-degradable HPMA polymer conjugates.[112–114] This approach enables the application of HPMA-based polymer-drug conjugates with molecular weights above the renal threshold.

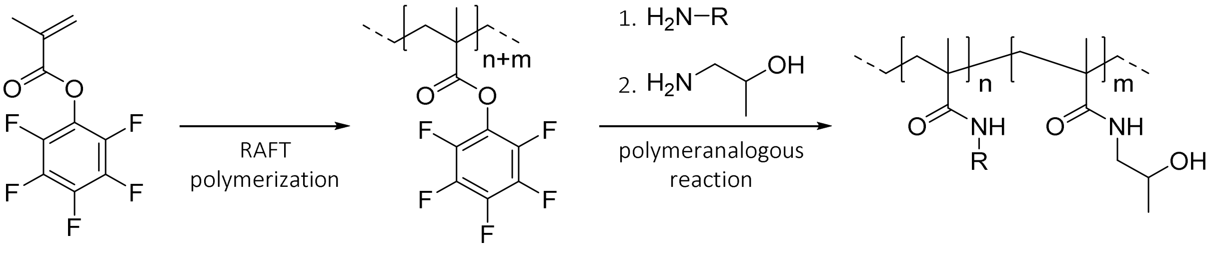

Figure 10. RAFT polymerization with reactive ester monomers, followed by polymeranalogous reaction, yielding in functionalized HPMA polymers. R = any functionality.

1.4.3 Imaging of drug delivery (systems)

In addition to an exclusively therapeutic utilization, increasing effort is put in the imaging of nanomedicine formulations. Non-invasive, functional imaging techniques are of great value, when it comes to the evaluation of DDSs. Frequently used techniques are optical imaging (OI) as well as single photon emission computed tomography (SPECT) and PET.

Fluorescence reflectance imaging, which is by far the most extensively used OI technique employed in drug delivery research, requires the attachment of near-infrared fluorophores. Different emission wavelengths of the fluorophores allow to image multiple fluorophores at the same time in the same animal. Compared to PET and SPECT it is less expensive and less time-consuming. However, its poor penetration depth (<1 cm) and its lack of 3D information, which make an absolute quantification impossible, are major drawbacks of this technique.[115,116] Fluorescence molecular tomography, which is a 3D OI technique, allowing for a more in-depth (<10 cm) and more quantitative investigation, was developed to overcome the afore-mentioned deficits. However, the diffusive scattering of fluorescence signals in the body, as well as the strong light absorption by highly perfused organs and tissues remain challenging, when it comes to quantification.[115,116]

SPECT requires gamma-emitting radionuclides (primarily ^{99m}Tc ($t_{1/2}$ = 6.006 h)).[13] The emitted gamma radiation of a specific energy is detected by a rotating gamma camera, which acquires 2-D images. Mechanical collimation, generated by lead septa in front of the scintillation detectors of the gamma camera, allow for a spatial allocation of the detected radiation. Computer-assisted reconstruction gives a 3D image of the distribution of the radiolabeled molecules. Although more expensive than OI, SPECT as well as PET, which is described in detail in chapter 1.1, have a much higher penetration depth and are quantifiable. So far, a spatial resolution of 1-2 mm[115] (small animal scanners) is achievable with both methods, yet PET resolution exceeds SPECT resolution in the clinic.

The mentioned techniques enable the non-invasive tracking of labeled drug delivery systems *in vitro* and *in vivo*, obtaining detailed information on their stability, blood circulation time, clearance mechanism, clearance rate as well as accumulation at the target side. These information are crucial during preclinical development, as they reveal structure-property relationships in order to design the most suitable system. Figure 11 shows examples in which PET was utilized to analyze the biodistribution of nanomedicine formulations varying in size or composition in order to reveal structure-property relationships.

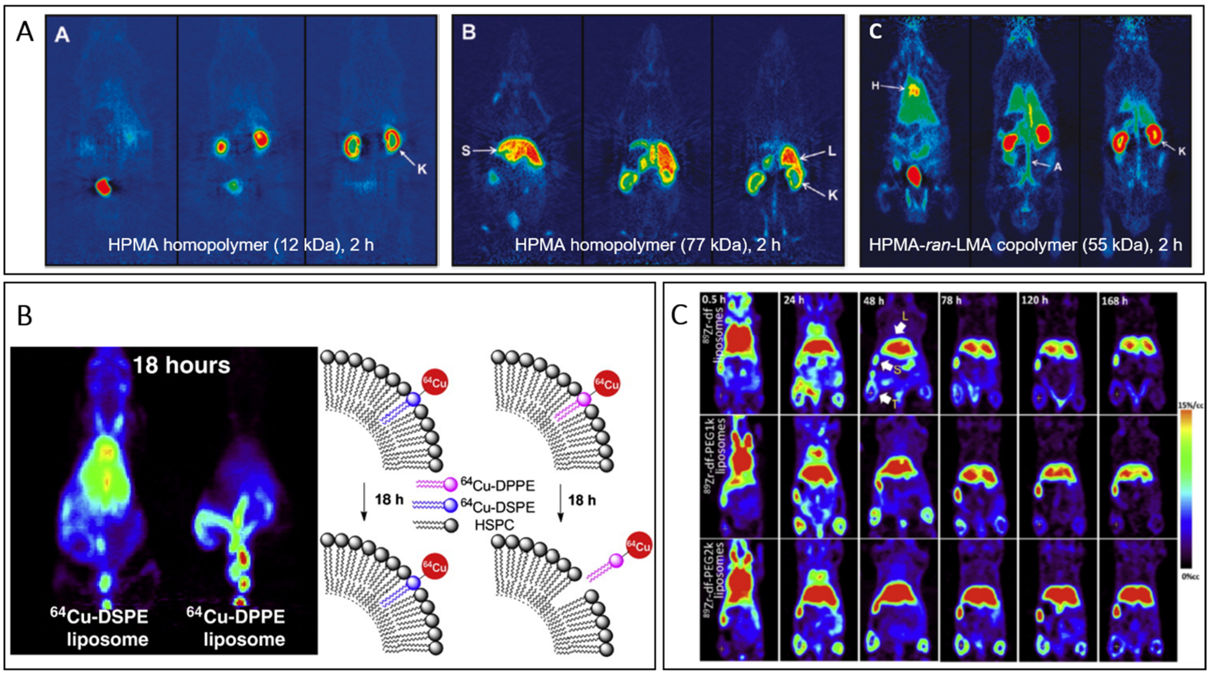
A
A
HPMA homopolymer (12 kDa), 2 h
K
B
S
L
K
HPMA homopolymer (77 kDa), 2 h
C
H
A
K
HPMA-*ran*-LMA copolymer (55 kDa), 2 h
B
18 hours
64Cu-DSPE liposome
64Cu-DPPE liposome
64Cu
18 h
64Cu-DPPE
64Cu-DSPE
HSPC
C
0.5 h
24 h
48 h
78 h
120 h
168 h
L
S
T
89Zr-df liposomes
89Zr-df-PEG1k liposomes
89Zr-df-PEG2k liposomes
15%/cc
0%cc

Figure 11. PET images of different DDSs varying in size or composition. Panel A[117]: Summed whole body PET images in different depths 120-135 min after intravenous (i.v.) injection of HPMA-based polymers radiolabeled with ^{18}F. The lightweight homopolymer (left) showed renal excretion via the kidneys (K), whereas the heavier homopolymer (middle) exhibited a much lesser renal excretion and uptake in spleen (S) and liver (L) instead. For the random (*ran*) HPMA copolymers consisting of HPMA and hydrophobic lauryl methacrylate (LMA) comonomers the blood circulation time (A: aorta, H: heart) was elongated. Panel B[118]: Summed whole body PET images 18-18.5 after i.v. injection of long circulating liposomes containing ^{64}Cu-labeled distearoyl and dipalmitoyl phosphatidylethanolamine (DSPE and DPPE). PET images show that ^{64}Cu-DSPE remained associated with the liposomes which was not the case for ^{64}Cu-DPPE. Panel C[119]: Whole body PET images revealing the pharmacokinetics of ^{89}Zr-labeled long circulating liposomes in a time span of 168 h. The blood clearance rate of all three liposomal formulations was similar. Radioactivity from ^{89}Zr-desferrioxamine (df)-PEG2k liposomes exhibited a longer retention in the tumors (T; right and left flank) than radioactivity from ^{89}Zr-df and ^{89}Zr-df-PEG1k liposomes.

However, the approach is not limited exclusively to the imaging of drug delivery systems. It is also possible to image the drug delivery, meaning the release of encapsulated molecules from DDSs. By loading radiolabeled therapeutics into evaluated DDSs, it is possible to gain information about drug release as well as drug accumulation at the target side. For comparability reasons it is inevitable to investigate the *in vivo* behavior of the unloaded DDS and the non-encapsulated therapeutic as well.

In conclusion, imaging is of great value in the development process of DDSs and significantly assists in predicting the therapeutic potential of nanomedicine formulations.

1.5 References

(1) Garrett, A. B. Radioactive Tracers: George de Hevesy. *J. Chem. Educ.* **1963**, *40*, 36.

(2) Hevesy, G. The Absorption and Translocation of Lead by Plants: A Contribution to the Application of the Method of Radioactive Indicators in the Investigation of the Change of Substance in Plants. *Biochem. J.* **1923**, *17*, 439–445.

(3) Niese, S. George de Hevesy (1885–1966): discoverer of hafnium, founder of radioanalytical chemistry and X-ray fluorescence analysis and father of nuclear medicine. *J. Radioanal. Nucl.*

Chem. 2017, *311*, 1035–1041.

(4) Ter-Pogossian, M. M.; Phelps, M. E.; Hoffman, E. J.; Mullani, N. A. A Positron-Emission Transaxial Tomograph for Nuclear Imaging (PETT). *Radiology* 1975, *114*, 89–98.

(5) Gambhir, S. S. Molecular Imaging of Cancer with Positron Emission Tomography. *Nat. Rev. Cancer* 2002, *2*, 683–693.

(6) Weber, W. A. Quantitative analysis of PET studies. *Radiother. Oncol.* 2010, *96*, 308–310.

(7) Levin, C. S. Primer on molecular imaging technology. *Eur. J. Nucl. Med. Mol. Imaging* 2005, *32*, S325–S345.

(8) Ache, H. J. Chemie des Positrons und Positroniums. *Angew. Chemie* 1972, *84*, 234–255.

(9) Abuelhia, E.; Kacperski, K.; Spyrou, N. M. Three-photon annihilation in PET: 2D imaging experiments. *J. Radioanal. Nucl. Chem.* 2007, *271*, 489–495.

(10) Korzhik, M.; Fedorov, A.; Annenkov, A.; Borissevitch, A.; Dossovitski, A.; Missevitch, O. Development of scintillation materials for PET scanners. *Nucl. Instruments Methods Phys. Res. Sect. A Accel. Spectrometers, Detect. Assoc. Equip.* 2007, *571*, 122–125.

(11) Humm, J. L.; Rosenfeld, A.; Del Guerra, A. From PET Detectors to PET Scanners. *Eur. J. Nucl. Med. Mol. Imaging* 2003, *30*, 1574–1597.

(12) Boellaard, R.; van Lingen, A.; Lammertsma, A. A. Experimental and Clinical Evaluation of Iterative Reconstruction (OSEM) in Dynamic PET: Quantitative Characteristics and Effects on Kinetic Modeling. *J. Nucl. Med.* 2001, *42*, 808–817.

(13) Herzog, H.; Rösch, F. Chemie und Physik der Bildgebung: PET- und SPECT-Technik. *Pharm. Unserer Zeit* 2005, *34*, 468–473.

(14) Townsend, D. W. Positron Emission Tomography/Computed Tomography. *Semin. Nucl. Med.* 2008, *38*, 152–166.

(15) Herzog, H.; Pietrzyk, U.; Shah, N. J.; Ziemons, K. The current state, challenges and perspectives of MR-PET. *Neuroimage* 2010, *49*, 2072–2082.

(16) Kinahan, P. E.; Hasegawa, B. H.; Beyer, T. X-Ray-Based Attenuation Correction for Positron Emission Tomography/Computed Tomography Scanners. *Semin. Nucl. Med.* 2003, *33*, 166–179.

(17) Mehranian, A.; Arabi, H.; Zaidi, H. Vision 20/20: Magnetic Resonance Imaging-Guided Attenuation Correction in PET/MRI: Challenges, Solutions, and Opportunities. *Med. Phys.* 2016, *43*, 1130–1155.

(18) Bé, M.-M.; Chisté, V.; Dulieu, C.; Browne, E.; Chechev, V.; Kuzmenko, N.; Helmer, R.; Nichols, A.; Schönfeld, E.; Dersch, R. *Table of Radionuclides (Vol. 1 - A = 1 to 150)*; Le Bureau International des Poids et Mesures: Sèvres, 2004.

(19) Roesch, F. Scandium-44: Benefits of a Long-Lived PET Radionuclide Available from the ^{44}Ti/^{44}Sc Generator System. *Curr. Radiopharm.* 2012, *5*, 187–201.

(20) Anderson, C. J.; Green, M. A.; Fujibayashi, Y. Chemistry of Copper Radionuclides and Radiopharmaceutical Products. In *Handbook of Radiopharmaceuicals: Radiochemistry and Applications*; Welch, M. J.; Redvanly, C. S., Eds.; Wiley: Chichester, 2003.

(21) Rowshanfarzad, P.; Jalilian, A. R.; Kiyomarsi, M.; Sabet, M.; Karimian, A. R.; Moradkhani, S.; Mirzaii, M. Production, Quality Control and Initial Imaging Studies of [^{82m}Rb]RbCl for PET Studies. *Nukleonika* 2006, *51*, 209–215.

(22) Rösch, F.; Knapp, F. F. Radionuclide Generators. In *Handbook of Nuclear Chemistry Volume 4: Radiochemistry and Radiopharmaceutical Chemistry in Life Science*; Rösch, F.; Vértes, A.; Nagy, S.; Klencsár, Z., Eds.; Kluwer Academic Publishers: Dordrecht, 2003.

(23) Holland, J. P.; Sheh, Y.; Lewis, J. S. Standardized Methods for the Production of High Specific-Activity Zirconium-89. *Nucl. Med. Biol.* 2009, *36*, 729–739.

(24) Clark, J. C.; Aigbirhio, F. I. Chemistry of Nitrogen-13 and Oxygen-15. In *Handbook of Radiopharmaceuicals: Radiochemistry and Applications*; Welch, M. J.; Redvanly, C. S., Eds.; Wiley: Chichester, 2003.

(25) Williams, H. A.; Robinson, S.; Julyan, P.; Zweit, J.; Hastings, D. A Comparison of PET Imaging Characteristics of Various Copper Radioisotopes. *Eur. J. Nucl. Med. Mol. Imaging* 2005, *32*, 1473–1480.

(26) de Goeij, J. J. M.; Bonardi, M. L. How do we define the concepts specific activity, radioactive concentration, carrier, carrier-free and no-carrier-added? *J. Radioanal. Nucl. Chem.* 2005, *263*, 13–18.

(27) Park, B. K.; Kitteringham, N. R.; O’Neill, P. M. Metabolism of Fluorine-Containing Drugs. *Annu. Rev. Pharmacol. Toxicol.* 2001, *41*, 443–470.

(28) Maruyama, Y. Production of Fluorine-18 by Small Research Reactor. *J. Nucl. Sci. Technol.* 1967, *4*, 185–189.

(29) Guillaume, M.; Luxen, A.; Nebeling, B.; Argentini, M.; Clark, J. C.; Pike, V. W. Recommendations for Fluorine-18 Production. *Int. J. Radiat. Appl. Instrumentation. Part A. Appl. Radiat. Isot.* 1991, *42*, 749–762.

(30) Ross, T. L.; Wester, H. J. ^{18}F: Labeling Chemistry and Labeled Compounds. In *Handbook of Nuclear Chemistry Volume 4: Radiochemistry and Radiopharmaceutical Chemistry in Life Science*; Rösch, F.; Vértes, A.; Nagy, S.; Klencsár, Z., Eds.; Kluwer Academic Publishers: Dordrecht, 2003.

(31) Bauser, M.; Lehmann, L. Positronen-Emissions-Tomographie. *Chemie unserer Zeit* 2012, *46*, 80–99.

(32) Jacobson, O.; Kiesewetter, D. O.; Chen, X. Fluorine-18 Radiochemistry, Labeling Strategies and Synthetic Routes. *Bioconjug. Chem.* 2015, *26*, 1–18.

(33) Ametamey, S. M.; Honer, M.; Schubiger, P. A. Molecular Imaging with PET. *Chem. Rev.* 2008, *108*, 1501–1516.

(34) Kolb, H. C.; Finn, M. G.; Sharpless, K. B. Click Chemistry: Diverse Chemical Function from a Few Good Reactions. *Angew. Chemie Int. Ed.* 2001, *40*, 2004–2021.

(35) Huisgen, R. 1,3-Dipolar Cycloadditions. *Proc. Chem. Soc.* 1961, *0*, 357.

(36) Worrell, B. T.; Malik, J. A.; Fokin, V. V. Direct Evidence of a Dinuclear Copper Intermediate in Cu(I)-Catalyzed Azide-Alkyne Cycloadditions. *Science (80-.).* 2013, *340*, 457–460.

(37) Kettenbach, K.; Schieferstein, H.; Ross, T. L. ^{18}F-Labeling Using Click Cycloadditions. *Biomed Res. Int.* 2014, *2014*, Article ID 361329.

(38) Bock, V. D.; Hiemstra, H.; Van Maarseveen, J. H. Cu^{I}-Catalyzed Alkyne-Azide “Click” Cycloadditions from a Mechanistic and Synthetic Perspective. *European J. Org. Chem.* 2006, *2006*, 51–68.

(39) Ross, T. L. The Click Chemistry Approach Applied to Fluorine-18. *Curr. Radiopharm.* 2010, *3*, 202–223.

(40) Marik, J.; Sutcliffe, J. L. Click for PET: rapid preparation of [^{18}F]fluoropeptides using Cu^{I} catalyzed 1,3-dipolar cycloaddition. *Tetrahedron Lett.* 2006, *47*, 6681–6684.

(41) Gaetke, L. M.; Chow, C. K. Copper toxicity, oxidative stress, and antioxidant nutrients. *Toxicology* 2003, *189*, 147–163.

(42) Debets, M. F.; Van Berkel, S. S.; Dommerholt, J.; Dirks, a. J.; Rutjes, F. P. J. T.; Van Delft, F. L. Bioconjugation with Strained Alkenes and Alkynes. *Acc. Chem. Res.* 2011, *44*, 805–815.

(43) Rösch, F. *Nuclear- and Radiochemistry Volume 1: Introduction*; Walter de Gruyter GmbH: Berlin/Boston, 2014.

(44) Rösch, F. *Nuclear- and Radiochemistry Volume 2: Modern Applications*; Walter de Gruyter GmbH: Berlin/Boston, 2016.

(45) Vallabhajosula, S. *Molecular Imaging : Radiopharmaceuticals for PET and SPECT*; Springer-Verlag: Berlin/Heidelberg, 2009.

(46) Luo, Y.-R. *Comprehensive Handbook of Chemical Bond Energies*; CRC Press: Boca Raton, Florida, 2007.

(47) Shi, J.; Votruba, A. R.; Farokhzad, O. C.; Langer, R. Nanotechnology in Drug Delivery and Tissue Engineering: From Discovery to Applications. *Nano Lett.* 2010, *10*, 3223–3230.

(48) Muller, P. Y.; Milton, M. N. The determination and interpretation of the therapeutic index in drug development. *Nat. Rev. Drug Discov.* 2012, *11*, 751–761.

(49) Parveen, S.; Misra, R.; Sahoo, S. K. Nanoparticles: A Boon to Drug Delivery, Therapeutics, Diagnostics and Imaging. *Nanomedicine Nanotechnology, Biol. Med.* 2012, *8*, 147–166.

(50) Wilczewska, A. Z.; Niemirowicz, K.; Markiewicz, K. H.; Car, H. Nanoparticles as Drug Delivery Systems. *Pharmacol. Reports* 2012, *64*, 1020–1037.

(51) Duncan, R.; Gaspar, R. Nanomedicine(s) under the Microscope. *Mol. Pharm.* 2011, *8*, 2101–2141.

(52) Shi, J.; Kantoff, P. W.; Wooster, R.; Farokhzad, O. C. Cancer nanomedicine: progress, challenges and opportunities. *Nat. Rev. Cancer* 2016, *17*, 20–37.

(53) Wicki, A.; Witzigmann, D.; Balasubramanian, V.; Huwyler, J. Nanomedicine in cancer therapy: Challenges, opportunities, and clinical applications. *J. Control. Release* 2015, *200*, 138–157.

(54) Kinnear, C.; Moore, T. L.; Rodriguez-Lorenzo, L.; Rothen-Rutishauser, B.; Petri-Fink, A. Form Follows Function: Nanoparticle Shape and Its Implications for Nanomedicine. *Chem. Rev.* 2017, *117*, 11476–11521.

(55) Daum, N.; Tscheka, C.; Neumeyer, A.; Schneider, M. Novel Approaches for Drug Delivery Systems in Nanomedicine: Effects of Particle Design and Shape. *Wiley Interdiscip. Rev. Nanomedicine Nanobiotechnology* 2012, *4*, 52–65.

(56) Chen, G.; Roy, I.; Yang, C.; Prasad, P. N. Nanochemistry and Nanomedicine for Nanoparticle-Based Diagnostics and Therapy. *Chem. Rev.* 2016, *116*, 2826–2885.

(57) Matsumura, Y.; Maeda, H. A New Concept for Macromolecular Therapeutics in Cancer Chemotherapy: Mechanism of Tumoritropic Accumulation of Proteins and the Antitumor Agent Smancs. *Cancer Res.* 1986, *46*, 6387–6392.

(58) Maeda, H. The Enhanced Permeability and Retention (EPR) Effect in Tumor Vasculature: The Key Role of Tumor-Selective Macromolecular Drug Targeting. *Adv. Enzyme Regul.* 2001, *41*, 189–207.

(59) Torchilin, V. Multifunctional and stimuli-sensitive pharmaceutical nanocarriers. *Eur. J. Pharm.*

Biopharm. 2009, *71*, 431–444.

(60) Li, Y.; Gao, G. H.; Lee, D. S. Stimulus-Sensitive Polymeric Nanoparticles and Their Applications as Drug and Gene Carriers. *Adv. Healthc. Mater.* 2013, *2*, 388–417.

(61) Bangham, A. D.; Standish, M. M.; Watkins, J. C. Diffusion of Univalent Ions across the Lamellae of Swollen Phospholipids. *J. Mol. Biol.* 1965, *13*, 238–252.

(62) Gregoriadis, G.; Ryman, B. E. Liposomes as Carriers of Enzymes or Drugs: A New Approach to the Treatment of Storage Diseases. *Biochem. J.* 1971, *124*, 58P.

(63) Gregoriadis, G. Drug Entrapment in Liposomes. *FEBS Lett.* 1973, *36*, 292–296.

(64) Gregoriadis, G. The Carrier Potential of Liposomes in Biology and Medicine. Part 1. *N. Engl. J. Med.* 1976, *295*, 704–710.

(65) Gregoriadis, G. The Carrier Potential of Liposomes in Biology and Medicine. Part 2. *N. Engl. J. Med.* 1976, *295*, 765–770.

(66) Barenholz, Y. Doxil® - the first FDA-approved nano-drug: Lessons learned. *J. Control. Release* 2012, *160*, 117–134.

(67) Bulbake, U.; Doppalapudi, S.; Kommineni, N.; Khan, W. Liposomal Formulations in Clinical Use: An Updated Review. *Pharmaceutics* 2017, *9*, 12.

(68) Frolov, V. A.; Shnyrova, A. V; Zimmerberg, J. Lipid Polymorphisms and Membrane Shape. *Cold Spring Harb. Perspect. Biol.* 2011, *3*, a004747.

(69) Akbarzadeh, A.; Rezaei-Sadabady, R.; Davaran, S.; Joo, S. W.; Zarghami, N.; Hanifehpour, Y.; Samiei, M.; Kouhi, M.; Nejati-Koshki, K. Liposome: classification, preparation, and applications. *Nanoscale Res. Lett.* 2013, *8*, 102.

(70) Pattni, B. S.; Chupin, V. V.; Torchilin, V. P. New Developments in Liposomal Drug Delivery. *Chem. Rev.* 2015, *115*, 10938–10966.

(71) Demel, R. A.; De Kruyff, B. The Function of Sterols in Membranes. *Biochim. Biophys. Acta - Rev. Biomembr.* 1976, *457*, 109–132.

(72) Papahadjopoulos, D.; Jacobson, K.; Nir, S.; Isac, I. Phase Transitions in Phospholipid Vesicles Fluorescence Polarization and Permeability Measurements Concerning the Effect of Temperature and Cholesterol. *Biochim. Biophys. Acta - Biomembr.* 1973, *311*, 330–348.

(73) Virden, J. W.; Berg, J. C. Sodium Chloride-Induced Aggregation of Dipalmitoylphoshpatidylglycerol Small Unilamellar Vesicles with Varying Amounts of Incorporated Cholesterol. *Langmuir* 1992, *8*, 1532–1537.

(74) Liu, D.-Z.; Chen, W.-Y.; Tasi, L.-M.; Yang, S.-P. Microcalorimetric and Shear Studies on the Effects of Cholesterol on the Physical Stability of Lipid Vesicles. *Colloids Surfaces A Physicochem. Eng. Asp.* 2000, *172*, 57–67.

(75) Briuglia, M.-L.; Rotella, C.; McFarlane, A.; Lamprou, D. A. Influence of cholesterol on liposome stability and on in vitro drug release. *Drug Deliv. Transl. Res.* 2015, *5*, 231–242.

(76) Choi, H. S.; Liu, W.; Misra, P.; Tanaka, E.; Zimmer, J. P.; Itty Ipe, B.; Bawendi, M. G.; Frangioni, J. V. Renal Clearance of Quantum Dots. *Nat. Biotechnol.* 2007, *25*, 1165–1170.

(77) Ernsting, M. J.; Murakami, M.; Roy, A.; Li, S.-D. Factors Controlling the Pharmacokinetics, Biodistribution and Intratumoral Penetration of Nanoparticles. *J. Control. Release* 2013, *172*, 782–794.

(78) Moghimi, S. M.; Hunter, A. C.; Murray, J. C. Long-Circulating and Target-Specific Nanoparticles: Theory to Practice. *Pharmacol. Rev.* 2001, *53*, 283–318.

(79) Juliano, R. L.; Stamp, D. The Effect of Particle Size and Charge on the Clearance Rates of Liposomes and Liposome Encapsulated Drugs. *Biochem. Biophys. Res. Commun.* 1975, *63*, 651–658.

(80) Gabizon, A.; Papahadjopoulos, D. The Role of Surface Charge and Hydrophilic Groups on Liposome Clearance in Vivo. *Biochim. Biophys. Acta* 1992, *1103*, 94–100.

(81) Levchenko, T. S.; Rammohan, R.; Lukyanov, A. N.; Whiteman, K. R.; Torchilin, V. P. Liposome Clearance in Mice: The Effect of a Separate and Combined Presence of Surface Charge and Polymer Coating. *Int. J. Pharm.* 2002, *240*, 95–102.

(82) Owens, D. E.; Peppas, N. a. Opsonization, Biodistribution, and Pharmacokinetics of Polymeric Nanoparticles. *Int. J. Pharm.* 2006, *307*, 93–102.

(83) Kelly, C.; Jefferies, C.; Cryan, S.-A. Targeted Liposomal Drug Delivery to Monocytes and Macrophages. *J. Drug Deliv.* 2011, *2011*, 727241.

(84) Lasic, D. D.; Needham, D. The “Stealth” Liposome: A Prototypical Biomaterial. *Chem. Rev.* 1995, *95*, 2601–2628.

(85) Immordino, M. L.; Dosio, F.; Cattel, L. Stealth Liposomes: Review of the Basic Science, Rationale, and Clinical Applications, Existing and Potential. *Int. J. Nanomedicine* 2006, *1*, 297–315.

(86) Klibanov, A. L.; Maruyama, K.; Torchilin, V. P.; Huang, L. Amphipathic Polyethyleneglycols Effectively Prolong the Circulation Time of Liposomes. *FEBS Lett.* 1990, *268*, 235–237.

(87) Blume, G.; Cevc, G. Liposomes for the sustained drug release in vivo. *Biochim. Biophys. Acta - Biomembr.* 1990, *1029*, 91–97.

(88) Allen, T. M.; Hansen, C.; Martin, F.; Redemann, C.; Yau-Young, A. Liposomes containing synthetic lipid derivatives of poly(ethylene glycol) show prolonged circulation half-lives in vivo. *Biochim. Biophys. Acta* 1991, *1066*, 29–36.

(89) Sushma, D.; Surabhi, K.; Ritesh, B.; Bhawna, K. Clinical Pharmacokinetic Aspects of Stealth Liposomes: A Review. *Int. J. Drug Dev. Res.* 2010, *2*, 871–878.

(90) Ishida, T.; Kirchmeier, M. J.; Moase, E. H.; Zalipsky, S.; Allen, T. M. Targeted delivery and triggered release of liposomal doxorubicin enhances cytotoxicity against human B lymphoma cells. *Biochim. Biophys. Acta - Biomembr.* 2001, *1515*, 144–158.

(91) Hatakeyama, H.; Akita, H.; Kogure, K.; Oishi, M.; Nagasaki, Y.; Kihira, Y.; Ueno, M.; Kobayashi, H.; Kikuchi, H.; Harashima, H. Development of a Novel Systemic Gene Delivery System for Cancer Therapy with a Tumor-Specific Cleavable PEG-Lipid. *Gene Ther.* 2007, *14*, 68–77.

(92) Kuai, R.; Yuan, W.; Qin, Y.; Chen, H.; Tang, J.; Yuan, M.; Zhang, Z.; He, Q. Efficient Delivery of Payload into Tumor Cells in a Controlled Manner by TAT and Thiolytic Cleavable PEG Co-Modified Liposomes. *Mol. Pharm.* 2010, *7*, 1816–1826.

(93) Müller, S. S.; Fritz, T.; Gimnich, M.; Worm, M.; Helm, M.; Frey, H. Biodegradable hyperbranched polyether-lipids with in-chain pH-sensitive linkages. *Polym. Chem.* 2016, *7*, 6257–6268.

(94) Hofmann, A. M.; Wurm, F.; Frey, H. Rapid Access to Polyfunctional Lipids with Complex Architecture via Oxyanionic Ring-Opening Polymerization. *Macromolecules* 2011, *44*, 4648–4657.

(95) Romberg, B.; Metselaar, J. M.; Baranyi, L.; Snel, C. J.; Bünger, R.; Hennink, W. E.; Szebeni, J.;

Storm, G. Poly(amino acid)s: Promising enzymatically degradable stealth coatings for liposomes. *Int. J. Pharm.* 2007, *331*, 186–189.

(96) Whiteman, K. R.; Subr, V.; Ulbrich, K.; Torchilin, V. P. Poly(HPMA)-coated liposomes demonstrate prolonged circulation in mice. *J. Liposome Res.* 2001, *11*, 153–164.

(97) Ringsdorf, H. Structure and Properties of Pharmacologically Active Polymers. *J. Polym. Sci. Polym. Symp.* 1975, *51*, 135–153.

(98) Larson, N.; Ghandehari, H. Polymeric Conjugates for Drug Delivery. *Chem. Mater.* 2012, *24*, 840–853.

(99) Lammers, T.; Ulbrich, K. HPMA copolymers: 30 years of advances. *Adv. Drug Deliv. Rev.* 2010, *62*, 119–121.

(100) Kopeček, J.; Bažilová, H. Poly[N-(2-hydroxypropyl)methacrylamide]—I. Radical Polymerization and Copolymerization. *Eur. Polym. J.* 1973, *9*, 7–14.

(101) Duncan, R. The Dawning Era of Polymer Therapeutics. *Nat. Rev. Drug Discov.* 2003, *2*, 347–360.

(102) Li, C.; Wallace, S. Polymer-Drug Conjugates: Recent Development in Clinical Oncology. *Adv. Drug Deliv. Rev.* 2008, *60*, 886–898.

(103) Duncan, R.; Coatsworth, J. K.; Burtles, S. Preclinical toxicology of a novel polymeric antitumour agent: HPMA copolymer-doxorubicin (PK1). *Hum. Exp. Toxicol.* 1998, *17*, 93–104.

(104) Seymour, L. W.; Duncan, R.; Strohalm, J.; Kopeček, J. Effect of molecular weight (M_w) of N-(2-hydroxypropyl)methacrylamide copolymers on body distribution and rate of excretion after subcutaneous, intraperitoneal, and intravenous administration to rats. *J. Biomed. Mater. Res.* 1987, *21*, 1341–1358.

(105) Duncan, R. Development of HPMA copolymer-anticancer conjugates: Clinical experience and lessons learnt. *Adv. Drug Deliv. Rev.* 2009, *61*, 1131–1148.

(106) Matyjaszewski, K.; Xia, J. Atom Transfer Radical Polymerization. *Chem. Rev.* 2001, *101*, 2921–2990.

(107) Chiefari, J.; Chong, Y. K. (Bill); Ercole, F.; Krstina, J.; Jeffery, J.; Le, T. P. T.; Mayadunne, R. T. A.; Meijs, G. F.; Moad, C. L.; Moad, G.; Rizzardo, E.; Thang, S. H. Living Free-Radical Polymerization by Reversible Addition−Fragmentation Chain Transfer: The RAFT Process. *Macromolecules* 1998, *31*, 5559–5562.

(108) Moad, G.; Rizzardo, E.; Thang, S. H. Living Radical Polymerization by the RAFT Process. *Aust. J. Chem.* 2005, *58*, 379–410.

(109) Save, M.; Weaver, J. V. M.; Armes, S. P.; McKenna, P. Atom Transfer Radical Polymerization of Hydroxy-Functional Methacrylates at Ambient Temperature: Comparison of Glycerol Monomethacrylate with 2-Hydroxypropyl Methacrylate. *Macromolecules* 2002, *35*, 1152–1159.

(110) Scales, C. W.; Vasilieva, Y. A.; Convertine, A. J.; Lowe, A. B.; McCormick, C. L. Direct, Controlled Synthesis of the Nonimmunogenic, Hydrophilic Polymer, Poly(*N*-(2-Hydroxypropyl)methacrylamide) via RAFT in Aqueous Media. *Biomacromolecules* 2005, *6*, 1846–1850.

(111) Eberhardt, M.; Mruk, R.; Zentel, R.; Théato, P. Synthesis of pentafluorophenyl(meth)acrylate polymers: New precursor polymers for the synthesis of multifunctional materials. *Eur. Polym. J.* 2005, *41*, 1569–1575.

(112) Yang, J.; Luo, K.; Pan, H.; Kopečková, P.; Kopeček, J. Synthesis of biodegradable multiblock copolymers by click coupling of RAFT-generated heterotelechelic polyHPMA conjugates. *React.*

Funct. Polym. 2011, *71*, 294–302.

(113) Luo, K.; Yang, J.; Kopečková, P.; Kopeček, J. Biodegradable Multiblock Poly[*N*-(2-hydroxypropyl)methacrylamide] via Reversible Addition−Fragmentation Chain Transfer Polymerization and Click Chemistry. *Macromolecules* 2011, *44*, 2481–2488.

(114) Pan, H.; Yang, J.; Kopečková, P.; Kopeček, J. Backbone Degradable Multiblock *N*-(2-Hydroxypropyl)methacrylamide Copolymer Conjugates via Reversible Addition−Fragmentation Chain Transfer Polymerization and Thiol−ene Coupling Reaction. *Biomacromolecules* 2011, *12*, 247–252.

(115) Rudin, M.; Weissleder, R. Molecular Imaging in Drug Discovery and Development. *Nat. Rev. Drug Discov.* 2003, *2*, 123–131.

(116) Kunjachan, S.; Ehling, J.; Storm, G.; Kiessling, F.; Lammers, T. Noninvasive Imaging of Nanomedicines and Nanotheranostics: Principles, Progress, and Prospects. *Chem. Rev.* 2015, *115*, 10907–10937.

(117) Allmeroth, M.; Moderegger, D.; Biesalski, B.; Koynov, K.; Rösch, F.; Thews, O.; Zentel, R. Modifying the Body Distribution of HPMA-Based Copolymers by Molecular Weight and Aggregate Formation. *Biomacromolecules* 2011, *12*, 2841–2849.

(118) Seo, J. W.; Qin, S.; Mahakian, L. M.; Watson, K. D.; Kheirolomoom, A.; Ferrara, K. W. Positron emission tomography imaging of the stability of Cu-64 labeled dipalmitoyl and distearoyl lipids in liposomes. *J. Control. Release* 2011, *151*, 28–34.

(119) Seo, J. W.; Mahakian, L. M.; Tam, S.; Qin, S.; Ingham, E. S.; Meares, C. F.; Ferrara, K. W. The pharmacokinetics of Zr-89 labeled liposomes over extended periods in a murine tumor model. *Nucl. Med. Biol.* 2015, *42*, 155–163.

2 Motivation and Objectives

2 Motivation and Objectives

Drug delivery systems (DDSs) gain more and more attention in medicine, as they possess several advantageous features, which can improve the pharmacological properties of therapeutics. Encapsulated drugs are protected from metabolization and excretion, which enlarges their blood circulation time. On the other hand the body is protected from a systemic and potentially toxic effect of the drugs, as they are released in a controlled manner. The linkage of targeting vectors on the surface of DDSs also enables active targeting, which further minimizes toxic side effects and significantly lowers the required dose of the therapeutic. However, the design of a successful DDS remains challenging, as problems with e.g. *in vivo* stability, rapid detection by the MPS or size control occur frequently.

In the developmental process of novel DDSs, a preclinical *in vivo* evaluation is essential, as many questions about the final performance of a DDS (depictured in Figure 12) can only be answered reliably in this way. In short, in *vivo* tracking reveals the influence of physicochemical properties of the nanoparticles on their pharmacokinetic profile.

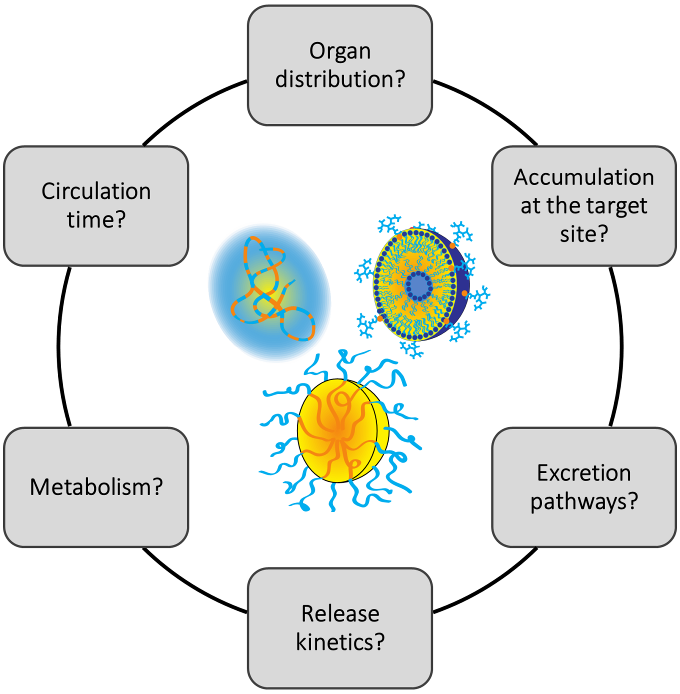

Figure 12. Questions that arise during the developmental process of DDSs and which can be answered by *in vivo* evaluation.

In order to follow the systems though the body, suitable imaging techniques are needed. In this regard, non-invasive, nuclear imaging techniques are of great value. Among them, PET is a powerful technique, providing an excellent spatial and temporal resolution and the possibility of quantification. Because of these advantages PET has a great potential in the examination of DDSs.

Against this background, this work concentrated on the *in vivo* evaluation of nanodimensional drug delivery systems via PET.

1. Novel dialkyl-based polyether lipids with different architectures of the polyether block (*hb*PG with molecular weights of 3000 and 5000 g mol^{-1} and PEG with 3000 g mol^{-1}) should be evaluated for the sterical stabilization of liposomes, with a special focus on *in vivo* stability. Structure-property relationships regarding size and architecture of the polyether block should be investigated in small animal PET and *ex vivo* biodistribution studies, involving a radiolabeling with ^{18}F. A direct comparison with cholesterol-based polyether lipids of a comparable architecture should be drawn as well.

2. Additionally there was a great interest in improving the liposome preparation process, regarding size reproducibility, time and radiation exposure for the experimentalist. Therefore, an automation of the liposome preparation should be attempted.

3. To ensure a complete removal of the cytotoxic copper, ^{18}F-radiolabeling of the polyether lipids via CuAAC was accomplished prior to the liposome preparation process, which entailed a time-consuming radiosynthesis. To overcome this problem, the radiolabeling of preformed liposomes should be tested. However, the cytotoxic properties of the utilized copper demanded for a close investigation of the amount of copper still associated with the liposome sample after purification, as there was a possibility, that copper is retained by the liposomes.

4. Based on former studies revealing favorable *in vivo* characteristics for ^{18}F-labeled HPMA-*ran*-LMA copolymers, including prolonged plasma half-life as well as an enhanced tumor accumulation, another aspect of this work should focus on the investigation of the long-term *in vivo* tracking of these polymers. In this respect, a replacement of ^{18}F against the longer-lived radioisotope ^{131}I was requested. The *ex vivo* biodistribution of the ^{131}I-labeled HPMA-*ran*-LMA copolymer should be examined over a time span of three days. Since *in vivo* deiodination is an issue, this should be investigated as well. Furthermore a direct comparison between physicochemical properties of the F- and the I-labeled polymer should be drawn. For this purpose, non-radioactive versions of the F- and I-labeled polymer were requested.

Active cancer immunotherapy implies the utilization of the immune system to trigger a tumor-specific immune response. In this context, DDS could be of great value. Instead of using the nanoparticles to just deliver therapeutics towards the tumor, they can be loaded with tumor-specific antigens and immunostimmulatory molecules. In this way they could be utilized to activate the innate and adaptive immune systems, to modulate immune tolerance and to induce an inflammation limited to the tumor. This very approach is also pursued by the Collaborative Research Center 1066, in whose context this work was carried out. In particular, it aims to develop new, multifunctional nanoparticulate drug carriers for the immunotherapy of the malignant melanoma. In order to effectively deliver loaded DDS to immune cells, suitable targeting vectors are needed, which are able to address immune cells *in vivo*. These targeting vectors can be coupled to the surface of DDSs by which tumor-specific antigens or activating molecules are transported. Trimannose, which is known to be recognized by immune cells, represents a promising targeting vector.

5. Against this background, liposomes bearing trimannose on their surface should be evaluated in cell and animal studies, regarding their ability to address immune cells. Trimannose should be coupled to polyether lipids in a first step, followed by fluorescent or radiolabeling and subsequent liposome preparation. Fluorescent polyether lipids and their corresponding liposomal formuations should be evaluated in cell studies on different immune cell types, in order to gain information on which immune cells bind the targeting vector preferably. Radiolabeled polyether lipids and respective liposomes should be examined in small animal PET and biodistribution studies, to reveal their pharmacokinetic profile.

3 Manuscripts

3 Manuscripts

The following chapters are based on different manuscripts, which are listed below. The contributions of the individual authors are described as well.

3.1 "Long-term biodistribution study of HPMA-*ran*-LMA copolymers *in vivo* by means of ^{131}I-labeling"

Karolin Wagener, Dorothea Moderegger, Mareli Allmeroth, Achim Reibel, Stefan Kramer, Barbara Biesalski, Nicole Bausbacher, Rudolf Zentel, Oliver Thews, Frank Rösch

in *Nuclear Medicine and Biology* 2018, *58*, 59-66.

Polymer syntheses and fluorescence labeling for fluorescence correlation spectroscopy measurements were performed by M. Allmeroth. Polymeranalogous reactions to obtain ^{127}I- and ^{19}F-labeled polymers were carried out by K.Wagener. Corresponding CMC and DLS measurements were conducted by S. Kramer. The main section on ^{131}I-radiolabeling and respective animal experiments is based on work by K. Wagener, D. Moderegger and A. Reibel. Animal experiments were conducted in cooperation with B. Biesalski and N. Bausbacher. *Ex vivo* metabolism studies, especially regarding the thyroid uptake, were performed by K. Wagener.

3.2 "Comparison of Linear and Hyperbranched Polyether Lipids for Liposome Shielding by ^{18}F-Radiolabeling and Positron Emission Tomography"

Karolin Wagener*, Matthias Worm*, Stefanie Pektor, Meike Schinnerer, Raphael Thiermann, Matthias Miederer, Holger Frey, Frank Rösch

* both authors contributed equally

in *Biomacromolecules,* 2018, dx.doi.org/10.1021/acs.biomac.8b00115.

Polymer syntheses were conducted by M. Worm. Radiosyntheses and liposome preparation were performed by K. Wagener, animal studies were conducted by K. Wagener and S. Pektor. Cryo-TEM measurements were carried out by R. Thiermann. DLS measurements were performed by M. Schinnerer and evaluated by K. Wagener.

3.3 “Copper-catalyzed click reactions: Quantification of retained copper using ^{64}Cu-spiked Cu(I), exemplified for CuAAC reactions on liposomes”

Karolin Wagener, Dennis Renisch, Meike Schinnerer, Matthias Worm, Yvonne Jakob, Klaus Eberhardt, Frank Rösch

submitted to *Radiochimica Acta*.

1,2-Bis(hexadecyl)glycerol-*hb*PG$_{32}$-alkyne was provided by M. Worm. Liposome preparation, radiosyntheses and CuAAC reactions were performed by K. Wagener. DLS measurements were performed by M. Schinnerer and evaluated by K. Wagener. Synthesis of F-TEG-N$_3$ was conducted by Y. Jakob under the supervision of K. Wagener. Planning of the irradiation at the TRIGA reactor was carried out by K. Wagener and K. Eberhardt. Gamma spectrometry was performed by K. Wagener and D. Renisch.

3.4 “Targeting of immune cells with trimannosylated liposomes”

Karolin Wagener, Matthias Krumb, Jens Langhanki, Matthias Bros, Stefanie Pektor, Matthias Worm, Meike Schinnerer, Matthias Miederer, Holger Frey, Till Opatz, Frank Rösch

in progress for submission.

Synthesis of trimannose was conducted by M. Krumb and J. Langhanki. Polyether lipids were provided by M. Worm. Their postmodification with trimannose and Oregon Green 488 was conducted by K. Wagener. Furthermore, radiosyntheses and liposome preparation were performed by K. Wagener, animal studies were conducted by K. Wagener and S. Pektor. DLS measurements were performed by M. Schinnerer and evaluated by K. Wagener.

3.1 Long-term biodistribution study of HPMA-*ran*-LMA copolymers *in vivo* by means of ^{131}I-labeling

Karolin Wagener[1], Dorothea Moderegger[1], Mareli Allmeroth[2], Achim Reibel[1], Stefan Kramer[2], Barbara Biesalski[3], Nicole Bausbacher[4], Rudolf Zentel[2], Oliver Thews[5], Frank Rösch[1]

[1]Institute of Nuclear Chemistry, Johannes Gutenberg University, Fritz-Strassmann-Weg 2,
55128 Mainz, Germany

[2]Institute of Organic Chemistry, Johannes Gutenberg University, Duesbergweg 10-14,
55128 Mainz, Germany

[3]Institute of Pathophysiology, University Medical Center, Duesbergweg 6, 55128 Mainz, Germany

[4]Clinic and Polyclinic of Nuclear Medicine, University Medical Center, Langenbeckstraße 1, 55101
Mainz, Germany

[5]Institute of Physiology, University Halle, Magdeburger Str. 6, 06097 Halle (Saale), Germany

Abstract

Background: For the evaluation of macromolecular drug delivery systems suitable pre-clinical monitoring of potential nanocarrier systems is needed. In this regard, both short-term as well as long-term *in vivo* tracking is crucial to understand structure-property relationships of polymer carrier systems and their resulting pharmacokinetic profile. Based on former studies revealing favorable *in vivo* characteristics for ^{18}F-labeled random (*ran*) copolymers consisting of *N*-(2-hydroxypropyl)methacrylamide (HPMA) and lauryl methacrylate (LMA) – including prolonged plasma half-life as well as enhanced tumor accumulation – the presented work focuses on their long-term investigation in the living organism.

Methods: In this respect, four different HPMA-based polymers (homopolymers as well as random copolymers with LMA as hydrophobic segment) were synthesized and subsequent radioactive labeling was accomplished via the longer-lived radioisotope ^{131}I. *In vivo* results, concentrating on the pharmacokinetics of a high molecular weight HPMA-*ran*-LMA copolymer, were obtained by means of biodistribution and metabolism studies in the Walker 256 mammary carcinoma model over a time-span of up to three days. Besides, a direct comparison with the ^{18}F-radiolabeled polymer was drawn. To consider physicochemical differences between the differently labeled polymer (^{18}F or ^{131}I) on the critical micelle concentration (CMC) and the size of the polymeric micelles, those properties were determined using the ^{19}F- or ^{127}I-functionalized polymer. Special emphasis was laid on the time-dependent correlation between blood circulation properties and corresponding tumor accumulation, particularly regarding the enhanced permeability and retention (EPR) effect.

Results: Studies revealed, at first, differences in the short time (2 h) body distribution, despite the very similar properties (molecular structure, CMC and size of the micellar aggregates) of the non-radioactive ^{19}F- and ^{127}I-functionalized polymers. Long-term investigations with the ^{131}I-labeled polymer demonstrated that, despite a polymer clearance from the blood within 72 hours, there was still an increase in tumor uptake observed over time. Regarding the stability of the ^{131}I-label, *ex vivo* biodistribution experiments, considering the uptake in the thyroid, indicated low metabolism rates.

Conclusion: The observed *in vivo* characteristics strongly underline the EPR effect. The findings illustrate the need to combine information of different labeling approaches and *in vivo* evaluation techniques to generate an overall pharmacokinetic picture of potential nanocarriers in the pre-clinical setting.

Advances in knowledge and implications for patients: The *in vivo* behavior of the investigated HPMA-*ran*-LMA copolymer demonstrates great potential in terms of an effective accumulation in the tumor.

Introduction

Polymeric nanocarrier systems are of emerging interest regarding their potential for anticancer therapy. Low molecular weight free drugs such as chemotherapeutic agents often suffer from short plasma half-lives, high clearance rates and undesirable side effects in healthy tissue. Macromolecular drug delivery vehicles can significantly improve the pharmacokinetic profile of those drugs. Prolonged blood-circulation times, enhanced tumor accumulation due to the enhanced permeability and retention (EPR) effect[1] as well as a decrease of toxic side effects are only some advantages to be named. The EPR effect has been proposed to lead to a further increase in intratumoral drug concentration over a longer period of time even with a decreasing plasma level.

Regarding clinical implementation, a polymeric drug carrier has to be non-toxic, non-immunogenic, biodegradable or at least biocompatible with appropriate molecular weight to ensure body excretion. Furthermore, narrow molecular weight distributions are needed to guarantee homogeneity of the final conjugates.[2,3] Poly(*N*-(2-hydroxypropyl)methacrylamide) (HPMA) as one class of various clinically investigated polymer structures additionally has the advantage of multifunctionality of the polymeric intermediate which allows a concomitant binding of drugs and targeting residues.[4] Therefore it is not surprising that already six poly(HPMA) anticancer conjugates entered clinical trials as reported in a recently published review[5] – demonstrating the potential of this multifunctional synthetic polymer in tumor treatment.

In terms of their therapeutic application area, it is essential that the utilized polymers are as well-defined as possible.[6] The introduction of controlled radical polymerization techniques like atom transfer radical polymerization (ATRP)[7] or reversible addition-fragmentation chain transfer (RAFT)[8,9] facilitated the synthesis of narrowly-distributed and well-defined polymer structures. Notably, the synthetic route to the used HPMA-based polymer systems, i.e. a combination of RAFT with reactive ester chemistry[10-12], is an elegant route to diverse polymer architectures.[13-15]

Besides the aforementioned high demands on the macromolecular carrier system, especially adequate diagnostic screening tools are crucial in order to plan an appropriate therapy for the individual patient.[16,17] In this regard, non-invasive molecular imaging techniques such as positron emission tomography (PET) or single photon emission computed tomography (SPECT) constitute helpful diagnostic tools enabling detailed information on the body disposition as well as tumor accumulation of the polymer-drug conjugate in the living organism. The diagnostic time frame can be adjusted from early phase accumulation, using isotopes with a short half-life, to long-term imaging over days or weeks by selecting radionuclides with a sufficiently longer half-life.

Former studies in our group already illustrated the successful radiolabeling of various HPMA-based polymers by means of the positron emitters $^{72/74}As$[18] and ^{18}F[19] thereby establishing µPET imaging for time-efficient screening of potential drug delivery systems. Further investigations on ^{18}F-labeled HPMA-based polymer systems revealed the major impact of molecular weight and aggregate formation[20] as well as the importance of the chosen tumor model[21] on the body distribution in the living animal. The examined polymer structures included homopolymers, random copolymers as well as block copolymers composed of a hydrophilic poly(HPMA) and a hydrophobic poly(lauryl methacrylate) (LMA) segment. These polymer architectures demonstrate a quiet different uptake by cells[13,22,23] and a different interaction scheme with plasma proteins.[24] While homo- and blockcopolymers show little interaction with cellular membranes[13], the statistical copolymers interact well with cellular membranes[13,22,23] and very low density lipoproteins.[24] This makes them e.g. interesting to transport hydrophobic drugs over the blood-brain-barrier.[22,23]

In direct comparison, the high molecular weight random (*ran*) copolymer (M_w = 55 kDa; LMA ratio 25 %) exhibited the most favorable *in vivo* characteristics – combining prolonged blood circulation times with the highest tumor uptake among the tested polymers as well as low liver accumulation and renal excretion properties.[20,21] However, this specific pharmacokinetic profile was investigated by means of ^{18}F ($t_{1/2}$ = 110 min) as the radioactive marker, whose short half-life is suitable to display the beginning of the EPR effect but cannot cover its whole time span. The significantly enhanced plasma half-life of the high molecular weight HPMA-*ran*-LMA copolymer however warranted investigation into its long-term biodistribution properties with respect to a possible sustained EPR effect. This would notably allow a sustained release and accumulation of drugs over days or weeks.[25,26] To evaluate the EPR effect for the previously presented HPMA-*ran*-LMA copolymer system, we decided on its radioactive labeling by incorporating the longer-lived β^--emitter ^{131}I ($t_{1/2}$ = 8.1 days). We intended to use ^{131}I because iodine is conveniently incorporated at tyramine groups which are also used for ^{18}F-labeling via [^{18}F]fluoroethylation. In this way a direct comparison to former ^{18}F-studies with the identical polymer batch was possible. For a detailed comparison of the radiolabeling process by means of ^{131}I, HPMA homopolymers (**P1** and **P2**) as well as random copolymers (**P3** and **P4**) – varying in molecular weight – were investigated. Furthermore radiolabeling using Iodogen™ (1,3,4,6-Tetrachloro-3a,6a-diphenylglycoluril) and Chloramine-T (*N*-chloro-4-methylbenzenesulfonamide sodium salt, CAT) as two different *in situ* oxidants were examined.

The aim of the present study focused on radiolabeling of HPMA-based polymers via ^{131}I and the consequent long-term monitoring of an HPMA-*ran*-LMA copolymer *in vivo*, particularly regarding its blood residence time as well as its tumor accumulation/retention properties over a time-window of three days. In addition a direct comparison to former studies with an ^{18}F-labeled HPMA-based random copolymer at the short time interval (2 h) was drawn.[20,21]

Material and methods

Materials

All solvents were of analytical grade, as obtained by Sigma Aldrich and Acros Organics. Dioxane was distilled over a sodium/potassium composition. LMA was distilled to remove the stabilizer and stored at -18 °C. 2,2'-Azo-bis-(isobutyronitrile) (AIBN) was recrystallized from diethyl ether and stored at - 18 °C as well. ^{131}I was obtained from GE Healthcare (Braunschweig, Germany).

Polymer synthesis

Synthesis of 4-cyano-4-((thiobenzoyl)sulfanyl)pentanoic acid (CTP)

4-cyano-4-((thio- benzoyl)sulfanyl)pentanoic acid was used as chain transfer agent (CTA) and synthesized according to the literature.[9]

Synthesis of pentafluorophenyl methacrylate (PFPMA)

Pentafluorophenyl methacrylate was prepared according to reference.[27]

Synthesis of random copolymers

RAFT polymerization of PFPMA with LMA by the help of CTP was performed in a Schlenk tube.[11,13,20] As an example, 4 g of PFPMA dissolved in 5 ml dioxane, LMA, AIBN and CTP were mixed. The molar ratio of CTP/AIBN was chosen to be 8:1. After three freeze-vacuum-thaw cycles, the mixture was immersed in an oil bath at 65 °C and stirred overnight. Afterwards, poly(PFPMA)-*ran*-poly(LMA) was precipitated three times in hexane, centrifuged and dried under vacuum at 40 °C overnight. A slightly pink powder was obtained. Yield: 54 %. ^{1}H-NMR (300 MHz, $CDCl_3$) δ/ppm: 0.84 (br t), 1.20-1.75 (br), 2.00-2.75 (br s). ^{19}F-NMR (400 MHz, $CDCl_3$) δ/ppm: -162.01 (br), -156.95 (br), -152 to -150 (br).

Removal of dithioester endgroups

The dithiobenzoate endgroup was removed using the protocol reported by Perrier et al.[28] Therefore a 25-fold molar excess of AIBN was added to the polymer dissolved in dioxane. After four hours of heating the solution in an oil bath at 70 °C, the polymer was precipitated twice in hexane, collected by centrifugation and dried under vacuum overnight. A colorless powder was obtained. Yield: 75 %. Removal of the dithioester endgroup could be proven by UV-Vis spectroscopy.

Polymeranalogous reaction of random copolymers

For radioactive labeling of random copolymers the protocol was applied as follows. 100 mg of PFPMA-*ran*-LMA copolymer were dissolved in 2 ml of absolute dioxane. As example, for the polymeric system

P3-R (see Table 1) 5 mg of tyramine and 10 mg of triethylamine were diluted in a DMSO/dioxane mixture and added to the vessel. After stirring for four hours at 35 °C, 30 mg of 2-hydroxypropylamine as well as 40 mg of triethylamine were added and the solution was stirred overnight. For the final removal of the reactive ester side groups further 30 mg of 2-hydroxypropylamine were added the next morning. The solution was precipitated two times in diethyl ether, centrifuged and finally dissolved in a DMSO/water solution for dialysis. After lyophilization a white powder could be obtained. Yield: 51 %. ^{1}H-NMR (400 MHz, d. DMSO) δ/ppm: 0.70-0.90 (br), 0.90-1.40 (br), 1.40-1.90 (br), 2.75-3.10 (br), 3.50-3.80 (br), 4.50-4.75 (br), 6.60-6.75 (br) and 6.85-7.00 (br). For additional fluorescent labeling, 100 mg of polymeric precursor were diluted in 2 ml of absolute dioxane and 2.9 mg of Oregon Green 488 cadaverine were added. Afterwards tyramine and 2-hydroxypropylamine were added, as described by the procedure above.

For ^{127}I-functionalization 12.5 mg of **P4b** (see Table 1) were dissolved in 833 µl of DMSO and 29 µl of phosphate buffered saline (PBS). Subsequently 55 µl of a NaI solution in PBS (10 mg/ml) and 83 µl of a CAT solution in PBS (10 mg/ml) were added, giving a final ratio of DMSO/PBS of 5:1. The reaction mixture was stirred at room temperature for three days. Afterwards it was diluted with water and dialyzed using a dialysis tube with a pore size of 3.5 kDa. ^{1}H-NMR (400 MHz, d. DMSO) δ/ppm: 0.70-0.90 (br), 0.90-1.10 (br), 1.15-1.40 (br), 1.40-2.10 (br), 2.75-3.10 (br), 3.55-4.00 (br), 4.50-4.80 (br), 6.60-6.73 (br), 6.73-6.85 (br) and 6.85-7.05 (br).

For ^{19}F-functionalization 12.5 mg of **P4b** (see Table 1) were dissolved in 668 µl of DMSO. Subsequently 6 µl of a 5 N NaOH solution and 332 µl of a 2-fluoroethyl 4-methylbenzenesulfonate (FETos) solution (20 mg/ml) were added. The reaction mixture was stirred at 60 °C for one day, then at room temperature for another two days. Afterwards it was diluted with water and dialyzed using a dialysis tube with a pore size of 3.5 kDa.^{1}H-NMR (400 MHz, d. DMSO) δ/ppm: 0.70-0.90 (br), 0.90-1.10 (br), 1.10-1.40 (br), 2.75-3.10 (br), 3.55-3.90 (br), 4.20 (br, d, J = 29.1 Hz), 4.40-4.80 (br, m), 6.75-6.95 (br), 7.12 (d, J = 8.5 Hz), 7.48 (d, J = 8.0 Hz). ^{19}F-NMR (400 MHz, d. DMSO, ^{1}H-decoupled) δ/ppm: -223.2 (s).

More details on the polymer syntheses as well as polymer characterization data (including experimental setups, NMR data and fluorescence correlation spectroscopy (FCS) measurements) are provided as supporting information.

Critical micelle concentration (CMC) by pyrene fluorescence spectroscopy

Stock solutions of HPMA-*ran*-LMA copolymer **P4b** (see Table 1), non-, ^{19}F- and ^{127}I- functionalized, were prepared at a concentration of 1 mg/ml by dissolving in PBS buffer supported by sonication for 1 h. The polymer stock solutions were then diluted to ten different concentrations down to 2.5*10^{-7} mg/ml using further PBS. Each sample was prepared by carefully dropping 60 µl of a pyrene solution (2.5*10^{-5} mol/l in acetone) into 2 ml Eppendorf tubes and evaporating the solvent overnight. On the next day, 2 ml of the polymer/PBS solutions was added, affording pyrene solutions of $7.5*10^{-7}$ mol/l. The mixtures were incubated for 24 h at room temperature with shaking. Steady-state fluorescence spectra of the air-equilibrated samples were recorded using a PerkinElmer luminescence spectrometer LS-50B (right angle geometry, 1 cm x 1 cm quartz cell) using the following conditions: excitation at 333±3 nm, detected emission spectrum from 350 to 450 nm. The intensities of pyrene's first and third vibronic band at 373 and 384 nm in PBS were evaluated, and their ratio was plotted versus the logarithmic polymer concentration. Linear extrapolations of steady ratio and decrease of ratio were done, and their intercept was determined as CMC.

Dynamic light scattering (DLS)

Dynamic light scattering measurements were performed using a Zetasizer Nano ZS (Malvern Instruments Ltd., Malvern, UK). Mean particle diameter (z-average) and polydispersity index (PDI) were calculated from 10 subruns. Measurements were taken at a scattering angle of 173 ° and at a temperature of 25 °C.

Radiolabeling

Radiolabeling procedures applied to study ^{131}I-radiolabeling of different HPMA-based polymers are provided as supplementary information. Radioiodination of the HPMA-*ran*-LMA copolymer **P4** (see Table 1) for *in vivo* experiments was performed using the following optimized labeling conditions applying the CAT procedure: 1 mg **P4** in 100 µl of DMSO, 200 µl CAT solution (1 mg/ml in 0.9 % sodium chloride solution), 200 µl PBS and 96±16 MBq of [^{131}I]iodide solution yielding 49±3 % (decay corrected) of ^{131}I-labeled **P4** after 4 min reaction time and subsequent preparative size exclusion chromatography (SEC) purification.

In vitro stability

Stability of the radiolabel was ensured by means of SEC purification in combination with thin layer chromatography after 2 days of storage in isotonic NaCl solution at 4 °C. SEC purification was accomplished using a disposable PD-10 column (GE Healthcare) which was preconditioned and eluted with 0.9 % (w/v) sodium chloride solution. Thin layer chromatography was done using Tec Control chromatography strips (Biodex Medical Systems, Inc., USA) with 0.9 % (w/v) sodium chloride solution as the mobile phase.

Tumor and animal model

Tumor experiments were performed with the Walker 256 mammary carcinoma cell line of the rat. Tumors were used when they reached a volume between 0.3 to 2.2 ml approximately 5 to 8 days after tumor cell inoculation. All experiments had previously been approved by the regional animal ethics committee and were conducted in accordance with the German Law for Animal Protection and the UKCCCR Guidelines.[29] Detailed information are provided in the supporting information.

Ex vivo biodistribution

In order to assess the distribution of the radiolabeled polymers in different organs of the animals, the polymer (1 mg in 1 ml of isotonic saline) was injected i.v. in anaesthetized tumor-bearing rats via the tail vein with a mean activity of 8.6±0.3 MBq (for ^{131}I) or 5.2±0.3 MBq (for ^{18}F). After 2, 24, 48 and 72 hours, the animals were sacrificed and different organs (kidney, liver, lung, spleen, blood, thyroid) as well as tumors were removed. The tissue samples were weighed and minced. Finally, the ^{131}I- or ^{18}F-activity in the organs was measured in a γ-counter (2470 WIZARD^2 Automatic Gamma Counter, PerkinElmer).

Ex vivo metabolism studies

Blood samples (ca. 200 µl), collected during the biodistribution, were mixed with heparin solution (150 µl) to avoid coagulation. Blood samples were weighed and the activity was measured in a γ-counter. 500 µl of PBS were added and the blood was centrifuged at 5000 rpm for 5 min in order to separate blood cells and plasma. The activity of the plasma fractions were measured in a γ-counter. Proteins were precipitated by adding 1000 µl of cold acetonitrile. To separate the proteins from plasma water the samples were centrifuged at 5000 rpm for 5 min. The activity of the supernatants were determined in a γ-counter. The percentage of radioactivity in the blood cell, protein and plasma water fractions was calculated by subtracting the activities of the supernatants from the activity of the whole blood sample. Efforts that were made to distinguish between free polymer and free ^{131}I in the plasma water fraction are provided in the supporting information. Ultimately the deiodination rate was estimated via the uptake in the thyroid.

Results and discussion

For the investigation of the long-term *in vivo* distribution of HPMA-based polymer structures – with special focus on tumor accumulation characteristics – two HPMA-based polymer architectures (homopolymers and random copolymers with LMA as hydrophobic group) were synthesized by combining reactive ester chemistry with the RAFT polymerization technique[8,9,27] followed by radiolabeling with ^{131}I. For a detailed comparison of the radiolabeling process, HPMA homopolymers (**P1** and **P2**) as well as random copolymers (**P3** and **P4**) – varying in molecular weight – were investigated. The polymer synthesis and the radioactive labeling procedure are depicted in Figure 1. The characterization data of the corresponding polymers are listed in Table 1. The precursor homopolymers **P1-R** and **P2-R** were synthesized starting from pentafluorophenyl methacrylate. By simultaneous addition of LMA the precursor random copolymers **P3-R** and **P4-R** were obtained. The polymerizations were accomplished according to the literature.[11,13,27] Through polymeranalogous reactions with 1-aminopropan-2-ol and tyramine the precursor polymers (P1-R – P4-R) were converted into the HPMA-based polymers (P1 – P4) in a clean conversion. Tyramine moieties were included with a percentage of 2-4 %. This approach gains access to well-defined and narrowly distributed polymer systems and polymeranalogous reactions with primary amines facilitate the incorporation of imaging moieties such as fluorescent dyes or radiolabels.

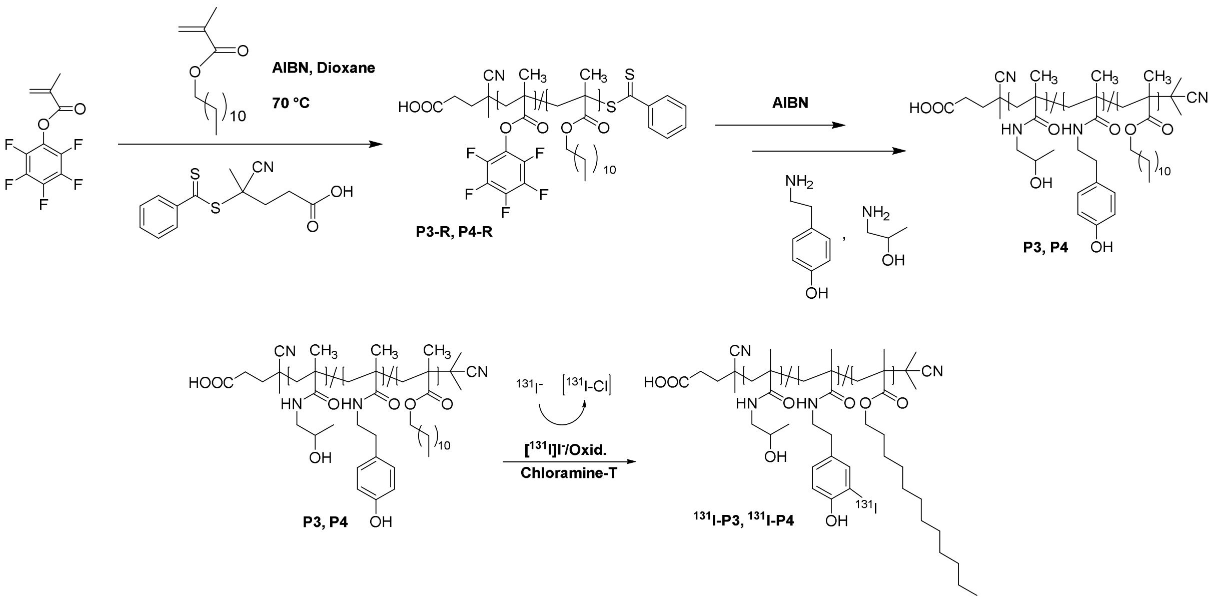

Scheme 1. Polymer synthesis via reactive ester approach with subsequent polymeranalogous reaction as well as radioactive labeling procedure by means of ^{131}I (for the preparation of P1 and P2 no LMA was added in the first step).

Table 1. Analytical data of reactive ester precursor polymers (P1-R - P4b-R) as well as final polymeric structures (P1 - P4b).

Notation	Polymeric structure	HPMA:LMA	M_n [g/mol]	M_w [g/mol]	PDI[b]	R_h[e] [nm]
P1-R	Homopolymer	100:0[a]	18000[b]	23000[b]	1.29	n.d.
P2-R	Homopolymer	100:0[a]	87000[b]	130000[b]	1.49	n.d.
P3-R	Random copolymer	80:20[a]	17000[b]	21000[b]	1.26	n.d.
P4-R	Random copolymer	80:20[a]	57000[b]	80000[b]	1.41	n.d.
P4b-R	Random copolymer	82:18[a]	61000[b]	98000[b]	1.59	n.d.
P1	Homopolymer	100:0[c]	9000[d]	12000[d]	1.29	1.1
P2	Homopolymer	100:0[c]	52000[d]	77000[d]	1.49	3.0
P3	Random copolymer	82:18[c]	11000[d]	14000[d]	1.26	33.4
P4	Random copolymer	75:25[c]	39000[d]	55000[d]	1.41	39.9
P4b	Random copolymer	80:20[c]	41000[d]	65000[d]	1.59	45.0[f]

[a] Calculated monomer ratio.

[b] Determination by gel permeation chromatography (GPC) in tetrahydrofuran (THF) as solvent.

[c] Monomer ratio determined by ^{1}H-NMR spectroscopy after polymeranalogous reaction with 2-hydroxy-propylamine.

[d] Calculated from the molecular weights of the reactive ester polymer P1-R as determined by GPC in THF as solvent.

[e] Hydrodynamic radii determined by fluorescence correlation spectroscopy (FCS).

[f] Hydrodynamic radii determined by using a Zetasizer Nano ZS.

Former ^{18}F-labeling of HPMA-based polymer systems has been accomplished via [^{18}F]fluoroethylation of tyramine groups[19,20] (~2-4 % incorporation as determined by ^{1}H-NMR) which provide highly activated phenolic rings. Hence, ^{131}I-incorporation can be accomplished by means of electrophilic aromatic substitution; enabling ^{131}I-labeling of the same HPMA-based polymers without prior derivatization of the polymer structure. This approach allows for chemically nearly identical polymers functionalized with isotopes for short- ^{18}F or long-term ^{131}I detection.

To look – despite the chemical similiarity – for possible consequences of the different types of label prepared by fluoroethylation or iodination we modified a reference polymer **P4b** (see Tab. 1) nearly identical to **P4** with cold fluorine or iodine to prepare **P4b-F** and **P4b-I**. Thereby we modified **P4b** with less than 20 % of iodine or fluorethyl-groups to get, on one side, a chemically detectable effect and, on the other side, to deviate not too strongly from the radiolabeled compound, for which modification is extremely low. For both these polymers we determined the CMC by pyrene spectroscopy and the hydrodynamic radius (R_h) with the help of a Zetasizer. These values are listed in Table 2 together with the data of the unmodified polymers **P4b** and **P4**. The comparison shows that both **P4b-F** and **P4b-I** are a bit more hydrophilic (higher CMC values) and they form slightly larger micellar aggregates then the "parent polymer" **P4b** which in turn is highly comparable with **P4**. In direct comparison **P4b-F** and **P4b-I** are however very similar to each other. Thus, the radiolabeled polymers, whose modification is extremely low, should be even more comparable to each other and to the non-functionalized polymer **P4**. This should allow a direct correlation of structure-property relationships between the ^{18}F- and the ^{131}I-labeled HPMA-*ran*-LMA copolymer *in vivo* as done in this paper.

Table 2. CMCs and hydrodynamic radii of the polymeric structures **P4**, **P4b**, **P4b-I** and **P4b-F**.

Notation	Polymeric structure	CMC[a)] [mg/ml]	R_h[c)] [nm]
P4	Random copolymer	1.6×10^{-3} [b)]	39.9[d)]
P4b	Random copolymer	2.0×10^{-3}	45.0
P4b-F	Random copolymer	7.2×10^{-3}	88.2
P4b-I	Random copolymer	1.9×10^{-2}	79.1

[a)] *Determination by pyrene fluorescence spectroscopy.*

[b)] *Determination by surface tension versus concentration applying the ring method of the "du Noüy" ring tensiometer.*

[c)] *Hydrodynamic radii determined by using a Zetasizer Nano ZS.*

[d)] *Hydrodynamic radii determined by fluorescence correlation spectroscopy.*

In order to promote incorporation of ^{131}I via direct electrophilic aromatic substitution, reaction conditions were studied to optimize the labeling technique for different HPMA-based architectures. Since direct electrophilic radioiodination requires the generation of an electrophilic radioiodine species by oxidation from [^{131}I]NaI, two different *in situ* oxidants were tested, being commonly applied for radioiodination of proteins: CAT and Iodogen.[30,31] Investigations on type and amount of oxidant revealed highest radiochemical yields (RCYs) for CAT regarding ^{131}I-labeling of the HPMA homopolymers (**P1** M_w = 12 and **P2** M_w = 77 kDa respectively) (see Figure S1 supporting information). Concerning the random copolymers, the low molecular weight random copolymer **P3** showed highest RCYs (41 %, decay corrected) for Iodogen whereas its high molecular weight counterpart **P4** exhibited best RCYs (44 %, decay corrected) using CAT (see Figure S3 supporting information). Radioiodination of the HPMA-*ran*-LMA copolymers (**P3** M_w = 11 kDa; **P4** M_w = 55 kDa) additionally concentrated on the appropriate choice of reaction solvents since the hydrophobic LMA side chains avoid complete dissolution of the polymers in pure PBS (solvent dependency see Figure S2 and S3 supporting information). *In vitro* stability tested by means of SEC purification in combination with thin layer chromatography, indicated less than 1 % radioiodine detachment from the polymer after 2 days of storage in isotonic NaCl solution at 4 °C.

Since former short-term studies by means of [^{18}F]fluoroethylation had shown that the high molecular weight HPMA-*ran*-LMA copolymer could be a suitable candidate for polymer drug delivery because of its long blood circulation[20,21], we here aimed to investigate its potential as polymeric nanocarrier in more detail and with respect to long-term pharmacokinetics. Hence [^{131}I]radioiodination of HPMA-*ran*-LMA copolymer **P4** for subsequent *in vivo* evaluation was accomplished using CAT as oxidizing agent as well as a mixture of DMSO and PBS in order to promote ^{131}I-incorporation in sufficient high yields – using 1 mg of polymer precursor in a total synthesis time (including SEC purification) of less than 20 min.

Biodistribution studies of ^{131}I-labeled polymer were carried out in Walker 256 tumor bearing rats. In order to follow the long-term biodistribution and tumor accumulation, time points were chosen to be 2 h, 24 h, 48 h and 72 h post injection. Radioiodination efficiencies were determined to be 49±3 % (decay corrected) after preparative SEC purification. Figure 2 shows the biodistribution of **^{131}I-P4** in organs of interest (liver, spleen, kidney, lung, heart, blood as well as thyroid), investigated over up to 72 h in comparison to short-term pharmacokinetics observed using **^{18}F-P4**.[20,21] Numeric values are provided in Table S1.

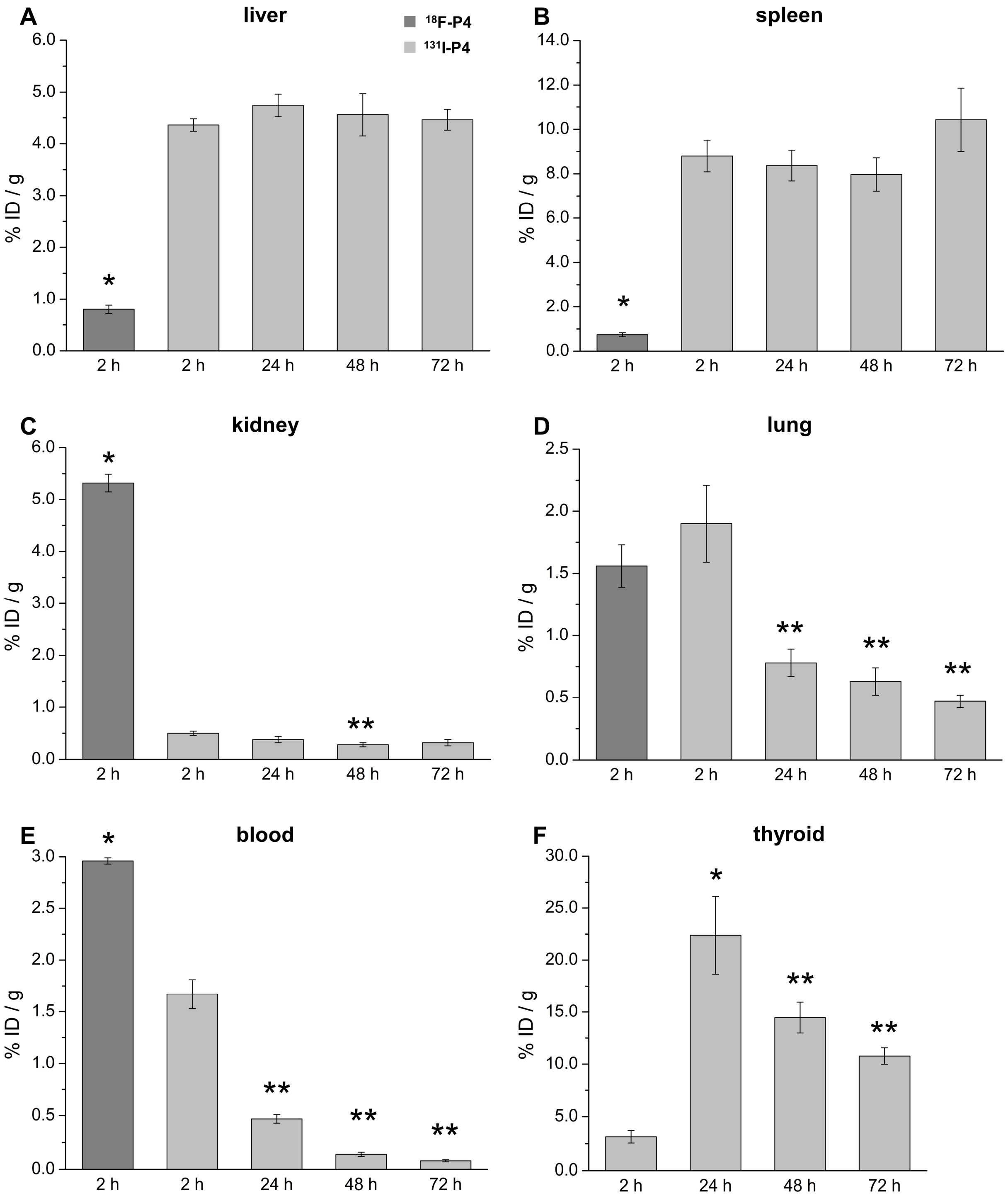

Figure 2. Biodistribution of the large HPMA-*ran*-LMA copolymer **P4** in different organs (liver, spleen, kidney, lung, blood and thyroid) 2 h p.i. using **^{18}F-P4** (n=3) and up to 72 h p.i. by means of **^{131}I-P4** (n=9, thyroid n=3 (2, 24 h) n=4 (48, 72 h)). Data is expressed as % ID/g tissue (mean±standard error of the mean (SEM)). (*) $p<0.05$ vs. ^{131}I-2 h; (**) $p<0.01$ vs. ^{131}I-2 h.

Concerning relevant organs for drug clearance – i.e. liver, spleen and kidney – significant differences between the short-term distribution (2 h) obtained with **^{18}F-P4** and with the ^{131}I-labeled analog were observed, despite their physicochemical similarity (see above). Hepatic and splenic uptake of ^{131}I-labeled **P4** were much higher after 2 h when comparing to the data measured with the ^{18}F-labeled polymer. After 2 h the liver concentration of the ^{131}I-labeled compound was 5-times higher compared to ^{18}F-labeling whereas the spleen showed 12-times higher values for **^{131}I-P4** (Figure 2A/B, Table S1). Given the similarity of the iodinated or fluoroethylated "cold" polymers **P4b-F** and **P4b-I** the accumulation of **^{131}I-P4** in the liver may be related to an active uptake of iodine functionalized thyramine. Since the liver is the most active organ for recycling and removal of thyroid hormones like e.g. thyroxine from the blood stream[32], it is likely that there are active uptake routes for this class of materials. An inverse pattern for the short-term distribution was observed regarding kidney concentrations of the high molecular weight random copolymer. Kidney uptake (Figure 2C) of **^{131}I-P4** was significantly reduced, displaying about 10-times lower concentrations compared to **^{18}F-P4**. This may be a result of the reduced blood concentration, as only a 1.8-times lower concentration of **^{131}I-P4** was found in the blood compared to **^{18}F-P4** (1.67±0.14 % ID/g vs. 2.96±0.03 % ID/g, respectively) 2 h after the injection (Figure 2E). Investigation of the polymer concentration in the blood over up to three days (Figure 2E) revealed a continuous clearance of **^{131}I-P4.** Major blood clearance was observed within the first 24 h after injection, with 28 % (0.47±0.04 % ID/g) of the polymer remaining in the blood compartment after one day. These findings demonstrate even higher blood levels compared to a study of Lammers *et al.*[33] determining the blood residence time of an ^{131}I-labeled HPMA copolymer of 31 kDa. In addition, concentrations at 72 h (0.08±0.01 % ID/g) indicated a total blood clearance of **P4** in less than three days. The lung as highly blood supplied organ reflected the already investigated course of the ^{131}I-labeled polymer **^{131}I-P4** in the blood (Figure 2D). In order to have a closer look on the distribution of **^{131}I-P4** in the blood, the blood samples obtained during the biodistribution were separated into different fractions (blood cells, proteins as well as plasma water). Figure 3 shows the amount of radioactivity in the different fractions with reference to the amount of radioactivity of the whole blood sample. After 2 h 50.5±0.1 % of the radioactivity was present in the plasma water which stayed relatively stable during the complete observation period of 72 h. In the fraction containing the proteins 41.1±0.1 % of the radioactivity was found which decreased to 21.3±2.9 % after 72 h. The amount of radioactivity in the blood cells followed a reverse pattern, starting with 8.5±0.2 % after 2 h through to 29.0±10.1 % after 72 h. These findings suggest, that the random copolymer interacts with serum proteins and with blood cells. From former studies in our group we know that HPMA-*ran*-LMA copolymers interact with very low density lipoproteins in the blood[24] and with cell membranes[22,23], which is in accordance with what we found herein. In order to examine the deiodination rate of **^{131}I-P4** the thyroid uptake (Figure 2F) was investigated. The amount of radioactivity in the thyroid gland increased strongly upon injection, reaching a maximum of 22.38±3.73 % ID/g at 24 h p.i. Thereafter it decreased slowly so that still 10.77±0.79 % ID/g were present in the thyroid after 72 h. The conversion of these values into % ID by multiplying with the mass of the thyroid reveals a percentage of <1 % of the injected dose being present in the thyroid at all timepoints. Together with the percentage of the injected dose in the kidneys which was also <1 % during the whole observation time, it suggests a low deiodination rate of the polymer *in vivo.*

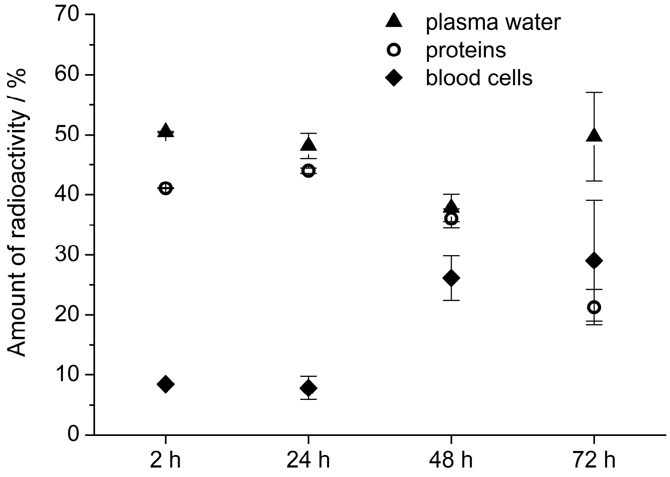

Figure 3. Distribution of the large HPMA-*ran*-LMA copolymer **P4** and its metabolites in the blood for up to 72 h using **^{131}I-P4** (n=3 (2, 24 h), n=4 (48, 72 h)). Data is expressed as percentage of the amount of radioactivity which was present in the whole blood sample (mean±SEM).

The tumor uptake of the random copolymer **P4** was studied in the Walker 256 carcinoma model. Even though a significant blood clearance of the copolymer was observed, the concentrations found in the tumor was gradually increasing over one day (Figure 4) and only slowly decreasing thereafter. After 72 h 0.64±0.08 % ID/g were still present in the tumor. Since more than 95 % of the polymer is being cleared from the blood within this time frame (Figure 2E), the increased retention of **P4** in the tumor indicates directly the EPR-mediated passive tumor accumulation of polymeric nanocarrier systems.[1,26,34] Former studies in our group already revealed a significant cellular uptake of the high molecular weight random copolymer **P4** in the Walker 256 mammary carcinoma cell line[21] hence assuming that the *in vivo* observed tumor characteristics are related to a combination of increased extravasation of polymer to the tumor tissue (EPR effect) as well as polymer-cell specific interactions at the tumor site. The highest tumor uptake of **^{131}I-P4** was observed 24 h after administration (0.93±0.06 % ID/g). However, the tumor/blood ratio increased over the complete observation period of 72 h (Figure 5) thus demonstrating the suitability of this HPMA-based copolymer system for anticancer treatment. Noteworthy, both **^{18}F-P4** and **^{131}I-P4** show similar tumor concentrations at 2 h of about 0.6 % ID/g. With these findings, both labeling strategies are assumed to be suitable to determine the tumor targeting ability of polymer based drug carrier systems. Although the shorter half-life of ^{18}F (~110 min) limits the diagnostic time frame to few hours, [^{18}F]fluoroethylation allows to assess the distribution of the drug carriers by PET imaging as valuable short-term preclinical tool. However, despite fast and efficient screening of potential polymeric drug delivery vehicles is enabled – with respect to assessing intratumoral distribution – careful interpretation regarding initial organ distribution has to be accomplished. Here application of diverse labeling approaches, not demanding for a prior variation of the polymer structure, are crucial, in order to reveal an overall pharmacokinetics as well as a long-term distribution, facilitating the choice of promising drug delivery compounds in the future.

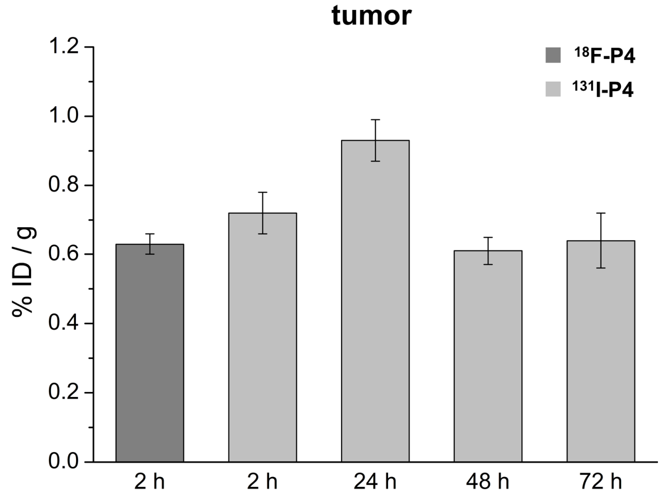

Figure 4. Tumor uptake of the large HPMA-*ran*-LMA copolymer **P4** in the Walker 256 mammary carcinoma model. Distribution was studied 2 h p.i. using **^{18}F-P4** (n=3) and for up to 72 h by means of **^{131}I-P4** (n=12 (2 h), n=18 (24, 48, 72 h)). Data is expressed as % ID/g tissue (mean±SEM).

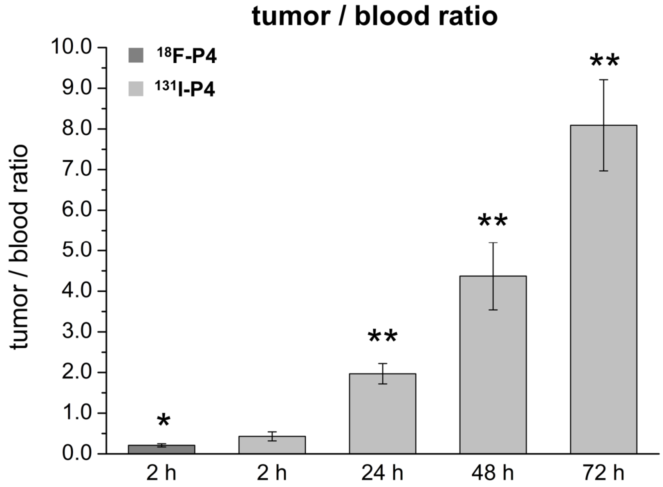

Figure 5. Tumor/blood ratios of the large HPMA-*ran*-LMA copolymer **P4** in the Walker 256 mammary carcinoma model. Distribution was studied 2 h p.i. using **^{18}F-P4** (n=3) and for up to 72 h by means of **^{131}I-P4** (n=9). Errors were calculated via error propagation of the SEMs. (*) $p<0.05$ vs. ^{131}I-2 h, (**) $p<0.01$ vs. ^{131}I-2 h.

Conclusion

In order to effectively deliver drugs to the tumor, a suitable drug carrier system has to meet unique requirements – particularly prolonged retention in the blood pool as well as an EPR mediated accumulation in the tumor tissue. In the present study we successfully introduced ^{131}I into HPMA-*ran*-LMA copolymer structures. *Ex vivo* biodistribution studies of the high molecular weight HPMA-based random copolymer **^{131}I-P4** over 72 h proved firstly a low accumulation of the radioactivity in the thyroid, suggesting that the polymer is deiodinated only to a minor degree and secondly an enhanced retention of the polymer in tumor tissue, despite its concurrent clearance from the blood pool. These characteristics can be directly correlated to the well-known EPR effect and underline the significance of tracking the pharmacokinetic profile of polymers in the long run. Furthermore a comparative short-term study of ^{18}F-labeled copolymer **P4** indicated a good accordance regarding tumor uptake of **^{131}I-P4** at the same time point (2 h p.i.). This observation is of major importance since initial organ distribution of the differently labeled copolymers revealed strong differences in organ accumulation, although, an identical polymer batch was used for both ^{131}I- and ^{18}F-labeling. Moreover, the investigation of “cold” **P4b-I** and **-F** revealed similar physicochemical properties (CMC, aggregate size). In this regard it is obvious that an investigation of the *in vivo* behavior is crucial. The results of the present study underline the significance of applying multiple and versatile labeling approaches to determine the potential of polymeric carrier systems for an efficient anticancer therapy. Although the statistical copolymers will have limited potential for a targeted transport of drugs which are just hydrophobically embedded, they might be great carriers for covalently bound drugs.

Acknowledgment

The authors would like to thank [redacted] for his support during animal studies. Special thanks go to [redacted] for providing introduction into radioiodination procedures. We also want to thank the Max-Planck Graduate Center (MPGC, K. Wagener, M. Allmeroth) as well as the Graduate School Materials Science in Mainz (Excellence Initiative, DFG/GSC 266, D. Moderegger) for financial support. In addition the authors are very thankful for financial support of the DFG (SFB 1066).

References

(1) Matsumura, Y.; Maeda, H. A New Concept for Macromolecular Therapeutics in Cancer Chemotherapy: Mechanism of Tumoritropic Accumulation of Proteins and the Antitumor Agents Smancs. *Cancer Res.* 1986, *46*, 6387–6392.

(2) Duncan, R. The Dawning Era of Polymer Therapeutics. *Nat. Rev. Drug Discov.* 2003, *2*, 347–360.

(3) Duncan, R. Polymer conjugates as anticancer nanomedicines. *Nat. Rev. Cancer* 2006, *6*, 688–701.

(4) Duncan, R.; Vicent, M. J. Do HPMA copolymer conjugates have a future as clinically useful nanomedicines? A critical overview of current status and future opportunities. *Adv. Drug Deliv. Rev.* 2010, *62*, 272–282.

(5) Wicki, A.; Witzigmann, D.; Balasubramanian, V.; Huwyler, J. Nanomedicine in cancer therapy: Challenges, opportunities, and clinical applications. *J. Control. Release* 2015, *200*, 138–157.

(6) Barz, M.; Luxenhofer, R.; Zentel, R.; Vicent, M. J. Overcoming the PEG-addiction: well-defined alternatives to PEG, from structure–property relationships to better defined therapeutics. *Polym. Chem.* 2011, *2*, 1900.

(7) Matyjaszewski, K.; Xia, J. Atom Transfer Radical Polymerization. *Chem. Rev.* 2001, *101*, 2921–2990.

(8) Chiefari, J.; Chong, Y. K. (Bill); Ercole, F.; Krstina, J.; Jeffery, J.; Le, T. P. T.; Mayadunne, R. T. A.; Meijs, G. F.; Moad, C. L.; Moad, G.; Rizzardo, E.; Thang, S. H. Living Free-Radical Polymerization by Reversible Addition−Fragmentation Chain Transfer: The RAFT Process. *Macromolecules* 1998, *31*, 5559–5562.

(9) Moad, G.; Rizzardo, E.; Thang, S. H. Living Radical Polymerization by the RAFT Process. *Aust. J. Chem.* 2005, *58*, 379–410.

(10) Eberhardt, M.; Théato, P. RAFT Polymerization of Pentafluorophenyl Methacrylate: Preparation of Reactive Linear Diblock Copolymers. *Macromol. Rapid Commun.* 2005, *26*, 1488–1493.

(11) Theato, P. Synthesis of Well-Defined Polymeric Activated Esters. *J. Polym. Sci. Part A Polym. Chem.* 2008, *46*, 6677–6687.

(12) Gauthier, M. A.; Gibson, M. I.; Klok, H.-A. Synthesis of Functional Polymers by Post-Polymerization Modification. *Angew. Chem. Int. Ed. Engl.* 2009, *48*, 48–58.

(13) Barz, M.; Luxenhofer, R.; Zentel, R.; Kabanov, A. V. The uptake of *N*-(2-hydroxypropyl)-methacrylamide based homo, random and block copolymers by human multi-drug resistant breast adenocarcinoma cells. *Biomaterials* 2009, *30*, 5682–5690.

(14) Gibson, M. I.; Fröhlich, E.; Klok, H.-A. Postpolymerization Modification of Poly(Pentafluorophenyl methacrylate): Synthesis of a Diverse Water-Soluble Polymer Library. *J. Polym. Sci. Part A Polym. Chem.* 2009, *47*, 4332–4345.

(15) Boyer, C.; Bulmus, V.; Davis, T. P.; Ladmiral, V.; Liu, J.; Perrier, S. Bioapplications of RAFT Polymerization. *Chem. Rev.* 2009, *109*, 5402–5436.

(16) Lammers, T.; Subr, V.; Ulbrich, K.; Hennink, W. E.; Storm, G.; Kiessling, F. Polymeric nanomedicines for image-guided drug delivery and tumor-targeted combination therapy. *Nano Today* 2010, *5*, 197–212.

(17) Lammers, T. Improving the efficacy of combined modality anticancer therapy using HPMA copolymer-based nanomedicine formulations. *Adv. Drug Deliv. Rev.* 2010, *62*, 203–230.

(18) Herth, M. M.; Barz, M.; Jahn, M.; Zentel, R.; Rösch, F. $^{72/74}$As-labeling of HPMA based polymers for long-term in vivo PET imaging. *Bioorg. Med. Chem. Lett.* 2010, *20*, 5454–5458.

(19) Herth, M. M.; Barz, M.; Moderegger, D.; Allmeroth, M.; Jahn, M.; Thews, O.; Zentel, R.; Rösch, F. Radioactive Labeling of Defined HPMA-Based Polymeric Structures Using [^{18} F]FETos for In Vivo Imaging by Positron Emission Tomography. *Biomacromolecules* 2009, *10*, 1697–1703.

(20) Allmeroth, M.; Moderegger, D.; Biesalski, B.; Koynov, K.; Rösch, F.; Thews, O.; Zentel, R. Modifying the Body Distribution of HPMA-Based Copolymers by Molecular Weight and Aggregate Formation. *Biomacromolecules* 2011, *12*, 2841–2849.

(21) Allmeroth, M.; Moderegger, D.; Gündel, D.; Koynov, K.; Buchholz, H.-G.; Mohr, K.; Rösch, F.; Zentel, R.; Thews, O. HPMA-LMA Copolymer Drug Carriers in Oncology: An in Vivo PET Study to Assess the Tumor Line-Specific Polymer Uptake and Body Distribution. *Biomacromolecules* 2013, *14*, 3091–3101.

(22) Hemmelmann, M.; Metz, V. V.; Koynov, K.; Blank, K.; Postina, R.; Zentel, R. Amphiphilic HPMA–LMA copolymers increase the transport of Rhodamine 123 across a BBB model without harming its barrier integrity. *J. Control. Release* 2012, *163*, 170–177.

(23) Clemens-Hemmelmann, M.; Kuffner, C.; Metz, V.; Kircher, L.; Schmitt, U.; Hiemke, C.; Postina, R.;

Zentel, R. Amphiphilic Copolymers Shuttle Drugs Across the Blood-Brain Barrier. *Macromol. Biosci.* 2016, *16*, 655–665.

(24) Hemmelmann, M.; Mohr, K.; Fischer, K.; Zentel, R.; Schmidt, M. Interaction of pHPMA-pLMA Copolymers with Human Blood Serum and Its Components. *Mol. Pharm.* 2013, *10*, 3769–3775.

(25) Maeda, H.; Bharate, G. Y.; Daruwalla, J. Polymeric drugs for efficient tumor-targeted drug delivery based on EPR-effect. *Eur. J. Pharm. Biopharm.* 2009, *71*, 409–419.

(26) Fang, J.; Nakamura, H.; Maeda, H. The EPR effect: Unique features of tumor blood vessels for drug delivery, factors involved, and limitations and augmentation of the effect. *Adv. Drug Deliv. Rev.* 2011, *63*, 136–151.

(27) Nuhn, L.; Barz, M.; Zentel, R. New Perspectives of HPMA-based Copolymers Derived by Post-Polymerization Modification. *Macromol. Biosci.* 2014, *14*, 607–618.

(28) Perrier, S.; Takolpuckdee, P.; Mars, C. A. Reversible Addition−Fragmentation Chain Transfer Polymerization: End Group Modification for Functionalized Polymers and Chain Transfer Agent Recovery. 2005.

(29) Workman, P.; Aboagye, E. O.; Balkwill, F.; Balmain, A.; Bruder, G.; Chaplin, D. J.; Double, J. A.; Everitt, J.; Farningham, D. A. H.; Glennie, M. J.; Kelland, L. R.; Robinson, V.; Stratford, I. J.; Tozer, G. M.; Watson, S.; Wedge, S. R.; Eccles, S.A. Guidelines for the welfare and use of animals in cancer research. *Br. J. Cancer* 2010, *102*, 1555–1577.

(30) Salacinski, P. R. P.; McLean, C.; Sykes, J. E. C.; Clement-Jones, V. V.; Lowry, P. J. Iodination of Proteins, Glycoproteins, and Peptides Using a Solid-Phase Oxidizing Agent, 1,3,4,6-Tetrachloro-3α,6α-diphenyl Glycoluril (Iodogen). *Anal. Biochem.* 1981, *117*, 136–146.

(31) Greenwood, F. C.; Hunter, W. M.; Glover, J. S. The Preparation of ^{131}I-Labelled Human Growth Hormone of High Specific Radioactivity. *Biochem. J.* 1963, *89*, 114–123.

(32) Malik, R.; Hodgson, H. The Relationship between the Thyroid Gland and the Liver. *QJM* 2002, *95*, 559–569.

(33) Lammers, T.; Kühnlein, R.; Kissel, M.; Subr, V.; Etrych, T.; Pola, R.; Pechar, M.; Ulbrich, K.; Storm, G.; Huber, P.; Peschke, P. Effect of physicochemical modification on the biodistribution and tumor accumulation of HPMA copolymers. *J. Control. Release* 2005, *110*, 103–118.

(34) Maeda, H. Macromolecular therapeutics in cancer treatment: The EPR effect and beyond. *J. Control. Release* 2012, *164*, 138–144.

Supplementary Data

Long-term biodistribution study of HPMA-*ran*-LMA copolymers *in vivo* by means of ^{131}I-labeling

Karolin Wagener[1], Dorothea Moderegger[1], Mareli Allmeroth[2], Achim Reibel[1], Stefan Kramer[2], Barbara Biesalski[3], Nicole Bausbacher[4], Rudolf Zentel[2], Oliver Thews[5], Frank Rösch[1]

[1]Institute of Nuclear Chemistry, Johannes Gutenberg University, Fritz-Strassmann-Weg 2,
55128 Mainz, Germany

[2]Institute of Organic Chemistry, Johannes Gutenberg University, Duesbergweg 10-14,
55128 Mainz, Germany

[3]Institute of Pathophysiology, University Medical Center, Duesbergweg 6, 55128 Mainz, Germany

[4]Clinic and Polyclinic of Nuclear Medicine, University Medical Center, Langenbeckstraße 1, 55101
Mainz, Germany

[5]Institute of Physiology, University Halle, Magdeburger Str. 6, 06097 Halle (Saale), Germany

Contents

1. Experimental section

I. Characterization of polymers

II. Synthesis of reactive ester homopolymers

III. Polymer analogous reaction of homopolymers

IV. Analytical data obtained in isotonic NaCl solution

V. Size determination by fluorescence correlation spectroscopy (FCS)

VI. Radiolabeling of polymers

VII. Tumor and animal model

VIII. *Ex vivo* metabolism studies

2. Figures

3. Tables

4. References

1. Experimental section

I. Characterization of polymers

^{1}H-NMR spectra were obtained by a Bruker AC-300 spectrometer at 300 MHz or on a Bruker Avance II at 400 MHz, ^{19}F-NMR analysis was carried out with a Bruker DRX-400 or with a Bruker Avance III HD-400 at 400 MHz. All measurements were accomplished at room temperature and spectroscopic data were analyzed using ACDLabs 9.0 1D NMR Manager or MestReNova Software (Version: 10.0.2-15465). The synthesized polymers were dried at 40 °C under vacuum overnight, followed by gel permeation chromatography (GPC). GPC was performed in tetrahydrofuran (THF) as solvent, using following equipment: pump PU 1580, autosampler AS 1555, UV detector UV 1575 and refractive index (RI) detector RI 1530 from Jasco as well as a miniDAWN Tristar light scattering detector from Wyatt. Columns were used from MZ Analysentechnik, 300x8.0 mm: MZ-Gel SDplus 106 Å 5 µm, MZ-Gel SDplus 104 Å 5 µm and MZ-Gel SDplus 102 Å 5 µm. GPC data were evaluated by using the software PSS WinGPC Unity from Polymer Standard Service Mainz. The flow rate was set to 1 ml/min with a temperature of 25 °C.

Analytical size exclusion chromatography (SEC) of ^{131}I-labeled polymers was performed using a HiTrap™ Desalting Column, Sephadex G-25 Superfine and a HPLC system consisting of a Waters pump (1500 series), a Waters UV-detector (2487 λ absorbance detector) and a Berthold LB 509 radiodetector. Radiochemical purity was determined using Tec Control chromatography strips (Biodex Medical Systems, Inc., USA). Preparative SEC for removal of free iodine was accomplished using disposable PD-10 Desalting Columns (GE Healthcare) which were preconditioned and eluted with 0.9% (w/v) sodium chloride solution.

II. Synthesis of reactive ester homopolymers

Reversible addition-fragmentation chain transfer (RAFT) polymerization of pentafluorophenyl methacrylate (PFPMA) with 4-cyano-4-((thiobenzoyl) sulfanyl)pentanoic acid (CTP) was carried out in a Schlenk tube.[1-3] For this purpose 4 g of PFPMA were dissolved in 5 ml of absolute dioxane, furthermore CTP and 2,2'-Azo-bis-(isobutyronitrile) (AIBN) were added. The molar ratio of CTP/AIBN was chosen to be 8:1. After three freeze-vacuum-thaw cycles, the mixture was immersed in an oil bath at 65 °C and stirred overnight. Afterwards, the polymeric solution was precipitated three times in hexane, centrifuged and dried under vacuum at 40 °C overnight. A slightly pink powder was obtained. Yield: 52 %. ^{1}H-NMR (300 MHz, $CDCl_3$) δ/ppm: 1.20-1.75 (br), 2.00-2.75 (br s). ^{19}F-NMR (400 MHz, $CDCl_3$) δ/ppm: -162.03 (br), -156.92 (br), -152 to -150 (br).

III. Polymer analogous reaction of homopolymers

Depending on the labeling technique necessary, either for a fluorescent or radioactive marker, two different routes were applied. For subsequent radioactive labeling, the protocol was carried out as follows. As example, 100 mg of the polymeric precursor (M_n = 18000 g/mol) were diluted in 2 ml of absolute dioxane. 5 mg of tyramine, diluted in a DMSO/dioxane mixture, and 10 mg of triethylamine were added. After stirring for four hours at 35 °C, 30 mg of 2-hydroxypropylamine as well as 40 mg of triethylamine were added and the solution was stirred overnight. For final removal of reactive ester side groups, further 30 mg of 2-hydroxypropylamine were added the next morning. The solution was precipitated two times in diethyl ether, centrifuged and finally dissolved in a DMSO/water solution for dialysis. After lyophilization a white powder could be obtained. Yield: 79%. ^{1}H-NMR (400 MHz, d. DMSO) δ/ppm: 0.60-1.40 (br), 1.45-2.20 (br), 2.75-3.10 (br), 3.50-3.80 (br), 4.60-4.80 (br), 6.60-6.70 (br) and 6.85-7.00 (br). For additional fluorescent labeling, the fluorescent marker Oregon Green 488 cadaverine was used. 100 mg of polymeric precursor were diluted in 2 ml of absolute dioxane and 2.75 mg of Oregon Green 488 cadaverine were added. Afterwards tyramine and 2-hydroxypropylamine were added, as described by the procedure above.

IV. Analytical data obtained in isotonic NaCl solution

Isotonic NaCl solution 0.9 % was obtained by B. Braun Melsungen AG and used without any purification. Stock solutions were prepared using 1 % of absolute DMSO in isotonic sodium chloride solution.

V. Size determination by fluorescence correlation spectroscopy (FCS)

The hydrodynamic radii of the polymeric systems were determined by FCS using a commercial FCS setup (Zeiss, Germany) consisting of the module ConfoCor 2 and an inverted microscope model Axiovert 200 with a Zeiss C-Apochromat 40 ×/1.2 W water immersion objective. The fluorophores were excited with an Argon laser (λ = 488 nm) and the emission was collected after filtering with a LP505 long pass filter. For detection, an avalanche photodiode, enabling single-photon counting, was used. As sample cell, eight-well, polystyrene-chambered cover glass (Laboratory-Tek, Nalge Nunc International) was applied. For sample preparation, stock solutions of 1 mg fluorescently labeled polymer/ml NaCl were applied, diluted to a final concentration of 0.1 mg/ml. The solution was kept at room temperature over night. For reference reason, free Oregon Green 488 cadaverine dye in NaCl-solution was studied, too. The calibration of the FCS observation volume was done using a dye with known diffusion coefficient, i.e. Rhodamine 6 G. For each solution, five measurement cycles with a total duration of 150 seconds were applied. Time dependent fluctuations of the fluorescence intensity $\delta I(t)$ were detected and evaluated by autocorrelation analysis, yielding the diffusion coefficient and the hydrodynamic radius of the fluorescent species.[4]

VI. Radiolabeling of polymers

In order to optimize the ^{131}I-radiolabeling of HPMA-based polymers, two different *in situ* oxidants were investigated. For radiolabeling using Iodogen™ (1,3,4,6-Tetrachloro-3a,6a-diphenylglycoluril) as oxidizing agent, the reaction vials were coated prior to the radiolabeling with the respective amount of Iodogen™. Consecutively 50 µl of 0.5 M phosphate buffer (pH = 7.4), 450 µl phosphate buffered saline (PBS), 100 µl of the respective polymer as well as 3-10 MBq of [^{131}I]I^{-} (0.05 N NaOH solution) were placed into the coated vial. At t = 4 min, 100 µl of an aqueous ascorbic acid solution (25 mg/ml, pH = 5.0) were added and after 1 min of shaking, the labeling mixture was transferred onto a PD-10 column for subsequent purification using fractionated elution with 0.9 % sodium chloride solution.

Radiolabeling procedure using Chloramine-T (*N*-chloro-4-methylbenzenesulfonamide sodium salt, CAT) was started by placing 3-10 MBq of [^{131}I]I^{-} (0.05 N NaOH solution) in a reaction vial, followed by 50 µl of 0.5 M phosphate buffer (pH = 7.4) and 400-x µl (x = volume of the CAT solution) of PBS. After addition of 200-500 µg of the respective polymer in 100 µl of a variable solvent, the radiolabeling reaction was started by adding x µl of a CAT solution (1 mg/ml in 0.9 % sodium chloride solution) resulting in a final volume of 550 µl for the radiolabeling mixture. After 4 min, the reaction was quenched and purified according to the Iodogen procedure.

VII. Tumor and animal model

Walker 256 mammary carcinoma cells were grown in culture in RPMI medium supplemented with 10 mM L-glutamine and 10 % fetal calf serum at 37 °C under a humidified 5 % CO_2 atmosphere and sub-cultivated twice per week. For tumor implantation male Sprague-Dawley rats (Charles River Wiga, Sulzfeld, Germany; body weight 150 to 300 g) housed in the animal care facility of the University of Mainz were used in this study. Solid carcinomas were heterotopically induced by injection of cell suspension (0.4 ml approximately 10^4 cells/µl) subcutaneously into the dorsum of the hind foot. Tumors grew as flat, spherical segments and replaced the subcutis and corium completely. Volumes were determined by measuring the three orthogonal diameters (d) of the tumors and using an ellipsoid approximation with the formula: tumor volume = $d_1 \times d_2 \times d_3 \times \pi/6$.

VIII. *Ex vivo* metabolism studies

In order to separate free polymer from free ^{131}I in the plasma water, 100 µl of a 5 M potassium iodide solution were added to the plasma water fractions followed by 2 ml of a 1 M silver nitrate solution. The precipitated silver iodide was separated by centrifugation at 5000 rpm for 5 min. The percentage of radioactivity in the blood cell, protein, silver iodide and free polymer plasma water fractions was calculated by subtracting the activities of the supernatants from the activity of the whole blood sample.

Nevertheless this procedure suggested high amounts of free [^{131}I]I$^-$ in the plasma water which contradicted the low amounts of radioactivity found in the thyroid. We believe, that the deiodination we quantify in terms of ^{131}I-uptake in the thyroid is the parameter we can trust in. Enzymatic deiodination transfers [^{131}I]I$^-$ into the thyroid, and so we correlate the enzymatic chemistry of deiodination with the ^{131}I-utilisation in the gland. We believe therefore, that there is an alternative mechanism to explain the results of our precipitation experiment and this is “adsorption”. During our precipitation experiment we assumed that direct precipitation of [^{131}I]I$^-$is not possible, since the amount of ^{131}I (either free or polymer bound) in the blood is very small (picomolar). Thus we added (0.5 mmol) of “cold” KI to the plasma water fractions in order to have a precipitable amount of iodide. So we precipitated in fact about 120 mg of AgI, which can absorb on its surface both free iodine, but also polymers. This latter aspect is reasonable as there are reports showing that polymers in fact readily adsorb on silver iodide surfaces.[5-7] Here we have to consider in addition (i) the huge excess of the freshly forming AgI (~0.5x10^{-3} mol) and (ii) the small amount of polymer (<<2.4x10^{-8} mol). So the adsorption of such a small amount of polymer to a massive excess of cold AgI can well explain the high accumulation of radioactivity in the precipitate as this represents not only free [^{131}I]I$^-$ but also ^{131}I still bound to polymers.

2. Figures

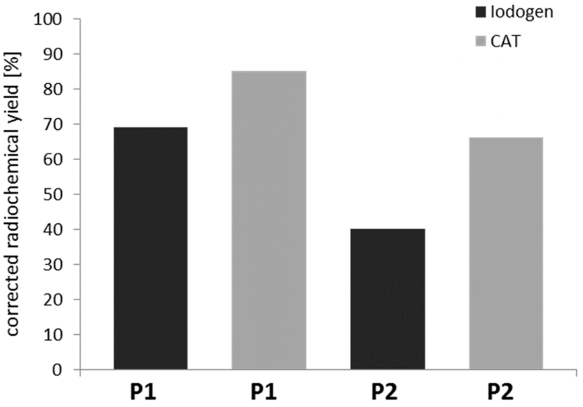

Figure S1. Corrected radiochemical yields for radioiodination of HPMA-based homopolymers **P1** and **P2** using 25 µg Iodogen™ or 200 µg CAT as determined using SEC.

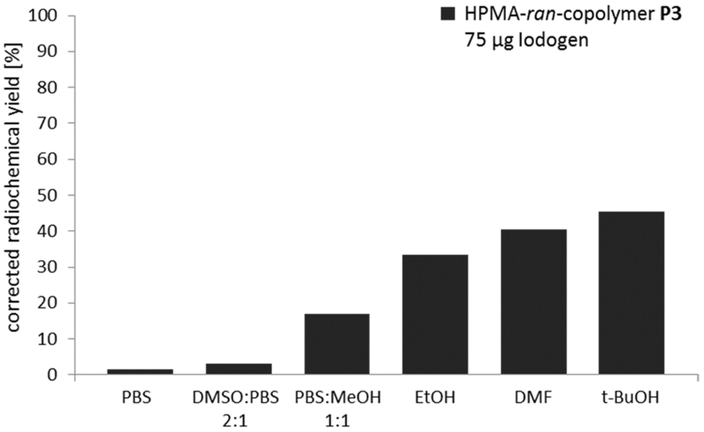

Figure S2. Influence of the solvent on the radioiodination of the HPMA-*ran*-LMA copolymer **P3** using 75 µg of Iodogen™ as determined using SEC.

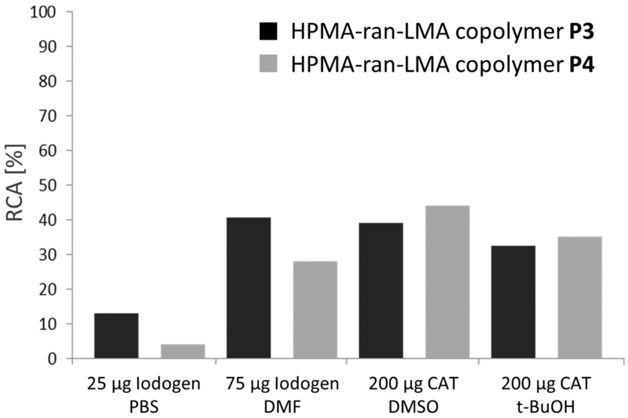

Figure S3. Corrected radiochemical yields of the HPMA-*ran*-LMA copolymers **P3** and **P4** using Iodogen™ and CAT for ^{131}I-radiolabeling as determined by means of SEC.

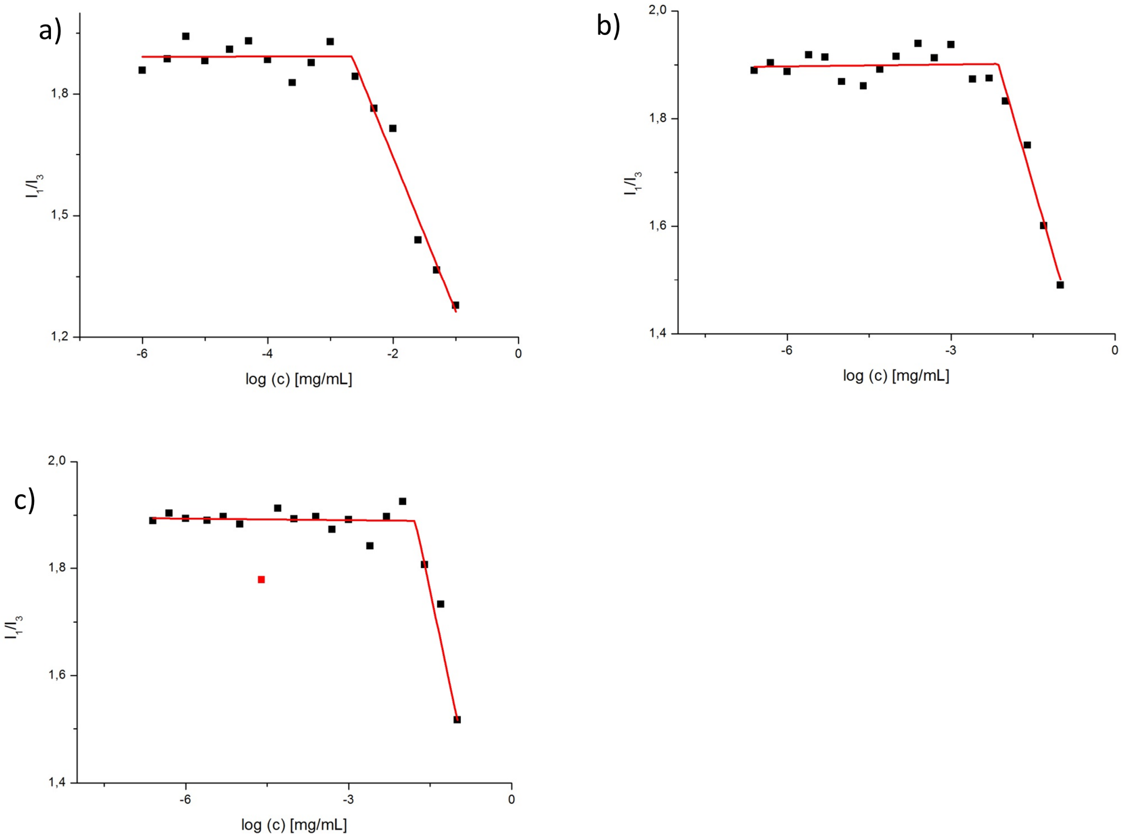

Figure S4. CMC measurements of functionalized **P4b** polymers by pyrene fluorescence spectroscopy; a) non-functionalized polymer b) fluorine functionalized polymer c) iodine functionalized polymer.

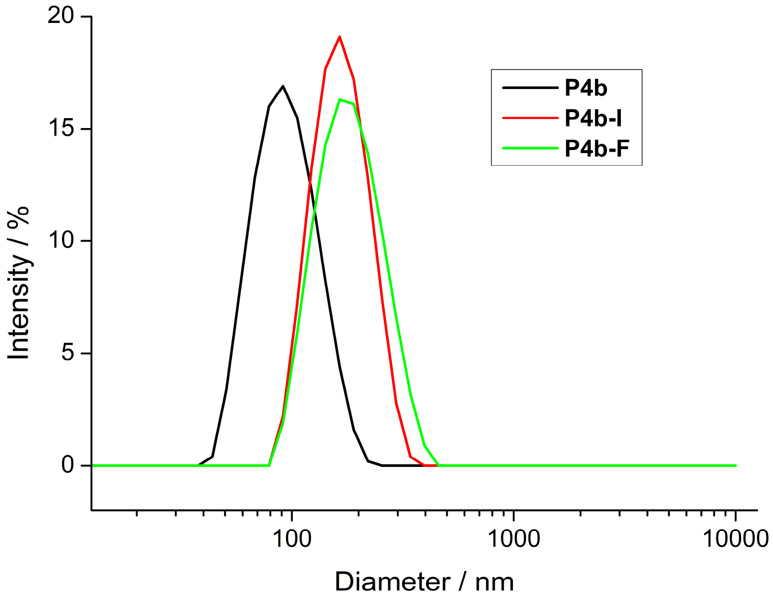

Figure S5. Size distribution intensity graph of **P4b**, **P4b-I** and **P4b-F** as revealed by DLS; black: non functionalized polymer; red: iodine functionalized polymer; green: fluorine functionalized polymer.

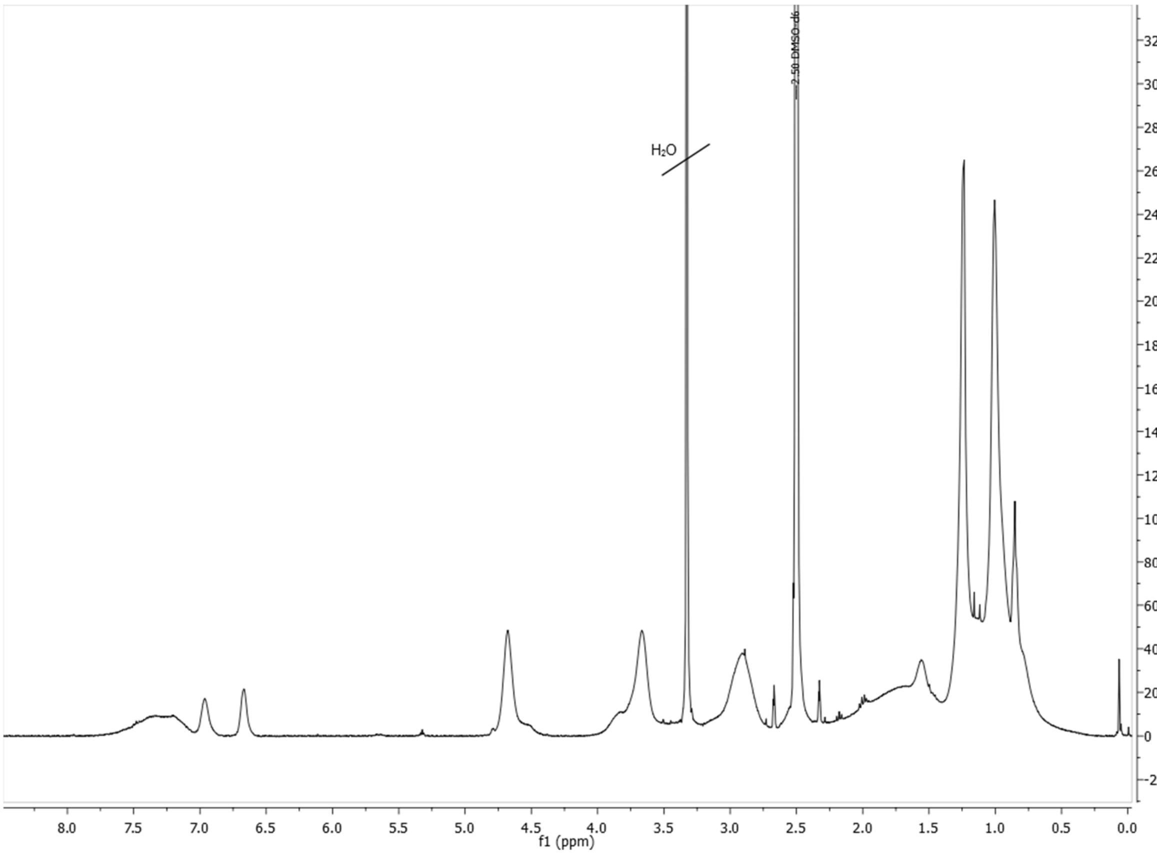

Figure S6. ^{1}H-NMR spectrum of non-functionalized **P4b** measured in DMSO-d_6 at 400 MHz.

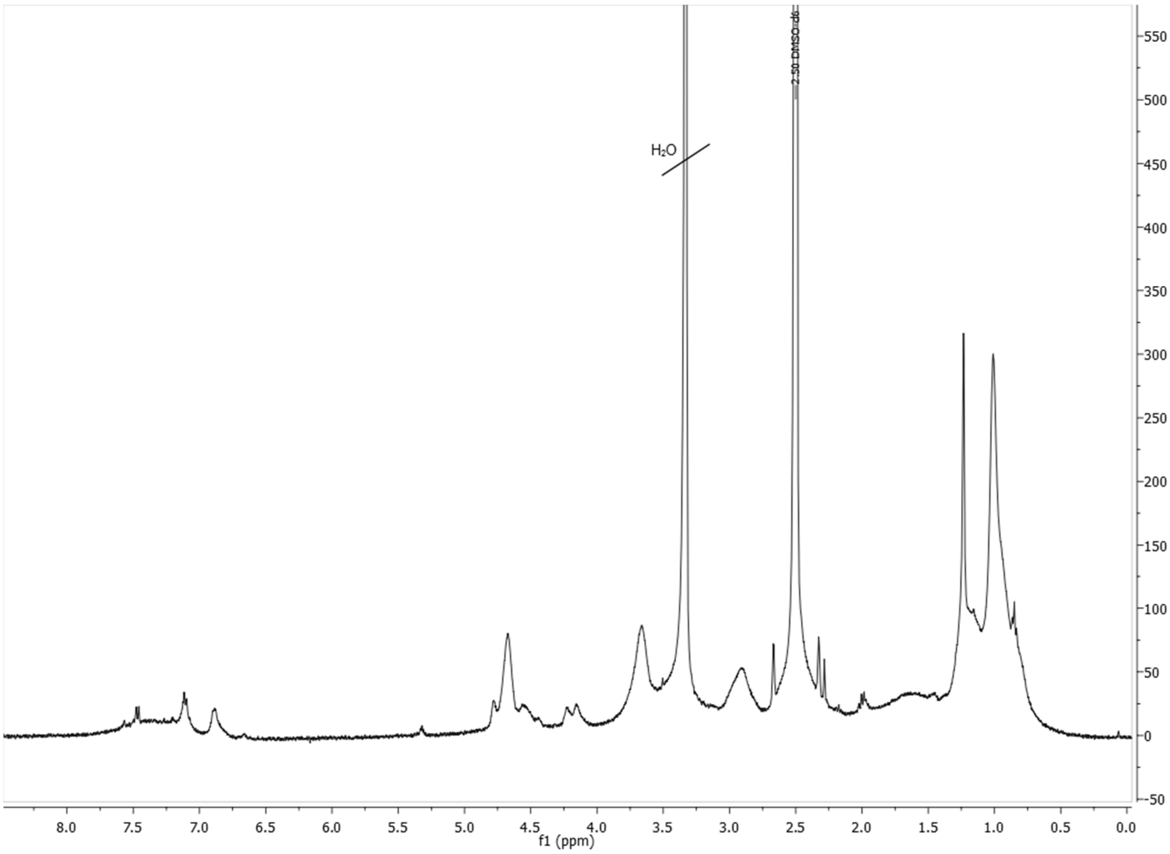

Figure S7. ^{1}H-NMR spectrum of ^{19}F-functionalized **P4b** (**P4b-F**) measured in DMSO-d_6 at 400 MHz.

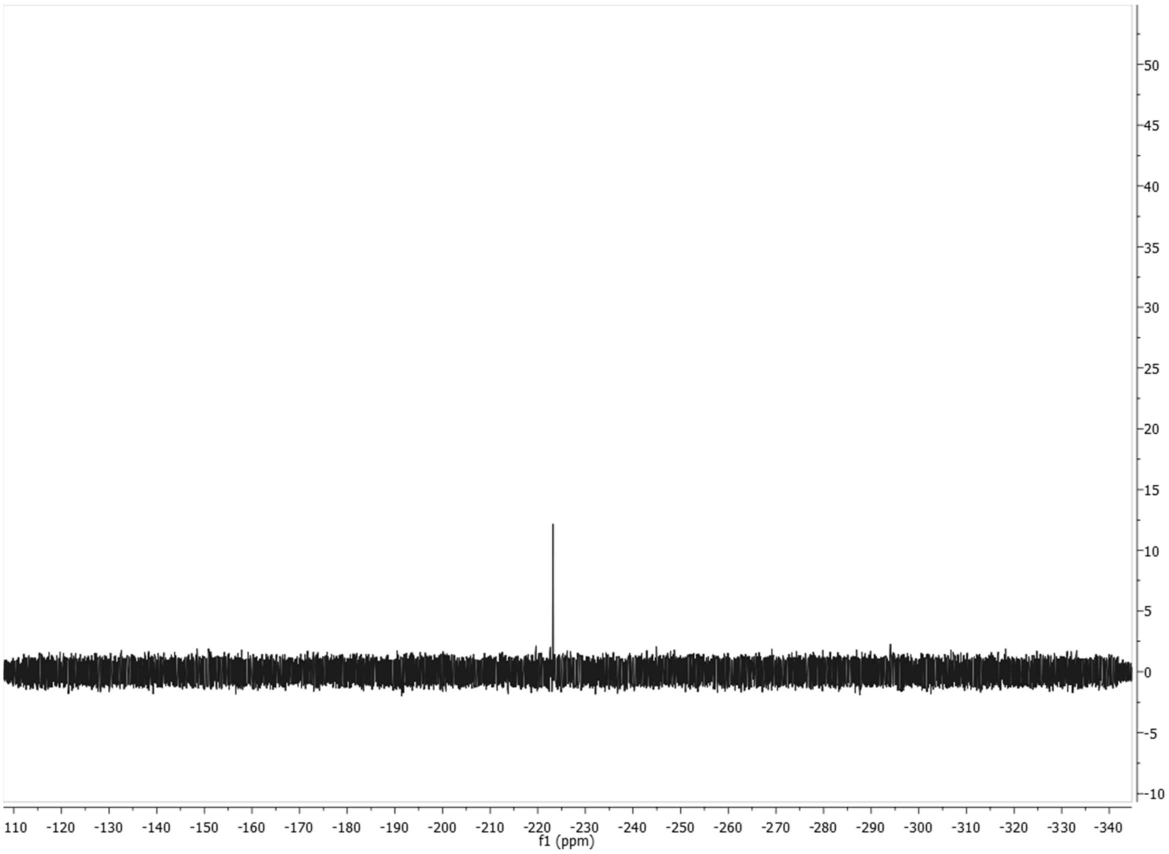

Figure S8. ^{19}F-NMR spectrum (^{1}H-decoupled) of ^{19}F-functionalized **P4b** (**P4b-F**) measured in DMSO-d_6 at 400 MHz.

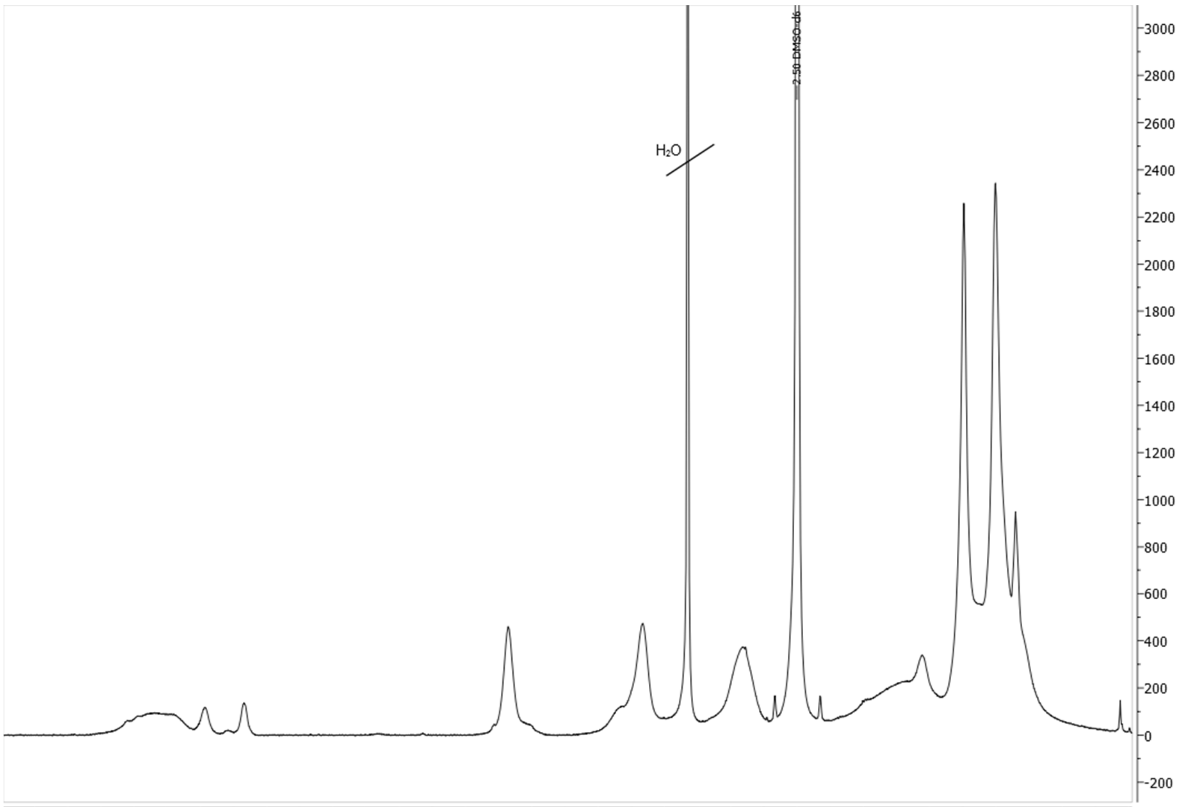

Figure S9. ^{1}H-NMR spectrum of ^{127}I-functionalized **P4b** (**P4b-I**) measured in DMSO-d_6 at 400 MHz.

3. Tables

Table S1. Biodistribution data of the ^{18}F- and ^{131}I-labeled HPMA-*ran*-LMA copolymer **P4** after i.v. administration in Walker 256 carcinoma bearing rats studied over a time course of up to three days. Data is represented as % ID/g tissue (mean±SEM).

	^{18}F-P4	^{131}I-P4			
organ	2 h[a)]	2 h[b)]	24 h[b)]	48 h[b)]	72 h[b)]
lung	1.56±0.17	1.90±0.31	0.78±0.11	0.63±0.11	0.47±0.05
blood	2.96±0.03	1.67±0.14	0.47±0.04	0.14±0.02	0.08±0.01
liver	0.80±0.08	4.36±0.12	4.74±0.22	4.56±0.41	4.46±0.20
spleen	0.74±0.09	8.80±0.71	8.37±0.69	7.97±0.75	10.43±1.43
kidney	5.32±0.17	0.50±0.04	0.38±0.06	0.28±0.04	0.32±0.06
thyroid	-	3.14±0.58[a)]	22.38±3.73[a)]	14.46±1.48[c)]	10.77±0.79[c)]
W 256 tumor	0.63±0.03	0.72±0.06[d)]	0.93±0.06[e)]	0.61±0.04[e)]	0.64±0.08[e)]

[a)] n=3, [b)] n=9, [c)] n=4, [d)] n=12, [e)] n=18.

4. References

(1) Allmeroth, M.; Moderegger, D.; Biesalski, B.; Koynov, K.; Rösch, F.; Thews, O.; Zentel, R. Modifying the Body Distribution of HPMA-Based Copolymers by Molecular Weight and Aggregate Formation. *Biomacromolecules* 2011, *12*, 2841–2849.

(2) Barz, M.; Luxenhofer, R.; Zentel, R.; Kabanov, A. V. The uptake of *N*-(2-hydroxypropyl)-methacrylamide based homo, random and block copolymers by human multi-drug resistant breast adenocarcinoma cells. *Biomaterials* 2009, *30*, 5682-5690.

(3) Theato, P. Synthesis of Well-Defined Polymeric Activated Esters. *J. Polym. Sci. Part A Polym. Chem.* 2008, *46*, 6677–6687.

(4) Rigler, R.; Elson, E. S. *Fluorescence Correlation Spectroscopy*; Springer Verlag: New York, 2001.

(5) Csempesz, F.; Rohrsetzer, S. Interfacial behaviour of binary polymer mixtures I. Effect of uncharged polymers and of their mixtures on the stability of silver iodide sol. *Colloids Surf.* 1984, *11*, 173-186.

(6) Nowicki, W.; Nowicka, G. Adsorption of large macromolecules on fine colloidal particles. *Colloid Polym. Sci.* 1995, *273*, 473-479.

(7) Csempesz, F.; Csáki, K. F. Mixed Adsorption Layers of Uncharged Polymers at Particle/Solution Interfaces. *Langmuir* 2000, *16*, 5917-5920.

3.2 Comparison of Linear and Hyperbranched Polyether Lipids for Liposome Shielding by ^{18}F-Radiolabeling and Positron Emission Tomography

Karolin Wagener[1], Matthias Worm[2], Stefanie Pektor[3], Meike Schinnerer[4], Raphael Thiermann[5], Matthias Miederer[3], Holger Frey[2] and Frank Rösch[1]

[1]Institute of Nuclear Chemistry, Johannes Gutenberg University, Fritz-Strassmann-Weg 2,
55128 Mainz, Germany

[2]Institute of Organic Chemistry, Johannes Gutenberg University, Duesbergweg 10-14,
55128 Mainz, Germany

[3]Clinic and Polyclinic of Nuclear Medicine, University Medical Center, Langenbeckstraße 1,
55101 Mainz, Germany

[4]Institute of Physical Chemistry, Johannes Gutenberg University, Jakob-Welder-Weg 11,
55128 Mainz, Germany

[5]Fraunhofer ICT-IMM, Carl-Zeiss-Str. 18-20, 55129 Mainz, Germany

Abstract

Multifunctional and highly biocompatible polyether structures play a key role in shielding liposomes from degradation in the bloodstream, providing also multiple functional groups for further attachment of targeting moieties. In this work hyperbranched polyglycerol (*hb*PG) bearing lipids with long alkyl chain anchor are evaluated with respect to steric stabilization of liposomes. The branched polyether lipids possess a hydrophobic bis(hexadecyl)glycerol membrane anchor for the liposomal membrane. *hb*PG was chosen as a multifunctional alternative to PEG, enabling the eventual linkage of multiple targeting vectors. Different *hb*PG lipids (M_n = 2900, 5200 g mol^{-1}) were examined. A linear bis(hexadecyl)glycerol-PEG lipid (M_n = 3000 g mol^{-1}) was investigated as well, comparing *hb*PG and PEG with respect to shielding properties. Radiolabeling of the polymers was carried out using 1-azido-2-(2-(2-[^{18}F]fluoroethoxy)ethoxy)ethane ([^{18}F]F-TEG-N_3) via copper-catalyzed alkyne-azide cycloaddition with excellent radiochemical yields exceeding 95 %. Liposomes were prepared by the thin-film hydration method followed by repeated extrusion. Use of a custom automatic extrusion device gave access to reproducible sizes of the liposomes (hydrodynamic radius of 60-94 nm). The *in vivo* fate of the bis(hexadecyl)glycerol polyethers and their corresponding assembled liposome structures were evaluated via non-invasive small animal positron emission tomography (PET) imaging and biodistribution studies (1 h after injection and 4 h after injection (only for liposomal formulations) in mice. Whereas the main uptake of the non-liposomal polyether lipids was observed in the kidneys and in the bladder after 1 h due to rapid renal clearance, in contrast, the corresponding liposomes showed uptake in the blood pool as well as in organs with good blood supply, i.e. heart and lung over the whole observation period of 4 h. The *in vivo* behavior of all three liposomal formulations was comparable, albeit with remarkable differences in splenic uptake. Overall, liposomes shielded by the branched polyglycerol lipids show a favorable biodistribution with greatly prolonged blood circulation times, rendering them promising novel nanovesicles for drug transport and targeting.

Introduction

One of the main objectives in the development of therapeutics is the improvement of the therapeutic index to maximize the efficiency in relation to the toxicity of a therapeutic agent. Commonly, small molecules exhibit a poor therapeutic index, showing fast renal clearance and short retention times in the blood pool. To achieve the desired therapeutic effect, the dose has to be enhanced, resulting in an increase of harmful side effects. To overcome this disadvantage, a large variety of drug delivery systems (DDSs) with a higher molecular weight and therefore prolonged circulation in the blood have been developed in the last decades,[1–3] and to date more than 200 related products have been either approved or are under clinical investigation.[4] One prominent class of DDSs are liposomes, which have been intensively investigated as drug carriers.[5,6] Several formulations are currently approved and commercially used.[7,8] Liposomes mimic endogenous biomembranes, as they consist of phospholipids and cholesterol. However, conventional liposomes suffer from fast detection by the mononuclear phagocyte system (MPS) via macrophages and uptake in liver and spleen.[5,9,10] As a result, *in vivo* circulation times are short as recognition, binding and uptake processes occur with half lives on the order of a few minutes or longer.[11] It has been reported that liposome size, composition and charges are the main parameters affecting recognition by the MPS.[9,10,12] However, when polyethylene glycol (PEG) chains are linked covalently to cholesterol or phospholipids and anchored in the lipid bilayer, detection by the MPS can be prevented, resulting in prolonged retention in the blood and a reduced MPS uptake.[13–16] However, the "gold standard" PEG used to achieve "stealth liposomes" lacks functional groups offering further functionalization, because commonly methoxyPEG (*m*PEG) is used. One promising alternative is the highly biocompatible and water-soluble hyperbranched polyglycerol (*hb*PG).[17,18] The multiple hydroxyl groups of *hb*PG facilitate functionalization with fluorescent markers, radiolabels or targeting ligands for directed drug delivery. Beyond its multifunctionality, which enables linkage to targeting vectors, it has been shown that *hb*PG reveals enhanced protein repulsion compared to PEG.[19,20] To evaluate the potential of those novel systems in terms of correlating structural and chemical features of new *hb*PG-shielded liposomes with their behavior *in vivo*, positron emission tomography (PET) can be employed to quantify the pharmacokinetic properties *in vivo*, as it proved to be an excellent method to measure the fate of radiolabeled nanoparticles[21,22], among them ^{18}F-radiolabeled liposomes.[23,24]

In 2010 Frey and coworkers introduced a synthetic approach for linear-hyperbranched polyether lipids. Cholesterol is directly used as an initiator for the oxyanionic ring-opening polymerization of various epoxide monomers. In this manner, a variety of polyether architectures with an adjustable number of hydroxyl groups can be synthesized.[25] Recently, our group investigated the *in vivo* fate of a multifunctional hyperbranched cholesterol lipid (Ch-PEG$_{30}$-*hb*PG$_{24}$-^{18}F) in comparison with a linear PEGylated lipid (Ch-PEG$_{27}$-^{18}F) and "naked" ^{18}F-cholesten. In addition, the liposomal formulations of these two polymers were compared with liposomes labeled with ^{18}F-cholesten.[26] In this study the desired stealth effect could not be demonstrated, which motivated us to conduct further investigations into structural modification of the components of the liposomes.

The key objective of this work was an improved stability of the liposomes. To this end, the cholesterol anchor of the polymers was exchanged for a 1,2-bis(hexadecyl)glycerol (BisHD) anchor, as recent results suggest fast intermembrane exchange of cholesterol anchored polyether lipids.[27] A strategy for the synthesis of bis(alkyl)glycerol polyether lipids was reported by Hofmann et al. in 2011.[28] In the present work, we focus on investigating the properties of *hb*PG lipids (BisHD-*hb*PG$_{32}$, $M_\mathrm{n} \approx 2900$ g mol^{-1} and BisHD-*hb*PG$_{63}$, $M_\mathrm{n} \approx 5200$ g mol^{-1}) employed for the steric stabilization of liposomes. To compare *hb*PG with PEG with respect to the liposome shielding properties, a BisHD-PEG$_{56}$ ($M_\mathrm{n} \approx 3000$ g/mol) lipid was examined in addition. Radiolabeling was carried out using the prosthetic group 1-azido-2-(2-(2-[^{18}F]fluoroethoxy)ethoxy)ethane ([^{18}F]F-TEG-N$_3$) via copper-catalyzed alkyne-azide cycloaddition reaction (CuAAC), which allows for high specificity and excellent yields under mild conditions and is frequently used to synthesize PET tracers.[29] Three different radiolabeled polyether lipids were obtained: BisHD-*hb*PG$_{32}$-CH$_2$-triazole-TEG-^{18}F (BisHD-*hb*PG$_{32}$-^{18}F), BisHD-*hb*PG$_{63}$-CH$_2$-triazole-TEG-^{18}F (BisHD-*hb*PG$_{63}$-^{18}F) and BisHD-PEG$_{56}$-CH$_2$-triazole-TEG-^{18}F (BisHD-PEG$_{56}$-^{18}F). Size and shape of the liposomes were analyzed via dynamic light scattering (DLS) and cryo-transmission electron microscopy (cryo-TEM). To achieve reproducible sizes of the liposomes, an automated liposome preparation process was established. Temperature-dependent stability profiles were tested via DLS. Finally, *in vivo* evaluation of the non-associated polyether lipids and their corresponding liposomal formulations (Figure 1) was performed in small animal studies via *in vivo* PET and *ex vivo* organ distribution.

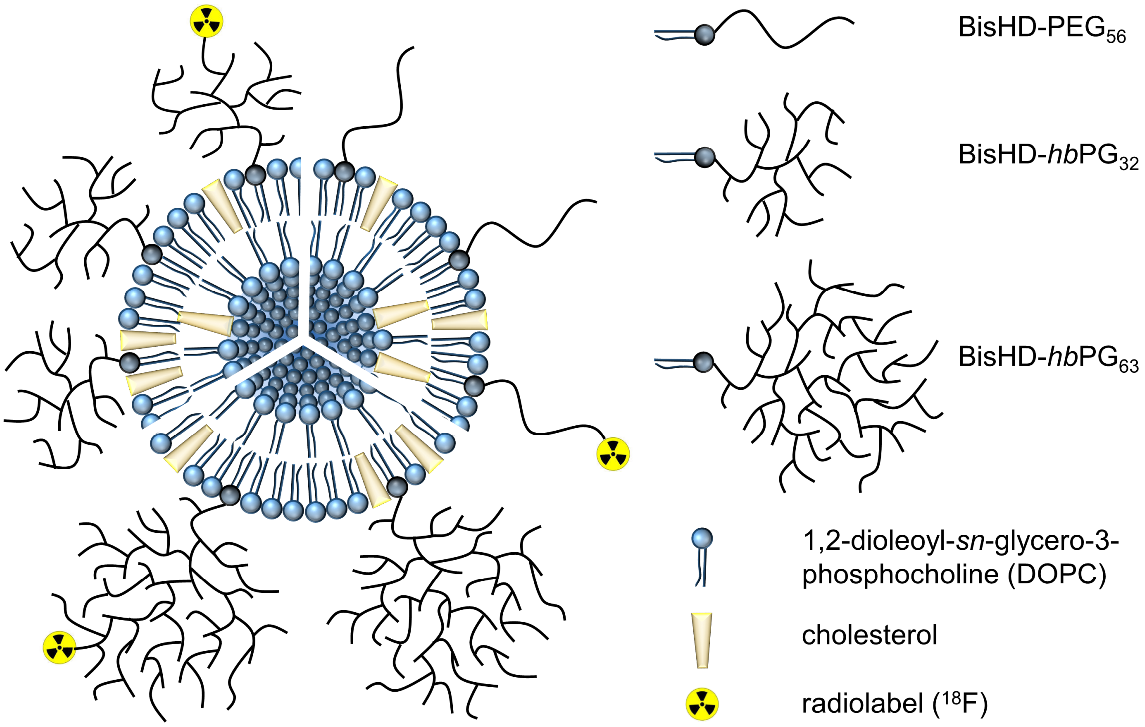

Figure 1. Illustration of the liposomal formulations containing te three different polyether lipids, BisHD-PEG$_{56}$, BisHD-*hb*PG$_{32}$ and BisHD-*hb*PG$_{63}$; the radiolabel is fluorine-18; the polymer chains inside the liposome are omitted for clarity, and the illustration is not drawn to scale.

Experimental

Materials

All chemicals were obtained from Sigma Aldrich, TCI Europe, VWR or Acros Organics unless stated otherwise. Deuterated solvents (C_6D_6, CD_2Cl_2, DMSO-d_6, pyridine-d_5) were purchased from Deutero GmbH. THF used for the anionic ring-opening polymerization of ethylene oxide (EO) was dried and stored over sodium/benzophenone. EO was purchased from Sigma Aldrich. Care must be taken when handling the flammable, toxic, and gaseous ethylene oxide. EO must be stored in pressure-proof gas bottles and used only in an appropriate fume hood with the respective safety precautions. Polymerizations of EO are carried out in flame-dried glassware, allowing for secure handling by using cryo-transfer techniques to transport EO inside the evacuated and sealed glass apparatus. Batch-sizes must not exceed 5 g of EO in a 250 ml flask to prevent spontaneous detachment of the septum and release of EO. Ethoxyethyl glycidyl ether (EEGE) was synthesized according to known literature protocols.[30] Glycidol was stirred over CaH_2 and freshly distilled prior use. Dry NMP (*N*-methylpyrrolidone) was stored over molecular sieve before use. Particle-free phosphate buffered saline (PBS) enabling exact light scattering experiments was obtained from Gibco™ by Thermo Fisher Scientific.

Methods

Characterization

^{1}H NMR and diffusion-ordered NMR (DOSY) spectra were measured on a Bruker Avance II 400 MHz (5 mm BBO probe, 256 Scans, and B-ACS 60 auto sampler) at 294 K. ^{13}C NMR spectra were recorded on a Bruker Avance II 400 (100.5 MHz, 5 mm BBO probe, and B-ACS 60 auto sampler) at 294 K. All spectra were processed with MestReNova v9.0 software. DOSY spectra were analyzed using MestReNova Bayesian DOSY Transform Software. Gel permeation chromatography (GPC) data were obtained using Agilent 1100 Series endowed with a PSS HEMA-column ($10^6/10^4/10^2$ Å porosity), LiBr/DMF (1 g/l) as eluent using refractive index (RI) detection. Molecular weights and dispersity ($Đ = M_w/M_n$) were determined with monodisperse PEG standards from Polymer Standard Service GmbH (PSS). MALDI-ToF mass spectrometry was conducted on an Axima CFR MALDI-ToF mass spectrometer using α-cyano-4-hydroxy-cinnamonic acid (CHCA) as matrix and potassium trifluoroacetate (KTFA) as a source for cations.

For multi-angle DLS cylindrical quartz cuvettes (Hellma Analytics, Mühlheim, Germany) were cleaned by dust-free distilled acetone and transferred to a dust free flow box. Solutions were diluted 1:100 with PBS and filtered into the cuvettes through Millex-LCR filters, 0.45 µm pore size (Merck Millipore). DLS measurements were performed by the following instruments at 20 °C. Apparatus 1 consists of a Uniphase He/Ne Laser (22.5 mW output power at $\lambda = 632.8$ nm) and an ALV/CGS-8F SLS/DLS 5022F goniometer with eight simultaneously working ALV 7004 correlators and eight ALV/High QEAPD avalanche photodiode detectors. Apparatus 2 consists of a Uniphase He/Ne Laser (22.5 mW output power at λ = 632.8 nm), an ALV/SP125 goniometer with an ALV 5000/E/PCI correlator and an ALV/High QEAPD Avalanche photodiode detector. The correlation functions of the particles were fitted using a sum of two exponentials. The z-average diffusion coefficient D_z was calculated by extrapolating D_{app} for q = 0. By formal application of Stokes law, the inverse z-average hydrodynamic radius is $R_\mathrm{h} = \langle R_\mathrm{h}^{-1} \rangle_z^{-1}$. The experimental uncertainties are estimated to ±2 % for R_h.

Cryo-transmission electron microscopy imaging was performed using a Zeiss Libra® 120 (Carl Zeiss AG), operating at 120 kV acceleration voltage. The images were taken with a 2k x 2k CCD-camera (UltraScan 1000XP, Gatan, Inc.). The samples were vitrified in a plunge freezer (Leica EM GP, Leica Microsystems) with liquid ethane at -180 °C on holey carbon-coated copper grids (Quantifoil® R2/1, Quantifoil Micro Tools). Vitreous ice grids were transferred into the electron microscope using a Gatan 626 holder (Gatan, Inc.), that maintains the grids at a temperature below -170 °C.

Radio-thin-layer chromatographys (radio-TLCs) were run on silica-coated aluminum-backed TLC plates (Merck) using EA/Hex 1:1 as mobile phase. The chromatograms, acquired on a RITA detector (Raytest), were analyzed using Gina Star TLC software (Raytest).

Polymer syntheses

1,2-Bis(hexadecyl)glycerol (BisHD-OH). The synthesis protocol has been described in previous reports.[28]

Ethoxyethyl glycidyl ether (EEGE). This compound has been synthesized according to known literature protocols.[30]

1,2-Bis(hexadecyl)glycerol-linPG (BisHD-linPG). BisHD-*lin*PG_{19} and BisHD-*lin*PG_{21} were synthesized according to the same procedure. As an example, the synthesis of BisHD-*lin*PG_{19} is described. BisHD-OH (100 mg, 0.155 mmol) and cesium hydroxide mono hydrate (15.6 mg, 0.139 mmol) were dissolved in benzene (6 ml) and stirred in a dry Schlenk flask under slightly reduced pressure at 60 °C for 15 min keeping the stopcock closed. Moisture was removed by azeotropic distillation of benzene and subsequent drying at 60 °C in high vacuum for 16 h. Under argon atmosphere, dry dioxane (10 ml) was added via syringe and the solution was heated to 40 °C. EEGE (1.09 ml, 7.42 mmol) was injected and the reaction mixture was stirred at 80 °C for 3 d. After removal of the solvent in vacuum, the resulting polymer was dissolved in a mixture of methanol (20 ml) and hydrochloric acid (2 ml, 2 mol l^{-1}) and stirred for 2 d at 40 °C. The solvent was partially removed under reduced pressure and the polymer was precipitated two times in cold diethyl ether. The pure polymer was obtained after drying in high vacuum. (Yield: 82 %) ^{1}H NMR (400 MHz, DMSO-d_6): δ [ppm] 4.85–4.20 (m, 18H, OH), 3.70–3.10 (m, 99H, $\mathrm{C}H_2$-O and CH_2-C*H-O*), 1.50–1.38 (m, 4H, C*H_2*-CH_2-O), 1.34–1.10 (m, 52H, CH_2), 0.84 (t, 6H, J_{AB} = 6.4 Hz, C*H_3*-CH_2).

1,2-Bis(hexadecyl)glycerol-hbPG (BisHD-hbPG). BisHD-*hb*PG_{32} and BisHD-*hb*PG_{63} were synthesized according to the same procedure. As an example, the synthesis of BisHD-*hb*PG_{32} is described. In a dry Schlenk flask, the BisHD-*lin*PG_{19} (600 mg, 0.321 mmol) and cesium hydroxide mono hydrate (102 mg, 0,61 mmol) were dissolved in benzene (6 ml) and stirred at 60 °C for 1 h. The macroinitiator was freeze-dried *in vacuo* for 16 h, dissolved in dry NMP (0.5 ml) and heated to 100 °C. A solution of glycidol in dry NMP (6.8 ml, 5 wt%, 4.59 mmol) was added within 8 h via a syringe pump and subsequently stirred for 2 h. After cooling to 22 °C, the polymerization was terminated with methanol (0.5 ml). The crude polymer was dialyzed (MWCO 500 Da) against methanol for 24 h and dried under *vacuo*. (Yield: 740 mg, 80 %) ^{1}H NMR (400 MHz, pyridine-*d_5*): *δ* [ppm] 6.66–5.76 (m, 32H, OH) 4.61–3.28 (m, 169H, C*H_2*-O and CH_2-C*H-O*), 1.78–1.59 (m, 4H, C*H_2*-CH_2-O), 1.54–1.20 (m, 52H, CH_2), 0.88 (t, 6H, J_{AB} = 6.4 Hz, C*H_3*-CH_2). ^{13}C NMR (100 MHz, pyridine-*d_5*): *δ* [ppm] 79.92–62.73 (101C, CH_2O, CHO), 32.48 (2C, O-CH_2-CH_2-*CH_2*), 31.01–29.97 (22C, CH_2), 26.96 (2C, -*CH_2*-CH_2-CH_3), 23.30 (2C, *CH_2*-*CH_3*), 14.65 (2C, CH_2-*CH_3*).

1,2-Bis(hexadecyl)glycerol-hbPG-alkyne (BisHD-hbPG-alkyne). BisHD-*hb*PG_{32}-alkyne and BisHD-*hb*PG_{63}-alkyne were synthesized according to the same procedure. The synthesis of BisHD-*hb*PG_{32}-alkyne is described as an example. BisHD-*hb*PG_{32} (300 mg, 0.102 mmol) was dissolved in dry DMF (10 ml) under argon atmosphere. The solution was cooled to 0 °C, sodium hydride (18.0 mg, 0.75 mmol) was added, and the mixture was stirred for 10 min. Propargyl bromide (31.7 mg, 0.21 mmol, 80 wt% in toluene) was injected via syringe and the reaction proceeded at 22 °C for 20 h. After the suspension was diluted with water (1 ml), the solvent was removed *in vacuo* and the final polymer was obtained via dialysis (MWCO 500 Da) against methanol for 5 h. (267 mg, 89 %) ^{1}H NMR (400 MHz, pyridine-*d_5*): *δ* [ppm] 4.98–4.37 (m, 31H, OH), 4.29–4.09 (m, 2H, OC*H_2*-CCH), 3.80–3.04 (m, 169H, CH_2O and CH_2-C*H-O*), 1.53–1.38 (m, 4H, C*H_2*-CH_2-O), 1.35–1.11 (m, 52H, CH_2), 0.85 (t, 6H, J_{AB} = 6.4 Hz, C*H_3*-CH_2).

1,2-Bis(hexadecyl)glycerol-PEG_{56} (BisHD-PEG_{56}). BisHD-OH (200 mg, 0.371 mmol) was dissolved in benzene (10 ml) and stirred in a dry Schlenk flask under slightly reduced pressure at 60 °C for 15 min keeping the stopcock closed. Moisture was removed by azeotropic distillation of benzene and subsequent drying at 70 °C in high vacuum for 16 h. After cooling to 22 °C, dry THF (15 ml) was cryo-transferred into the Schlenk flask and potassium naphthalenide in THF (0.37 ml, 0.18 mmol, c = 0.5 mol l^{-1}, prepared from potassium (235 mg, 6.0 mmol) and naphthalene (770 mg, 6.0 mmol) in dry THF (12 ml) in a glovebox under argon) was added via syringe. Generated hydrogen was removed in vacuum and ethylene oxide (1.11 ml, 22.3 mmol) was cryo-transferred via a graduated ampule into the initiator solution. The reaction was allowed to proceed at 40 °C for 3 h and subsequently continued at 60 °C for 3 d. The polymerization was quenched with methanol (2 ml), and the polymer was precipitated in cold diethyl ether. After removing all volatiles under vacuum, the pure polymer was obtained. (Yield: 82 %) ^{1}H NMR (400 MHz, DMSO-d_6): δ [ppm] 3.70–3.20 (m, 257H, CH_2-O and CH$_2$-CH-O), 1.50–1.38 (m, 4H, CH_2-CH$_2$-O), 1.34–1.10 (m, 52H, CH$_2$), 0.84 (t, 6H, J_{AB} = 6.4 Hz, CH_3-CH$_2$).

1,2-Bis(hexadecyl)gycerol-PEG$_{56}$-alkyne (BisHD-PEG$_{56}$-alkyne). In a dry Schlenk flask, BisHD-PEG$_{56}$ (300 mg, 0.115 mmol) was dissolved in dry THF (15 ml) under argon atmosphere. The solution was cooled to 0 °C, sodium hydride (8.3 mg, 0.34 mmol) was added, and the mixture was stirred for 10 min. Propargyl bromide (51.1 mg, 0.34 mmol, 80 wt% in toluene) was injected via syringe and the reaction proceeded at 22 °C for 20 h. After filtration the solution was reduced to a small volume and the polymer was precipitated in cold diethyl ether (280 mg, 92 %). ^{1}H NMR (400 MHz, C_6D_6): δ [ppm] 3.94 (d, 2H, $^4J_{AB}$ = 2.4 Hz, OCH_2-CCH), 3.86–3.25 (m, 190H, CH$_2$O and CH$_2$-CH-O), 2.14 (m, 1H, OCH$_2$-CCH), 1.71–1.54 (m, 4H, CH_2-CH$_2$-O), 1.52–1.19 (m, 52H, CH$_2$), 0.90 (t, 6H, J_{AB} = 6.4 Hz, CH_3-CH$_2$). ^{13}C NMR (100.6 MHz, C_6D_6): δ [ppm] 100.46 (1C, O_2CH-CH$_3$), 80.47 (1C, OCH$_2$-CCH), 78.86 (1C, CH-CH$_2$O), 74.70 (1C, OCH$_2$-CCH), 73.24–64.97 (87C, CH$_2$O), 58.38 (1C, OCH$_2$-CCH), 32.36 (2C, CH$_3$-CH$_2$-CH_2), 30.86-29.85 (24C, CH$_2$), 26.76 (2C, CH_2-CH$_2$-CH$_2$O), 23.14 (2C, CH_2-CH$_3$), 19.96 (1C, O$_2$CH-CH_3), 14.40 (2C, CH$_2$-CH_3).

Precursor synthesis

2-(2-(2-Azidoethoxy)ethoxy)ethyl-p-toluenesulfonate (Ts-TEG-N$_3$). The synthesis was accomplished according to published procedures.[26]

Radiosyntheses

1-azido-2-(2-(2-[^{18}F]fluoroethoxy)ethoxy)ethane. [^{18}F]F-TEG-N$_3$ was synthesized on a semiautomatic custom modular system with radiochemical yields (RCY) up to 91 % (TLC, EA/nHex 1:1, R_f: 0.8) (Figure S-7) according to a previous report.[26]

BisHD-polyether-CH$_2$-triazole-TEG-^{18}F. The radiolabeling of the BisHD polyethers via CuAAC was adapted from Reibel *et al*.[26] A solution of the respective BisHD polyether (7 mg BisHD-PEG$_{56}$-alkyne, 6 mg BisHD-*hb*PG$_{32}$-alkyne or 6 mg BisHD-*hb*PG$_{63}$-alkyne) was dissolved in 1 ml of PBS buffer and the solution was added to a [^{18}F]F-TEG-N$_3$-coated vial with a stir bar. Subsequently, 12.5 µl DMSO, 15 µl CuSO$_4$ (1 M in MilliQ water, 15 µmol) and 25 µl sodium ascorbate (2.4 M in PBS buffer, 60 µmol) were added in this order. The mixture was heated at 70 °C for 10 min. The RCY was determined via radio-TLC (EA/nHex 1:1, R_f: 0). To remove cytotoxic copper, the reaction mixture was passed through Chelex 100 (Bio-Rad) (600 mg in a 3 ml SPE tube, preconditioned with 0.8 ml HCl (1 M), 5 ml H$_2$O, 0.8 ml NaOH (1 M), 5 ml H$_2$O). The cartridge was eluted with 1.5 ml of abs. ethanol, and the solvent was removed using a miniature rotating evaporator. For the animal studies the polyether lipids were subsequently dissolved in PBS buffer.

Liposome formation

Liposomes were prepared by the thin film hydration method followed by several extrusion steps. Liposome components were 1,2-dioleoyl-*sn*-glycero-3-phosphocholine (DOPC), cholesterol and radiolabeled BisHD polyether (BisHD-*hb*PG_{32}-^{18}F, BisHD-*hb*PG_{63}-^{18}F or BisHD-PEG_{56}-^{18}F) at molar ratios of 55:40:5 mol%. M_n values, determined by ^1H NMR spectroscopy, were used to calculate the lipid compositions. A solution of DOPC in ethanol, cholesterol in ethanol and the radiolabeled polyether lipid were blended, and the solvent was evaporated in a miniature rotating evaporator to obtain a thin film of the liposome components. 0.8 ml of PBS were added resulting in large multilamellar vesicles. To obtain small unilamellar vesicles, the liposome suspension was sonicated at 50 °C for 10 min, followed by extrusion through polycarbonate membranes (400 nm, 21 times then 100 nm, 21 times. Liposomes containing BisHD-*hb*PG_{63}-^{18}F were additionally extruded through a 50 nm membrane 21 times) using a Mini-Extruder (AVESTIN Europe GmbH) driven by a custom-built device (Figure S-9 in the Supporting Information). Finally, the liposomes were purified via size exclusion chromatography (SEC) using Sephacryl S-400 HR as a resin (~4 ml packed in a 6 ml empty SPE tube with 20 µm PTFE frits at top and bottom) and PBS as a mobile phase. Fractions of 0,5 ml were collected. Liposomes eluted in the fractions 3-5.

Liposome stability

Experiments regarding storage stability and temperature stability of the liposomes are provided in the Supporting Information.

Animal studies

Male C57BL/6 mice (Janvier Labs; body weight: 23.3±2.2 g; age: 6-8 weeks) housed in the animal care facility of the University of Mainz were used in this study. The anesthetization of the animals was accomplished using an isoflurane vaporizer, where 2.5 % of isoflurane were admixed with air. Anesthetized animals were injected with 6.05±0.67 MBq of the respective radiolabeled compound in 100-150 µl of PBS via a tail vein (1 h animals) or retroorbital (4 h animals). The applied masses of polyether lipids alone were <0.34 mg for BisHD-PEG_{56}-^{18}F and <0.18 mg for BisHD-*hb*PG_{32}-^{18}F. For the corresponding liposomal formulations the applied masses were <0.084 mg for BisHD-PEG_{56}-^{18}F, <0.047 mg for BisHD-*hb*PG_{32}-^{18}F and <0.055 mg for BisHD-*hb*PG_{63}-^{18}F. All experiments had previously been approved by the regional animal ethics committee and were conducted in accordance with the German Law for Animal Protection and the UKCCCR Guidelines.[31]

In vivo µPET studies

PET scans were run on a microPET Focus 120 (Siemens). For the dynamic PET scans of 1 h data acquisition was started at the time of injection. For the 3.5 to 4 h static PET scans the mice were anesthetized for the injection, but were awake in the timespan between injection and PET scan. During the PET scan the animals lay in a head first prone position. The list mode data files were reconstructed using a filtered-backprojection reconstruction algorithm. The reconstruction was done using ASIPro 1.2. software. AMIDE software was utilized for image processing purposes. To accomplish the analysis of the PET data PMOD 3.6 software was used.

Ex vivo biodistribution

In order to assess the distribution of the radiolabeled compounds in different organs, injected animals were sacrificed after 1 h or 4 h and organs of interest were collected. The tissue samples were weighed and the radioactivity in the samples was measured in a γ-counter (2470 WIZARD^2 Automatic Gamma Counter, PerkinElmer).

Results and discussion

Synthesis of 1,2-Bis(hexadecyl)glycerol-*hb*PG and -PEG lipids

In a previous work, we aimed at elucidating the *in vivo* behavior of liposomes endowed with cholesterol-based polyether lipids.[26] However, recent findings have highlighted the importance of a stable lipid anchorage of polyether lipids in the liposomal membrane and revealed superior stability of dialkyl-functional lipids compared to cholesterol-derived lipid structures.[27] This motivated us to investigate the performance of dialkyl-based polyether lipids in liposomal formulations with different architectures of the polyether blocks. In this study, we focused on examining the *in vivo* biodistribution of dialkyl-functional lipids containing hyperbranched polyglycerol (*hb*PG) and polyethylene glycol (PEG). To ensure comparability between the shielding properties of *hb*PG and PEG, molecular weights were chosen to be ~3000 g mol^{-1}. In order to study the impact of the polyether size, also an *hb*PG-lipid with a molecular weight of ~5000 g mol^{-1} was investigated. To this end, we synthesized polyether lipids based on a 1,2-bis-*n*-hexadecyl glycerol anchor unit following the synthesis routes illustrated in Scheme 1. First, BisHD-OH was obtained according to literature protocols[28] and was used as an initiator for the anionic ring-opening polymerization (AROP) of ethoxyethyl glycidyl ether (EEGE) to generate a BisHD-PEEGE prepolymer. The PEEGE precursor could be converted into BisHD-*lin*PG by acidic hydrolysis of the acetal protecting groups. Using the *lin*PG macroinitiator for the slow addition of glycidol, BisHD-*hb*PG lipids were accessible (see Scheme 1, right path). The synthesis of dialkyl-based *hb*PG lipids has been reported in a previous work that built upon a poly(isopropylidene glyceryl glycidyl ether) lipid precursor used as an initiator for the "hypergrafting" of glycidol.[28] Here, we employed a novel oligo(EEGE) precursor as an alternative macroinitiator, extending the scope of dialkyl-derived PG-lipids. For comparative purposes, a PEG-functional BisHD lipid of similar molecular weight was synthesized utilizing BisHD-OH to initiate the AROP of ethylene oxide. The polymerization was conducted in THF using potassium naphtalenide to deprotonate the initiator (See Scheme 1, left path).

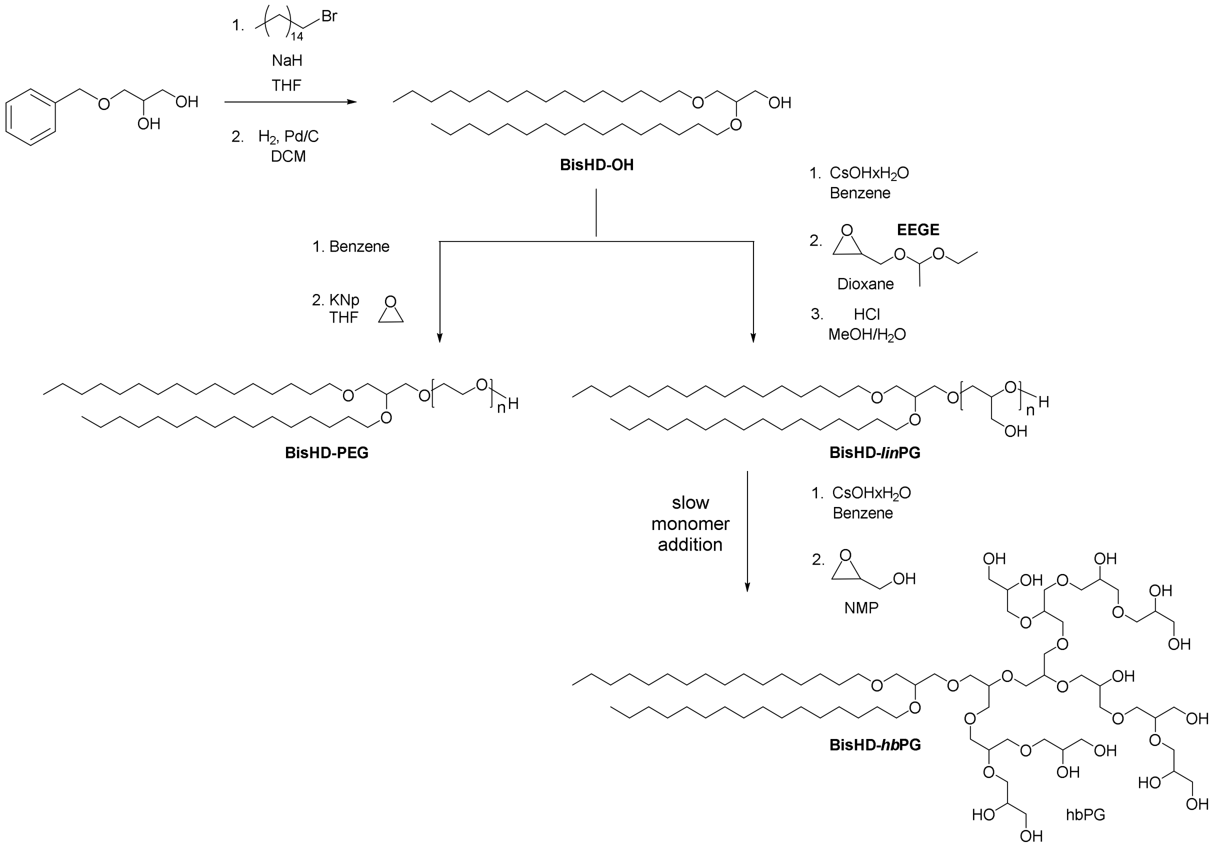
1.
14
Br
NaH
THF
2. H2, Pd/C
DCM
BisHD-OH
1. CsOHxH2O
Benzene
2. EEGE
Dioxane
3. HCl
MeOH/H2O
1. Benzene
2. KNp
THF
BisHD-PEG
BisHD-linPG
slow monomer addition
1. CsOHxH2O
Benzene
2.
NMP
BisHD-hbPG
hbPG

Scheme 1. Synthesis of novel BisHD-PEG (left) and BisHD-*hb*PG lipids (right).

Table 1 summarizes the molecular characteristics of the polymer lipids discussed in this study. Average molecular weights were determined by ^{1}H NMR spectroscopy via end group analysis and SEC in DMF using PEG calibration. A detailed description of the procedure is provided in the Supporting Information. BisHD-*lin*PG macroinitiators were obtained with molecular weights M_n of 1800 g mol^{-1} and 2200 g mol^{-1} and were used for the hypergrafting of glycidol to generate *hb*PG-functional lipids.

Table 1. Molecular characteristics of hyperbranched and linear bis(hexadecyl)glycerol lipids.

Sample	M_n (NMR) / g mol^{-1}	M_n (SEC) / g mol^{-1}	$Đ$
BisHD-*lin*PG$_{19}$	1950	1800	1.06
BisHD-*hb*PG$_{32}$	2910	2200	1.21
BisHD-*lin*PG$_{21}$	2100	1800	1.18
BisHD-*hb*PG$_{63}$	5210	3500	1.36
BisHD-PEG$_{56}$	3010	2200	1.05

M_n (NMR): Molecular weights of polymers calculated from ^{1}H NMR via end group analysis. M_n (SEC): Molecular weights of polymers obtained from SEC using PEG standards for calibration. $Đ = M_w/M_n$: Molecular weight distribution determined from SEC using PEG standards.

BisHD-*hb*PG lipids were synthesized with molecular weights of 2900 and 5200 g mol^{-1} exhibiting moderate dispersities $Đ$ below 1.4. Figure 2 includes SEC traces of the PEEGE prepolymers (black traces), *lin*PG macroinitiators (red traces) and BisHD-*hb*PG lipids (blue traces) revealing monomodal molecular weight distributions for all polymers with shifts to lower elution volume for increasing molecular weights. As a linear PEG analog, BisHD-PEG$_{56}$ was synthesized with a molecular weight of 3000 g mol^{-1} to allow for comparative studies.

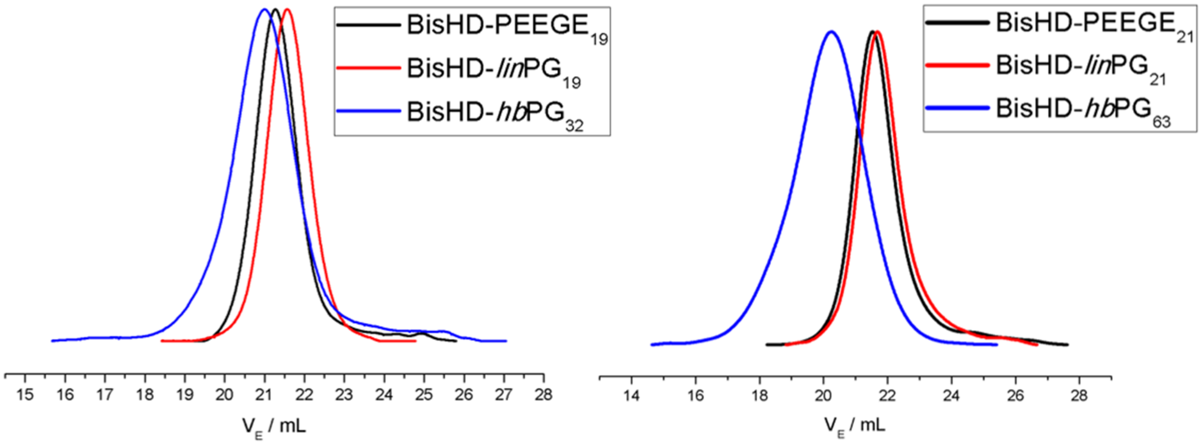

Figure 2. SEC traces of BisHD-PEEGEs (black), BisHD-*lin*PGs (red), BisHD-*hb*PGs (blue) using DMF as eluent and RI detection.

To enable radioactive labeling of the polyether lipids via CuAAC, alkyne moieties were introduced in a post-modification step. To this end, PEG and *hb*PG lipids were functionalized by transformation of terminal hydroxyl groups with propargyl bromide, as depicted in Scheme 2. This reaction has been reported in the literature,[26] and was adapted for the dialkyl-based lipids in this study.

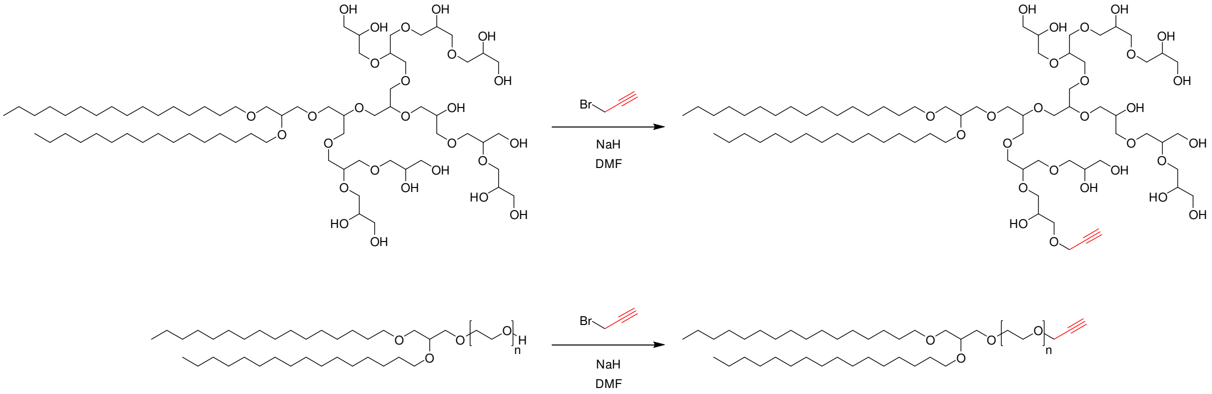

Scheme 2. Post-modification of BisHD-*hb*PG (top) and BisHD-PEG (bottom) with propargyl bromide to attach alkyne functionalities.

Figure 3 shows typical ^{1}H NMR spectra of BisHD-*hb*PGs before and after alkyne functionalization. The proton signals of the initiator (δ = 0.8 – 1.7 ppm) are clearly separated from the polyether backbone (δ = 3.2 – 4.4 ppm) and the multiple hydroxyl groups (δ = 6.0 – 6.7 ppm). Molecular weights were calculated from the spectra by comparing the integrals of the backbone resonances and the hydroxyl groups with the methyl proton signals of the dialkyl chains (δ = 0.91 ppm). Successful functionalization of lipids was confirmed by the appearance of the characteristic resonances for the propargyl methylene protons (δ = 4.5 – 4.7 ppm). ^{13}C NMR and diffusion-ordered NMR spectroscopy (DOSY) provided additional evidence for the attachment of alkyne moieties to the polymers (See Supporting Information, Figure S-2 and Figure S-3). Two alkyne-functional, hyperbranched lipids with the following structures BisHD-*hb*PG$_{32}$-(CH$_2$CCH)$_1$, BisHD-*hb*PG$_{63}$-(CH$_2$CCH)$_4$ were obtained and used in this study. NMR spectra of BisHD-PEG are included in the Supporting Information (Figure S-4).

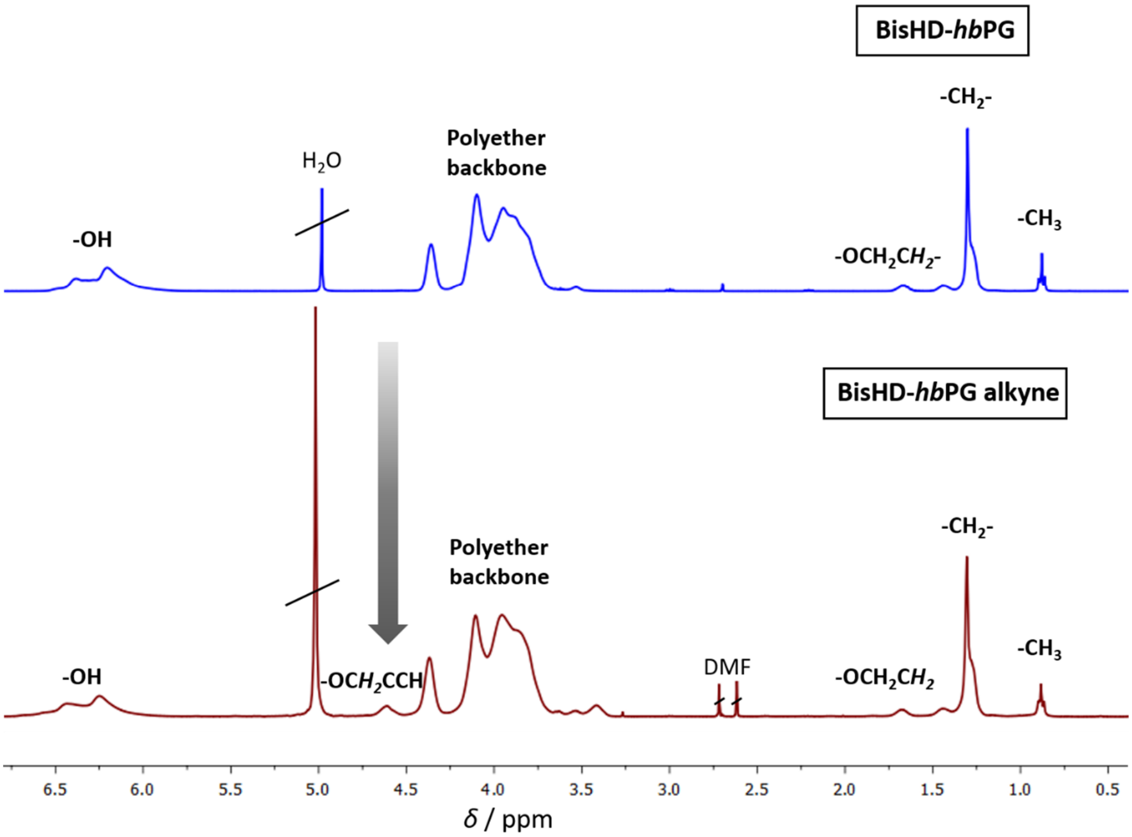

Figure 3. ^{1}H NMR spectra of BisHD-*hb*PG$_{63}$ (top) and BisHD-*hb*PG$_{63}$ alkyne (bottom) measured in pyridine-d_5 at 400 MHz.

Radiosyntheses

The required [^{18}F]F-TEG-N$_3$ was prepared by nucleophilic fluorination of Ts-TEG-N$_3$ using a semi-automatic custom modular system (Supporting Information Figure S-6) in yields up to 91 %. A representative radio-TLC of the reaction mixture prior to HPLC purification is provided in Figure S-7 in the Supporting Information. Subsequently, the respective polyether lipid was radiolabeled using [^{18}F]F-TEG-N$_3$ via CuAAC, which works reliable in radiochemical yields (RCYs) above 95 % after 10 min (Scheme 3). In order to start the CuAAC, the last component added was sodium ascorbate, which reduces Cu(II) to Cu(I). The success of the CuAAC within 10 min strongly depends on the amount of alkyne functionalities relative to the amount of [^{18}F]F-TEG-N$_3$. For example 3 mg BisHD-PEG$_{56}$ alkyne resulted in yields of 20.3 % whereas 7 mg gave RCYs of 97 % when 4 GBq of [^{18}F]F-TEG-N$_3$ were used. This finding gives evidence, that a certain ratio of the reactants is needed in order to obtain quantitative yields in a short time.

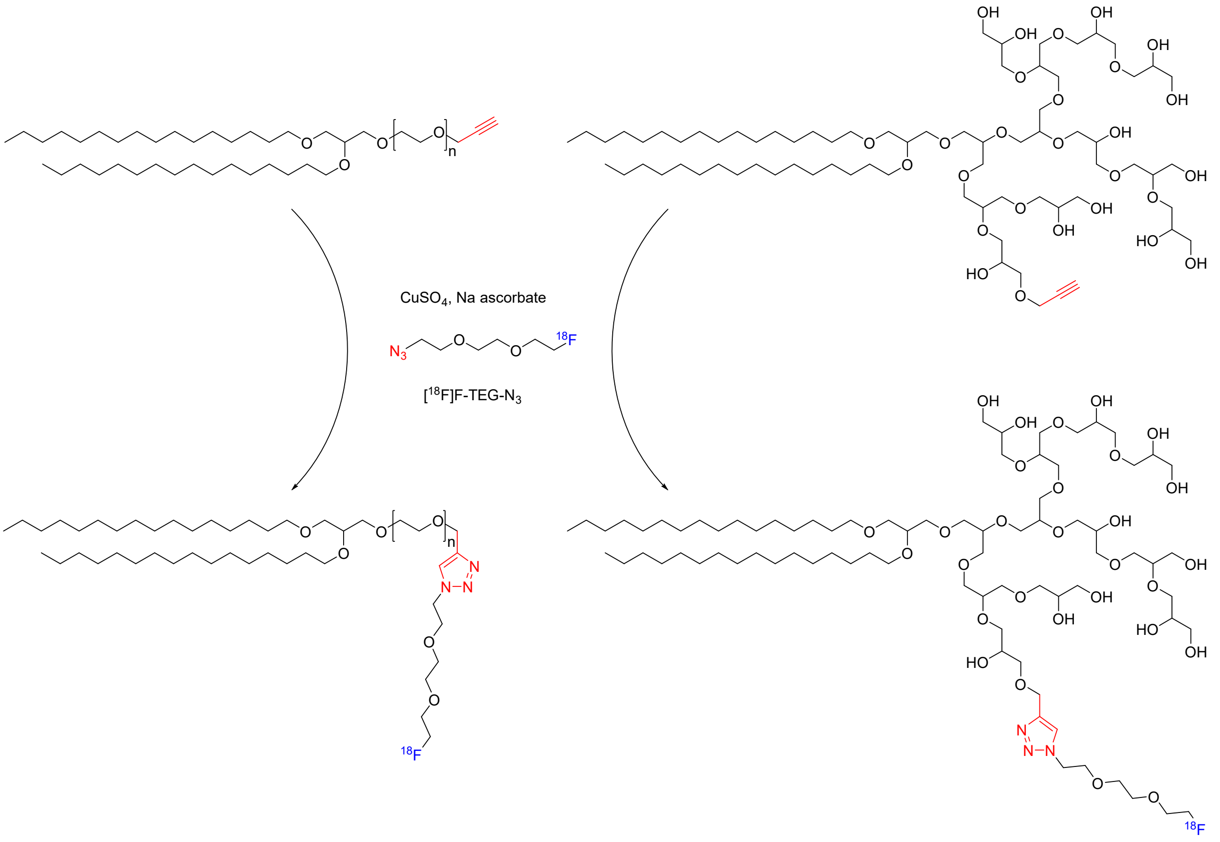

Scheme 3. Radiolabeling of BisHD-*hb*PG-alkyne and BisHD-PEG-alkyne via CuAAC.

Fluorine-18 was chosen because it combines ideal properties for PET imaging like a sufficient half-life of 109.7 min, a low energy of the emitted positron ($E_{\beta+,max}$ = 0.63 MeV) and a high ratio of β^+-decay (96.9 %).[32] Because of its small size and its lack of charge, the polymer structure is altered almost negligibly. Additionally, the structure of the synthon, [^{18}F]F-TEG-N$_3$, mimics the polyether structure to result in a radiolabeled polyether lipid, which is believed to show an almost identical *in vivo* behavior as non-radiolabeled polyether lipids.

Liposome formation and characterization

Liposomes were manufactured by the thin film hydration method followed by extrusion through polycarbonate membranes of 400 nm then 100 nm. Since BisHD-*hb*PG$_{63}$-shielded liposomes tended to be larger, they were additionally extruded through a 50 nm membrane. Performing the extrusion manually led to two major problems: First, a high radiation exposure for the experimentalist and second, strong fluctuations of the liposomes sizes even with the same shielding polymer. Therefore we developed an automatic extrusion device (Figure S-9 in the Supporting Information), which permits to apply reproducible pressure during the extrusion process and has a separate control module. Via the automatization of the extrusion process, it was possible to obtain liposomes with reproducible size control (Figure S-9 in the Supporting Information). Furthermore, the separate control module allows for a remote control of the extrusion device and therefore considerably reduces radiation exposure. After the extrusion, liposomes were separated from non-integrated lipids via SEC with PBS as mobile phase.

The size of the liposomes was determined via DLS when they did not radiate any more (~18 h). Liposomes containing BisHD-PEG$_{56}$ (5 mol%) exhibited a hydrodynamic radius R_h of 90 nm, whereas liposomes shielded with BisHD-*hb*PG$_{32}$ (5 mol%) and BisHD-*hb*PG$_{63}$ (5 mol%) showed R_h values of 61 nm and 94 nm, respectively (underlying DLS data are provided in Figure S-11 in the Supporting Information). Since extrusion was conducted in the same manner for all liposomes, aberrations in size might derive from the different steric demands of the polyether lipids. The rather globular structure of hyperbranched lipids compared to linear PEG lipids of the same molecular weight is held responsible for the increased size of PEG-shielded liposomes. As for the two *hb*PG-shielded liposomes, the drop in size with lower molecular weight of the polymer can be attributed to decreased steric bulk. In order to examine the shape of the liposomes cryo-TEM measurements were accomplished. Representative images of BisHD-PEG$_{56}$-shielded liposomes and BisHD-*hb*PG$_{32}$-shielded liposomes are shown in Figure 4. Further images are provided in Figure S-10 in the Supporting Information. It can be seen that the liposomes are unilamellar spheres with narrow size distribution. Furthermore storage stability and temperature stability experiments were conducted, indicating that the liposomes are stable between 20 to 50 °C. The results are included in the Supporting Information (Figure S-12 and Figure S-13).

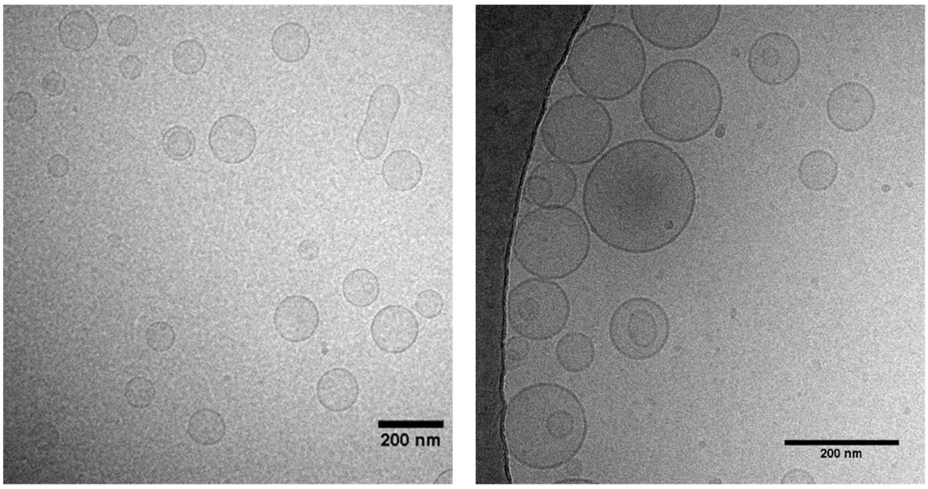

Figure 4. Representative cryo-TEM images of BisHD-PEG$_{56}$-shielded liposomes (left) and BisHD-*hb*PG$_{32}$-shielded liposomes (right).

Animal studies

In vivo µPET studies

To investigate the *in vivo* fate of the polyether lipids and their corresponding liposomal formulations, µPET studies were conducted in healthy, male C57BL/6 mice. Dynamic scans of 1 h were started at the time of injection in order to follow the initial distribution. For the liposomal formulations also static scans of 30 min were run 3.5 h after injection to gain information regarding pharmacokinetics at later stages. Figure 5 shows coronal, whole-body maximum intensity projections (MIPs) of the polyether lipids BisHD-*hb*PG$_{32}$ and BisHD-PEG$_{56}$ as representative illustrations for PEG and *hb*PG lipids.

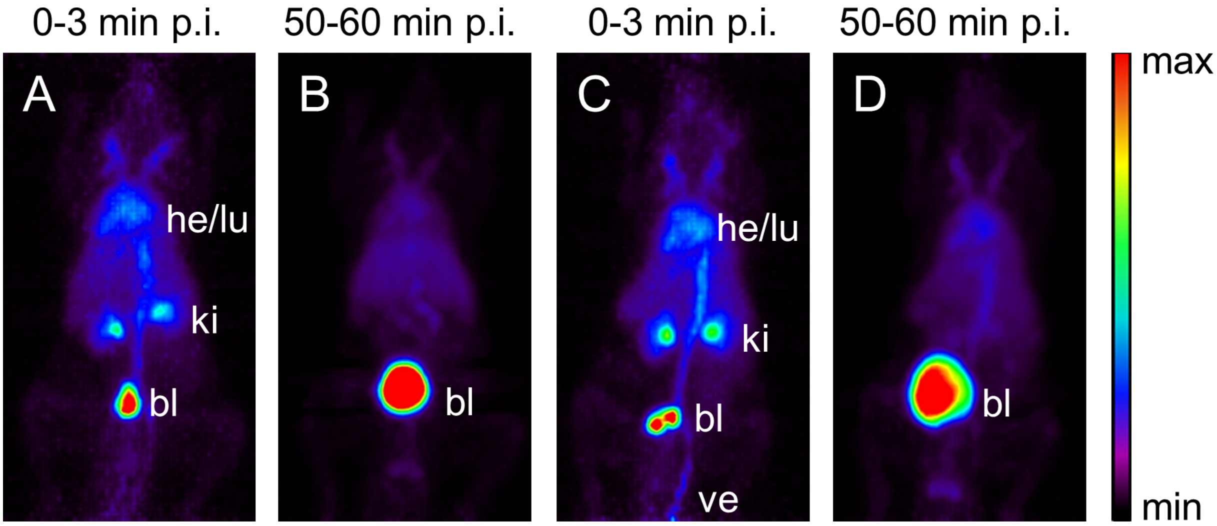

Figure 5. Coronal, whole-body MIPs in different time frames for BisHD-PEG$_{56}$-^{18}F (A & B) and BisHD-*hb*PG$_{32}$-^{18}F (C & D). he: heart, ve: vein, lu: lung, li: liver, bl: bladder, ki: kidney.

Both non-liposomal polyether lipids show an initial uptake in the bloodstream (0-3 min) and subsequently undergo rapid renal excretion. As expected, after 1 h the main uptake can be found in the bladder for both polyether lipids, since their molecular weight is below the renal threshold and the hydrophilic polyether block impedes accumulation in the liver.

In contrast, the liposomal formulations behave fundamentally different from the non-associated polymers. Figure 6 shows coronal, whole-body MIPs of BisHD-*hb*PG$_{32}$-^{18}F-liposomes, BisHD-PEG$_{56}$-^{18}F-liposomes and BisHD-*hb*PG$_{63}$-^{18}F-liposomes at different times after injection. All liposomes show an initial uptake (0-3 min) in the blood and well perfused organs, such as heart and lung. After 60 min, the main activity is still observed in the blood. These findings prove that the liposomes remain intact, because the polyether lipids by themselves would rapidly be excreted via the kidneys and the bladder (see Figure 5). After 4 h, the liver uptake becomes dominant, but one can still see activity in well perfused organs like heart and lung, revealing that a fraction of the liposomes is continuously circulating in the blood. In case of the *hb*PG$_{63}$- and for the PEG$_{56}$-shielded liposomes, a significantly higher spleen uptake is observed after 4 h compared to the *hb*PG_{32}-shielded liposomes. We ascribe this to the different sizes of the liposomes. The liver features a filtration cutoff of 50-100 nm, thus particles smaller than 50-100 nm will interact with hepatocytes.[33] All of the investigated liposomal formulations had diameters above 100 nm, so liver accumulation at least caused by the size should not be dominant and indeed it was not. In contrast, particles exceeding 200 nm tend to accumulate in the spleen.[34] Accordingly, BisHD-*hb*PG_{63}-shielded liposomes, with a diameter of 188 nm, showed the highest accumulation in the spleen. Liposomes containing BisHD-PEG_{56} had a diameter of 180 nm and exhibited the second highest splenic accumulation, whereas BisHD-*hb*PG_{32}-shielded liposomes, with a diameter of only 122 nm showed a much lesser uptake in the spleen. Besides, during the liposome formation process, the polyether lipids may be incorporated into the liposomes to slightly different degrees, although 5 mol% were added to each formulation, because of the different steric demand of PEG_{56}, *hb*PG_{32} and *hb*PG_{63}. This may also cause a different rate of recognition and uptake by the MPS. Further evaluation of the PET data as well as PET images of the liposomes shielded by cholesterol-anchored polyether lipids are provided in the Supporting Information.

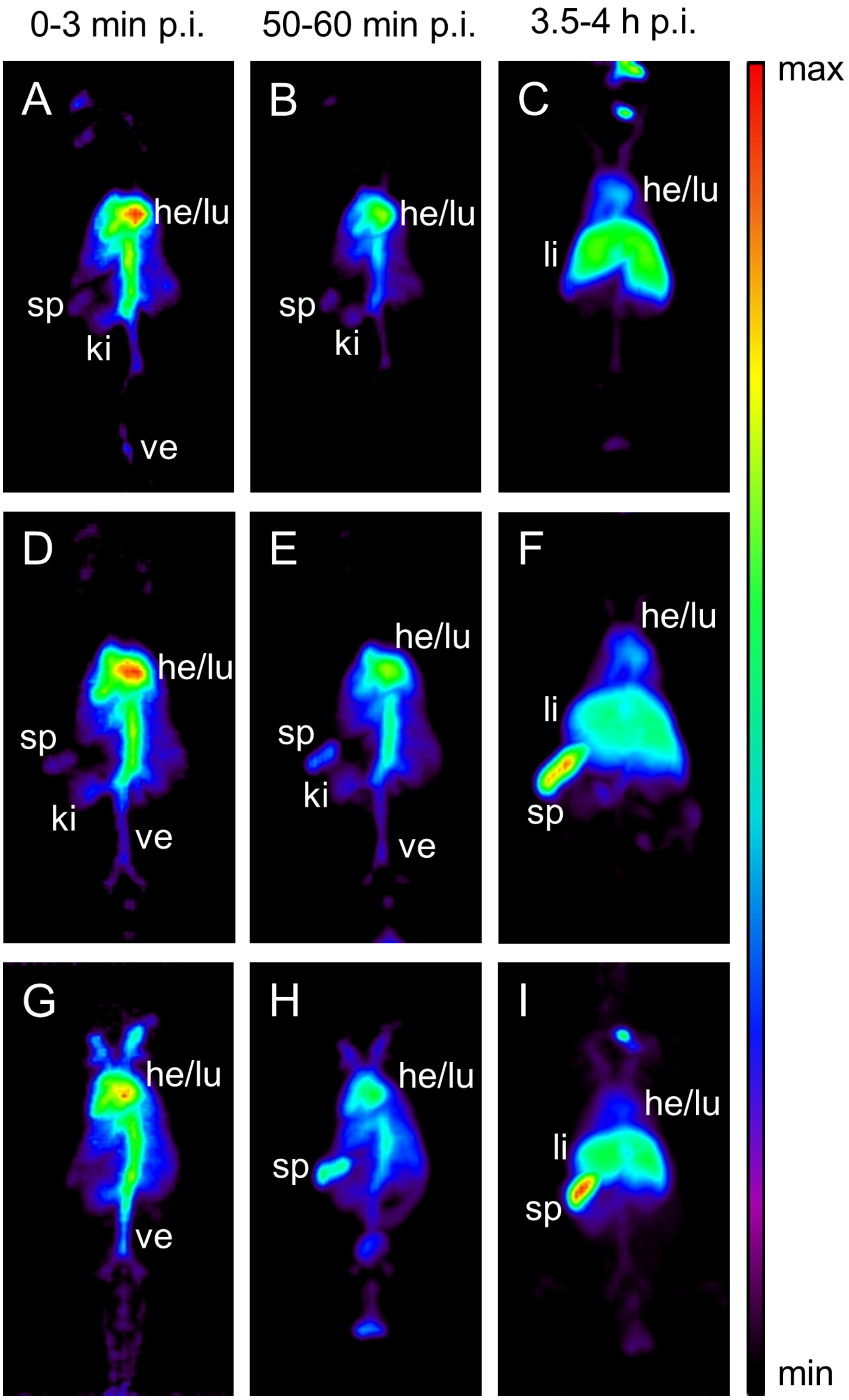
0-3 min p.i.
50-60 min p.i.
3.5-4 h p.i.
A
he/lu
sp
ki
ve
B
he/lu
sp
ki
C
he/lu
li
D
he/lu
sp
ki
ve
E
he/lu
sp
ki
ve
F
he/lu
li
sp
G
he/lu
ve
H
he/lu
sp
I
he/lu
li
sp
max
min

Figure 6. Coronal, whole-body MIPs at different time points (left column: 0-3 min p.i., middle column: 50-60 min p.i., right column: 3.5-4 h p.i.) for BisHD-*hb*PG_{32}-^{18}F-liposomes (A, B, C), BisHD-PEG_{56}-^{18}F-liposomes (D, E, F) and BisHD-*hb*PG_{63}-^{18}F-liposomes (G, H, I). he: heart, ve: vein, lu: lung, li: liver, sp: spleen, ki: kidney.

Ex vivo biodistribution

Ex vivo biodistribution studies were conducted in order to obtain quantitative conclusions regarding the in vivo accumulation of the ^{18}F-labeled compounds in different organs. Figure 7 shows the results for the polyether lipids BisHD-*hb*PG_{32}-^{18}F and BisHD-PEG_{56}-^{18}F, and Figure 8 summarizes the results for the liposomal formulations that differs strongly from Fig. 7. Table S1 in the Supporting Information provides the underlying data.

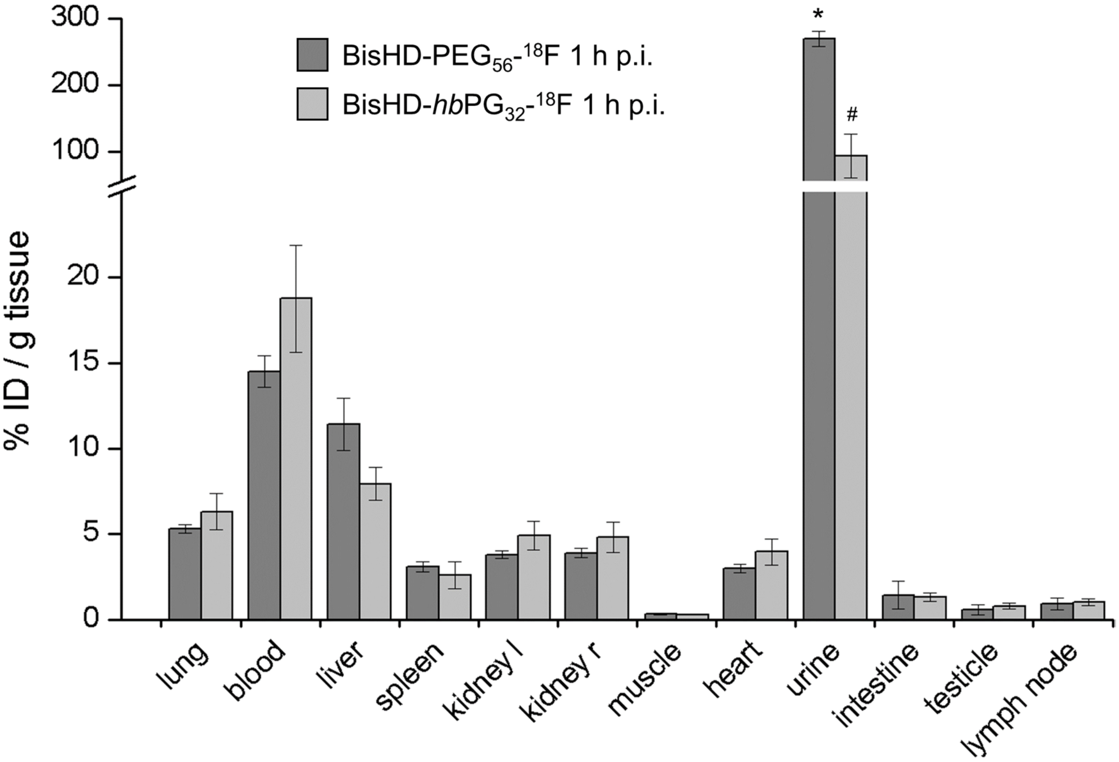

Figure 7. Summarized *ex vivo* biodistribution data of the polyether lipids BisHD-*hb*PG$_{32}$-^{18}F and BisHD-PEG$_{56}$-^{18}F 1 h p.i (n=5; asterisk indicates n=3, hash implies n=4).

From Figure 7 it can be seen that after 1 h both polyether lipids (most probably as micelles) are mainly found in the urine (BisHD-PEG$_{56}$-^{18}F: 269.3±11.2 % ID / g tissue and BisHD-*hb*PG$_{32}$-^{18}F: 93.6±33.2 % ID / g tissue), which confirms that they are quickly excreted via the renal pathway, except for a small amount still circulating in the bloodstream (BisHD-PEG$_{56}$-^{18}F: 14.5±0.9 % ID / g tissue and BisHD-*hb*PG$_{32}$-^{18}F: 18.8±3.1 % ID / g tissue). These findings are in accordance with the results of the PET studies. However, fast excretion of the polyether lipids via the renal system is favorable, as it ensures quick elimination of degraded liposomes from the body.

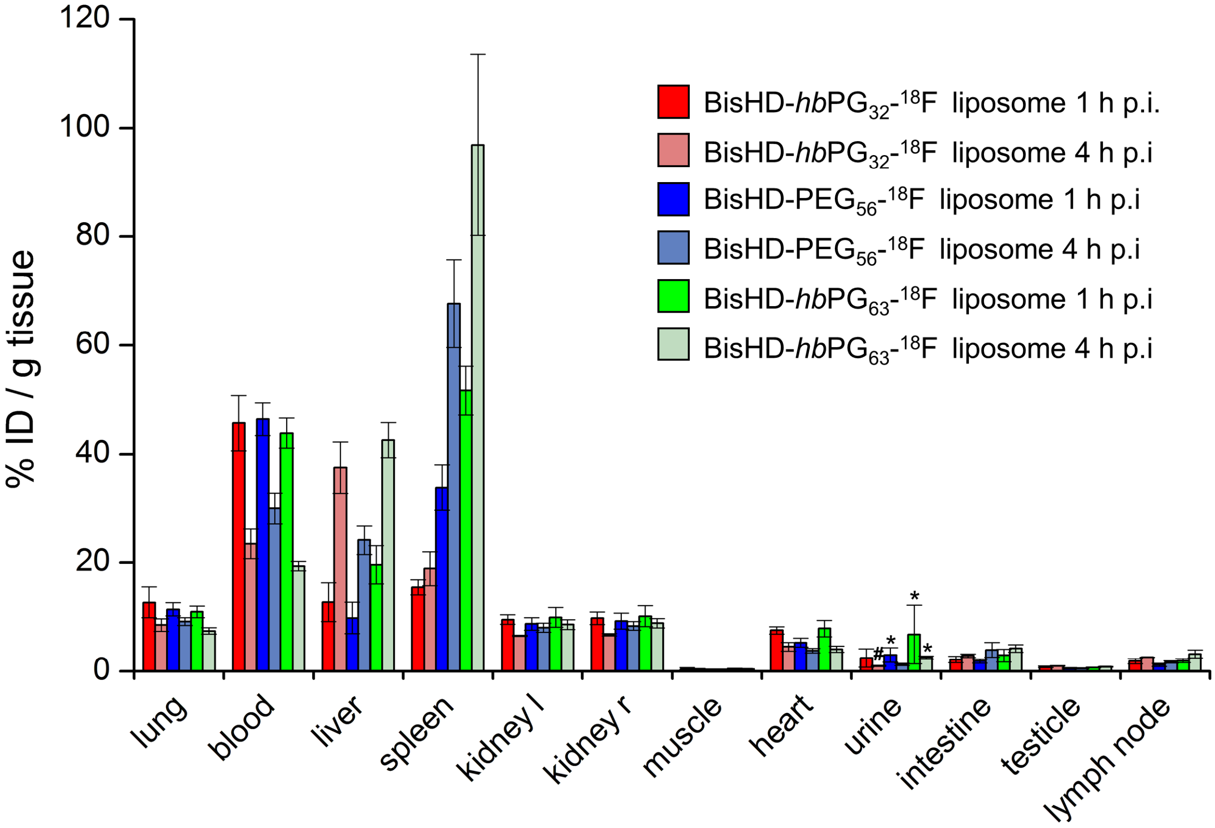

Figure 8. Summarized *ex vivo* biodistribution data of the liposomal formulations (1 h p.i.: n=5; 4 h p.i.: n=3 (BisHD-hbPG$_{32}$-^{18}F-liposomes, BisHD-PEG$_{56}$-^{18}F-liposomes), n=5 (BisHD-hbPG$_{63}$-^{18}F-liposomes)). Asterisks indicate n=4, hash implies n=2.

The results of the *ex vivo* biodistribution studies of the corresponding liposomal formulations confirm the observations of the *in vivo* PET studies. After 1 h, the three liposomal formulations show high uptake in the blood. For example 45.7±5.1 % ID / g tissue are present in the blood pool after 1 h for the *hb*PG$_{32}$-shielded liposomes. In contrast to the high accumulation in the blood, the concentration in the urine is marginal after 1 h. These findings prove that the liposomes remain intact. The non-associated dialkylglycerol polyether lipids by themselves would have been excreted via the kidneys and the bladder after this time. The observed uptake in lung, kidneys and heart is most likely caused by blood that remained in these organs upon harvesting. Overall it can be concluded that the different liposomes behave in a similar manner, with one exception, which is their splenic accumulation. Regarding the *hb*PG$_{32}$-shielded liposomes 15.5±1.4 % ID / g tissue are found in the spleen after 1 h. In contrast, the larger-sized *hb*PG-shielded liposomes show a 3.3-fold higher uptake in the spleen, whereas the splenic uptake of the PEG-shielded liposomes is twice as high after 1 h. We ascribe this to the different sizes of the liposomes, as discussed in the previous paragraph. Nevertheless compared to liposomes shielded by cholesteryl-anchored polyethers, recently investigated in our group, *in vivo* liposome stability after 1 h could be improved greatly. For example Ch-PEG$_{30}$-*hb*PG$_{24}$-^{18}F (5 mol%)-shielded liposomes exhibited only 7.7±1.9 % ID / g tissue in the blood pool and 221±48 % ID / g tissue in the urine after 1 h[26] compared to 45.7±5.1 % ID / g tissue in the blood pool and 2.5±1.7 % ID / g tissue in the urine after 1 h for the BisHD-*hb*PG$_{32}$-shielded liposomes investigated herein.

The enhanced stability motivated us to investigate the distribution of the liposomes also at 4 h p.i. in order to gain information on the later stage pharmacokinetics. After 4 h the uptake in the blood pool decreased to values in the range of 20-30 % ID / g tissue, and the accumulation in the liver increased. In this context is worth mentioning that the PEG-shielded liposomes exhibited the lowest uptake in the liver. Regarding the splenic uptake the values doubled both for the larger-sized *hb*PG-shielded and for the PEG-shielded liposomes, whereas the uptake for the *hb*PG$_{32}$-shielded liposomes did not change significantly between 1 and 4 h p.i., supporting stability of a considerable fraction of the shielded liposomes even after 4 h in the bloodstream. To the best of our knowledge, this is the first report demonstrating the stable membrane anchorage of dialkyl-functional *hb*PG lipids in liposomes during blood circulation. Furthermore, our data suggest a superior *in vivo* performance of *hb*PG-shielded liposomes as opposed to PEG-shielded liposomes with comparable molecular weight of the polyether lipid with respect to splenic MPS recognition. Future research efforts will focus on the benefits of multifunctional polyether lipids in liposomes for targeted drug delivery.

Conclusion

In this study, the *in vivo* properties of dialkyl-anchored, hyperbranched and linear polyether lipids in liposomes were investigated based on radioactive labeling. To this end, well-defined novel polyether lipids with C16-alkyl tails based on hyperbranched polyglycerol and PEG were synthesized with molecular weights of $M_n \approx 3000$ g mol^{-1}. For this purpose, a bis(hexadecyl)glycerol (BisHD) precursor as an initiator for the AROP of epoxide monomers was designed. The BisHD-*lin*PG macroinitiator granted access to the hyperbranched lipids with narrow dispersity, relying on slow monomer addition of glycidol. Additionally, a higher molecular weight BisHD-*hb*PG lipid ($M_n \approx 5000$ g mol^{-1}) was included to study the effect of molecular weight. Radiolabeling of the alkyne-functional BisHD polyethers was established via CuAAC giving excellent radiochemical yields above 95 % after 10 min. The usage of a custom automatic extrusion device gave access to more reproducible sizes of the liposomes while additionally it considerably lowered the radiation exposure of the experimentalist. As a main result of this work *in vivo* PET and *ex vivo* biodistribution studies revealed that the liposomes stay intact and circulate in the blood over the investigated period of 4 h. The three investigated liposomal formulations showed a comparable *in vivo* behavior with differences in splenic uptake. In our study, liposomes shielded with *hb*PG$_{32}$-lipids (3 kg mol^{-1}) provided the lowest splenic uptake both after 1 and 4 h p.i. and are presumably subjected to the lowest detection by the MPS. We therefore consider BisHD-*hb*PG$_{32}$ as the most promising candidate for future investigation regarding targeting and drug delivery. In contrast to mPEG-shielded liposomes, hyperbranched polyether lipids enable the attachment of a variety of structures, such as targeting vectors and radiolabels, facilitating cell-specific drug delivery combined with simultaneous carrier trafficking. With respect to different polymer anchors we conclude that a change of the polymer anchor from cholesterol to bis(alkyl)glycerol leads to a significant increase in the stability of the liposomes and may enable "stealth" behavior in combination with multifunctionality. The polyglycerol-coated liposomes are currently tested with respect to various therapeutic payloads.

Acknowledgment

Special thanks go to [redacted] for providing introduction into the radiolabeling procedures. The authors would like to thank the mechanical and the electrical workshop of the Institute of Nuclear Chemistry for the construction of the automatic extruder device. We are also very grateful to the Max-Planck Graduate Center (MPGC, K. Wagener, M. Worm) as well as to the DFG in the context of the SFB 1066 for financial support. K. Wagener, M. Worm and M. Schinnerer are members of the graduate school of the SFB 1066.

References

(1) Wicki, A.; Witzigmann, D.; Balasubramanian, V.; Huwyler, J. Nanomedicine in cancer therapy: Challenges, opportunities, and clinical applications. *J. Control. Release* 2015, *200*, 138–157.

(2) Chen, G.; Roy, I.; Yang, C.; Prasad, P. N. Nanochemistry and Nanomedicine for Nanoparticle-Based Diagnostics and Therapy. *Chem. Rev.* 2016, *116*, 2826–2885.

(3) Shi, J.; Kantoff, P. W.; Wooster, R.; Farokhzad, O. C. Cancer nanomedicine: progress, challenges and opportunities. *Nat. Rev. Cancer* 2016, *17*, 20–37.

(4) Min, Y.; Caster, J. M.; Eblan, M. J.; Wang, A. Z. Clinical Translation of Nanomedicine. *Chem. Rev.* 2015, *115*, 11147–11190.

(5) Allen, T. M.; Cullis, P. R. Liposomal drug delivery systems: From concept to clinical applications. *Adv. Drug Deliv. Rev.* 2013, *65*, 36–48.

(6) Pattni, B. S.; Chupin, V. V.; Torchilin, V. P. New Developments in Liposomal Drug Delivery. *Chem. Rev.* 2015, *115*, 10938–10966.

(7) Bulbake, U.; Doppalapudi, S.; Kommineni, N.; Khan, W. Liposomal Formulations in Clinical Use: An Updated Review. *Pharmaceutics* 2017, *9*, 12.

(8) Barenholz, Y. Doxil® - The first FDA-approved nano-drug: Lessons learned. *J. Control. Release* 2012, *160*, 117–134.

(9) Ishida, T.; Harashima, H.; Kiwada, H. Liposome Clearance. *Biosci. Rep.* 2002, *22*, 197–224.

(10) Juliano, R. L.; Stamp, D. The Effect of Particle Size and Charge on the Clearance Rates of Liposomes and Liposome Encapsulated Drugs. *Biochem. Biophys. Res. Commun.* 1975, *63*, 651–658.

(11) Allen, T. M.; Hansen, C. Pharmacokinetics of stealth versus conventional liposomes: effect of dose. *Biochim. Biophys. Acta - Biomembr.* 1991, *1068*, 133–141.

(12) Harashima, H.; Sakata, K.; Funato, K.; Kiwada, H. Enhanced Hepatic Uptake of Liposomes Through Complement Activation Depending on the Size of Liposomes. *Pharmaceutical Research*, 1994, *11*, 402–406.

(13) Lasic, D. D.; Needham, D. The “Stealth” Liposome: A Prototypical Biomaterial. *Chem. Rev.* 1995, *95*, 2601–2628.

(14) Immordino, M. L.; Dosio, F.; Cattel, L. Stealth liposomes: review of the basic science, rationale, and clinical applications, existing and potential. *Int. J. Nanomedicine* 2006, *1*, 297–315.

(15) van Vlerken, L. E.; Vyas, T. K.; Amiji, M. M. Poly(ethylene glycol)-modified Nanocarriers for Tumor-targeted and Intracellular Delivery. *Pharm. Res.* 2007, *24*, 1405–1414.

(16) Allen, T. M.; Hansen, C.; Martin, F.; Redemann, C.; Yau-Young, A. Liposomes containing synthetic lipid derivatives of poly(ethylene glycol) show prolonged circulation half-lives in vivo. *Biochim. Biophys. Acta* 1991, *1066*, 29–36.

(17) Wilms, D.; Stiriba, S.-E.; Frey, H. Hyperbranched Polyglycerols: From the Controlled Synthesis of Biocompatible Polyether Polyols to Multipurpose Applications. *Acc. Chem. Res.* 2010, *43*, 129–141.

(18) Kasza, G.; Kali, G.; Domján, A.; Pethő, L.; Szarka, G.; Iván, B. Synthesis of Well-Defined Phthalimide Monofunctional Hyperbranched Polyglycerols and Its Transformation to Various Conjugation Relevant Functionalities. *Macromolecules* 2017, *50*, 3078–3088.

(19) Siegers, C.; Biesalski, M.; Haag, R. Self-Assembled Monolayers of Dendritic Polyglycerol Derivatives on Gold That Resist the Adsorption of Proteins. *Chem. - A Eur. J.* 2004, *10*, 2831–2838.

(20) Yeh, P. Y. J.; Kainthan, R. K.; Zou, Y.; Chiao, M.; Kizhakkedathu, J. N. Self-Assembled Monothiol-Terminated Hyperbranched Polyglycerols on a Gold Surface: A Comparative Study on the Structure, Morphology, and Protein Adsorption Characteristics with Linear Poly(ethylene glycol)s. *Langmuir* 2008, *24*, 4907–4916.

(21) Kunjachan, S.; Ehling, J.; Storm, G.; Kiessling, F.; Lammers, T. Noninvasive Imaging of Nanomedicines and Nanotheranostics: Principles, Progress, and Prospects. *Chem. Rev.* 2015, *115*, 10907–10937.

(22) Stockhofe, K.; Postema, J.; Schieferstein, H.; Ross, T. Radiolabeling of Nanoparticles and Polymers for PET Imaging. *Pharmaceuticals* 2014, *7*, 392–418.

(23) Marik, J.; Tartis, M. S.; Zhang, H.; Fung, J. Y.; Kheirolomoom, A.; Sutcliffe, J. L.; Ferrara, K. W. Long-circulating liposomes radiolabeled with [^{18}F]fluorodipalmitin ([^{18}F]FDP). *Nucl. Med. Biol.* 2007, *34*, 165–171.

(24) Urakami, T.; Akai, S.; Katayama, Y.; Harada, N.; Tsukada, H.; Oku, N. Novel Amphiphilic Probes for [^{18}F]-Radiolabeling Preformed Liposomes and Determination of Liposomal Trafficking by Positron Emission Tomography. *J. Med. Chem.* 2007, *50*, 6454–6457.

(25) Hofmann, A. M.; Wurm, F.; Huhn, E.; Nawroth, T.; Langguth, P.; Frey, H. Hyperbranched Polyglycerol-Based Lipids via Oxyanionic Polymerization: Toward Multifunctional Stealth Liposomes. *Biomacromolecules* 2010, *11*, 568–574.

(26) Reibel, A. T.; Müller, S. S.; Pektor, S.; Bausbacher, N.; Miederer, M.; Frey, H.; Rösch, F. Fate of Linear and Branched Polyether-Lipids In Vivo in Comparison to Their Liposomal Formulations by ^{18}F-Radiolabeling and Positron Emission Tomography. *Biomacromolecules* 2015, *16*, 842–851.

(27) Fritz, T.; Voigt, M.; Worm, M.; Negwer, I.; Müller, S. S.; Kettenbach, K.; Ross, T. L.; Roesch, F.; Koynov, K.; Frey, H.; Helm, M. Orthogonal Click Conjugation to the Liposomal Surface Reveals the Stability of the Lipid Anchorage as Crucial for Targeting. *Chem. - A Eur. J.* 2016, *22*, 11578–11582.

(28) Hofmann, A. M.; Wurm, F.; Frey, H. Rapid Access to Polyfunctional Lipids with Complex Architecture via Oxyanionic Ring-Opening Polymerization. *Macromolecules* 2011, *44*, 4648–4657.

(29) Kettenbach, K.; Schieferstein, H.; Ross, T. L. ^{18}F-Labeling Using Click Cycloadditions. *Biomed Res. Int.* 2014, *2014*, Article ID 361329.

(30) Fitton, A. O.; Hill, J.; Jane, D. E.; Millar, R. Synthesis of Simple Oxetanes Carrying Reactive 2-Substituents. *Synthesis* 1987, *1987*, 1140–1142.

(31) Workman, P.; Aboagye, E. O.; Balkwill, F.; Balmain, A.; Bruder, G.; Chaplin, D. J.; Double, J. A.; Everitt, J.; Farningham, D. A. H.; Glennie, M. J.; Kelland, L. R.; Robinson, V.; Stratford, I. J.; Tozer, G. M.; Watson, S.; Wedge, S. R.; Eccles, S.A. Guidelines for the welfare and use of animals in cancer research. *Br. J. Cancer* 2010, *102*, 1555–1577.

(32) Bé, M.-M.; Chisté, V.; Dulieu, C.; Browne, E.; Chechev, V.; Kuzmenko, N.; Helmer, R.; Nichols, A.; Schönfeld, E.; Dersch, R. *Table of Radionuclides (Vol. 1 - A = 1 to 150)*; Le Bureau International des Poids et Mesures: Sèvres, 2004.

(33) Ernsting, M. J.; Murakami, M.; Roy, A.; Li, S.-D. Factors controlling the pharmacokinetics, biodistribution and intratumoral penetration of nanoparticles. *J. Control. Release* 2013, *172*, 782–794.

(34) Moghimi, S. M.; Hunter, A. C.; Murray, J. C. Long-Circulating and Target-Specific Nanoparticles: Theory to Practice. *Pharmacol. Rev.* 2001, *53*, 283–318.

Supplementary Data

Comparison of Linear and Hyperbranched Polyether Lipids for Liposome Shielding by ^{18}F-Radiolabeling and Positron Emission Tomography

Karolin Wagener[1,*], Matthias Worm[2,*], Stefanie Pektor[3], Meike Schinnerer[4], Raphael Thiermann[5], Matthias Miederer[3], Holger Frey[2] and Frank Rösch[1]

* both authors contribute equally

[1]Institute of Nuclear Chemistry, Johannes Gutenberg University, Fritz-Strassmann-Weg 2,
55128 Mainz, Germany

[2]Institute of Organic Chemistry, Johannes Gutenberg University, Duesbergweg 10-14,
55128 Mainz, Germany

[3]Clinic and Polyclinic of Nuclear Medicine, University Medical Center, Langenbeckstraße 1,
55101 Mainz, Germany

[4]Institute of Physical Chemistry, Johannes Gutenberg University, Jakob-Welder-Weg 11,
55128 Mainz, Germany

[5]Fraunhofer ICT-IMM, Carl-Zeiss-Str. 18-20, 55129 Mainz, Germany

Content

S1. Polyether lipid characterization

- a. Determination of molecular weights M_n by ^{1}H NMR spectroscopy
- b. Spectra of polyether lipids

S2. Radiolabeling

- a. [^{18}F]F-TEG-N_3
- b. Polyether lipids

S3. Liposome formation

S4. Liposome characterization

S5. Liposome stability

S6. Animal studies

- a. Positron emission tomography (PET) studies
- b. Biodistribution studies

S7. Liposomes shielded by cholesterol-anchored polyethers (previously published results)

S1. Polyether lipid characterization

a. Determination of molecular weights M_n by ^{1}H NMR spectroscopy

Molecular weights M_n of polyether lipids given in this study were determined from the corresponding ^{1}H NMR spectra measured in pyridine-*d₅*. To this end, the integral of the BisHD initiator protons (2 x CH_3, 6H) at δ = 0.91 ppm was normalized to a value of 6. The degree of polymerization was calculated from the integral of the polyether backbone signals between δ = 3.2 – 4.4 ppm by first subtracting underlying initiator protons (4 x CH_2O + CHO, 9H) and then dividing the resulting value (total number of polyether backbone protons) by the number of protons per monomer repeating unit (PEG = 4, *hb*PG = 5). In case of *hb*PG lipids, alternatively the integral of hydroxyl proton signals at δ = 6.0 – 6.7 ppm can be used to read out the degree of polymerization as each repeating unit corresponds to a single hydroxyl proton in the structure.

b. Spectra of polyether lipids

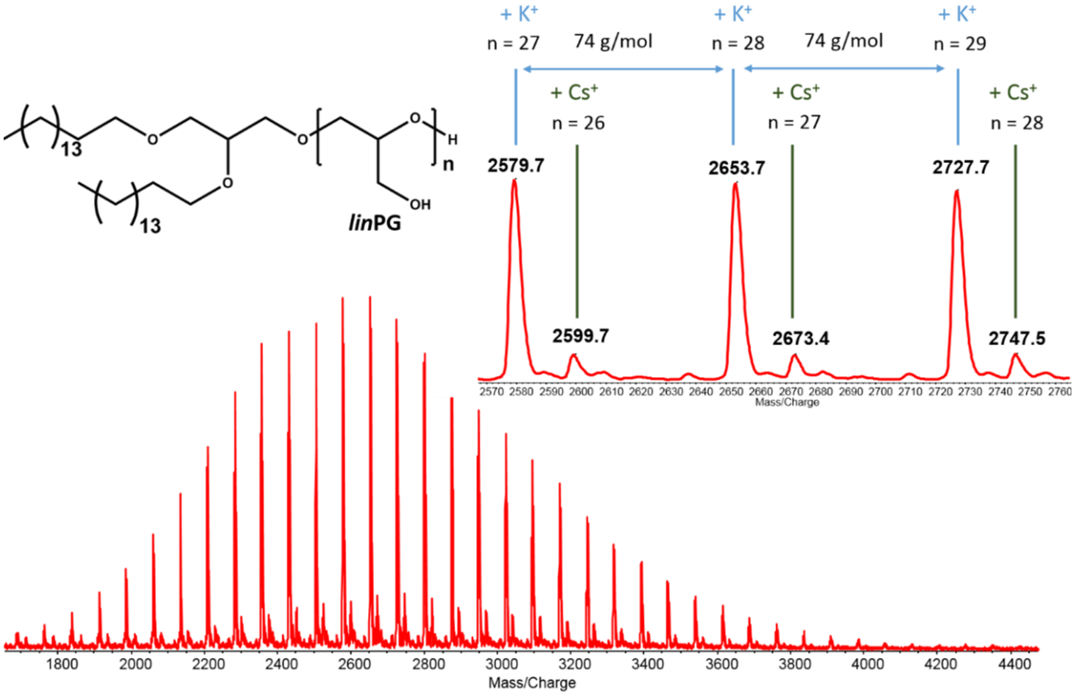

Figure S-1. MALDI ToF MS spectrum of BisHD-*lin*PG$_{19}$ recorded using KTFA as salt and CHCA as matrix.

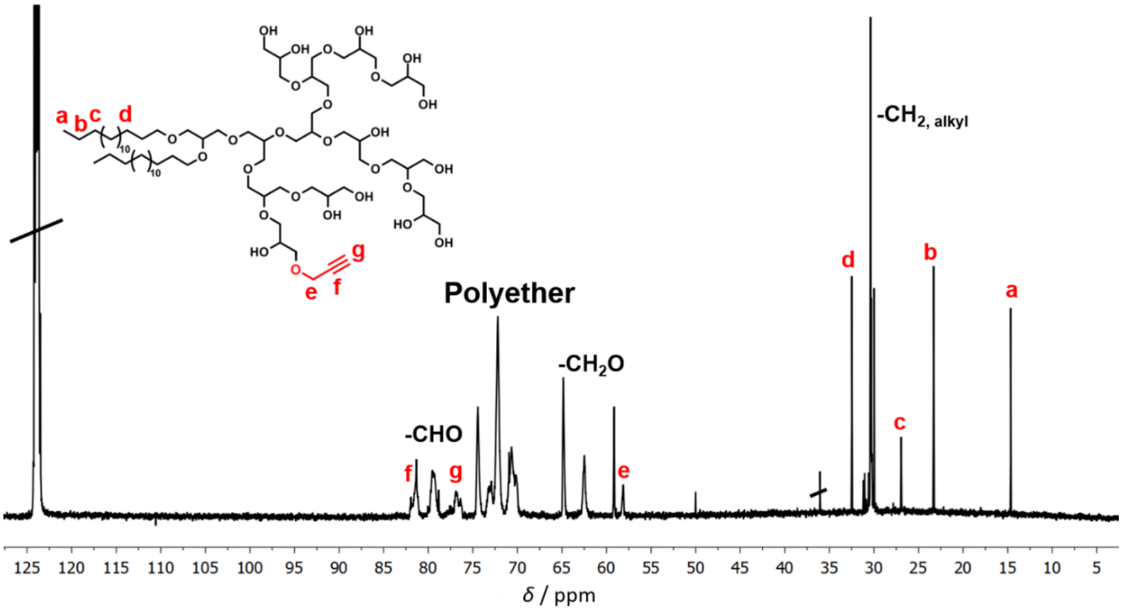

Figure S-2. ^{13}C NMR spectrum of BisHD-*hb*PG$_{63}$-alkyne measured in pydrine-d_5 at 100 MHz.

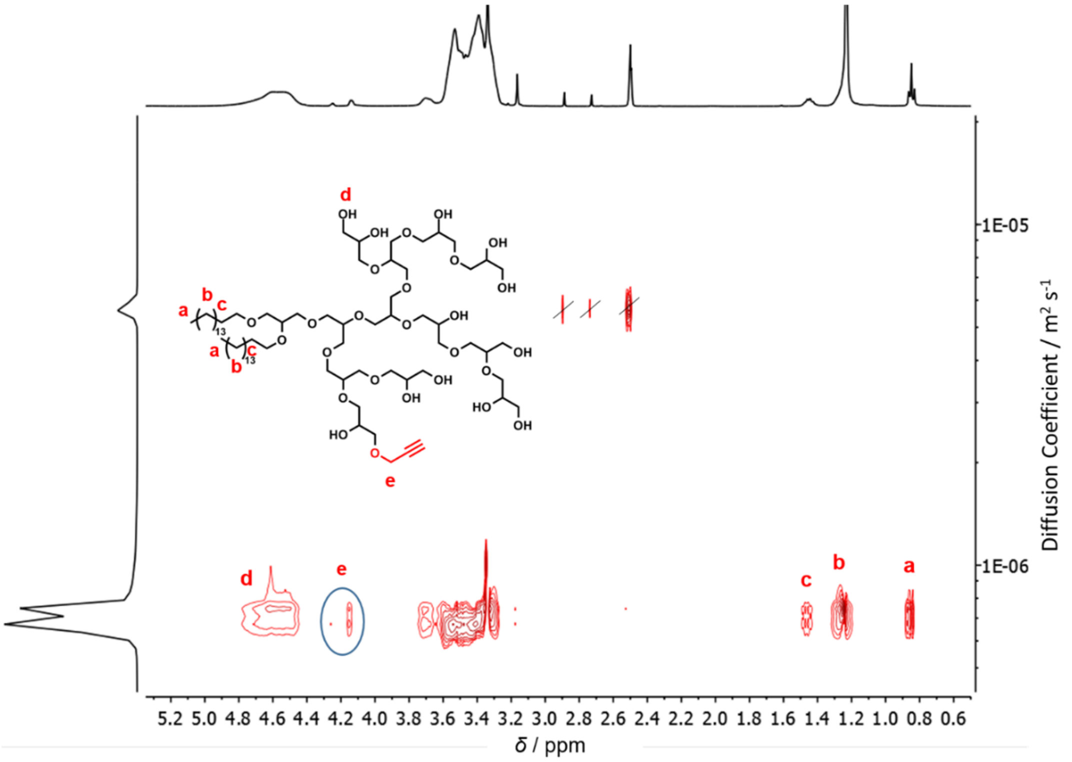

Figure S-3. Diffusion-ordered NMR spectrum (DOSY) of BisHD-*hb*PG$_{32}$-alkyne measured in DMSO-*d*$_6$.

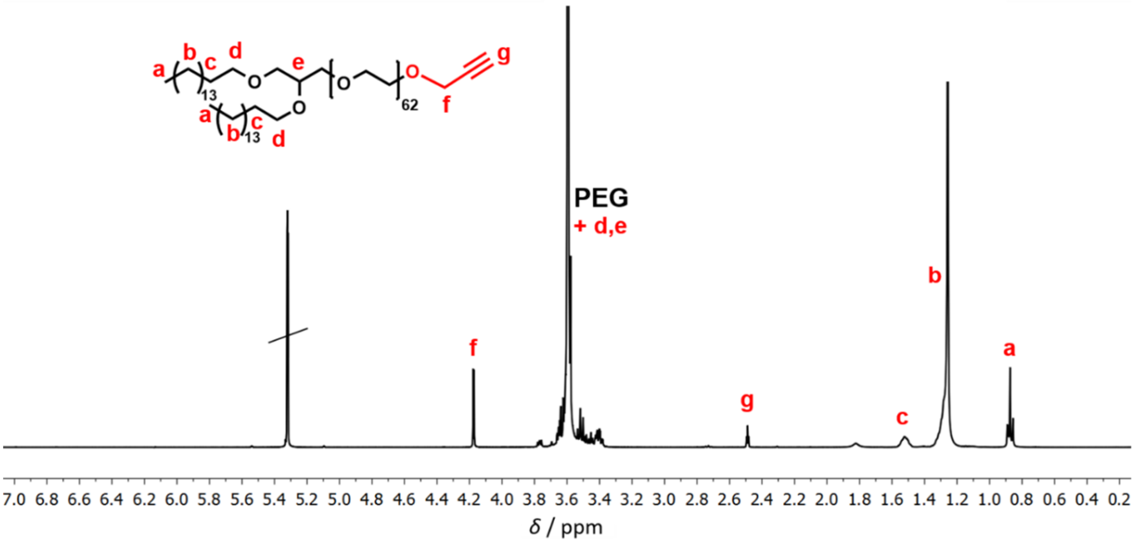

Figure S-4. ^{1}H NMR spectrum of BisHD-PEG$_{56}$-alkyne measured in CD_2Cl_2 at 400 MHz.

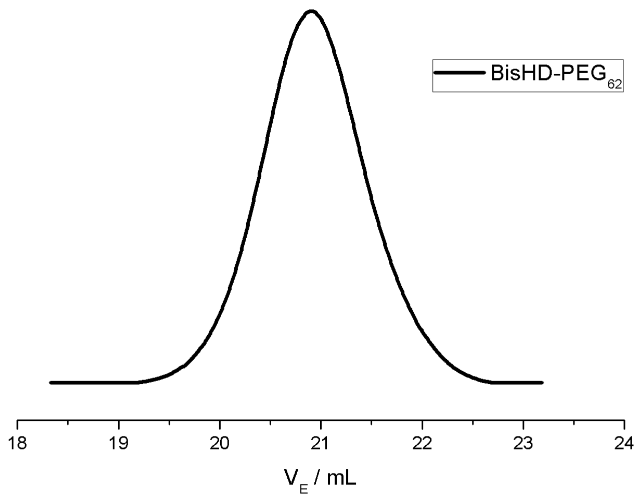

Figure S-5. SEC traces of BisHD-PEG$_{56}$ using DMF as eluent and RI detection.

S2. Radiolabeling

Subsequent to the click reaction, we removed copper using a Chelex 100 resin (obtained from Bio-Rad), which (according to the supplier) exhibits uniquely high selectivities for metal ions. In order to investigate the efficiency, we added sodium sulfide to a sample of the purified reaction mixture and to a sample prior to the removal of copper. In the first case, we observed no precipitation of copper sulfide, whereas in the second case we obtained a darkish precipitate of copper sulfide.

a. [^{18}F]F-TEG-N$_3$

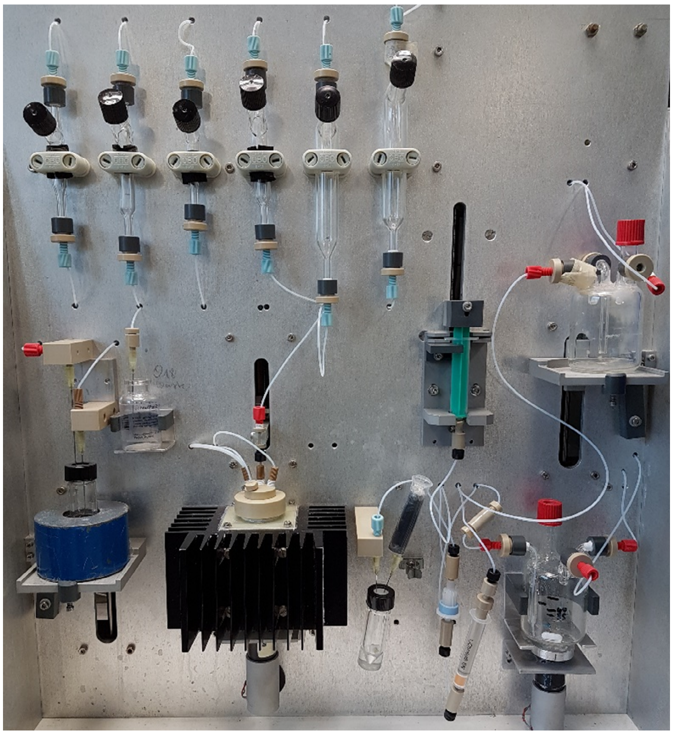

Figure S-6. Front panel of the semi-automatic custom modular system used for the synthesis of [^{18}F]F-TEG-N$_3$.

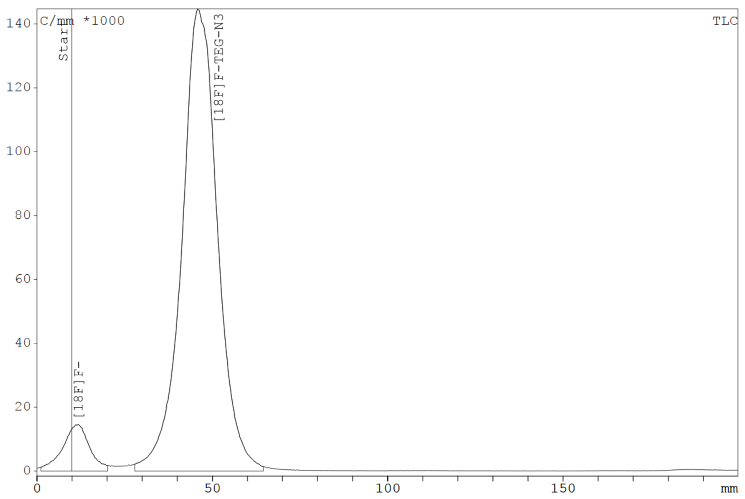

Figure S-7. Radio-TLC of the [^{18}F]F-TEG-N$_3$ synthesis after 10 min with a RCY of 91 %.

b. Polyether lipids

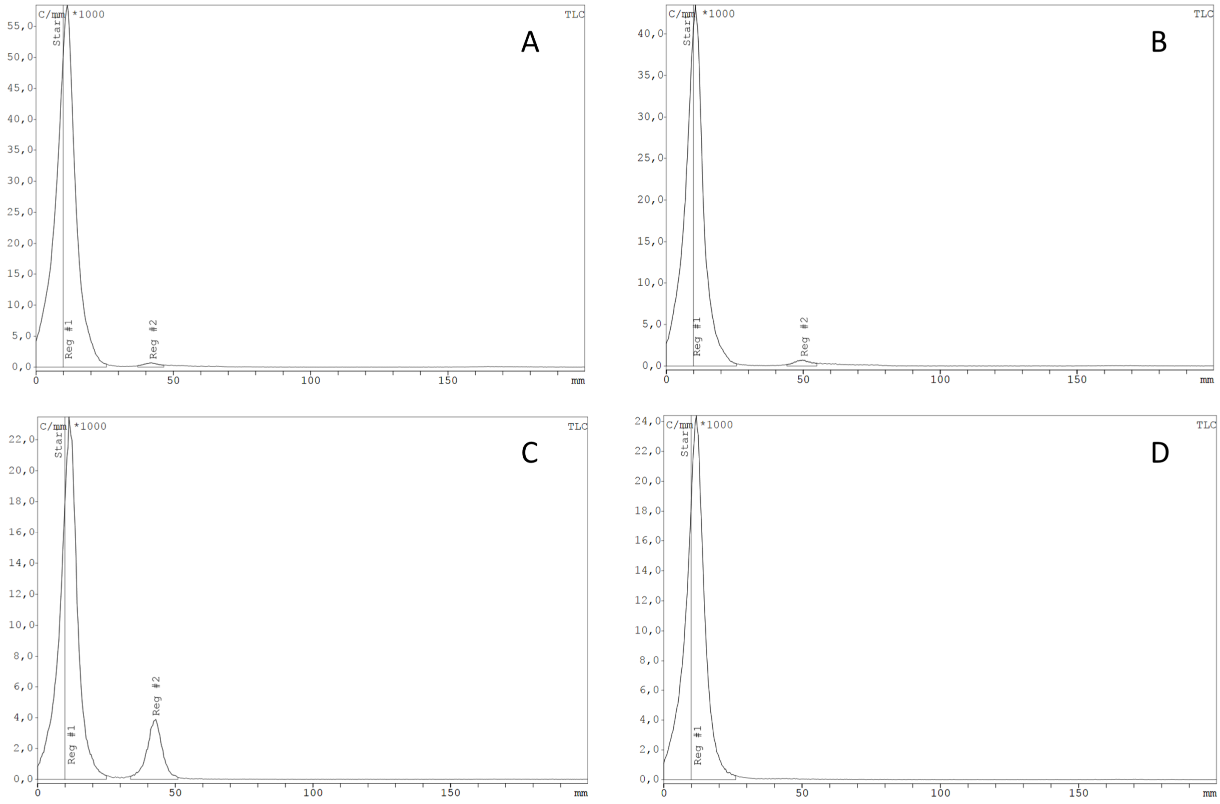

Figure S-8. Radio-TLCs of the radiolabeling of A: BisHD-PEG$_{56}$-alkyne (reaction time 10 min, RCY 97 %), B: BisHD-*hb*PG$_{32}$-alkyne (reaction time 10 min, RCY 96 %) and C & D: BisHD-*hb*PG$_{63}$-alkyne (C: reaction time 1 min, RCY 86 %; D: reaction time 10 min, RCY 98 %) with [^{18}F]F-TEG-N$_3$ via CuAAC. Reg #1 corresponds to the respective polyether lipid, Reg #2 attributes to [^{18}F]F-TEG-N$_3$. Different migration distances of [^{18}F]F-TEG-N$_3$ are explained by different running distances of the mobile phase.

S3. Liposome formation

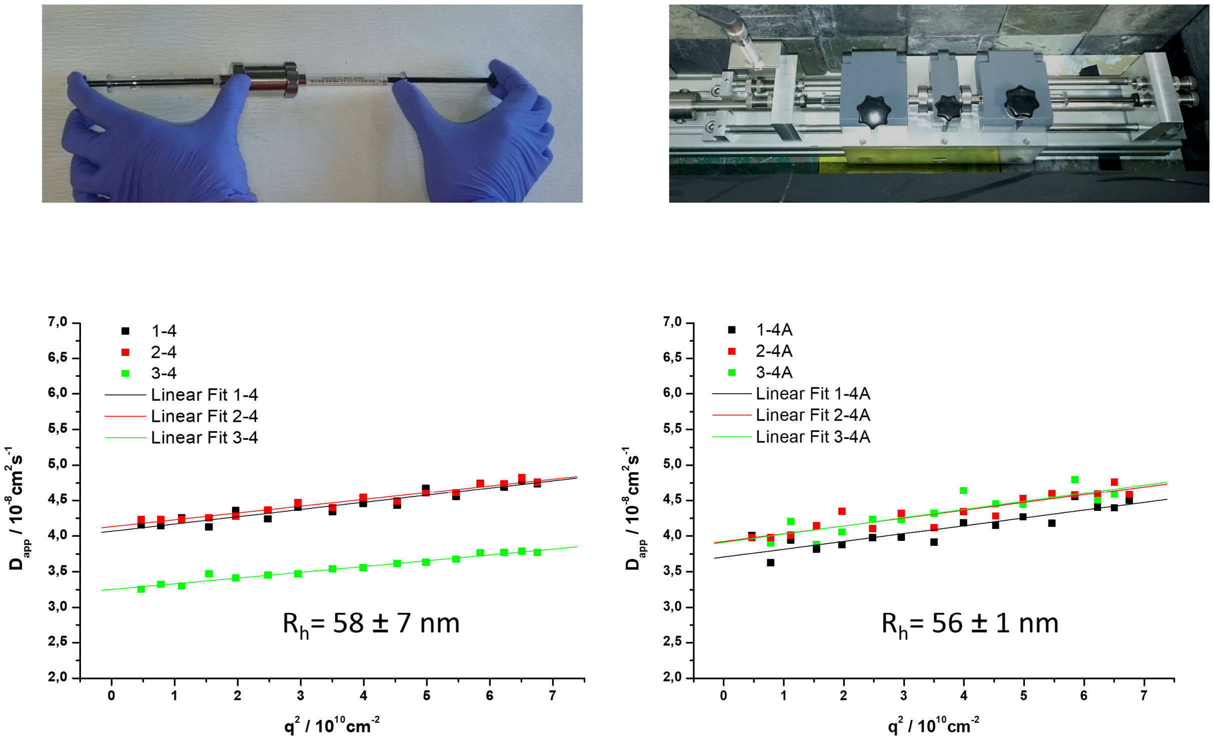

Figure S-9. Comparison of the size reproducibility of identical batches of BisHD-PEG$_{56}$-shielded liposomes extruded by hand (left side) or automatically (right side). n=3. Sizes were determined via dynamic light scattering (DLS).

S4. Liposome characterization

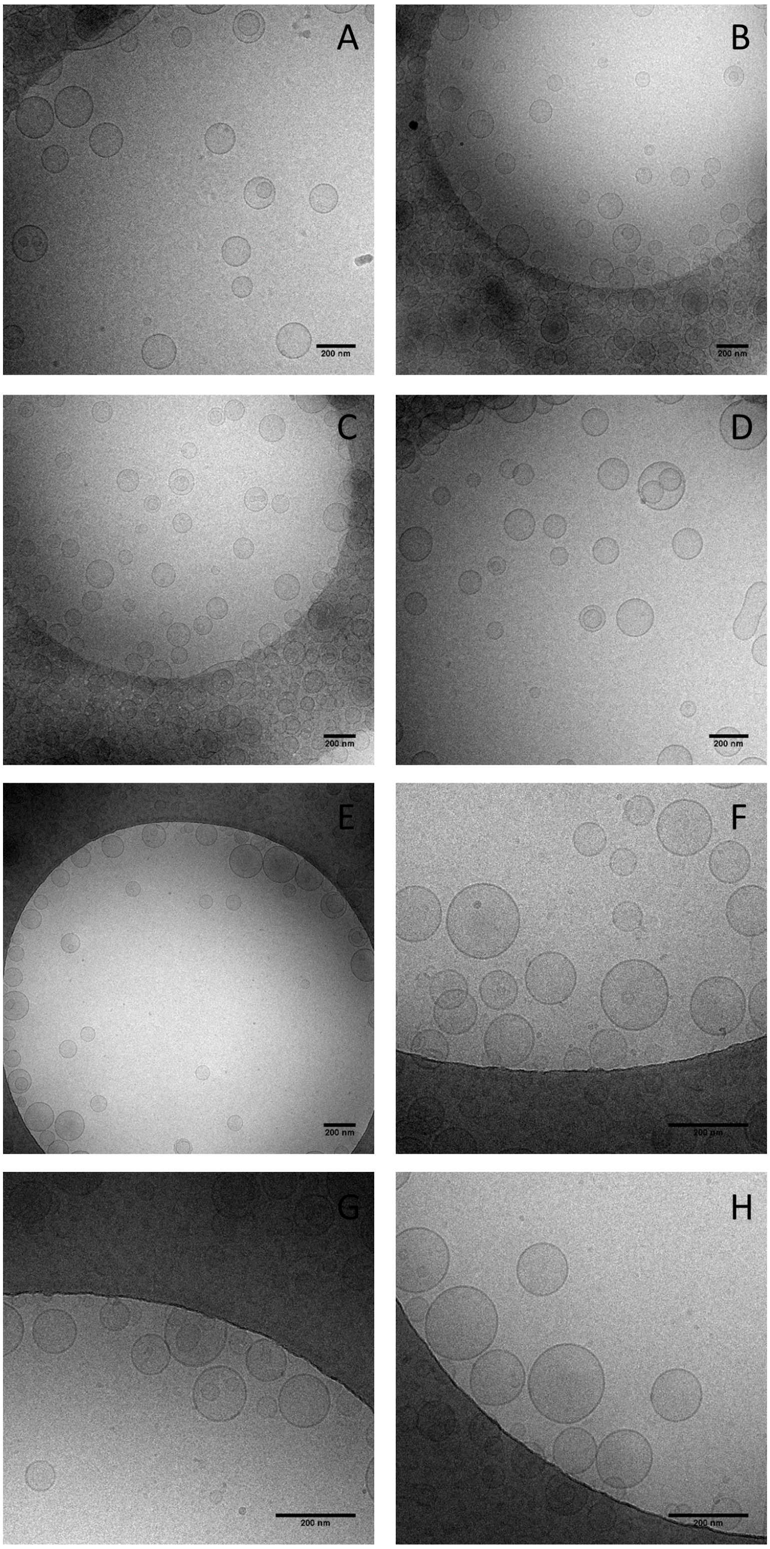
A
200 nm
B
200 nm
C
200 nm
D
200 nm
E
200 nm
F
200 nm
G
200 nm
H
200 nm

Figure S-10. Cryo-TEM images of BisHD-PEG$_{56}$-shielded liposomes (A-D) and BisHD-*hb*PG$_{32}$-shielded liposomes (E-H), showing unilamellar liposome structure.

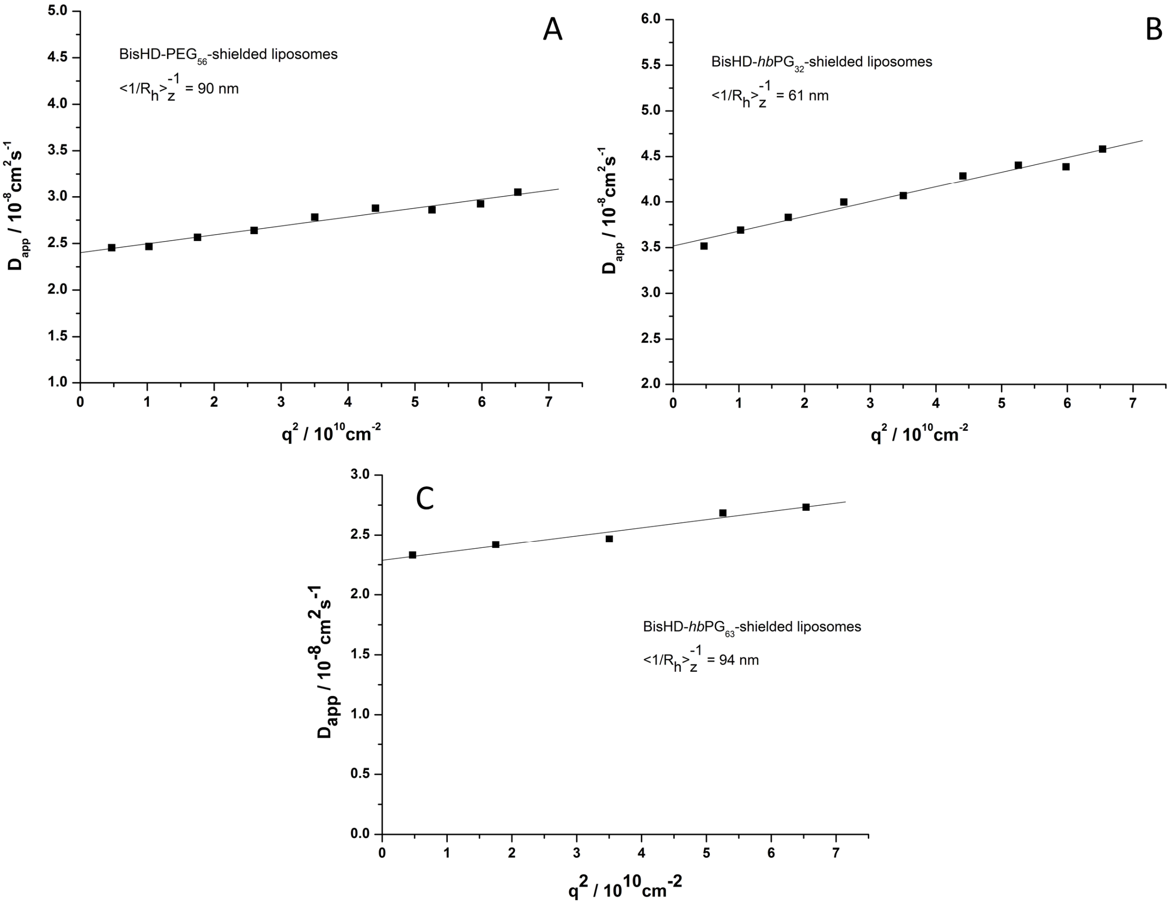

Figure S-11. D_{app} plotted against q^2 data and thereof calculated hydrodynamic radii of BisHD-PEG$_{56}$-shielded liposomes (A), BisHD-*hb*PG$_{32}$-shielded liposomes (B) and BisHD-*hb*PG$_{63}$-shielded liposomes (C).

S5. Liposome stability

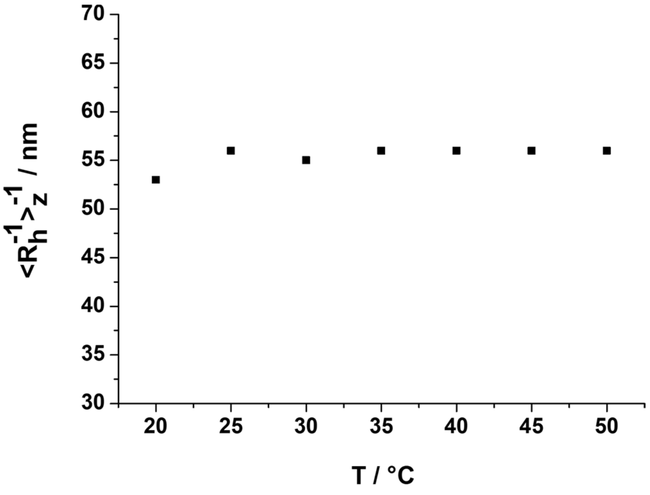

T / °C	20	25	30	35	40	45	50
R$_h$ / nm	53	56	55	56	56	56	56

Figure S-12. Examination of the temperature stability of BisHD-PEG$_{56}$-shielded liposomes via dynamic light scattering.

The hydrodynamic radius ($<R_h^{-1}>_z^{-1}$) of BisHD-PEG$_{56}$-shielded liposomes was determined via DLS at 20 °C. Subsequently the sample chamber was heated in steps of 5 °C till 50 °C were reached. At each temperature step the size of the liposomes was measured. Figure S-12 shows the development of the hydrodynamic radius of the liposomes depending on the temperature. It can be seen, that the size of the liposomes fluctuates only marginal, indicating that the liposomes are stable between 20 to 50 °C. No degradation is observed which would lead to smaller hydrodynamic radii.

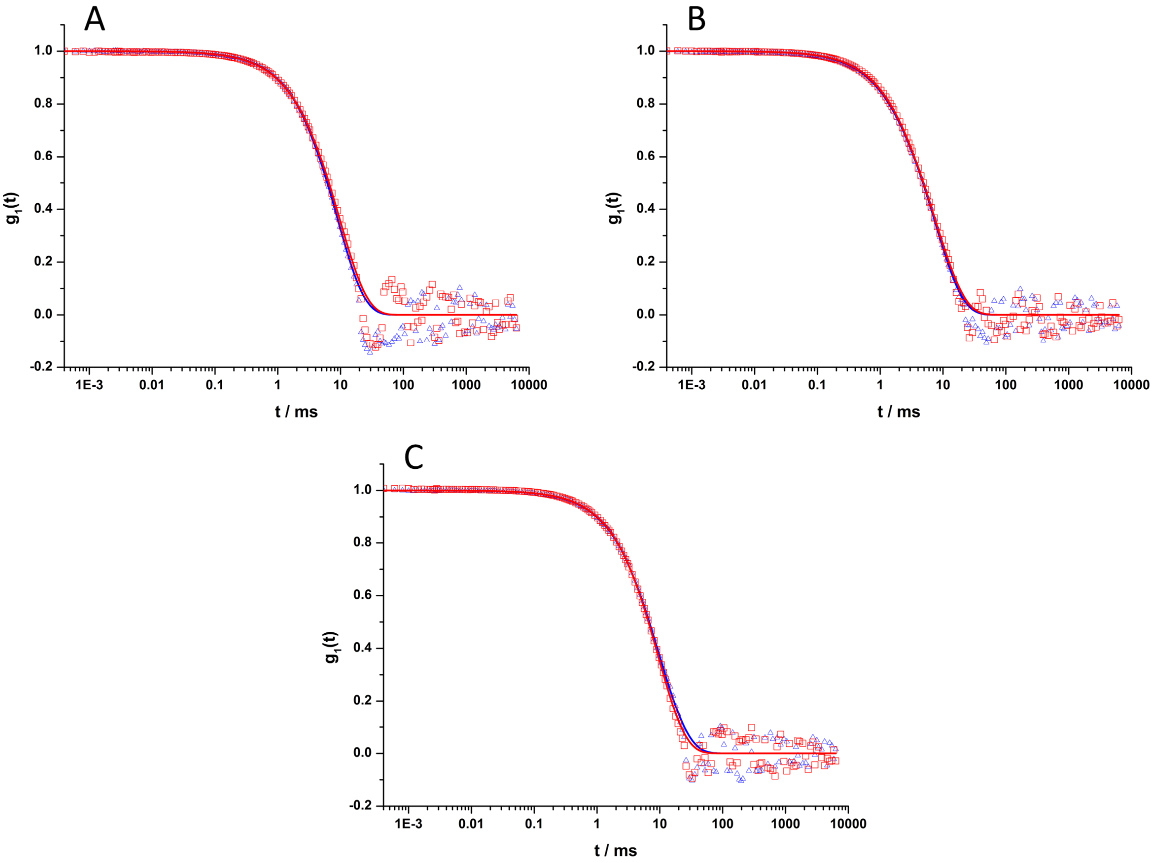

Figure S-13. Autocorrelation functions of BisHD-PEG$_{56}$-shielded liposomes (A), BisHD-*hb*PG$_{32}$-shielded liposomes (B) and BisHD-*hb*PG$_{63}$ (C). Blue curves are acquired shortly after the manufacturing of the liposomes. Red curves are acquired at least one month later (A, B: 4 months later; C: 1 month later).

An aliquot of the liposomes (BisHD-PEG$_{56}$-shielded, BisHD-*hb*PG$_{32}$-shielded and BisHD-*hb*PG$_{63}$-shielded) in PBS buffer used for the animal experiments was stored at 4 °C until complete disappearance of radiation. Subsequently, the size of the liposomes was determined via DLS. Following these experiments the samples were stored at 4 °C for at least one month and were then re-measured via DLS. Figure S-13 shows overlays of the two measurements of the same liposome sample, each at different time points. Since all curves overlay and the shape of the curves did not change, this strongly indicates that the liposomes are stable within the respective period of time (A, B: 4 months; C: 1 month).

S6. Animal studies

a. Positron emission tomography (PET) studies

To track the pharmacokinetic profile during the first hour after intravenous administration of the ^{18}F-radiolabeled, polyether-shielded liposomes and the respective non-liposomal polymers, time activity curves were determined by defining volumes of interest (VOIs) around important organs and quantifying the amount of radioactivity inside the VOIs (Fig. S-14, S-15).

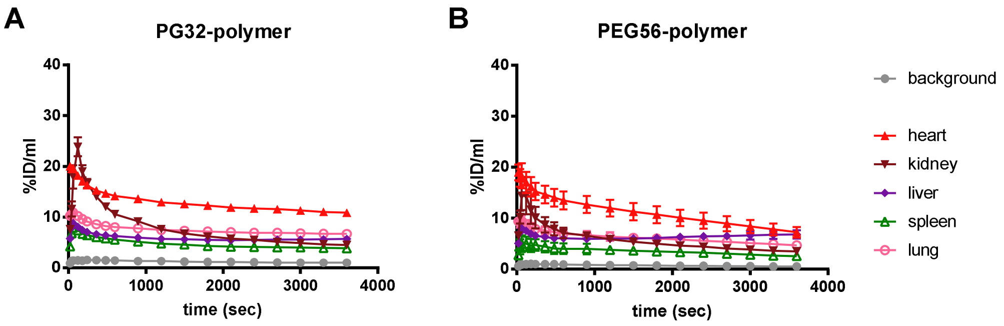

Figure S-14. Time activity curves of the accumulation of BisHD-*hb*PG$_{32}$-^{18}F (A) and BisHD-PEG$_{56}$-^{18}F (B) in organs of interest of male C57BL/6 mice.

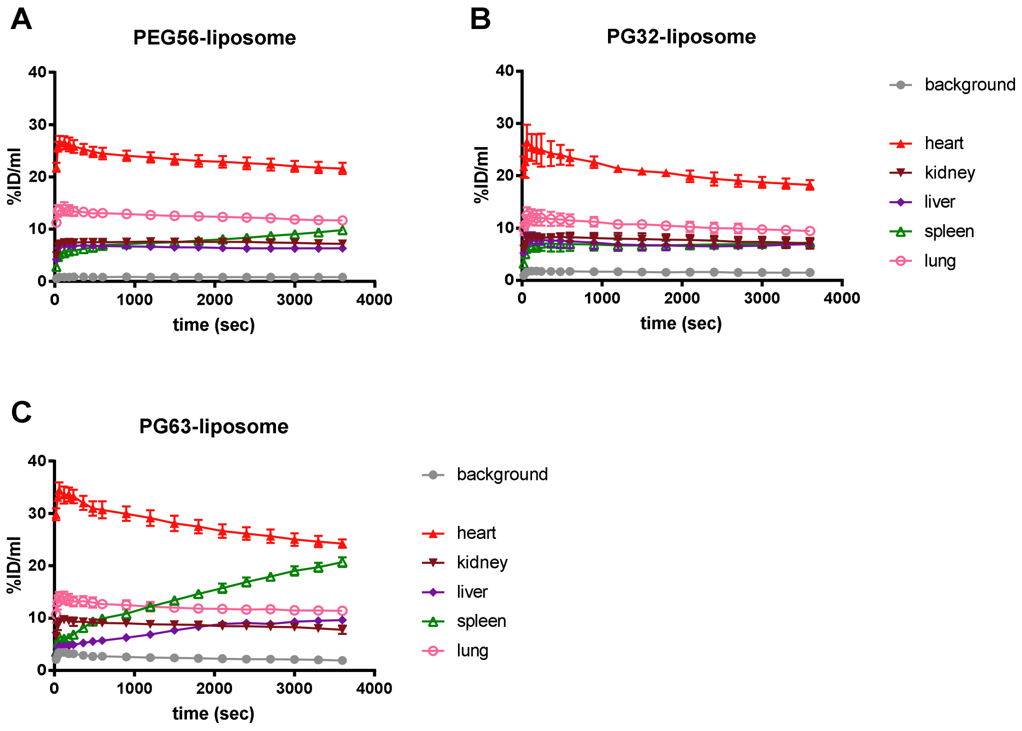

Figure S-15. Time activity curves of the accumulation of ^{18}F-radiolabeled BisHD-PEG$_{56}$-shielded liposomes (A), BisHD-*hb*PG$_{32}$-shielded liposomes (B) and BisHD-*hb*PG$_{63}$-shielded liposomes (C) in organs of interest of male C57BL/6 mice.

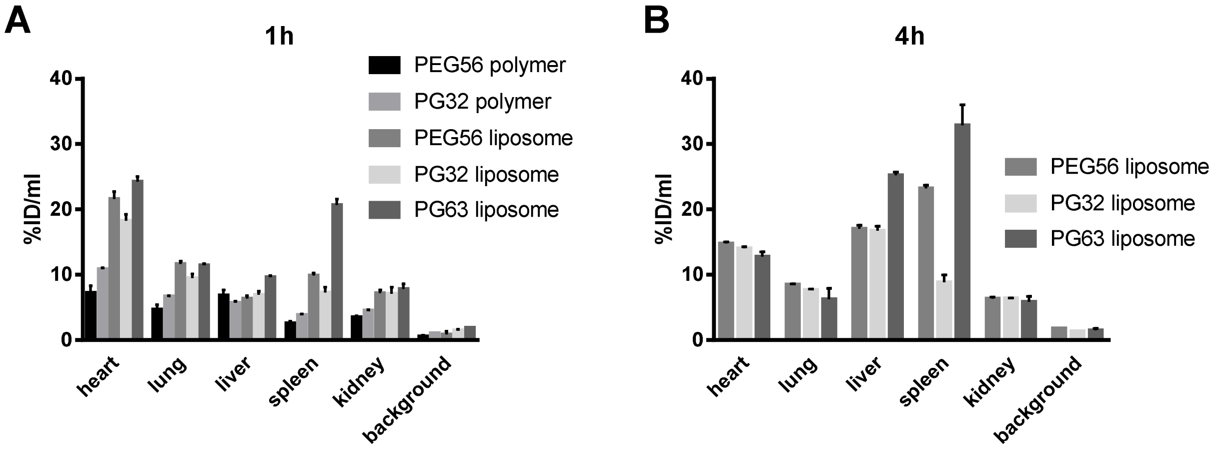

Figure S-16. Accumulated activity in relevant organs of male C57BL/6 mice 1 h (A) and 4 h (B) after injection of the ^{18}F-radiolabeled, differentially shielded liposomes and the respective polymers determined by defining VOIs around important organs and quantifying the amount of radioactivity inside the VOIs. The legend read from top to bottom corresponds to the bars from left to right, respectively.

Table S-1. *Ex vivo* biodistribution data for polyether lipids and liposomal formulations in male C57BL/6 mice.

organ	BisHD-PEG$_{56}$	BisHD-*hb*PG$_{32}$	BisHD-PEG$_{56}$ liposomes (1 h)	BisHD-PEG$_{56}$ liposomes (4 h)	BisHD-*hb*PG$_{32}$ liposomes (1 h)	BisHD-*hb*PG$_{32}$ liposomes (4 h)	BisHD-*hb*PG$_{63}$ liposomes (1 h)	BisHD-*hb*PG$_{63}$ liposomes (4 h)
lung	5.32±0.24	6.30±1.06	11.43±1.23	9.18±0.69	12.69±2.85	8.51±1.13	10.96±1.08	7.45±0.58
blood	14.51±0.93	18.77±3.12	46.41±3.01	29.96±2.85	45.69±5.05	23.46±2.72	43.86±2.78	19.34±0.86
liver	11.42±1.51	7.92±0.95	9.83±2.88	24.12±2.64	12.74±3.58	37.50±4.70	19.61±3.52	42.57±3.24
spleen	3.10±0.30	2.60±0.79	33.82±4.20	67.67±8.07	15.47±1.38	18.88±3.13	51.66±4.48	96.90±16.64
kidney l	3.79±0.23	4.91±0.82	8.73±1.17	8.07±0.84	9.54±0.86	6.55±0.11	9.95±1.83	8.63±0.91
kidney r	3.90±0.28	4.80±0.88	9.23±1.45	8.36±0.83	9.77±1.15	6.74±0.20	10.17±1.94	8.88±0.87
muscle	0.34±0.06	0.31±0.04	0.36±0.09	0.32±0.05	0.54±0.18	0.40±0.04	0.44±0.10	0.43±0.06
heart	2.97±0.24	3.95±0.76	5.27±0.81	3.77±0.40	7.54±0.68	4.53±0.80	7.90±1.50	4.05±0.56
urine	269.28±11.15	93.61±33.16	3.02±1.31	1.26±0.18	2.47±1.67	1.01±0.11	6.76±5.39	2.50±0.27
intestine	1.42±0.81	1.33±0.25	1.91±0.36	3.94±1.35	2.19±0.57	2.85±0.30	2.91±1.16	4.21±0.69
testes	0.58±0.32	0.79±0.18	0.57±0.12	0.54±0.07	0.82±0.13	1.00±0.03	0.73±0.07	0.83±0.07
lymph nodes inguinal	0.92±0.34	1.03±0.18	1.21±0.28	1.72±0.21	1.86±0.47	2.56±0.05	1.95±0.36	3.18±0.76
	n=5	n=5	n=5	n=3	n=5	n=3	n=5	n=5
	urine n=3	urine n=4	urine n=4	urine n=3	urine n=5	urine n=2	urine n=4	urine n=4

S7. Liposomes shielded by cholesterol-anchored polyethers (previously published results)

In order to facilitate the comparison between the current liposomes shielded by BisHD-anchored polyethers and the liposomes shielded by cholesterol-anchored polyethers, Figure S-17 shows the PET images of the liposomes shielded by cholesterol-anchored polyethers. The evaluation of these liposomes is described in detail in a previous report.[1]

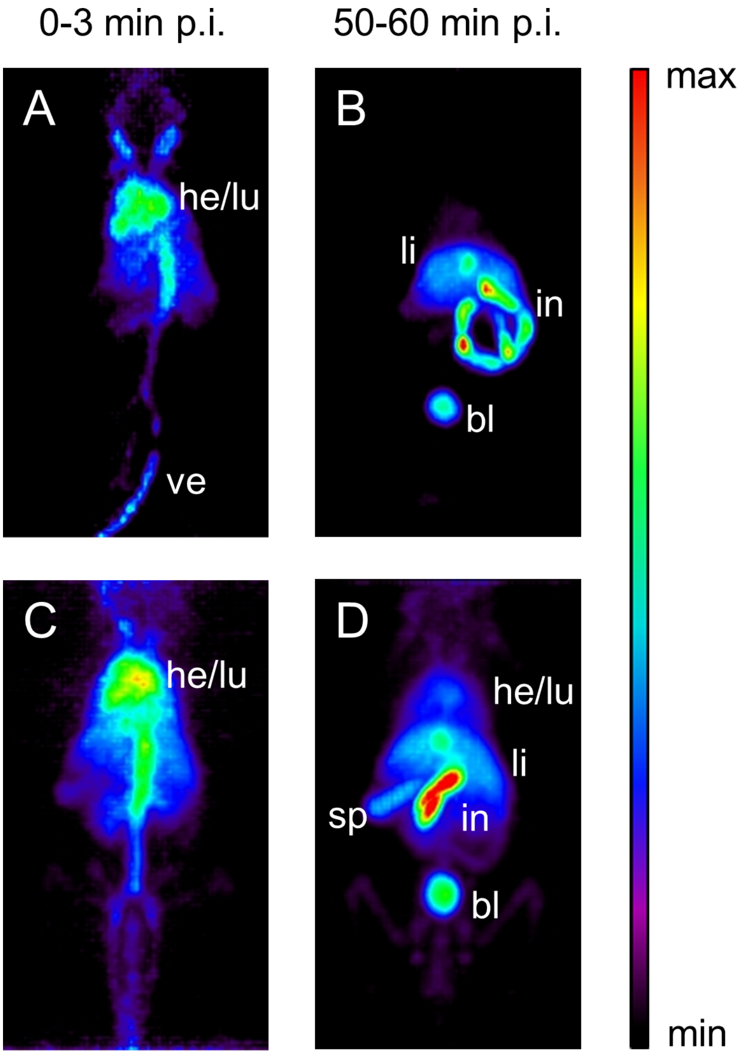

Figure S-17. Coronal MIPs at different time points (left column: 0-3 min p.i., right column: 50-60 min p.i.) for Cholesterol-PEG$_{27}$-^{18}F liposomes (A, B) and Cholesterol-PEG$_{30}$-*hb*PG$_{24}$-^{18}F liposomes (C, D). Liposomes contained 20 mol% of the shielding polyether lipid. he: heart, lu: lung, ve: vein, li: liver, in: intestine, bl: bladder, sp: spleen.

References

(1) Reibel, A. T.; Müller, S. S.; Pektor, S.; Bausbacher, N.; Miederer, M.; Frey, H.; Rösch, F. Fate of Linear and Branched Polyether-Lipids In Vivo in Comparison to Their Liposomal Formulations by ^{18}F-Radiolabeling and Positron Emission Tomography. *Biomacromolecules* 2015, *16*, 842–851.

3.3 Copper-catalyzed click reactions: Quantification of retained copper using ^{64}Cu-spiked Cu(I), exemplified for CuAAC reactions on liposomes

Karolin Wagener[1], Dennis Renisch[1], Meike Schinnerer[2], Matthias Worm[3], Yvonne Jakob[1], Klaus Eberhardt[1], Frank Rösch[1]

[1]Institute of Nuclear Chemistry, Johannes Gutenberg University, Fritz-Strassmann-Weg 2,
55128 Mainz, Germany

[2]Institute of Physical Chemistry, Johannes Gutenberg University, Jakob-Welder-Weg 11,
55128 Mainz, Germany

[3]Institute of Organic Chemistry, Johannes Gutenberg University, Duesbergweg 10-14,
55128 Mainz, Germany

Abstract

The Cu(I)-catalyzed azide-alkyne cycloaddition (CuAAC) is a powerful, highly reliable and selective reaction which allows for a rapid synthesis in high yields and under mild conditions (pH, temperature). Problematic with the usage of copper is its cytotoxicity. This requires a complete removal of the copper prior to an application. In a former study, we used CuAAC to obtain radiolabeled liposomes. Therein, we firstly radiolabeled the shielding polyether lipids, removed the copper and did the liposome formation afterwards. This procedure entailed a time-consuming radiosynthesis, which made us think about whether a direct radiolabeling of liposomes via CuAAC might be possible. Usually, macromolecular structures can easily be purified from light-weighted substances by size exclusion chromatography (SEC), unless the substances are retained by the macromolecular structure. In terms of a CuAAC, this would lead to a non-removable fraction of copper, making a usage of the respective drug delivery systems impossible. Thus, a close investigation of a possible inclusion or adsorption of copper is inevitable.

In this respect, 1 ml of a 1 M Cu(II) nitrate solution was irradiated at the TRIGA Mark II research reactor Mainz to obtain 310 MBq of *c.a.* [^{64}Cu]Cu(II). The irradiated solution was directly used for CuAAC between 1-azido-2-(2-(2-fluoroethoxy)ethoxy)ethane (F-TEG-N_3) and liposomes. Subsequently, liposomes were purified via SEC. Combined liposome containing fractions as well as a sample containing the same amount of [^{64}Cu]Cu(II) nitrate solution that was used for the CuAAC were measured in a gamma detector. Comparison of the resulting values gave the amount of copper still associated with the liposomes after purification. Subsequently, radiolabeling of liposomes with [^{18}F]F-TEG-N_3 via CuAAC was tested.

Only 0.018 % of the added ^{64}Cu-radioactivity was still present in the liposome containing fractions after purification. This refers to a total amount of copper of 0.17 ng. First attempts to radiolabel liposomes directly with [^{18}F]F-TEG-N_3 gave radiochemical yields (RCY) up to 27.4 % after 10 min.

The ration of retained copper is so low, that an *in vivo* application of the liposomes is absolutely reasonable. This avoids subsequent purification protocols, significantly simplifies the radiosynthesis, saves time, enables a higher amount of radioactivity per volume and results in a lesser radiation exposure for the experimentalist. Besides this particular study, the experimental methodology may be applied to study many other CuAAC reactions, used for the synthesis of radiolabeled or non-radioactive species, which are intended for human applications.

Introduction

Non-invasive imaging techniques like positron emission tomography (PET) bear great potential to assist in the developmental process of macromolecular drug delivery systems (DDS). In this regard, suitable radiolabeling procedures are needed. The Cu(I)-catalyzed azide-alkyne cycloaddition (CuAAC) has been utilized for this purpose to a growing extent and with great success.[1-3] In this reaction, a terminal azide is coupled to a terminal alkyne with the aid of a Cu(I) catalyst. The Cu(I) species can be added directly in the form of a Cu(I) salt, most commonly copper iodide, or it can be generated *in situ* by comproportionation of Cu(0) and Cu(II) or by reduction of a Cu (II) salt.[4] For the latter, Cu(II) sulfate together with sodium ascorbate as reducing agent is a widely used system. The product of the CuAAC is a 1,2,3-triazole ring which exhibits excellent biological properties since it mimics a peptide bond.[5] While the CuAAC tolerates a whole range of both azide and alkyne reactants, it is orthogonal with a lot of other organic functional groups and works with many different solvents and at a wide range of pH values.[4] Further advantages are its high reliability, efficiency and selectivity, which allows for a rapid synthesis in high yields and under mild conditions (pH, temperature).[1,6] If a radiolabeled terminal azide or alkyne is used as a prosthetic group, it can be coupled to a DDS via a CuAAC in high yields and under mild reaction conditions.[1,5] This approach has been published in 2006 by Marik and Sutcliffe for the first time, using ω-[^{18}F]fluoro-alkynes to radiolabel *N*-(3-azidopropionyl) peptides in a CuAAC.[7]

Copper is an essential trace element, which is required in a variety of different biological processes, including iron metabolism, antioxidant defense, neuropeptide synthesis and immune function.[8] Yet, relatively low amounts of <100 mg Cu are stored inside the human body[9] and humans dietary reference values for Cu range between 0.9 to 2 mg per day in different countries.[8] Copper inside the body is normally bound to different proteins. Free copper species, resulting from an external supply or from an internal release, are capable of disrupting important cellular events and they participate in the formation of reactive oxygen species, which cause oxidative damage.[8] These properties are responsible for the cytotoxicity of copper. Thus, effective purification protocols as well as their validation by exact quantification of the final copper content is of utmost importance for formulations intended for an application *in vivo*, especially if their synthesis requires copper. Commonly used quantification methods for copper include inductively coupled plasma mass spectrometry (ICP-MS), electrothermal atomic absorption spectrometry (ETAAS) and total reflection X-ray fluorescence (TXRF), because they provide a high sensitivity and at the same time require a low sample quantity. On the other hand they involve a significant sample manipulation, which bears the risk of contaminating the sample.[10]

Recently, our group investigated the *in vivo* fate of liposomes shielded by multifunctional hyperbranched polyglycerol (*hb*PG) with a 1,2-bis(hexadecyl)glycerol (BisHD) anchor for stable incorporation into the bilayer of the liposomes.[11] There, radiolabeling was carried out via CuAAC using the prosthetic group 1-azido-2-(2-(2-[^{18}F]fluoroethoxy)ethoxy)ethane ([^{18}F]F-TEG-N_3), whereas the polyether lipids exhibited terminal alkyne functionalities. The CuAAC was accomplished prior to the liposome formation to ensure a quantitative removal of copper. Due to the intrinsic cytotoxicity of copper[12], a complete removal of the copper prior to an application is inevitable. However, to radiolabel the shielding polyether lipids, remove the copper and do the liposome formation afterwards entails a time-consuming radiosynthesis, which made us think about whether a direct radiolabeling of liposomes via CuAAC, in terms of purification of the final product, might be possible. Figure 1 illustrates this issue in detail. Usually, macromolecular structures can easily purified from light-weighted substances by size exclusion chromatography (SEC), unless the substances are retained by the macromolecular structure. In terms of a CuAAC, this would lead to a non-removable fraction of copper, making a usage of the DDSs impossible. Thus, a close investigation of a possible inclusion or adsorption of copper during the ^{18}F-radiolabeling of liposomes via CuAAC is inevitable, which we did herein.

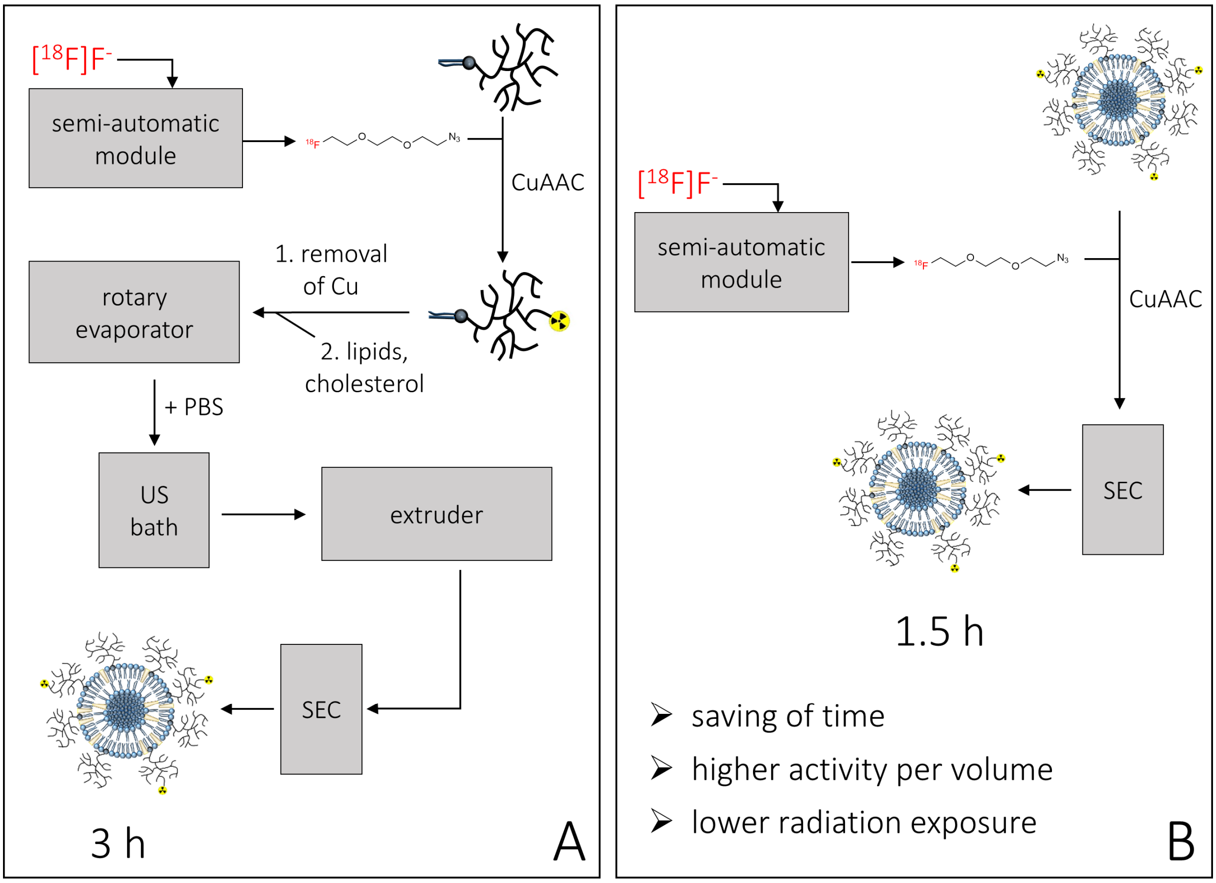
[^{18}F]F$^-$
semi-automatic module
^{18}F
O
O
N_3
CuAAC
1. removal of Cu
2. lipids, cholesterol
rotary evaporator
+ PBS
US bath
extruder
SEC
3 h
A
[^{18}F]F$^-$
semi-automatic module
CuAAC
SEC
1.5 h
➢ saving of time
➢ higher activity per volume
➢ lower radiation exposure
B

Figure 1. Procedure of the radiolabeling via CuAAC prior to liposome preparation (A) in comparison to the procedure of the radiolabeling of preformed liposomes via CuAAC (B). The time entry indicates the duration of the radiosynthesis.

In order to track the added copper, a Cu(II) nitrate solution was irradiated at a the TRIGA Mark II research reactor Mainz to obtain traceable [^{64}Cu]Cu(II). Subsequently, liposomes were reacted with 1-azido-2-(2-(2-fluoroethoxy)ethoxy)ethane (F-TEG-N_3) in a CuAAC, where the irradiated Cu(II) nitrate solution was directly used as a catalyst. After CuAAC and liposome purification, the copper still associated with the liposomes was examined via gamma spectrometry. After successful evaluation of the remaining copper content, the radiochemical yield (RCY) of the CuAAC was investigated as well, by radiolabeling the liposomes with $[^{18}F]F$-TEG-N_3.

Experimental

Materials

Chemicals were obtained from common suppliers such as Sigma Aldrich, TCI Europe, VWR or Acros Organics unless stated otherwise. 1,2-Dioleoyl-*sn*-glycero-3-phosphocholine (DOPC) was bought from Avanti Polar Lipids. Particle-free phosphate-buffered saline (PBS) enabling exact light scattering experiments was obtained from Gibco™ by Thermo Fisher Scientific. $[^{18}F]F^-_{aq}$ was produced by irradiation of enriched $[^{18}O]H_2O$ with protons at a PETtrace 700S cyclotron (GE Healthcare). A common production run lasted 30 min at a beam current of 25 µA, yielding an ^{18}F-activity of 20 GBq.

Methods

Characterization

Dynamic light scattering (DLS) for liposome characterization

For multi-angle DLS cylindrical quartz cuvettes (Hellma Analytics, Mühlheim, Germany) were cleaned with dust-free distilled acetone and transferred to a dust free flow box. Solutions were diluted 1:100 with PBS, then filtered into the cuvettes through Millex-LCR filters, 0.45 µm pore size (Merck Millipore). DLS measurements were performed at 20 °C by the following instruments. Apparatus 1 consists of a Uniphase He/Ne Laser (22.5 mW output power at λ = 632.8 nm) and an ALV/CGS-8F SLS/DLS 5022F goniometer with eight simultaneously working ALV 7004 correlators and eight ALV/High QEAPD avalanche photodiode detectors. Apparatus 2 consists of a Uniphase He/Ne Laser (22.5 mW output power at λ = 632.8 nm), an ALV/SP125 goniometer with an ALV 5000/E/PCI correlator and an ALV/High QEAPD Avalanche photodiode detector. The correlation functions of the particles were fitted using a sum of two exponentials. The z-average diffusion coefficient D_z was calculated by extrapolating D_{app} for q = 0. By formal application of Stokes law, the inverse z-average hydrodynamic radius is $R_h = \langle R_h^{-1} \rangle_z^{-1}$. The experimental uncertainties are estimated to ±2 % for R_h.

Radio-thin layer chromatography (TLC)

To determine the RCY of the ^{18}F-labeling with $[^{18}F]F$-TEG-N_3, radio-TLCs were run on silica-coated aluminum-backed TLC plates (Merck) using EA/Hex 1:1 as mobile phase. To distinguish between free copper and copper associated with liposomes, radio-TLCs were run with 0,1 M citrate buffer (pH = 4).

The chromatograms were acquired on a RITA detector (Raytest) with an acquisition time of 1 min. Analyzation was done using Gina Star TLC software (Raytest).

Synthesis of 1-azido-2-(2-(2-[^{18}F]fluoroethoxy)ethoxy)ethane ([^{18}F]F-TEG-N_3)

The synthesis of the precursor and the radiolabeling with ^{18}F were accomplished according to published procedures.[13] [^{18}F]F-TEG-N_3 was obtained in RCYs up to 91 % (TLC, EA/nHex 1:1, R_f: 0.8).

Synthesis of 1-azido-2-(2-(2-fluoroethoxy)ethoxy)ethane (F-TEG-N_3)

100 mg (0.6 mmol, 1 eq) of 2-(2-(2-azidoethoxy)ethoxy)ethanol were dissolved in 4 ml dichloromethane and 100 mg (0.6 mmol, 1 eq) of *N,N*-diethylaminosuflur trifluoride (DAST) were added at room temperature. The reaction mixture was stirred at room temperature for 2 h. To quench the reaction, 5 ml of water were added, followed by extraction with dichloromethane (3 x 5 ml). The combined organic phases were dried with sodium sulfate and the solvent was removed by careful distillation (product is volatile). The raw product was purified by silica column chromatography (ethyl acetate/hexane, 1:4) to give a colorless oil (49.6 mg, 0.28 mmol, 46.7 %). ^{1}H-NMR: δ [ppm] = 4.56 (dt, 2H, CH_2-F, $^2J_{F\text{-}H}$ = 47.7 Hz, $^3J_{H\text{-}H}$ = 4.2 Hz), 3.75 (dt, 2H, CH_2-CH$_2$-F, $^3J_{F\text{-}H}$ = 29.9 Hz, $^3J_{H\text{-}H}$ = 4.2 Hz), 3.68 (m, CH_2, 6H), 3.39 (t, 2H, CH_2-N$_3$, $^3J_{H\text{-}H}$ = 5.1 Hz), NMR spectrum is provided in the Supporting Information (Figure S1).

Synthesis of 1,2-Bis(hexadecyl)glycerol-*hb*PG$_{32}$-alkyne (BisHD-*hb*PG$_{32}$-alkyne)

The synthesis of BisHD-*hb*PG$_{32}$-alkyne is described in detail in a previous report.[11] In short, synthesis of the polyether lipid was started from 1,2-Bis(hexadecyl)glycerol. The final product was synthesized by anionic ring-opening polymerization, followed by a postmodification reaction with propargyl bromide.

Liposome formation

Liposomes were prepared by the thin film hydration method followed by several extrusion steps. Liposome components were 1,2-dioleoyl-*sn*-glycero-3-phosphocholine (DOPC), cholesterol and BisHD-*hb*PG$_{32}$-alkyne at molar ratios of 55:40:5 mol%. Solutions of DOPC in ethanol, cholesterol in ethanol and BisHD-*hb*PG$_{32}$-alkyne in ethanol were blended, and the solvent was evaporated in a miniature rotating evaporator to obtain a thin film of the liposome components. 0.8 ml of PBS were added resulting in large multilamellar vesicles. To obtain small unilamellar vesicles, the liposome suspension was sonicated at 50 °C for 10 min, followed by extrusion through polycarbonate membranes (400 nm, then 100 nm, then 50 nm, 21 times each) using a Mini-Extruder (AVESTIN Europe GmbH) driven by a custom-built device (Figure S2 in the Supporting Information). Finally, the liposomes were purified via size exclusion chromatography (SEC) using Sephacryl S-400 HR (GE Healthcare) as a resin (~4 ml packed in a 6 ml empty SPE tube with 20 µm PTFE frits at top and bottom) and PBS as a mobile phase. Fractions of 0,5 ml were collected. Liposomes eluted in the fractions 3-5.

Activation of $Cu(NO_3)_2$

1 ml of a 1 M $Cu(NO_3)_2$ solution in water was irradiated with neutrons at the TRIGA Mark II research reactor Mainz. The flux of thermal neutrons is $7 \cdot 10^{11}$ $n \cdot cm^{-2} \cdot s^{-1}$ on average. The irradiation time was 5 h. A waiting time of 5 min after the irradiation was chosen to enable the decay of short-lived radiation products.

CuAAC

Testing of the CuAAC with $Cu(NO_3)_2$ and $Cu(CH_3COO)_2$: 3 mg of the BisHD-hbPG$_{32}$-alkyne in 1 ml PBS were added to a [^{18}F]F-TEG-N_3-coated vial. Subsequently, 12.5 µl DMSO, 15 µl $Cu(NO_3)_2$ or 15 µl of $Cu(CH_3COO)_2$ (1 M in MilliQ water, 15 µmol) and 25 µl sodium ascorbate (2.4 M in PBS buffer, 60 µmol) were added in this order. The mixture was heated at 70 °C for 15 min. The RCY was determined via radio-TLC (EA/nHex 1:1, R_f: 0). RCYs were examined after 1, 2, 5, 10 and 15 min reaction time.

CuAAC with [^{64}Cu]$Cu(NO_3)_2$ and F-TEG-N_3: A solution of 8.37 ng of F-TEG-N_3 (refers to a radioactivity of 3 GBq, common for radiolabeling with [^{18}F]F-TEG-N_3) in 500 µl PBS was prepared via dilution. 500 µl of the liposome suspension (fraction 4 from SEC purification) were added. Subsequently, 12.5 µl DMSO, 15 µl [^{64}Cu]$Cu(NO_3)_2$ (1 M in MilliQ water, 15 µmol) and 25 µl sodium ascorbate (2.4 M in PBS buffer, 60 µmol) were added in this order. The mixture was heated at 45 °C for 10 min. Purification of the liposomes was done via size SEC using Sephacryl S-400 HR (GE Healthcare) as a resin (~4 ml packed in a 6 ml empty SPE tube with 20 µm PTFE frits at top and bottom) and PBS as a mobile phase. Fractions of 0,5 ml were collected. Liposomes eluted in the fractions 3-5.

^{18}F-labeling of liposomes with [^{18}F]F-TEG-N_3 via CuAAC: 1 ml of the liposome suspension (fraction 3+5 from SEC purification) was added to a [^{18}F]F-TEG-N_3-coated vial. Subsequently, 12.5 µl DMSO, 15 µl $CuSO_4$ (1 M in MilliQ water, 15 µmol) and 25 µl sodium ascorbate (2.4 M in PBS buffer, 60 µmol) were added in this order. The mixture was heated at 45 °C for 20 min. The RCY was determined via radio-TLC (EA/nHex 1:1, R_f: 0). RCYs were examined after 1, 2, 5, 10 and 20 min reaction time. Purification of the liposomes was done via SEC using Sephacryl S-400 HR (GE Healthcare) as a resin (~4 ml packed in a 6 ml empty SPE tube with 20 µm PTFE frits at top and bottom) and PBS as a mobile phase. Fractions of 0,5 ml were collected. Liposomes eluted in the fractions 3-5. [^{18}F]F-TEG-N_3 eluted in fraction 7-10.

Gamma spectrometry

Gamma spectrometry was used to quantify the amount of copper associated with the liposomes after purification. Measurements were performed with a high-purity germanium (HPGe) detector (P-type, relative efficiency: 20 %; ORTEC). Combined liposome containing fractions (fractions 3-5; 1.5 ml) as well as a sample containing the same amount of [^{64}Cu]Cu(II) nitrate that was used for the CuAAC (100 % value) were examined. The 100 % value sample was filled up with water to a volume of 1.5 ml so that both samples had the same geometry. The measurement time and position was selected in such a way, that the netto peak area of the 511 keV peak reached at least 10.000 counts. This ensured that the error of the number of counts was below 1 %. Because of the high amount of radioactivity present in the 100 % value sample, it was measured at a distance of 33 cm from the detector for 2 min, whereas the liposome sample was measured at a distance of 1 cm for 60 min. In order to compare the obtained values, an efficiency calibration, using a multiple gamma-ray-emitting standard (model 7601; Eckert & Ziegler), was done. Analysis of the data was performed with Genie 2000 (version 3.2.1, Aug 26, 2009; Canberra Industries). Comparison of the resulting values provided the amount of copper still associated with the liposomes after purification.

Results and Discussion

CuAAC with $Cu(NO_3)_2$ and $Cu(CH_3COO)_2$ and activation of $Cu(NO_3)_2$

The irradiation of Cu(II) sulfate, which is usually used in CuAAC, would lead to long-lived isotopes besides ^{64}Cu interfering with the experiment. Therefore, the CuAAC was tested with Cu(II) nitrate as well as with Cu(II) acetate prior to the irradiation. Relating reaction kinetics and radio-TLC chromatograms are provided in the Supporting Information (Figure S3 and S4). Both reactions provided quantitative yields after 10 min. Thus, both Cu(II) salts are suitable for a usage in CuAAC. Ultimately, a Cu(II) nitrate solution was irradiated with neutrons at the TRIGA Mark II research reactor Mainz. During irradiation, the following radioisotopes are formed: ^{16}N ($t_{1/2}$=7.1 s)[14], ^{19}O ($t_{1/2}$=26.9 s)[15], ^{64}Cu ($t_{1/2}$=12.7 h)[16] and ^{66}Cu ($t_{1/2}$=5.120 min)[17]. Besides ^{64}Cu, the radioisotopes are short-lived and thus were decayed prior to the following investigations. The observed signal in radio-TLC and gamma spectrometry measurements is derived exclusively from ^{64}Cu, by implication. The calculated radioactivity generated by ^{64}Cu after the end of irradiation was 310 MBq. This related to a specific acitivity of 4.88 MBq/mg.

Investigations of the inclusion of copper via radio-TLC and gamma spectrometry

In order to enable detection of copper, the CuAAC was accomplished according to Figure 2. The liposomes were reacted with non-radioactive F-TEG-N_3 in a CuAAC using traceable $[^{64}Cu]Cu(NO_3)_2$ as a catalyst. DLS measurements of the liposomes before and after the CuAAC revealed that the size of the liposomes changed only to a minor degree, ensuring that the liposomes stayed intact during the CuAAC. Aggregate formation as well as breakdown of the liposomes would lead to much bigger or much lower sizes. Underlying data are provided in the Supporting Information (Figure S5). Radio-TLC as well as gamma spectrometry measurements shed light on the amount of copper still associated with the liposomes after CuAAC and purification.

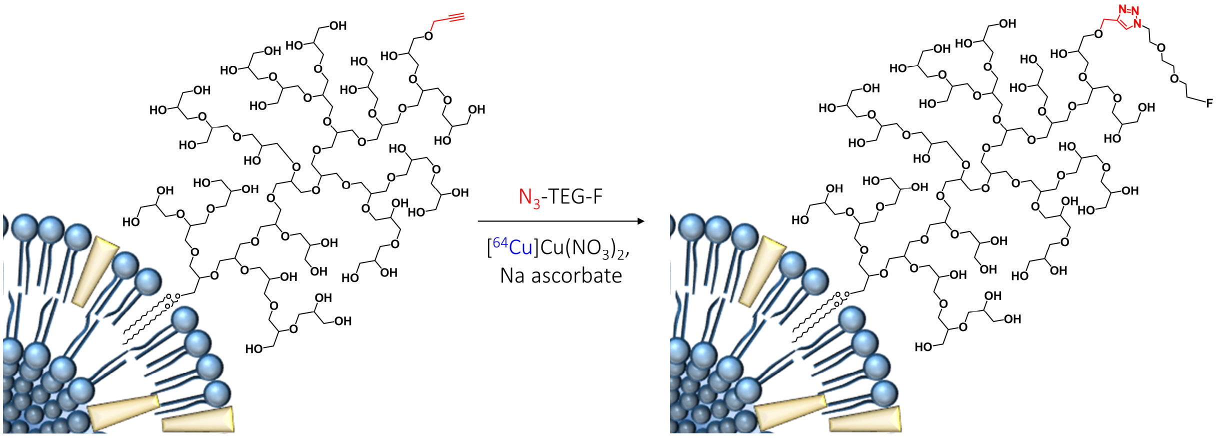

Figure 2. Reaction between liposomes containing BisHD-*hb*PG$_{32}$-alkyne and non-radioactive F-TEG-N$_3$ via CuAAC using [^{64}Cu]Cu(NO$_3$)$_2$.

Radio-TLC measurements were accomplished in citrate buffer, so that the free copper migrated whereas copper associated with liposomes stayed on the baseline. Figure 3 shows the radio-TLCs of the reaction mixture (A) as well as of the liposome fractions after the purification (B). It can be seen, that the copper in the reaction mixture existed almost exclusively in the free form (Figure 3, A, Reg #2), whereas the amount of copper associated with the liposomes is very small (Figure 3, A, Reg #1). After purification via SEC, the amount of copper was no longer detectable via radio-TLC (Figure 3, B), indicating that copper can successfully be separated from the liposomes via SEC and that it is not retained by the liposomes.

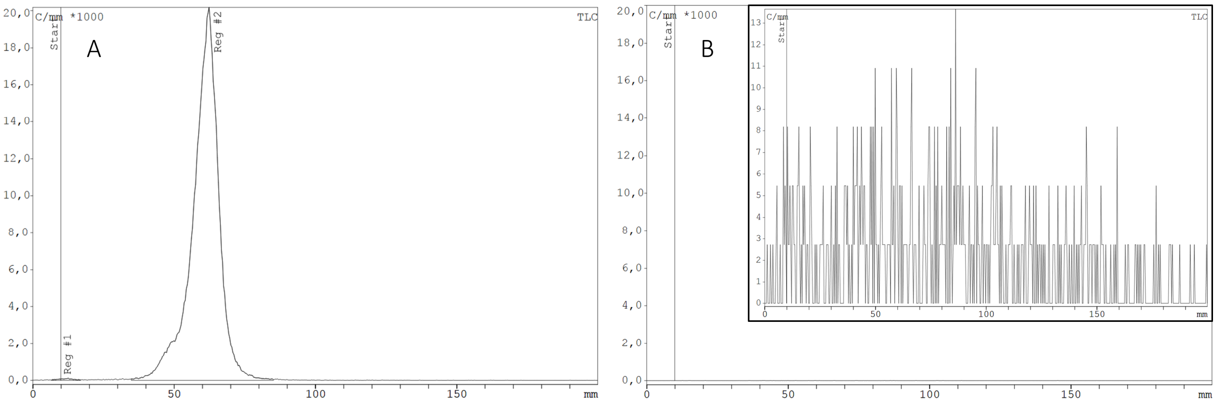

Figure 3. A: radio-TLC of the reaction mixture of the CuAAC between BisHD-*hb*PG$_{32}$-alkyne and F-TEG-N$_3$ using [^{64}Cu]Cu(NO$_3$)$_2$ as catalyst, reaction time 10 min, Reg #1 corresponds to ^{64}Cu associated with liposomes, Reg #2 attributes to free ^{64}Cu. B: radio-TLC of the liposome containing sample after SEC purification, black box: smaller scaling of y-axis.

To verify this hypothesis, gamma spectrometry was accomplished. Combined liposome containing fractions (fraction 3-5) after SEC as well as a sample containing the same amount of [^{64}Cu]Cu(II) nitrate that was used for the CuAAC (100 % value) were measured in a gamma detector. Figure 4 shows the acquired spectra (not corrected for time or distance to the detector).

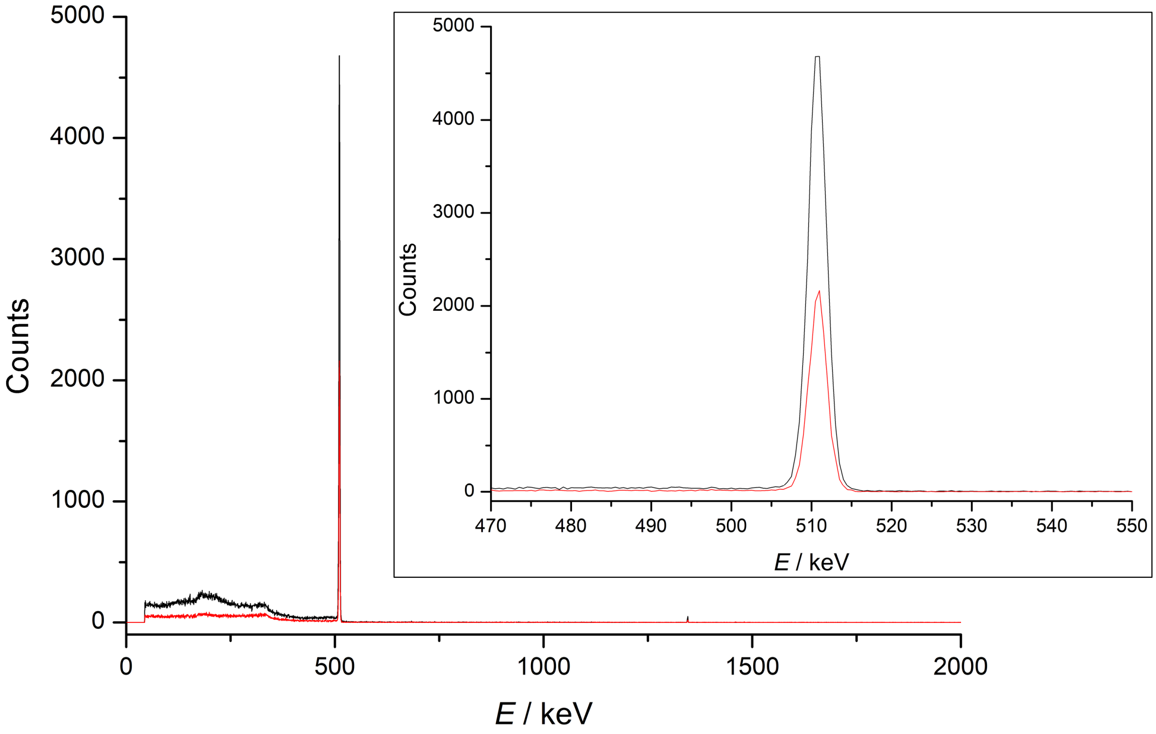

Figure 4. Gamma spectra of the combined liposome containing fractions (fraction 3-5) after SEC (red) and of a sample containing the same amount of [^{64}Cu]Cu(II) nitrate that was used for the CuAAC (black), a discriminator threshold was set for energies below 44 keV, box: zoomed in on the photopeak at an energy of 511 keV.

For both samples, the expected photopeak at an energy of 511 keV, derived from annihilation photons, is clearly visible. Counts below 511 keV arise from Compton scattering and represent the Compton continuum. The small peak at 1346 keV stems from a gamma emission subsequent to an electron capture and is characteristic for ^{64}Cu. For the sample containing the 100 % value an activity of 2.35±0.04 MBq was calculated, whereas the calculated value for the liposome-containing sample was 0.429±0.008 kBq. These values can directly be compared to each other, revealing, that only 0.018±0.001 % of the copper was still present in the liposome containing fraction after SEC purification. Since the absolute amount of copper added was 953 ng (15 µmol), this refers to a total amount of copper of 0.17 ng. For humans dietary reference values for Cu range between 0.9 to 2 mg per day in different countries[8], so that the residual 0.17 ng of copper are absolutely uncritical in terms of an application *in vivo*.

^{18}F-labeling of liposomes with [^{18}F]F-TEG-N$_3$ via CuAAC

Subsequently, first attempts to radiolabel the liposomes with [^{18}F]F-TEG-N$_3$ (see Figure 5) to investigate the yield of the CuAAC were accomplished. It can be seen from Figure 6 that the reaction proceeded fast until it reached a plateau of about 25 % after 5 min. The highest RCY of 27.4 % was reached after 10 min of reaction time. Compared to the radiolabeling of the polyether lipid alone with [^{18}F]F-TEG-N$_3$, which gave quantitative RCYs after 10 min, the first attempt to radiolabel the liposomes directly was less effective. This is most probably caused by the proportionally lower concentration of the alkyne-bearing polyether lipids, which has several reasons. Firstly, during liposome formation, not all of the added polyether lipids become part of the liposomes, secondly, only fraction 4 of the three liposome containing fractions (fraction 3-5 after purification) was used for in this experiment and thirdly, the polyether lipids are non-homogeneously distributed in the reaction mixture, when they are part of the liposomes. Increasing the concentration of the polyether lipids by either increasing the liposome concentration in the reaction mixture or increasing the polyether lipid content of the liposomes should lead to an increase of the RCY of the CuAAC. DLS measurements of the liposomes before and after the CuAAC revealed that the liposomes did not change in size, ensuring that the liposomes stayed intact during the CuAAC. Underlying data are provided in the Supporting Information (Figure S5).

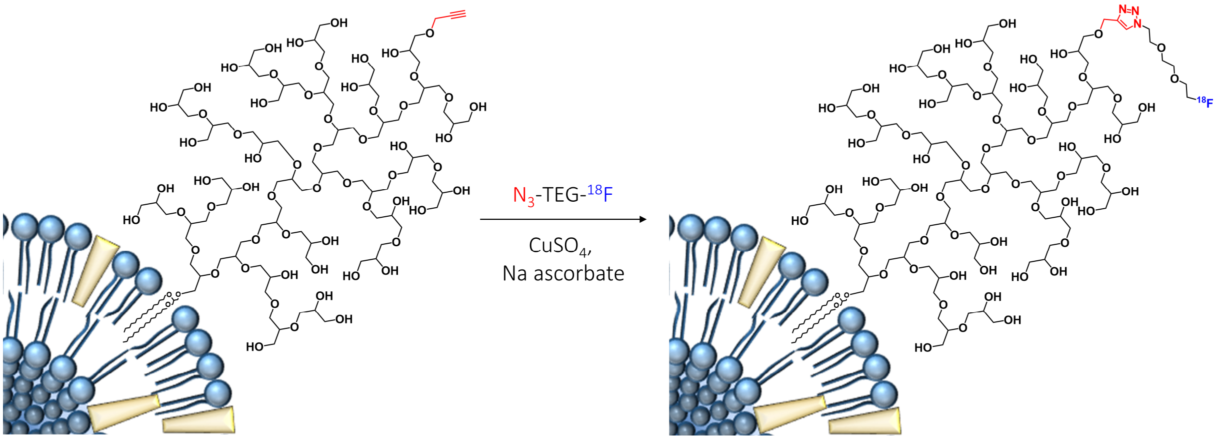

Figure 5. Reaction between liposomes containing BisHD-*hb*PG$_{32}$-alkyne and [^{18}F]F-TEG-N$_3$ via CuAAC.

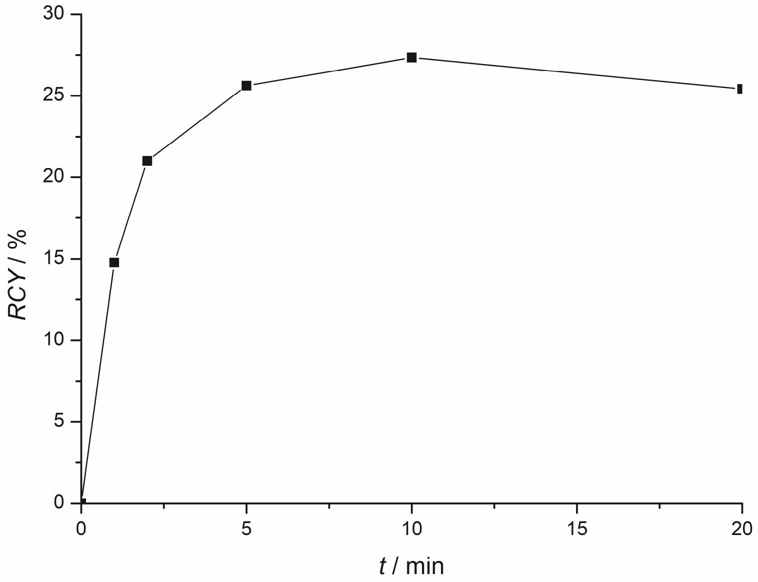

Figure 6. Reaction kinetics of the radiolabeling of BisHD-*hb*PG$_{32}$-alkyne-containing liposomes with [^{18}F]F-TEG-N$_3$ via CuAAC.

Conclusion

The CuAAC is a powerful reaction to be used in the radiolabeling of DDSs such as liposomes. However, the applied copper needs to be separated prior to an application *in vivo* because of its toxicity. But is SEC suitable for a quantitative removal of copper or is there a fraction that is retained by the liposomes? In the present study, we used gamma spectrometry to investigate this very question. In order to track the added copper, the CuAAC between liposomes containing BisHD-*hb*PG_{32}-alkyne and F-TEG-N_3 was done with [^{64}Cu]Cu(II) nitrate. Studies revealed that only 0.018 % of the added radioactivity was still present in the liposome containing fractions after purification via SEC. This refers to a total amount of copper of 0.17 ng which is absolutely uncritical in terms of an application *in vivo* (human dietary reference values for Cu range between 0.9 to 2 mg per day)[8]. The above question can therefore be answered in the following way: Yes, in our case, SEC is suitable for a quantitative removal of copper and no, copper is not retained by the liposomes. Subsequent attempts to radiolabel liposomes directly with [^{18}F]F-TEG-N_3 gave RCY up to 27.4 % after 10 min, which should be improvable by either increasing the liposome concentration in the reaction mixture or increasing the polyether lipid content of the liposomes. The possibility to radiolabel liposomes directly, instead of radiolabel components, remove copper and do the liposome formation afterwards, significantly simplifies the radiosynthesis, which saves time, enables a higher amount of radioactivity per volume and results in a lesser radiation exposure for the experimentalist.

Beyond that particular study on the fate of copper during CuAAC-assisted radiolabeling of liposomes, the experimental methodology may be applied to study many other CuAAC reactions, used for the synthesis of radiolabeled or non-radioactive species, which are intended for human applications. The utilization of a ^{64}Cu-spiked Cu catalyst, in the same amount as for the “normal” CuAAC, will then easily reveal the specific amount of copper, remaining after each purification step. The detection of ^{64}Cu radioactivity will allow for the easy quantification of even very small amounts of copper, which may be hardly to measure by conventional analytical methods and without manipulating or destroying the sample.

Acknowledgment

The authors are very grateful to the Max-Planck Graduate Center (MPGC, K. Wagener) as well as to the DFG in the context of the SFB 1066 for financial support. K. Wagener and M. Schinnerer and M. Worm are members of the graduate school of the SFB 1066.

References

(1) Kettenbach, K.; Schieferstein, H.; Ross, T. L. ^{18}F-Labeling Using Click Cycloadditions. *Biomed Res. Int.* 2014, *2014*, Article ID 361329.

(2) Meyer, J.-P.; Adumeau, P.; Lewis, J. S.; Zeglis, B. M. Click Chemistry and Radiochemistry: The First 10 Years. *Bioconjug. Chem.* 2016, *27*, 2791–2807.

(3) Nwe, K.; Brechbiel, M. W. Growing Applications of “Click Chemistry” for Bioconjugation in Contemporary Biomedical Research. *Cancer Biother. Radiopharm.* 2009, *24*, 289–302.

(4) Bock, V. D.; Hiemstra, H.; Van Maarseveen, J. H. Cu^{I}-Catalyzed Alkyne-Azide “Click” Cycloadditions from a Mechanistic and Synthetic Perspective. *European J. Org. Chem.* 2006, *2006*, 51–68.

(5) Ross, T. L. The Click Chemistry Approach Applied to Fluorine-18. *Curr. Radiopharm.* 2010, *3*, 202–223.

(6) Kolb, H. C.; Finn, M. G.; Sharpless, K. B. Click Chemistry: Diverse Chemical Function from a Few Good Reactions. *Angew. Chemie Int. Ed.* 2001, *40*, 2004–2021.

(7) Marik, J.; Sutcliffe, J. L. Click for PET: rapid preparation of [^{18}F]fluoropeptides using Cu^{I} catalyzed 1,3-dipolar cycloaddition. *Tetrahedron Lett.* 2006, *47*, 6681–6684.

(8) Bost, M.; Houdart, S.; Oberli, M.; Kalonji, E.; Huneau, J.-F.; Margaritis, I. Dietary copper and human health: Current evidence and unresolved issues. *J. Trace Elem. Med. Biol.* 2016, *35*, 107–115.

(9) Turnlund, J. R. Human whole-body copper metabolism. *Am. J. Clin. Nutr.* 1998, *67*, 960S–964S.

(10) Cerchiaro, G.; Manieri, T. M.; Bertuchi, F. R. Analytical methods for copper, zinc and iron quantification in mammalian cells. *Metallomics* 2013, *5*, 1336–1345.

(11) Wagener, K.; Worm, M.; Pektor, S.; Schinnerer, M.; Thiermann, R.; Miederer, M.; Frey, H.; Rösch, F. Comparison of Linear and Hyperbranched Polyether Lipids for Liposome Shielding by ^{18}F-Radiolabeling and Positron Emission Tomography. *Biomacromolecules* 2018, dx.doi.org/10.1021/acs.biomac.8b00115.

(12) Gaetke, L. M.; Chow, C. K. Copper toxicity, oxidative stress, and antioxidant nutrients. *Toxicology* 2003, *189*, 147–163.

(13) Reibel, A. T.; Müller, S. S.; Pektor, S.; Bausbacher, N.; Miederer, M.; Frey, H.; Rösch, F. Fate of Linear and Branched Polyether-Lipids In Vivo in Comparison to Their Liposomal Formulations by ^{18}F-Radiolabeling and Positron Emission Tomography. *Biomacromolecules* 2015, *16*, 842–851.

(14) Carneiro De Sousa, F. N.; Eichholz, G. G. Dosimetry of Gamma Rays from Nitrogen-16 Decay. *Int. J. Appl. Radiat. Isot.* 1985, *36*, 981–984.

(15) Tahir, S. N. A.; Chettle, D. R. Identification of oxygen-19 during *in vivo* neutron activation analysis of water phantoms. *Physiol. Meas.* 2015, *36*, N127–N134.

(16) Bé, M.-M.; Chisté, V.; Dulieu, C.; Browne, E.; Chechev, V.; Kuzmenko, N.; Helmer, R.; Nichols, A.; Schönfeld, E.; Dersch, R. *Table of Radionuclides (Vol. 1 - A = 1 to 150)*; Le Bureau International des Poids et Mesures: Sèvres, 2004.

(17) Horen, D. J.; Meyerhof, W. E. Decay of Copper-66. *Phys. Rev.* 1958, *111*, 559–561

Supplementary Data

Copper-catalyzed click reactions: Quantification of retained copper using ^{64}Cu-spiked Cu(I), exemplified for CuAAC reactions on liposomes

Karolin Wagener[1], Dennis Renisch[1], Meike Schinnerer[2], Matthias Worm[3], Yvonne Jakob[1], Klaus Eberhardt[1], Frank Rösch[1]

[1]Institute of Nuclear Chemistry, Johannes Gutenberg University, Fritz-Strassmann-Weg 2,
55128 Mainz, Germany

[2]Institute of Physical Chemistry, Johannes Gutenberg University, Jakob-Welder-Weg 11,
55128 Mainz, Germany

[3]Institute of Organic Chemistry, Johannes Gutenberg University, Duesbergweg 10-14,
55128 Mainz, Germany

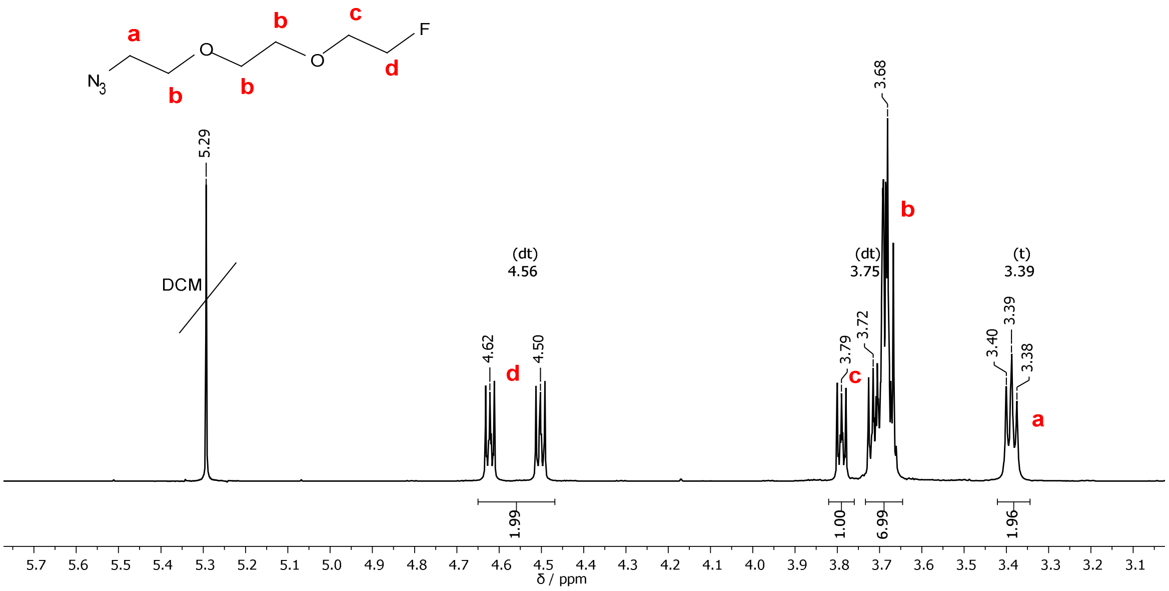

Figure S1. ^{1}H-NMR spectrum of F-TEG-N_3.

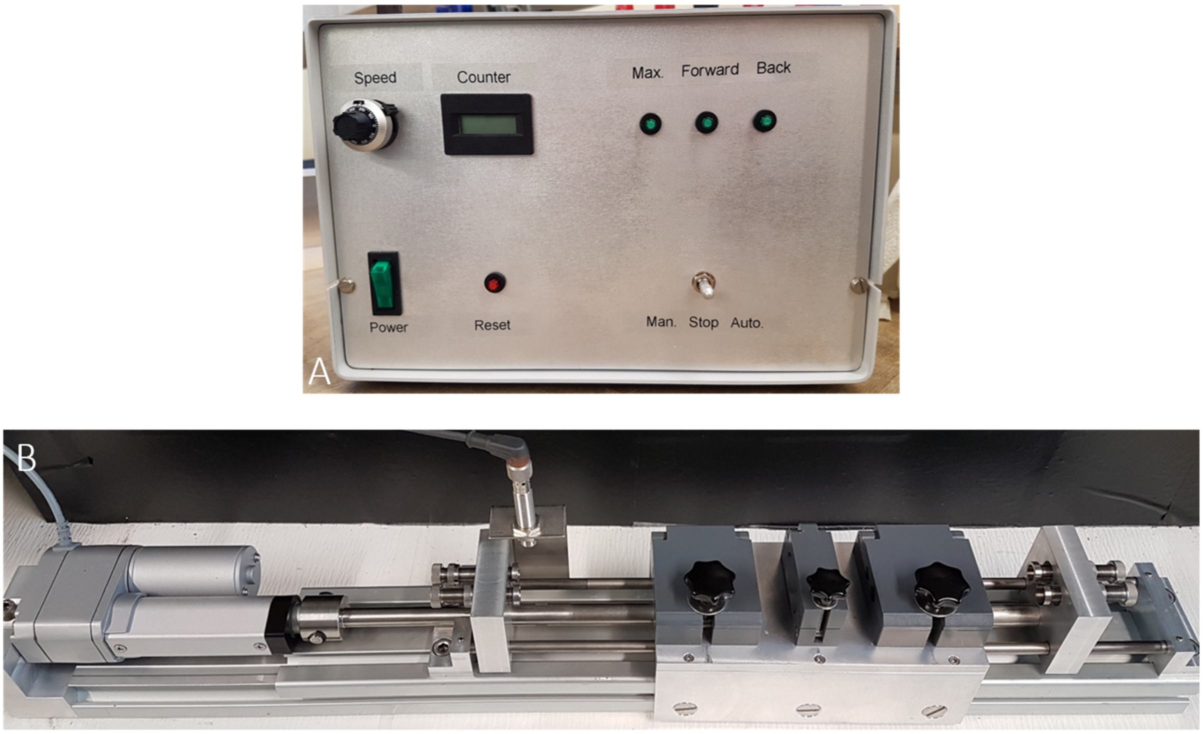
Speed
Counter
Max.
Forward
Back
Power
Reset
Man.
Stop
Auto.
A
B

Figure S2. Custom-built, automatic extrusion device (B) with separate control unit (A).

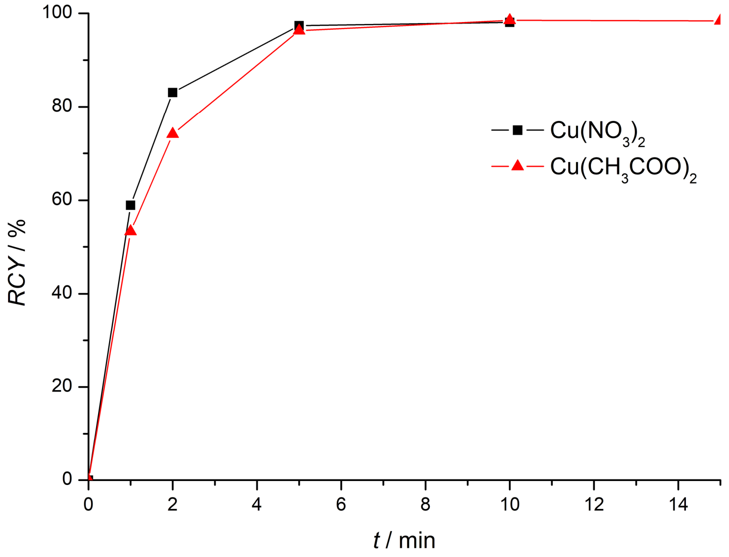

Figure S3. Reaction kinetics of the radiolabeling of BisHD-*hb*PG$_{32}$-alkyne with [^{18}F]F-TEG-N$_3$ via CuAAC. Black curve: using Cu(NO$_3$)$_2$, red curve: using Cu(CH$_3$COO)$_2$.

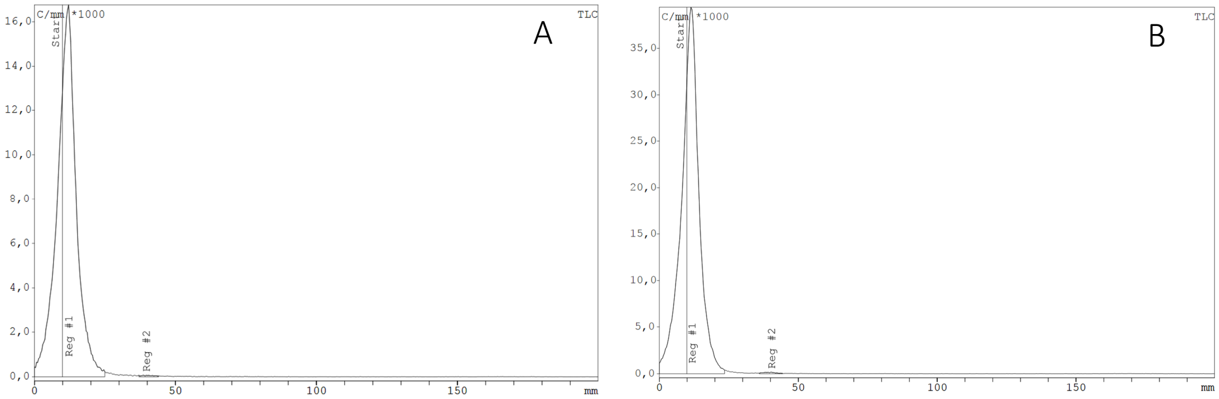

Figure S4. Radio-TLCs of the radiolabeling of BisHD-*hb*PG$_{32}$-alkyne with [^{18}F]F-TEG-N$_3$ via CuAAC. A: using Cu(NO$_3$)$_2$, reaction time 10 min, RCY 98 %, B: using Cu(CH$_3$COO)$_2$, reaction time 10 min, RCY 98 %. Reg #1 corresponds to the ^{18}F-labeled polyether lipid, Reg #2 attributes to [^{18}F]F-TEG-N$_3$.

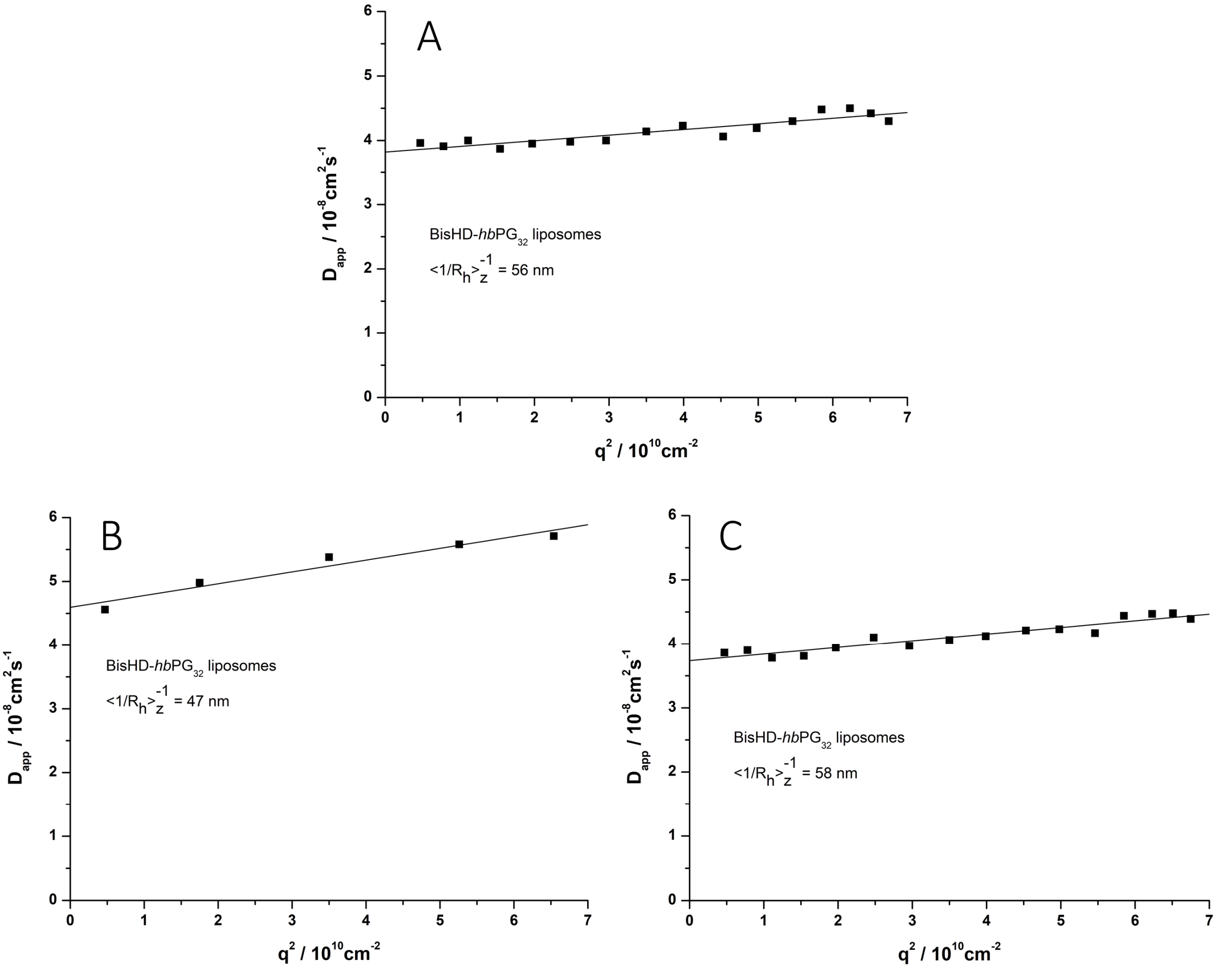

Figure S5. D_{app} plotted against q^2 data and thereof calculated hydrodynamic radii of BisHD-*hb*PG$_{32}$-shielded liposomes after their formation (A), after the CuAAC with non-radioactive F-TEG-N$_3$ using [^{64}Cu]Cu(NO$_3$)$_2$ (B) and after the radiolabeling with [^{18}F]F-TEG-N$_3$ via CuAAC (C).

3.4 Targeting of Immune Cells with Trimannosylated Liposomes

Karolin Wagener[1], Matthias Krumb[2], Jens Langhanki[2], Matthias Bros[3], Stefanie Pektor[4], Matthias Worm[2], Meike Schinnerer[5], Matthias Miederer[4], Holger Frey[2], Till Opatz[2], Frank Rösch[1]

[1]Institute of Nuclear Chemistry, Johannes Gutenberg University, Fritz-Strassmann-Weg 2,
55128 Mainz, Germany

[2]Institute of Organic Chemistry, Johannes Gutenberg University, Duesbergweg 10-14,
55128 Mainz, Germany

[3]Clinical Research Unit Allergology, Department of Dermatology, University Medical Center,
Langenbeckstraße 1, 55101 Mainz, Germany

[4]Clinic and Polyclinic of Nuclear Medicine, University Medical Center, Langenbeckstraße 1,
55101 Mainz, Germany

[5]Institute of Physical Chemistry, Johannes Gutenberg University, Jakob-Welder-Weg 11,
55128 Mainz, Germany

Abstract

Dentritic cells (DCs) are a compelling target in cancer immunotherapy, as they initialize all antigen-specific immune responses. Drug delivery systems, such as liposomes, provide the opportunity to deliver antigens and immunostimulatory molecules to DCs and thereby to initiate an antigen-specific immune response. To address predominantly dendritic cells, the drug delivery systems need to be equipped with DC-specific targeting vectors. This study evaluates liposomes, bearing the oligosaccharide trimannose on their surface, regarding their ability to address DCs *in vivo*. Trimannose as a saccharidic structure is known to be recognized by receptors on the surface of DCs. To obtain trimannosylated liposomes, azide-bearing trimannose was coupled to alkyne-functionalized hyperbranched polyglycerol (*hb*PG) with a bis(hexadecyl)glycerol (BisHD) anchor in a Cu(I)-catalyzed alkyne-azide cycloaddition (CuAAC). In order to enable tracking of the liposomes *in vivo*, the trimannosylated BisHD-*hb*PG lipids were radiolabeled with ^{18}F in a CuAAC. Subsequently, liposomes were produced via the thin-film hydration method followed by extrusion. The behavior of the trimannosylated liposomes was evaluated in *in vivo* µPET and *ex vivo* biodistribution studies in healthy, male C57BL/6 mice and the results were compared to similar liposomes bearing no trimannose on their surface.

Introduction

Dendritic cells (DCs) are professional antigen-presenting cells, which are capable of initiating and shaping an immune response upon stimulation.[1] Firstly discovered in 1973 by Steinman and Cohn[2], it was not before the early 1990s, when methods where developed, by which DCs can readily be generated from progenitors in sufficient amounts.[3–5] In their immature state, DCs are present in most tissues, with an increased abundance at body surfaces like skin and pharynx and internal or mucosal surfaces like the respiratory and gastro-intestinal tract.[6,7] Another subset, called plasmacytoid DCs, is located in lymphoid organs such as spleen, bone marrow and lymph nodes.[8] Immature DCs are extremely efficient in capturing antigens. Exogenous pathogens are taken up via receptor-mediated endocytosis and phagocytosis, which initializes the activation on a DC. In an early phase of DC activation, the antigen uptake capacity is up-regulated, followed by down-regulation. Subsequently, the surface expression of antigen-loaded class II major histocompatibility complexes and costimulatory receptors is up-regulated. At the same time, the DC migrates to lymphoid tissues. Upon arrival, it sequentially contacts numerous T cells. Due to the presence of costimulatory molecules, antigen-specific T cells are activated. Fully activated CD8+ T cells, termed cytotoxic T lymphocytes are able to recognize and kill antigen-presenting infected and malignant cells.[9] In contrast, activated CD4+ T cells polarize towards different so-called T helper cell populations, which contribute to both CD8+ T cell and B cell activation.[10] By this, both a cellular and a humoral adaptive immune response are initiated.

The unique ability of DCs to stimulate even naive T cells, makes them a very interesting target for an active cancer immunotherapy, which aims to destroy tumor cells with the help of the immune system. On this view, administration of tumor-specific antigens plus adjuvants to DCs is intended to induce a tumor-specific immune response, which aims to destroy both the primary tumor and metastases. To date, this approach remains challenging, as its success not only depends on the effective delivery of carefully selected tumor antigens, but also on the overcoming of several mechanisms that mediate immune tolerance.[11] An initial step that may result in a suboptimal immune response, is an insufficient activation of DCs, caused by a poor delivery of adjuvants. Furthermore, the amount of antigens delivered might be too low, in order to result in an antigen-specific immune response. Drug delivery systems (DDSs) have the potential to overcome these problems, since large numbers of antigens and activating molecules can effectively by transported within these systems. With regard to clinical implementation, one of the most successful types of DDSs are liposomes.[12] These spherical vesicles are biodegradable, have an excellent biocompatibility and exhibit a low toxicity, since phospholipids as their main components are also the building blocks of cellular membranes.[13] The linkage of hydrophilic polymers to these phospholipids results in liposomes with a shielding polymer shell on their surface. These so-called stealth liposomes show a prolonged retention in the blood as the polymer shell prevents detection by the mononuclear phagocytic system (MPS) via steric repulsion.[14]

However, in order to deliver antigens as well as adjuvants to a DC, suitable targeting vectors are needed to address DCs. These targeting vectors can be coupled to the surface of DDSs by which the antigens and DC-activating molecules are transported. Saccharidic structures, especially mannose-rich structures, are promising targeting vectors as they are recognized by receptors on the surface of DCs.[15,16] To date, several of these glycan-binding receptors are known, among them the macrophage mannose receptor, dectin-1, dendritic cell-specific ICAM-3 grabbing nonintegrin (DC-SIGN) and langerin, expressed in different cells of the immune system.[17] Although each receptor type binds mannose-containing structures, their different morphology causes individual recognition profiles for different structures. The macrophage mannose receptor, for instance, is rather adapted for the recognition of end-standing single mannose or a dimannoside cluster, whereas the tetrameric DC-SIGN, which is highly expressed on dendritic cells and only very restrictedly on macrophages[18], has a higher affinity for branched mannoside structures with short spacing between the residues.[19] Drickamer and coworkers showed that the branched mannose (Man)-rich oligosaccharide $Man_9GlcNAc_2$ binds 130-fold more tightly to DC-SIGN than mannose.[20] Crystal structures of carbohydrate-recognition domains of DC-SIGN bound to oligosaccharides revealed that the trimannose core structure Manα1-3[Manα1-6]Manα (present twice in the afore mentioned Man$_9$GlcNAc$_2$) is important for the binding.[21] Furthermore, Feinberg *et al*. suggested that multiple modes of binding enhance the affinity for DC-SIGN.[22] In fact, liposomes, coated with multiple trimannose molecules on their surface, gave promising results in cell studies on DCs.[23,24]

Thus, we aimed to investigate the potential of stealth liposomes, bearing multiple molecules of the afore mentioned trimannose core structure Manα1-3[Manα1-6]Manα on their surface, to address DCs *in vivo*. The shielding polymer shell of the liposomes consisted of the highly biocompatible and water-soluble hyperbranched polyglycerol (*hb*PG)[25,26], whose anchorage in the lipid bilayer was provided by an 1,2-bis(hexadecyl)glycerol (BisHD) anchor. This multifunctional polyether lipid has recently been investigated by our group and featured a stable anchorage in the lipid bilayer, while corresponding liposomes exhibited a favorable biodistribution with a prolonged circulation in the blood stream.[27] To obtain trimannosylated liposomes, (1-(2-(2-(2-(2-azidoethoxy)ethoxy)ethoxy)ethyl)-1*H*-1,2,3-triazole-4-yl)methoxy)-3,6-di-O-α-D-mannopyranosyl-α-D-mannopyranoside (trimannose azide) was reacted with alkyne$_4$-BisHD-*hb*PG$_{63}$ in a copper-catalyzed alkyne-azide cycloaddition reaction (CuAAC). To track the liposomes *in vivo*, the trimannosylated polyether lipids were radiolabeled with the prosthetic group 1-azido-2-(2-(2-[^{18}F]fluoroethoxy)ethoxy)ethane ([^{18}F]F-TEG-N$_3$) via CuAAC, resulting in an [^{18}F]F-TEG-triazole ([^{18}F]FTT) group. Similar non-mannosylated polyether lipids were ^{18}F-radiolabeled in the same manner, to enable a comparison. For future cells studies, the trimannosylated polyether lipids were also labeled with the fluorescent dye Oregon Green 488 (OG 488). Subsequently, liposomes were manufactured via thin-film hydration followed by automated extrusion. Figure 1 depicts trimannosylated liposomes labeled with fluorescent dye and ^{18}F, respectively. Finally, *in vivo* µPET and *ex vivo* organ distribution studies were performed in healthy, male C57BL/6 mice , in order to investigate the fate of both, polyether lipids and the respective liposomal formulations.

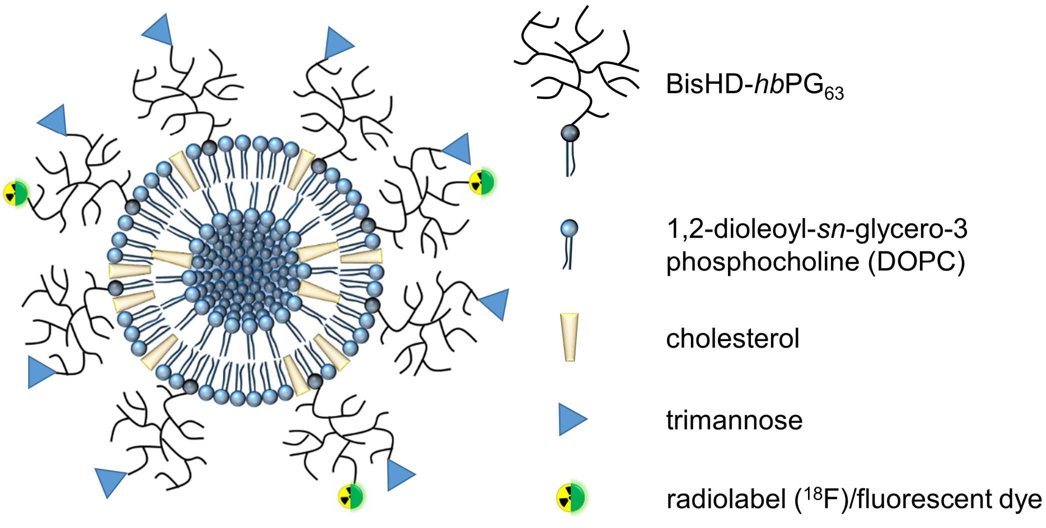
BisHD-*hb*PG$_{63}$
1,2-dioleoyl-*sn*-glycero-3 phosphocholine (DOPC)
cholesterol
trimannose
radiolabel (^{18}F)/fluorescent dye

Figure 1. Illustration of the investigated trimannosylated liposomes with fluorescent label and radiolabel. The polymer chains inside the liposome are omitted for clarity, and the illustration is not drawn to scale.

Results and discussion

Organic syntheses and radiosyntheses

In a previous work, we aimed at elucidating the *in vivo* behavior of liposomes shielded by dialkyl-based polyether lipids.[27] As a main result of this work, it emerged, that the liposomes stay intact and circulate in the blood over the investigated period of 4 h. Thus, it was evident to apply a targeting vector as a next step, which should be the aforementioned trimannose, in order to address DCs. For this purpose, the already evaluated alkyne$_4$-BisHD-*hb*PG$_{63}$[27] was an ideal choice, since it exhibited four alkyne functionalities, allowing for a simultaneous linkage of trimannose and of a radiolabel to track the system *in vivo*. To this end, we synthesized [^{18}F]FTT-trimannose-alkyne-BisHD-*hb*PG$_{63}$ following the synthesis routes illustrated in Scheme 1. For future cell studies, trimannose-alkyne-BisHD-*hb*PG$_{63}$, labeled with the fluorescent dye OG 488, was synthesized as well. In the first step, alkyne$_4$-BisHD-*hb*PG$_{63}$ was functionalized with trimannose azide in a CuAAC. The usage of two equivalents of trimannose azide resulted in a degree of functionalization of 1.5, revealed by diffusion-ordered NMR spectroscopy (Figure S28 in the Supporting Information). Due to the difference in size between trimmanose azide and alkyne$_4$-BisHD *hb*PG$_{63}$, purification via spin filtration purification worked straightforwardly and time-efficiently. Subsequently, functionalization with OG 488 was accomplished via CuAAC as well. In contrast to the functionalization with trimmanose, which required only small amounts of DMSO, the reaction had to be carried out in a 1:1 mixture of water/DMSO due to the poor solubility of OG 488 in an aqueous environment. Dialysis of the reaction mixture against water enabled the removal of DMSO, which would have damaged the subsequently used spinfilter. Since the lipophilic fluorescent dye forms micelles with the amphiphilic polyether lipids, the spinfiltration had to be carried out many times (18x), in order to reach an appropriate separation (UV-Vis spectra of the final concentrate as well as of representative filtrates are provided in the Supporting Information, Figure S29).

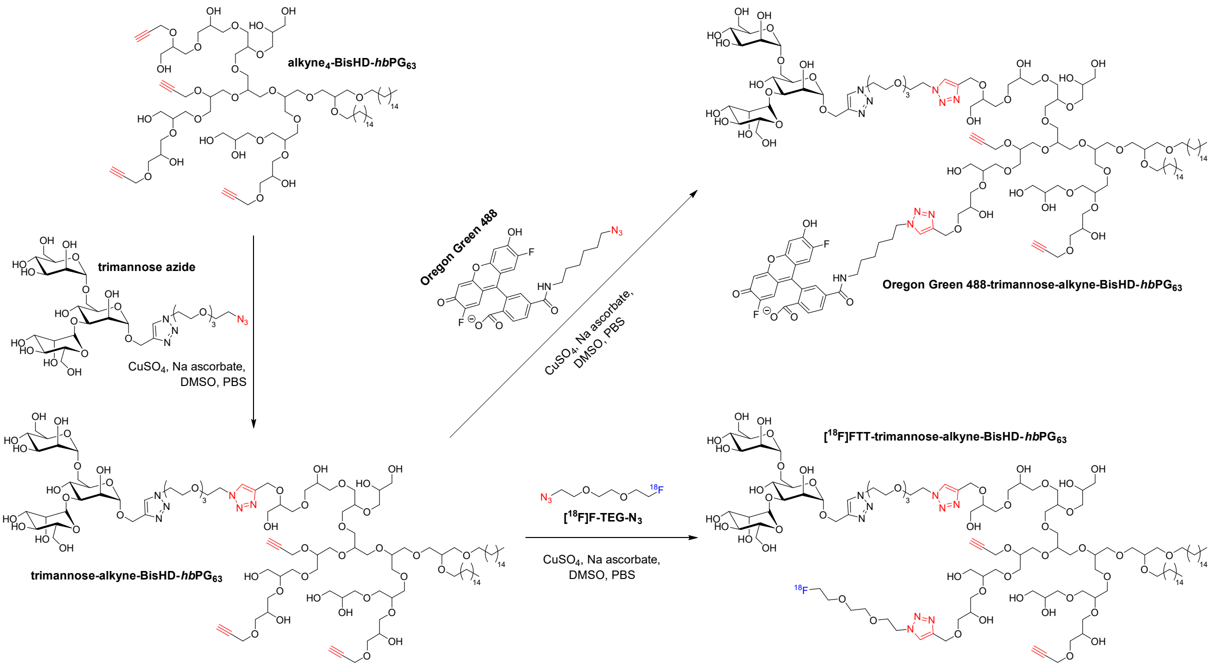
alkyne$_4$-BisHD-*hb*PG$_{63}$
trimannose azide
CuSO$_4$, Na ascorbate, DMSO, PBS
Oregon Green 488
CuSO$_4$, Na ascorbate, DMSO, PBS
Oregon Green 488-trimannose-alkyne-BisHD-*hb*PG$_{63}$
trimannose-alkyne-BisHD-*hb*PG$_{63}$
[^{18}F]F-TEG-N$_3$
CuSO$_4$, Na ascorbate, DMSO, PBS
[^{18}F]FTT-trimannose-alkyne-BisHD-*hb*PG$_{63}$

Scheme 1. Synthesis route of [^{18}F]FTT-trimannose-alkyne-BisHD-*hb*PG$_{63}$ and of OG 488-trimannose-alkyne-BisHD-*hb*PG$_{63}$. Alkyne$_4$-BisHD-hbPG$_{63}$ without trimannose-label was radio- and fluorescence-labeled in the same manner.

To enable *in vivo* tracking of trimannose-alkyne-BisHD-*hb*PG$_{63}$ and respective liposomes, trimannose-alkyne-BisHD-*hb*PG$_{63}$ was radiolabeled with [^{18}F]F-TEG-N$_3$ in a CuAAC. The required [^{18}F]F-TEG-N$_3$ was prepared by nucleophilic fluorination of Ts-TEG-N$_3$ using a semi-automatic custom modular system in yields up to 91 %. The synthesis is described in detail in previous reports.[27,28] The subsequent radiolabeling of trimannose-alkyne-BisHD-*hb*PG$_{63}$ via CuAAC proceeded reliably in radiochemical yields (RCYs) exceeding 95 % after 10 min (Figure S30 in the Supporting Information). Reaction conditions were adopted from the radiolabeling of alkyne$_4$-BisHD-*hb*PG$_{63}$, specified in a previous report.[27] Radiolabeling and fluorescence labeling of alkyne$_4$-BisHD-*hb*PG$_{63}$ was accomplished in the same manner as for its trimannosylted counterpart (Figure S29 and S30 in the Supporting Information).

Liposome formation and characterization

Liposomes were manufactured by the thin film hydration method followed by repeated extrusion through polycarbonate membranes with pore diameters of 400 nm, then 100 nm, then 50 nm. The extrusion was performed with the help of an automatic extrusion device described in a previous report[27], which allows for a reproducible pressure during the extrusion process and has a separate control module. Via this automatization, it was possible to obtain liposomes with reproducible sizes (see below). Furthermore, the separate control module allows for remote control of the extrusion device and therefore considerably reduces the radiation exposure for the experimentalist. After the extrusion, liposomes were separated from non-integrated lipids via size exclusion chromatography (SEC) with phosphate-buffered saline (PBS) as mobile phase. Liposomes eluted in the fractions 3-5.

The size of the liposomes was determined via DLS, when ^{18}F-radioactivity (^{18}F has an half-life of 109.7 min)[29] had ceased (~18 h). Alkyne$_4$-BisHD-*hb*PG$_{63}$-shielded (5 mol%) liposomes exhibited a hydrodynamic radius R_h of 94 nm, whereas liposomes shielded with trimannose-alkyne-BisHD-*hb*PG$_{63}$ (5 mol%) showed an R_h value of 109 nm (DLS data are provided in Figure S31 in the Supporting Information). Furthermore, storage stability experiments were conducted, indicating that the liposomes are stable at least over a period of one month (Figure S32 in the Supporting Information).

Animal studies

In vivo µPET studies

To investigate the in vivo fate of the trimannosylated versus the non-mannosylated polyether lipids and their corresponding liposomal formulations, µPET studies were conducted in healthy, male C57BL/6 mice. Dynamic scans of 1 h were started at the time of injection in order to follow the initial distribution. For the liposomal formulations also static scans of 30 min were run 3.5 h after injection to gain information regarding pharmacokinetics at later stages. Figure 2 shows coronal, whole-body maximum intensity projections (MIPs) of the polyether lipids [^{18}F]FTT-alkyne-BisHD-*hb*PG$_{63}$ and [^{18}F]FTT-trimannose-alkyne-BisHD-*hb*PG$_{63}$. Shortly after injection, both polyether lipids show an initial uptake in the bloodstream (0-3 min) and subsequently undergo renal excretion. As expected, after 1 h they are both mainly found in the bladder, since the molecular weight of both polyether lipids is below the renal threshold and the large hydrophilic polyether block prevents a hepatobiliary excretion. However, despite the competing renal excretion, small differences in liver and spleen uptake can be observed, as [^{18}F]FTT-trimannose-alkyne-BisHD-*hb*PG$_{63}$ exhibits a higher uptake in the mentioned organs than the non-mannosylated [^{18}F]FTT-alkyne-BisHD-*hb*PG$_{63}$.

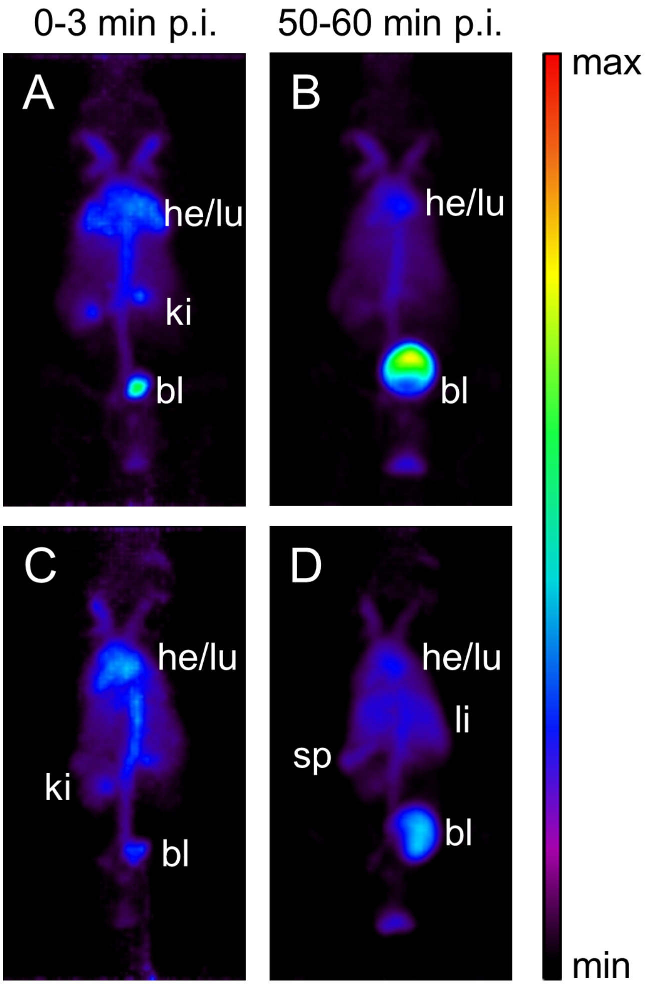

Figure 2. Coronal, whole-body MIPs of different time frames for [^{18}F]FTT-alkyne-BisHD-*hb*PG$_{63}$ (A & B) and [^{18}F]FTT-trimannose-alkyne-BisHD-*hb*PG$_{63}$ (C & D). he: heart, lu: lung, bl: bladder, ki: kidney, sp: spleen, li: liver.

In contrast, the liposomal formulations behaved fundamentally different from the non-associated polyether lipids. Figure 3 shows coronal, whole-body MIPs of liposomes shielded by [^{18}F]FTT-alkyne-BisHD-*hb*PG$_{63}$ or by [^{18}F]FTT-trimannose-alkyne-BisHD-*hb*PG$_{63}$ at different times after injection. Both liposome types initially (0-3 min) circulate in the blood stream, which can be seen from the fact that the activity is located in well perfused organs, such as heart and lung. Yet, the trimannosylated liposomes already exhibit a significant uptake in the spleen (Figure 3D), which is missing for the non-mannosylated liposomes (Figure 3A). After 60 min the difference is considerably more pronounced. For the non-mannosylated liposomes, the activity is still mainly found in the blood stream with some uptake in the spleen (Figure 3B), which can be attributed to a partial detection by the MPS. After 4 h, the liver and spleen uptake become dominant, but one can still see activity in well perfused organs like heart and lung (Figure 3C), revealing that a fraction of the liposomes is continuously circulating in the blood. The situation with the mannosylated liposomes is completely different. Here, already after 1 h almost no circulation in the blood stream is observable, instead there is an accumulation in the liver and a strong accumulation in the spleen (Figure 3E). This effect has intensified after 4 h, so that the activity can now only be found in liver and especially in the spleen (Figure 3F). We assign this differences directly to the trimannose moieties on the surface of the liposomes, since the investigated liposomal formulations had similar hydrodynamic radii around 100 nm and possessed the same composition besides the trimannose label. Further details concerning the PET data are provided in the Supporting Information (Figure S33 and S34).

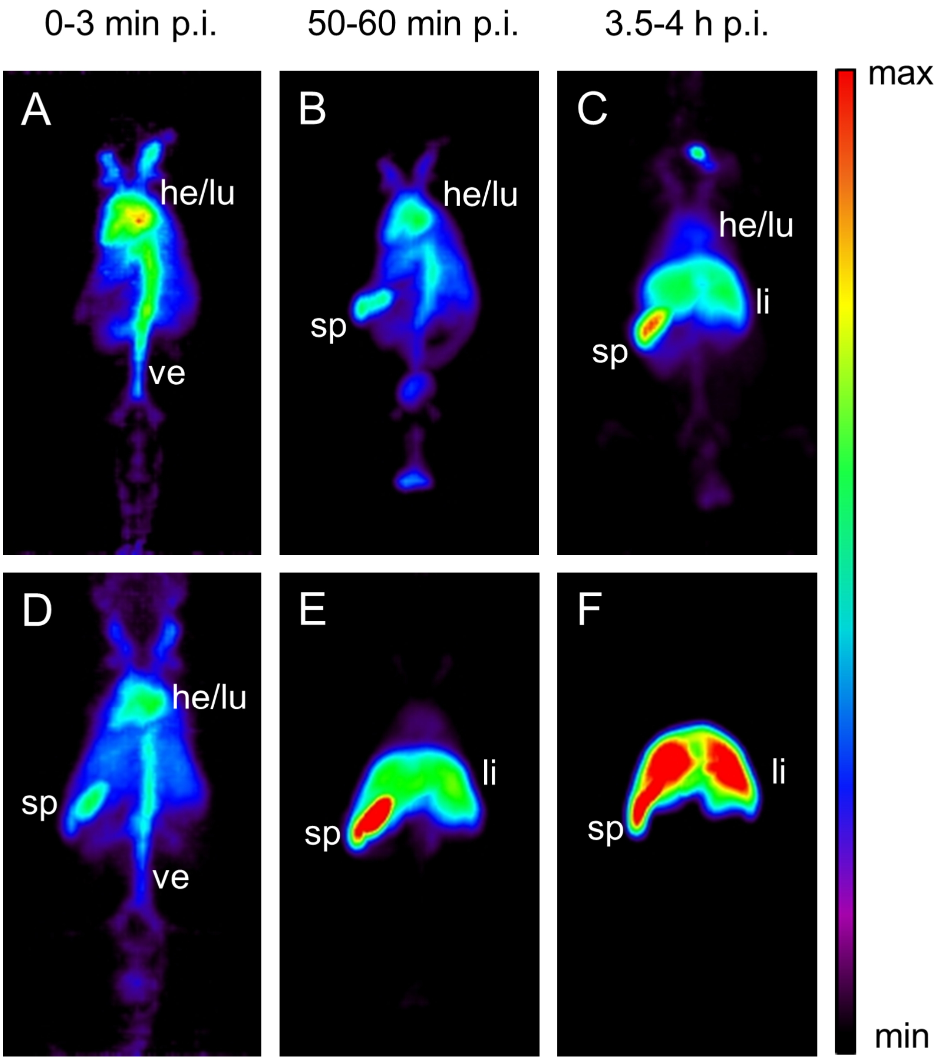

Figure 3. Coronal, whole-body MIPs at different time points (left column: 0-3 min p.i., middle column: 50-60 min p.i., right column: 3.5-4 h p.i.) for [^{18}F]FTT-alkyne-BisHD-*hb*PG$_{63}$ liposomes (A, B, C) and for [^{18}F]FTT-trimannose-alkyne-BisHD-*hb*PG$_{63}$ liposomes (D, E, F). he: heart, lu: lung, ve: vein, sp: spleen, li: liver.

Ex vivo biodistribution studies

Ex vivo biodistribution studies were performed in order to gain quantitative conclusions regarding the *in vivo* accumulation of the ^{18}F-labeled compounds in different organs. Figure 4 shows the results for the non-mannosylated in comparison to the mannosylated polyether lipids (underlying data are provide in Table S1 in the Supporting Information).

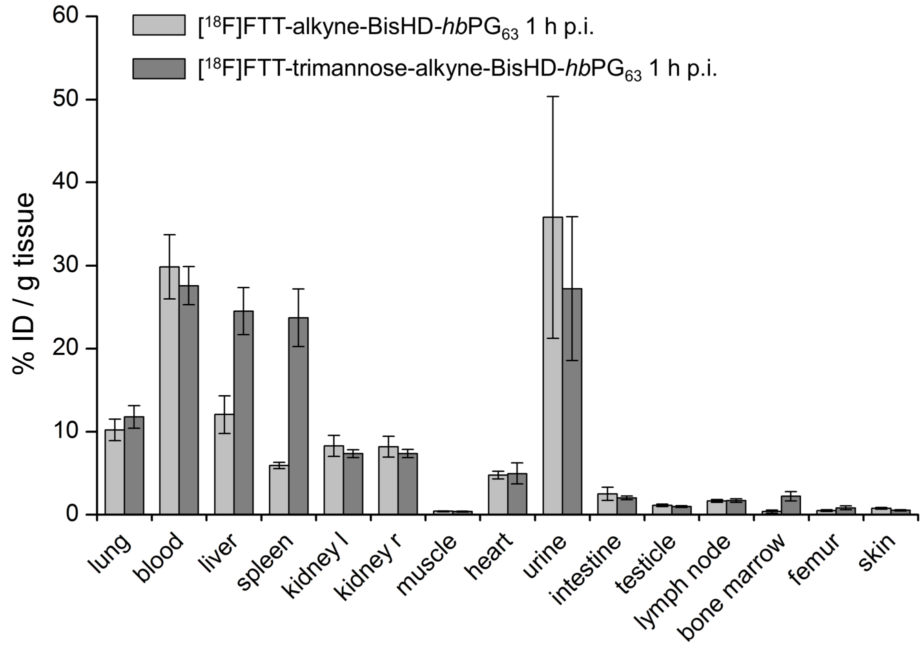

Figure 4. *Ex vivo* biodistribution data 1 h p.i of the polyether lipids [^{18}F]FTT-alkyne-BisHD-*hb*PG$_{63}$ and [^{18}F]FTT-trimannose-alkyne-BisHD-*hb*PG$_{63}$ (n=5, each).

From Figure 4 it can be seen that after 1 h [^{18}F]FTT-alkyne-BisHD-*hb*PG$_{63}$ is mainly found in the urine (35.8±14.6 % ID / g tissue) and in the blood (29.8±3.9 % ID / g tissue), which confirms that it circulates in the blood stream until it is excreted via the renal pathway. [^{18}F]FTT-trimannose-alkyne-BisHD-*hb*PG$_{63}$ also circulates in the blood (27.6±2.3 % ID / g tissue) and is then excreted in the urine (27.2±8.7 % ID / g tissue). However, in contrast to its non-mannosylated counterpart, it has a significantly higher uptake in liver (24.5±2.9 versus 12.1±2.3 % ID / g tissue, factor 2), spleen (23.7±3.5 versus 5.9±0.4 % ID / g tissue, factor 4) and bone marrow (2.2±0.6 versus 0.4±0.2 % ID / g tissue, factor 5.5) after 1 h. These findings reveal, that the trimannose structure leads to an altered biodistribution. Despite a competing renal excretion, the mannosylated polyether lipids are increasingly taken up into lymphatic organs, where dendritic cells are located, which is not the case for the non-mannosylated polyether lipids.

The results of the *ex vivo* biodistribution studies of the corresponding liposomal formulations are shown in Figure 5 (underlying data are provide in Table S1 in the Supporting Information). Here it is directly visible that already 1 h after the injection the mannosylated liposomes are almost exclusively present in liver (87.7±20.0 % ID / g tissue) and especially in the spleen (128.7±18.7 % ID / g tissue). After 4 h the situation has not changed much, only blood and lung uptake have halved, whereas lymph node and bone marrow uptake doubled. Still, uptake in liver (82.7±9.8 % ID / g tissue) and spleen (140.2±12.6 % ID / g tissue) is most prominent. The non-mannosylated liposomes show a different biodistribution. After 1 h a significant amount of the liposomes is located in the blood (43.9±2.8 % ID / g tissue). Another major part of the activity can be found in liver

(19.6±3.5 % ID / g tissue) and spleen (51.7±4.5 % ID / g tissue). After 4 h liver and spleen uptake doubled, whereas the uptake in the blood halved. We ascribe this pattern to a recognition by the MPS over time. In summary, the non-mannosylated liposomes circulate in the blood until they are recognized by the MPS and enriched in liver and spleen. The mannosylated liposomes, on the other hand, immediately accumulate in the liver and especially in the spleen and widely disappear from the blood after just 1 h. In comparison, this results in an 8.3-fold decreased accumulation in the blood, a 4.5-fold increased accumulation in the liver and a 2.5-fold increased accumulation in the spleen after 1 h for the mannosylated liposomes. These findings clearly prove a significant influence of the trimannose on the *in vivo* fate of the liposomes. We tentatively ascribe this to a recognition of the trimannosylated liposomes by DCs, obviously paired with a recognition by the MPS. Future cell studies will shed light on the distribution of the investigated systems in different murine splenic immune cells.

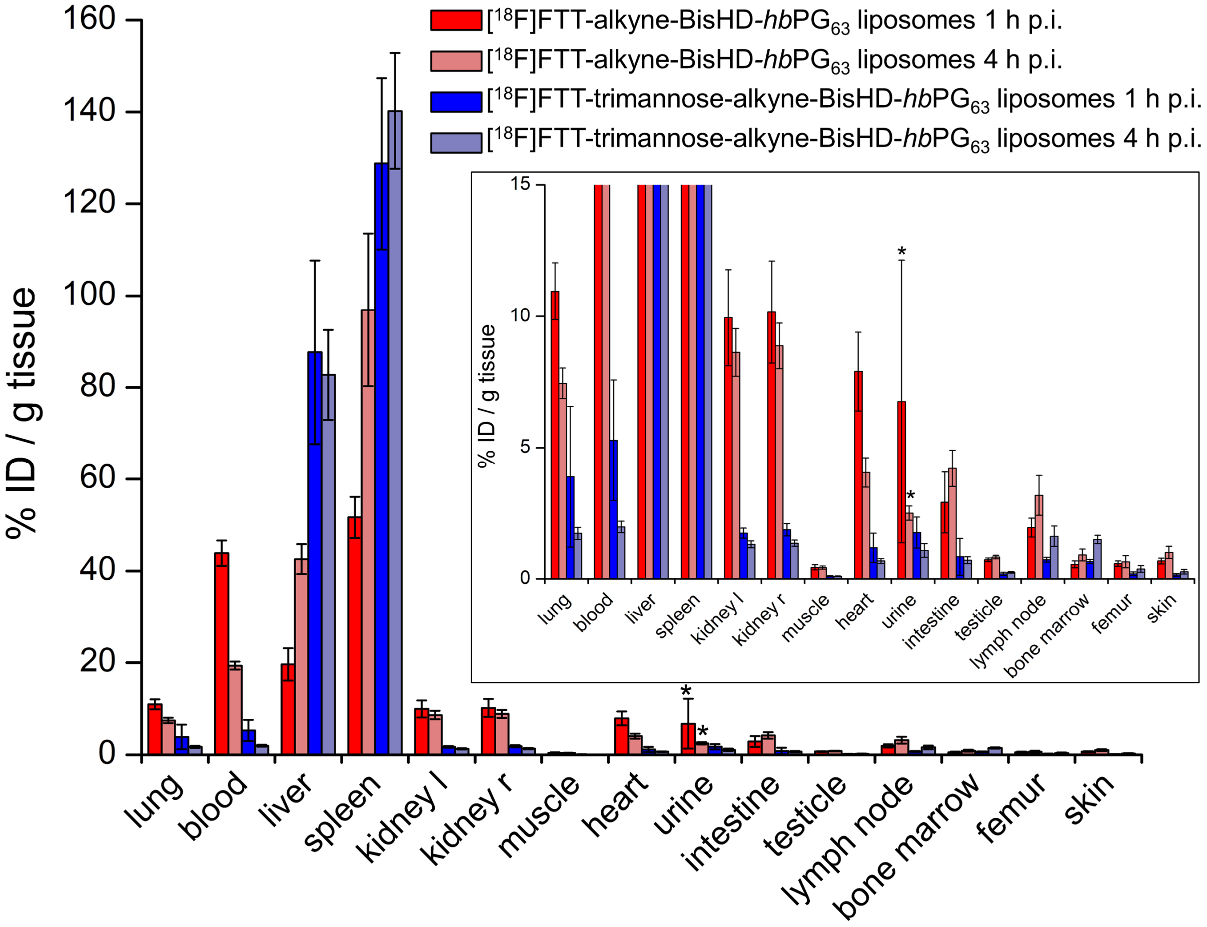

Figure 5. *Ex vivo* biodistribution data 1 h p.i. and 4 h p.i. of [^{18}F]FTT-alkyne-BisHD-*hb*PG$_{63}$ liposomes and of [^{18}F]FTT-trimannose-alkyne-BisHD-*hb*PG$_{63}$ liposomes (n=5, for each time point and each liposome type). Asterisks indicate n=4. Box: zoomed in on % ID / g tissue values below 15.

Concusion

In this study, the fate of mannosylated and similar non-mannosylated polyether lipids and their respective liposomal formulations was investigated, utilizing radioactive labeling with ^{18}F and subsequent *in vivo* µPET and *ex vivo* biodistribution studies in mice. It was found that the mannosylated polyether lipids increasingly accumulated in liver, spleen and bone marrow, compared to the non-mannosylated polyether lipids. For the liposomal formulations, this effect was even more pronounced. To the best of our knowledge, this is the first report demonstrating, the influence of trimannose moieties, as active targeting vectors to DCs, on the distribution of liposomes *in vivo*. We tentatively ascribe these differences to a recognition of the trimannose moieties by DCs, which are located particularly in spleen and bone marrow and also to some extent in the liver. This is in accordance with earlier cell studies, which revealed, that the trimannose structure is bound by DCs.[23,24] However, it cannot be excluded that other antigen-presenting cells besides DCs may also be targeted. Therefore, cell studies on murine splenic immune cells via fluorescence-activated cell sorting (FACS), using the OG 488-labeled polyether lipids and respective liposomal formulations, are planned in the near future to find out which cell types are addressed particularly and to which extent.

Experimental section

Materials: All chemicals were obtained from common chemical suppliers such as Sigma Aldrich, TCI Europe, VWR or Acros Organics unless stated otherwise. OG 488 azide was purchased from Click Chemistry Tools. Deuterated pyridine-d_5 was purchased from Deutero GmbH. Particle-free phosphate-buffered saline (PBS) enabling exact light scattering experiments was obtained from Gibco™ by Thermo Fisher Scientific. Spin filtration was done with Microsep Advance centrifugal filters (molecular weight cut-off: 1 kDa; Pall). Dialysis was accomplished using Spectra/Por® 7 dialysis tubing (molecular weight cut-off: 1 kDa, material: regenerated cellulose; Spectrum). $[^{18}F]F^{-}_{aq}$ was produced by irradiation of enriched $[^{18}O]H_2O$ with protons at a PETtrace 700S cyclotron (GE Healthcare). A common production run lasted 30 min at a beam current of 25 µA, yielding an ^{18}F-activity of 20 GBq.

Characterization: ^{1}H NMR and DOSY spectra of the polymer lipids were measured either on a Bruker Avance III HD 400 MHz (5 mm BBFO SmartProbe and SampleXPress 60 auto sampler) or on a Bruker Avance II 400 MHz (5 mm BBFO probe and SampleXPress 60 auto sampler) at 23 °C. All spectra were processed with MestReNova v11.0 software. DOSY spectra were analyzed using MestReNova Bayesian DOSY Transform. Coupling constants (*J*) are reported in Hertz (Hz) (splitting abbreviations: s, singlet; d, doublet; t, triplet; q, quartet; m, multiplet; br, broad; and combinations thereof).

UV-Vis spectra were acquired on a V-630 UV-Vis spectrophotometer (Jasco), using quartz cuvettes with a layer thickness of 10 mm. Samples of purified polyether lipids were diluted with water (1:1) prior to the measurement. Filtrates of the spin filtration were measured without dilution. Analyzation was carried out with Spectra Manager (version 2.04; Jasco).

For multi-angle DLS cylindrical quartz cuvettes (Hellma Analytics, Mühlheim, Germany) were cleaned with dust-free distilled acetone and transferred to a dust free flow box. Solutions were diluted 1:100 with PBS and filtered into the cuvettes through Millex-LCR filters, 0.45 µm pore size (Merck Millipore). DLS measurements were performed by the following instruments at 20 °C. Apparatus 1 consists of a Uniphase He/Ne Laser (22.5 mW output power at λ = 632.8 nm) and an ALV/CGS-8F SLS/DLS 5022F goniometer with eight simultaneously working ALV 7004 correlators and eight ALV/High QEAPD avalanche photodiode detectors. Apparatus 2 consists of a Uniphase He/Ne Laser (22.5 mW output power at λ = 632.8 nm), an ALV/SP125 goniometer with an ALV 5000/E/PCI correlator and an ALV/High QEAPD Avalanche photodiode detector. The correlation functions of the particles were fitted biexponentially. The z-average diffusion coefficient D_z was calculated by extrapolating D_{app} for q = 0. By formal application of Stokes law, the inverse z-average hydrodynamic radius is $R_h = \langle R_h^{-1} \rangle_z^{-1}$. The experimental uncertainties are estimated to ±2 % for R_h.

Radio-thin-layer chromatographys (radio-TLCs) were run on silica-coated aluminum-backed TLC plates (Merck) using EA/Hex 1:1 as mobile phase. The chromatograms, acquired on a RITA detector (Raytest), were analyzed using Gina Star TLC software (Raytest).

Synthesis of (1-(2-(2-(2-(2-azidoethoxy)ethoxy)ethoxy)ethyl)-1H-1,2,3-triazole-4-yl)methoxy)-3,6-di-O-α-d-mannopyranosyl-α-d-mannopyranoside (trimannose azide): Experimental procedures as well as characterization data are provided in the Supporting Information (Scheme S1-S3 and Figure S1-S26).

Synthesis of alkyne$_4$-1,2-bis(hexadecyl)glycerol-hbPG$_{63}$ (alkyne$_4$-BisHD-hbPG$_{63}$): The synthesis protocol was described in a previous report.[27]

Synthesis of trimannose-alkyne-1,2-bis(hexadecyl)glycerol-hbPG$_{63}$: Alkyne$_4$-BisHD-*hb*PG$_{63}$(18 mg, 3.4 µmol, 1 eq.) was dissolved in 1 ml of PBS. Subsequently, a solution of trimannose azide (5 mg, 6.7 µmol, 2 eq.) in 1 ml PBS, DMSO (25 µl), $CuSO_4$ (30 µl, 1 M in MilliQ water, 30 µmol) and sodium ascorbate (50 µl 2.4 M in PBS, 120 µmol) were added in this order. The mixture was stirred at room temperature for 12 h under argon atmosphere. Purification was accomplished by spin filtration (30 min, 4696 *g*). The concentrate was washed 10 times with 1 ml of MilliQ water, which was added to the concentrate and then centrifuged again (15 min, 4696 *g*). Lyophilization gave the desired product as a brownish solid (22.5 mg, 1.5 × trimannose per BisHD-*hb*PG$_{63}$, calculated from ^{1}H NMR spectroscopy (Figure S27 in the Supporting Information). ^{1}H NMR (400 MHz, pyridine-d_5) δ (ppm) = 8.18 (s, br, 3H,

$H_{triazole}$, $H'_{triazole}$), 5.91 (s, br, 1.5H, H-1‘$_{trimannose}$), 5.60 (s, br, 1.5H, H-1$_{trimannose}$), 5.33 (s, br, 1.5H, H-1‘‘$_{trimannose}$), 4.91–3.30 (m, 359H, all others), 1.74–1.58 (m, 4H, CH_2-CH_2-O_{BisHD}), 1.51–1.36 (m, 4H, CH_2-CH_2-CH_2-O_{BisHD}), 1.36–1.18 (m, 48H, $CH_{2\ BisHD}$), 0.87 (t, 6H, J_{AB} = 6.6 Hz, CH_3-$CH_{2\ BisHD}$).

Synthesis of OG 488-trimannose-alkyne-1,2-bis(hexadecyl)glycerol-hbPG$_{63}$ and OG 488-alkyne-1,2-bis(hexadecyl)glycerol-hbPG$_{63}$: Both compounds were synthesized according to the same procedure. The synthesis of OG 488-alkyne-BisHD-*hb*PG$_{63}$ is described as an example. Alkyne$_4$-BisHD-*hb*PG$_{63}$ (3 mg, 0.6 µmol, 1 eq.) was dissolved in 0.5 ml of PBS. Subsequently, a solution of OG 488 azide (0.5 mg, 0.8 µmol, 1.4 eq.) in 0.5 ml DMSO, $CuSO_4$ (15 µl, 1 M in MilliQ water, 15 µmol) and sodium ascorbate (25 µl, 2.4 M in PBS, 60 µmol) were added in this order. The orange mixture was stirred at room temperature for 12 h protected from light under argon atmosphere. Purification was accomplished by dialysis against water (3 × 600 ml) followed by spin filtration (30 min, 4696 *g*). The concentrate was washed 10 times with 2 ml of MilliQ/ethanol 9:1, then 8 times with 2 ml MilliQ, which was added to the concentrate and then centrifuged again (15 min, 4696 *g*). Lyophilization gave the desired product as a brownish solid (2.9 mg). The successful linkage of the fluorescent dye and the separation of unbound dye was determined by UV-Vis spectroscopy. The respective spectra are provided in the Supporting Information (Figure S29)

Synthesis of 2-(2-(2-Azidoethoxy)ethoxy)ethyl-p-toluenesulfonate (Ts-TEG-N$_3$): The synthesis was accomplished according to published procedures.[28]

Radiosynthesis of 1-Azido-2-(2-(2-[^{18}F]fluoroethoxy)ethoxy)ethane. [^{18}F]F-TEG-N_3 was synthesized on a semiautomatic custom modular system with radiochemical yields (RCY) up to 91 % (TLC, EA/nHex 1:1, R_f: 0.8) according to a previous report.[28]

Radiosynthesis of [^{18}F]FTT-trimannose-alkyne-1,2-bis(hexadecyl)glycerol-hbPG$_{63}$ and [^{18}F]FTT-alkyne 1,2-bis(hexadecyl)glycerol-hbPG$_{63}$: The radiolabeling procedure for alkyne$_4$-BisHD-*hb*PG$_{63}$ is described in a previous report.[27] Trimannose-alkyne-BisHD-*hb*PG$_{63}$ was radiolabeled equally.

Liposome Formation: Liposomes were prepared by the thin film hydration method followed by several extrusion steps. Liposome components were 1,2-dioleoyl-*sn*-glycero-3-phosphocholine (DOPC), cholesterol and fluorescent/radiolabeled BisHD polyether (OG 488-trimannose-alkyne-BisHD-*hb*PG$_{63}$, OG 488-alkyne-BisHD-*hb*PG$_{63}$, [^{18}F]FTT-trimannose-alkyne-BisHD-*hb*PG$_{63}$ or [^{18}F]FTT-alkyne-BisHD-*hb*PG$_{63}$) at molar ratios of 55:40:5 mol%. M_n values, determined by ^{1}H NMR spectroscopy, were used to calculate the lipid compositions. A solution of DOPC in ethanol, cholesterol in ethanol and the fluorescent labeled/radiolabeled polyether lipid were blended, and the solvent was evaporated in a miniature rotating evaporator to obtain a thin film of the liposome components. 0.8 ml of PBS were added. The liposome suspension was sonicated at 50 °C for 10 min, followed by automated extrusion through polycarbonate membranes with different pore diameters (400 nm, then 100 nm, then 50 nm, 21 times each) using a Mini-Extruder (AVESTIN Europe GmbH) driven by a custom-built device[27]. Finally, the liposomes were purified via size exclusion chromatography (SEC) using Sephacryl S-400 HR as a resin (~4 ml packed in a 6 ml empty SPE tube with 20 µm PTFE frits at top and bottom) and PBS as a mobile phase. Fractions of 0,5 ml were collected. Liposomes eluted in the fractions 3-5.

Animal Studies: Male C57BL/6 mice (Janvier Labs; body weight: 22.4±1.7 g; age: 6-8 weeks) housed in the animal care facility of the University of Mainz were used in this study. The anesthetization of the animals was accomplished using an isoflurane vaporizer, where 2.5 % of isoflurane were admixed with air. Anesthetized animals were injected with 5.29±0.56 MBq of the respective radiolabeled compound in 100-150 µl of PBS via a tail vein (PET animals) or retroorbital (biodistribution animals). The applied masses for the non-associated polyether lipids were <0.030 mg for [^{18}F]FTT-alkyne-BisHD-*hb*PG$_{63}$ and <0.88 mg for [^{18}F]FTT-trimannose-alkyne-BisHD-*hb*PG$_{63}$. For the corresponding liposomal formulations the applied masses were <0.055 mg for [^{18}F]FTT-alkyne-BisHD-*hb*PG$_{63}$ and <0.061 mg for [^{18}F]FTT-trimannose-alkyne-BisHD-*hb*PG$_{63}$. All experiments had previously been approved by the regional animal ethics committee and were conducted in accordance with the German Law for Animal Protection and the UKCCCR Guidelines.[30]

PET scans were run on a microPET Focus 120 (Siemens). For the dynamic PET scans of 1 h data acquisition was started at the time of injection. For the 3.5 to 4 h static PET scans the mice were anesthetized for the injection, but were awake in the timespan between injection and PET scan. During the PET scan the animals lay in a head first prone position. The list mode data files were reconstructed using a filtered-backprojection reconstruction algorithm. The reconstruction was done using ASIPro 1.2. software. AMIDE software was utilized for image processing purposes. To accomplish the analysis of the PET data PMOD 3.6 software was used.

In order to assess the distribution of the radiolabeled compounds in different organs, injected animals (n=5, per time point and per polyether lipid or liposome) were sacrificed after 1 h or 4 h and organs of interest were collected. The tissue samples were weighed and the radioactivity in the samples was measured in a γ-counter (2470 WIZARD^2 Automatic Gamma Counter, PerkinElmer).

Acknowledgements

Special thanks go to [redacted] for scientific support and helpful discussions regarding NMR spectroscopy of the investigated compounds. We are also very grateful to the Max-Planck Graduate Center (MPGC, K. Wagener, M. Worm) as well as to the DFG in the context of the SFB 1066 for financial support. K. Wagener, M. Krumb, J. Langhanki, M. Worm and M. Schinnerer are members of the graduate school of the SFB 1066.

References

(1) Banchereau, J.; Steinman, R. M. Dendritic cells and the control of immunity. *Nature* 1998, *392*, 245–252.

(2) Steinman, R. M.; Cohn, Z. A. Identification of a Novel Cell Type in Peripheral Lymphoid Organs of Mice. I. Morphology, Quantitation, Tissue Distribution. *J. Exp. Med.* 1973, *137*, 1142–1162.

(3) Inaba, K.; Inaba, M.; Romani, N.; Aya, H.; Deguchi, M.; Ikehara, S.; Muramatsu, S.; Steinman, R. M. Generation of Large Numbers of Dendritic Cells from Mouse Bone Marrow Cultures Supplemented with Granulocyte/Macrophage Colony-Stimulating Factor. *J. Exp. Med.* 1992, *176*, 1693–1702.

(4) Caux, C.; Dezutter-Dambuyant, C.; Schmitt, D.; Banchereau, J. GM-CSF and TNF-α cooperate in the generation of dendritic Langerhans cells. *Nature* 1992, *360*, 258–261.

(5) Romani, N.; Gruner, S.; Brang, D.; Kämpgen, E.; Lenz, A.; Trockenbacher, B.; Konwalinka, G.; Fritsch, P. O.; Steinman, R. M.; Schuler, G. Proliferating Dendritic Cell Progenitors in Human Blood. *J. Exp. Med.* 1994, *180*, 83–93.

(6) Lipscomb, M. F.; Masten, B. J. Dendritic Cells: Immune Regulators in Health and Disease. *Physiol. Rev.* 2002, *82*, 97–130.

(7) Steinman, R. M.; Banchereau, J. Taking dendritic cells into medicine. *Nature* 2007, *449*, 419–426.

(8) Larsson, M.; Beignon, A.-S.; Bhardwaj, N. DC-Virus Interplay: A Double Edged Sword. *Semin. Immunol.* 2004, *16*, 147–161.

(9) Berg, R. E.; Forman, J. The role of CD8 T cells in innate immunity and in antigen non-specific protection. *Curr. Opin. Immunol.* 2006, *18*, 338–343.

(10) Luckheeram, R. V.; Zhou, R.; Verma, A. D.; Xia, B. CD4 $^+$ T Cells: Differentiation and Functions. *Clin. Dev. Immunol.* 2012, *2012*, Article ID 925135.

(11) Makkouk, A.; Weiner, G. J. Cancer Immunotherapy and Breaking Immune Tolerance: New Approaches to an Old Challenge. *Cancer Res.* 2015, *75*, 5–10.

(12) Bulbake, U.; Doppalapudi, S.; Kommineni, N.; Khan, W. Liposomal Formulations in Clinical Use: An Updated Review. *Pharmaceutics* 2017, *9*, 12.

(13) Akbarzadeh, A.; Rezaei-Sadabady, R.; Davaran, S.; Joo, S. W.; Zarghami, N.; Hanifehpour, Y.; Samiei, M.; Kouhi, M.; Nejati-Koshki, K. Liposome: Classification, Preparation, and Applications. *Nanoscale Res. Lett.* 2013, *8*, 102.

(14) Pattni, B. S.; Chupin, V. V.; Torchilin, V. P. New Developments in Liposomal Drug Delivery. *Chem. Rev.* 2015, *115*, 10938–10966.

(15) Holla, A.; Skerra, A. Comparative analysis reveals selective recognition of glycans by the dendritic cell receptors DC-SIGN and Langerin. *Protein Eng. Des. Sel.* 2011, *24*, 659–669.

(16) Figdor, C. G.; van Kooyk, Y.; Adema, G. J. C-Type Lectin Receptors on Dendritic Cells and Langerhans Cells. *Nat. Rev. Immunol.* 2002, *2*, 77–84.

(17) McGreal, E. P.; Miller, J. L.; Gordon, S. Ligand recognition by antigen-presenting cell C-type lectin receptors. *Curr. Opin. Immunol.* 2005, *17*, 18–24.

(18) Soilleux, E. J.; Morris, L. S.; Leslie, G.; Chehimi, J.; Luo, Q.; Levroney, E.; Trowsdale, J.; Montaner, L. J.; Doms, R. W.; Weissman, D.; Coleman, N.; Lee, B. Constitutive and induced expression of DC-SIGN on dendritic cell and macrophage subpopulations in situ and in vitro. *J. Leukoc. Biol. 71*, 445–457.

(19) Irache, J. M.; Salman, H. H.; Gamazo, C.; Espuelas, S. Mannose-targeted systems for the delivery of therapeutics. *Expert Opin. Drug Deliv.* 2008, *5*, 703–724.

(20) Mitchell, D. A.; Fadden, A. J.; Drickamer, K. A Novel Mechanism of Carbohydrate Recognition by the C-Type Lectins DC-SIGN and DC-SIGNR. Subunit Organization and Binding to Multivalent Ligands. *J. Biol. Chem.* 2001, *276*, 28939–28945.

(21) Feinberg, H.; Mitchell, D. A.; Drickamer, K.; Weis, W. I. Structural Basis for Selective Recognition of Oligosaccharides by DC-SIGN and DC-SIGNR. *Science* 2001, *294*, 2163–2166.

(22) Feinberg, H.; Castelli, R.; Drickamer, K.; Seeberger, P. H.; Weis, W. I. Multiple Modes of Binding Enhance the Affinity of DC-SIGN for High Mannose *N*-Linked Glycans Found on Viral Glycoproteins. *J. Biol. Chem.* 2007, *282*, 4202–4209.

(23) Copland, M. J.; Baird, M. A.; Rades, T.; McKenzie, J. L.; Becker, B.; Reck, F.; Tyler, P. C.; Davies, N. M. Liposomal delivery of antigen to human dendritic cells. *Vaccine* 2003, *21*, 883–890.

(24) White, K. L.; Rades, T.; Furneaux, R. H.; Tyler, P. C.; Hook, S. Mannosylated liposomes as antigen delivery vehicles for targeting to dendritic cells. *J. Pharm. Pharmacol.* 2006, *58*, 729–737.

(25) Wilms, D.; Stiriba, S.-E.; Frey, H. Hyperbranched Polyglycerols: From the Controlled Synthesis of Biocompatible Polyether Polyols to Multipurpose Applications. *Acc. Chem. Res.* 2010, *43*, 129–141.

(26) Kasza, G.; Kali, G.; Domján, A.; Pethő, L.; Szarka, G.; Iván, B. Synthesis of Well-Defined Phthalimide Monofunctional Hyperbranched Polyglycerols and Its Transformation to Various Conjugation Relevant Functionalities. *Macromolecules* 2017, *50*, 3078–3088.

(27) Wagener, K.; Worm, M.; Pektor, S.; Schinnerer, M.; Thiermann, R.; Miederer, M.; Frey, H.; Rösch, F. Comparison of Linear and Hyperbranched Polyether Lipids for Liposome Shielding by ^{18}F-Radiolabeling and Positron Emission Tomography. *Biomacromolecules* 2018, dx.doi.org/10.1021/acs.biomac.8b00115.

(28) Reibel, A. T.; Müller, S. S.; Pektor, S.; Bausbacher, N.; Miederer, M.; Frey, H.; Rösch, F. Fate of Linear and Branched Polyether-Lipids in Vivo in Comparison to Their Liposomal Formulations by ^{18}F-Radiolabeling and Positron Emission Tomography. *Biomacromolecules* 2015, *16*, 842–851.

(29) Bé, M.-M.; Chisté, V.; Dulieu, C.; Browne, E.; Chechev, V.; Kuzmenko, N.; Helmer, R.; Nichols, A.; Schönfeld, E.; Dersch, R. *Table of Radionuclides (Vol. 1 - A = 1 to 150)*; Le Bureau International des Poids et Mesures: Sèvres, 2004.

(30) Workman, P.; Aboagye, E. O.; Balkwill, F.; Balmain, A.; Bruder, G.; Chaplin, D. J.; Double, J. A.; Everitt, J.; Farningham, D. A. H.; Glennie, M. J.; Kelland, L. R.; Robinson, V.; Stratford, I. J.; Tozer, G. M.; Watson, S.; Wedge, S. R.; Eccles, S.A. Guidelines for the welfare and use of animals in cancer research. *Br. J. Cancer* 2010, *102*, 1555–1577.

Supplementary Data

Targeting of Immune Cells with Trimannosylated Liposomes

Karolin Wagener[1], Matthias Krumb[2], Jens Langhanki[2], Matthias Bros[3], Stefanie Pektor[4], Matthias Worm[2], Meike Schinnerer[5], Matthias Miederer[4], Holger Frey[2], Till Opatz[2], Frank Rösch[1]

[1]Institute of Nuclear Chemistry, Johannes Gutenberg University, Fritz-Strassmann-Weg 2,
55128 Mainz, Germany

[2]Institute of Organic Chemistry, Johannes Gutenberg University, Duesbergweg 10-14,
55128 Mainz, Germany

[3]Clinical Research Unit Allergology, Department of Dermatology, University Medical Center,
Langenbeckstraße 1, 55101 Mainz, Germany

[4]Clinic and Polyclinic of Nuclear Medicine, University Medical Center, Langenbeckstraße 1,
55101 Mainz, Germany

[5]Institute of Physical Chemistry, Johannes Gutenberg University, Jakob-Welder-Weg 11,
55128 Mainz, Germany

Content

S1. Synthesis and characterization of (1-(2-(2-(2-(2-azidoethoxy)ethoxy)ethoxy)ethyl)-1*H*-1,2,3-triazole-4-yl)methoxy)-3,6-di-*O*-α-D-mannopyranosyl-α-D-mannopyranoside (trimannose azide)

  a. General procedures

  b. Reaction schemes

  c. Synthetic procedures

  d. ^{1}H and ^{13}C NMR spectra

S2. Characterization of trimannose-alkyne-1,2-bis(hexadecyl)glycerol-*hb*PG$_{63}$

S3. Fluorescent labeling with Oregon Green 488 (OG 488) azide

S4. Radiolabeling

  a. Polyether lipids

  b. Removal of copper

S5. Liposome characterization

  a. Liposome size

  b. Liposome stability

S6. Animal studies

  a. Positron emission tomography (PET) studies

  b. Biodistribution studies

References

S1. Synthesis and characterization of (1-(2-(2-(2-(2-azidoethoxy)-ethoxy)ethoxy)ethyl)-1*H*-1,2,3-triazole-4-yl)methoxy)-3,6-di-*O*-α-D-mannopyranosyl-α-D-mannopyranoside (trimannose azide)

a. General procedures

Solvents and Reagents: All chemicals were obtained from common chemical suppliers such as Sigma Aldrich, TCI Europe, VWR or Acros Organics unless stated otherwise. Deuterated solvents were purchased from Deutero GmbH. All reagents were reagent grade and used without further purification unless otherwise noted. Extra dry dimethylformamide (DMF) and pyridine (AcroSeal® glass bottle) were purchased from Acros Organics. Acetonitrile (MeCN) and dichloromethane (DCM) were distilled from calcium hydride. The eluents for column chromatography (cyclohexane and ethyl acetate (EA)) were distilled prior to use. Chloroform-*d* was stored over alumina (Brockmann activity I).

Reactions Conditions: All reactions involving air or moisture sensitive reagents or intermediates were performed under an inert atmosphere of argon in glassware that was oven dried using standard Schlenk techniques. Reaction temperatures referred to the temperature of the particular cooling/heating bath.

Chromatography: Thin-layer chromatography (TLC) was carried out on silica gel 60 F254 plates (Merck) or on RP silica gel RP-18 F254s plates (Merck). UV active compounds were visualized using UV light (λ = 254 nm). Oxidation labile compounds werde visualized by immersion in a solution of cerium(IV) sulfate (1 g) and phosphomolybdic acid (2.5 g) in water (95 ml) and concentrated sulfuric acid (4 ml) followed by heating. Alternatively, the TLC plates were immersed in a solution of *m*-methoxyphenol (0.1 ml) in ethanol (95 ml) and sulfuric acid (2 ml) followed by heating to color carbohydrate compounds specifically.

Chromatography was performed using flash chromatography of the indicated solvent system on 35-70 µm silica gel (Acros Organics) unless otherwise noted. Alternatively, purification was performed on an Isolera™ Flash Purification System (Biotage®) with an integrated diode array detector.

Preparative reverse phase separation was carried out on a Smartline HPLC system (Knauer) with mixtures of acetonitrile or methanol and water as eluents on an ACE 5 C18-PFP, 150 mm×30 mm column (Macherey& Nagel), at a flow rate of 37.5 ml/min. The eluents were degassed prior to use by means of ultrasonication for 30 min. Two Smartline K-1800 pumps (pump head size: 100 ml each, high pressure gradient mode; Knauer) and an S-2600 diode array detector (Knauer) were used.

NMR spectroscopy: NMR spectra were recorded on an Avance III HD 300 (300 MHz ^{1}H NMR, 75 MHz ^{13}C NMR, COSY, HSQC, HMBC; Bruker), an Avance II 400 (400 MHz ^{1}H NMR, 100.6 MHz ^{13}C NMR, COSY, HSQC, HMBC; Bruker), an Avance III HD 400 (400 MHz ^{1}H NMR, 100.6 MHz ^{13}C NMR, COSY, HSQC, HMBC, NOESY; Bruker) or an Avance III 600 (600 MHz ^{1}H NMR, 151 MHz ^{13}C NMR, COSY, TOCSY, HSQC, HMBC, NOESY; Bruker) using 5 mm probe heads at a temperature of 23 C. The ^{13}C-NMR spectra are ^{1}H broadband decoupled. The HSQC sectra are phase-sensitive (opposite signs for CH/CH_3 and CH_2).The ^{1}H and ^{13}C chemical shifts (δ) were referenced to the residual solvent signal as internal standard ($CDCl_3$: $\delta = 7.26$ ppm and 77.16 ppm, DMSO-d_6: $\delta = 2.50$ ppm and 39.52 ppm, CD_3OD: $\delta = 3.31$ ppm and 49.00 ppm for ^{1}H and ^{13}C NMR, respectively).[1] Coupling constants (J) are reported in Hz (splitting abbreviations: s, singlet; d, doublet; t, triplet; q, quartet; m, multiplet; br, broad; and combinations thereof).

Mass spectrometry: HPLC-ESI-MS^n was performed on a 1200 series HPLC system with a UV diode array detector coupled with a LC/MSD trap XCT mass spectrometer (Agilent Technologies). Mixtures of water (with 0.1 % formic acid) and acetonitrile were used as eluents at a total flow rate of 0.5 to 1.0 ml/min. An Ascentis Express C18 column (pore size: 2.7 µm, length: 3 cm, diameter: 2.1 mm; Supelco) was used at a temperature of 40 °C.

High-resolution masses (HRMS) were recorded on a Q-ToF-Ultima 3 instrument (Waters) with LockSpray® interface and a suitable external calibrator.

IR spectroscopy: Fourier-transform IR spectra were recorded on a Tensor 27 spectrometer (Bruker) equipped with a diamond ATR unit.

Optical rotation: Optical rotation of chiral compounds was determined on a Perkin-Elmer 241 MC polarimeter. Compounds were dissolved in chloroform or methanol. Concentrations are given in g/100 ml.

b. Reaction schemes

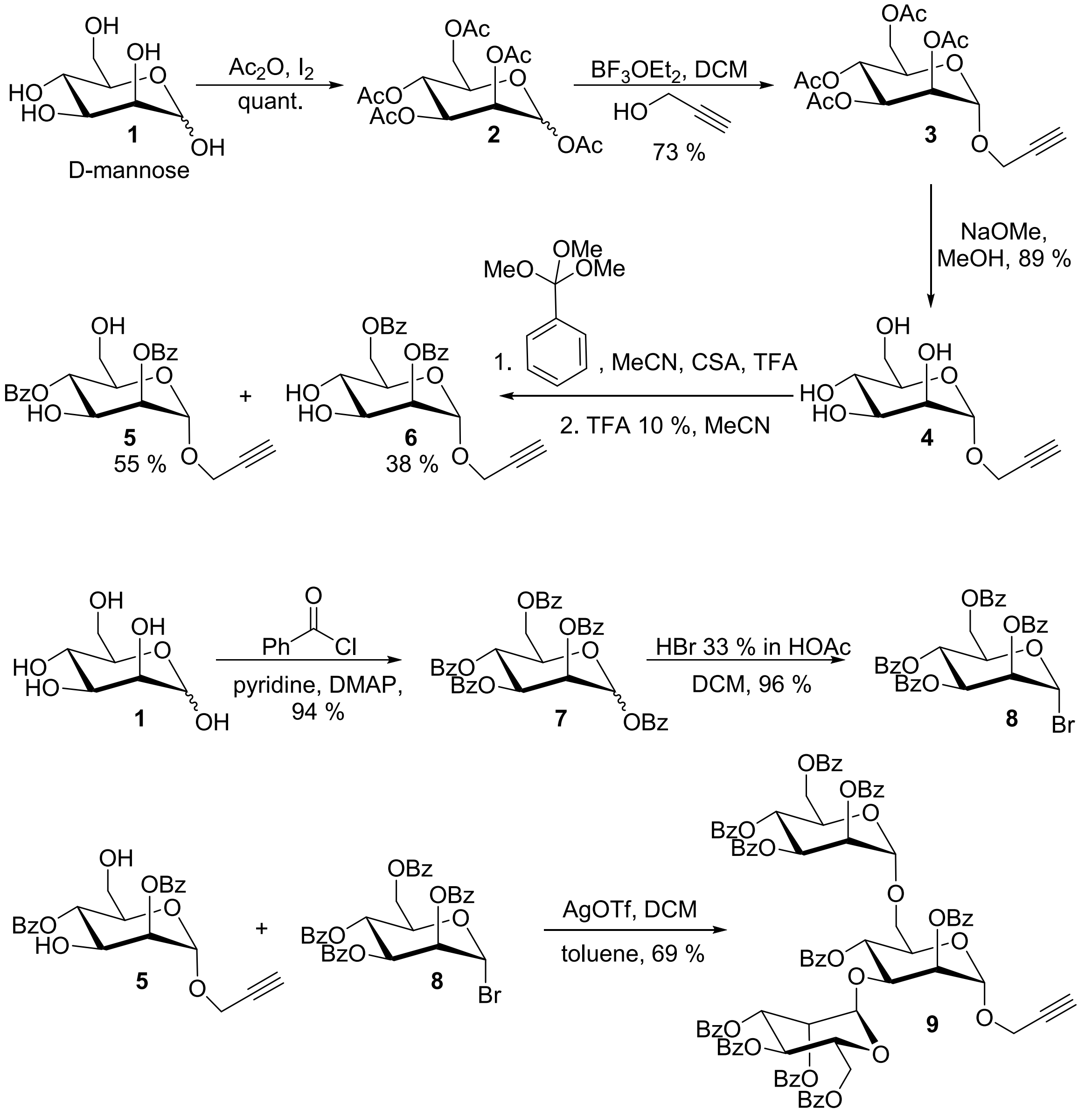
1
D-mannose
Ac2O, I2
quant.
2
BF3OEt2, DCM
HO
73 %
3
NaOMe,
MeOH, 89 %
4
OMe
MeO
OMe
1.
, MeCN, CSA, TFA
2. TFA 10 %, MeCN
5
55 %
+
6
38 %
1
Ph
Cl
pyridine, DMAP,
94 %
7
HBr 33 % in HOAc
DCM, 96 %
8
Br
5
+
8
AgOTf, DCM
toluene, 69 %
9

Scheme S1. Synthesis of 2,4-di-O-benzoyl-3,6-di-O-(2,3,4,6-tetra-O-benzoyl-α-D-mannopyranoside)-1-propargyl-α-D-mannopyranoside (trimannose alkyne; **9**).

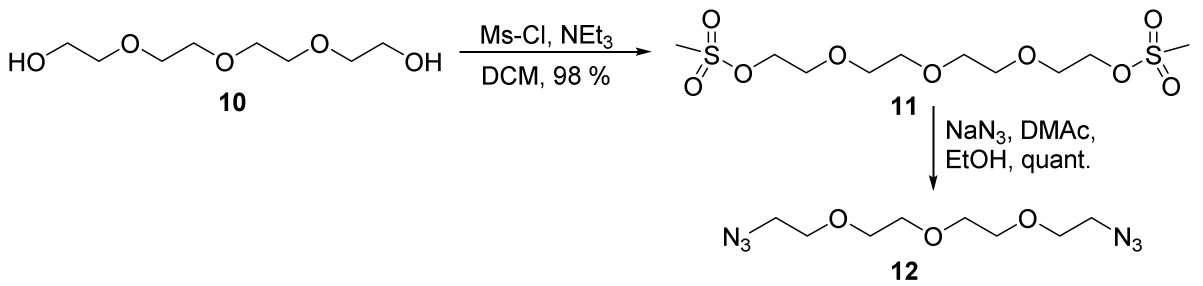
HO
OH
10
Ms-Cl, NEt3
DCM, 98 %
11
NaN3, DMAc,
EtOH, quant.
N3
N3
12

Scheme S2. Synthesis of 1-azido-2-(2-(2-(2-azidoethoxy)ethoxy)ethoxy)ethane (**12**).

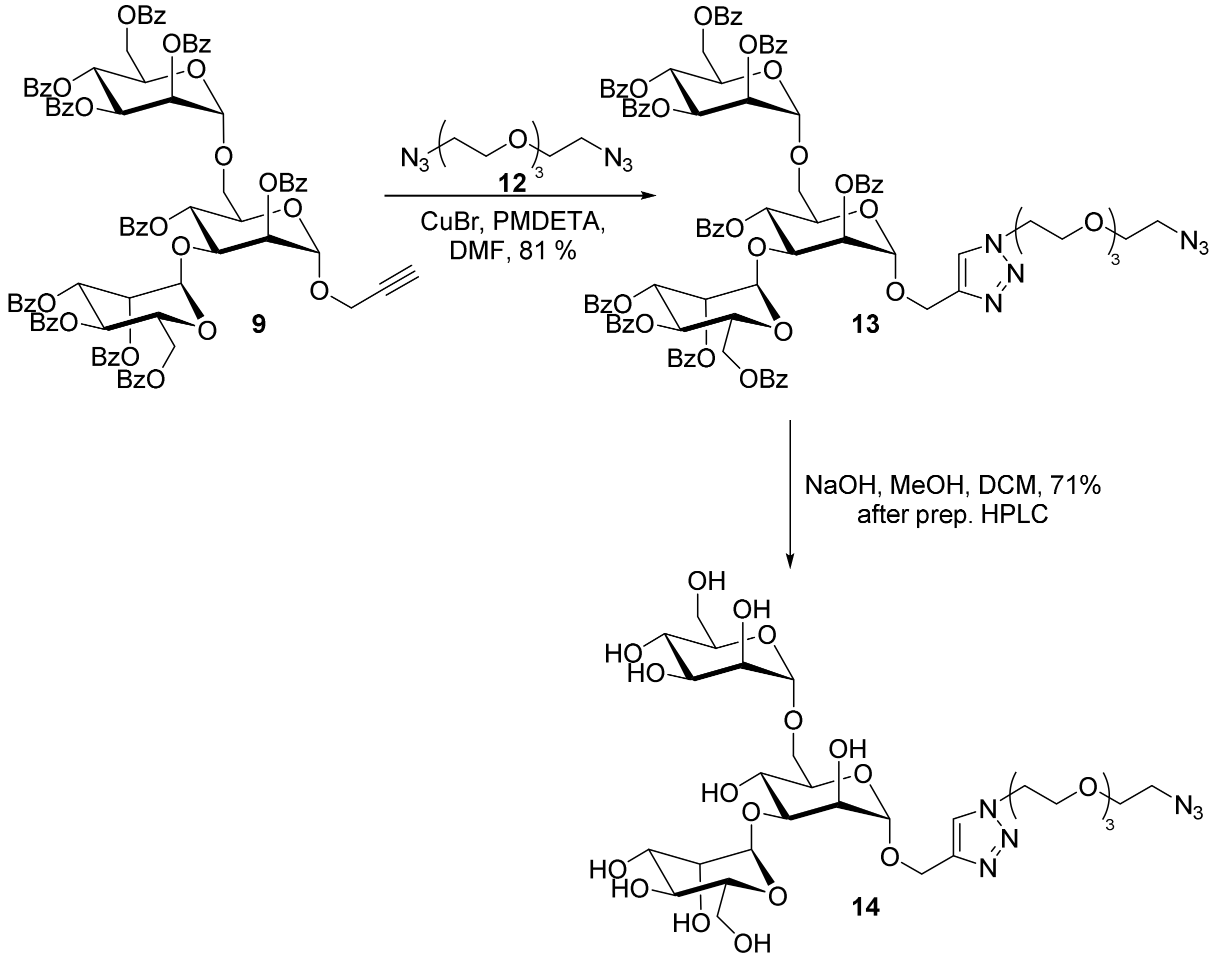

Scheme S3. Synthesis of (1-(2-(2-(2-(2-azidoethoxy)ethoxy)ethoxy)ethyl)-1H-1,2,3-triazole-4-yl)methoxy)-3,6-di-O-α-D-mannopyranosyl-α-D-mannopyranoside (trimannose azide; **14**).

c. Synthetic procedures

1,2,3,4,6-Penta-O-acetyl-α,β-D-mannopyranose (**2**): Iodine (560 mg, 2.2 mmol, 0.04 eq.) and acetic anhydride (50 ml) were mixed under an argon atmosphere. D-Mannose (**1**, 10.0 g, 55.5 mmol, 1.0 eq.) was added portion by portion at 0 °C. After stirring for 30 min at 0 °C and additionally for 18 hours at room temperature, TLC (cyclohexane/toluene/ethyl acetate 3:3:1) showed complete consumption of the starting material. The reaction mixture was diluted with dichloromethane (50 ml) and was washed twice with cold saturated aqueous Na_2SO_3 solution (2 × 80 ml), then with a saturated aqueous solution of $NaHCO_3$ (4 × 50 ml). The separated organic layer was dried over anhydrous $MgSO_4$. The solvent was remove *in vacuo* to afford the desired peracetylated D-mannose (21.5 g, 55.1 mmol, 99 %, mixture of both anomers α/β 4.75:1) as a yellowish, highly viscous oil.

R_f = 0.30 (silica gel, cyclohexane/toluene/ethyl acetate, 3:3:1).

Signals assignable to α-anomer: ^{1}H NMR, COSY (600 MHz, $CDCl_3$) δ (ppm) = 6.09 (d, ^3J = 1.9 Hz, 1H, H-1), 5.34–5.36 (m, 2H, H-3, H-4), 5.25–5.27 (m, 1H, H-2), 4.28 (dd, ^2J = 12.4 Hz, ^3J = 4.9 Hz, 1H, H-6a), 4.10 (dd, ^2J = 12.4 Hz, ^3J = 2.5 Hz, 1H, H-6b), 4.03-4.07 (m, 1H, H-5), 2.18, 2.17, 2.10, 2.05, 2.01 (5 × s, 15H, CO*C*H_3); ^{13}C NMR, HSQC, HMBC (151 MHz, $CDCl_3$) δ (ppm) = 170.8, 170.2, 169.9, 169.7, 168.2 (5 × *C*OCH_3), 90.7 (C-1), 70.7 (C-5), 68.8 (C-3), 68.4 (C-2), 65.6 (C-4), 62.2 (C-6), 21.0, 20.9, 20.9, 20.8, 20.8 (5 × CO*C*H_3).

The spectral data are in accordance with the literature.[2]

Propargyl 2,3,4,6-tetra-O-acetyl-α-D-mannopyranoside (**3**): 1,2,3,4,6-Penta-*O*-acetyl-α,β-D-mannopyranose (**2**, 10.0 g, 25.6 mmol, 1.0 eq.) and propargyl alcohol (7.18 g, 7.48 ml, 128 mmol, 5.0 eq.) were dissolved in dichloromethane (100 ml). After stirring for 20 min at room temperature, the reaction mixture was cooled to 0 °C and BF_3OEt_2 (16.22 ml, 128 mmol, 5.0 eq.) was added dropwise. The mixture was stirred for 15 min at this temperature then at room temperature for 24 h. The solution was treated with saturated $NaHCO_3$ solution (25 ml), the aqueous layer was extracted with dichloromethane (2 × 50 ml) and the combined organic layers were dried over anhydrous $MgSO_4$. The solvent was removed *in vacuo* and the residue was purified by flash column chromatography (cyclohexane/ethyl acetate, 1:1) to give compound **3** (7.23 g, 18.7 mmol, 73 %) as a colorless, viscous oil.

R_f = 0.43 (silica gel, cyclohexane/ethyl acetate, 1:1).

^{1}H NMR, COSY (400 MHz, $CDCl_3$) δ (ppm) = 5.36 (m, 3H, H-2, H–3, H-4), 5.02 (d, 1H, ^3J = 1.7 Hz, H-1), 4.31–4.25 (m, 3H, H-6$_a$, C*H*$_2$–C≡C), 4.10 (dd, ^2J = 12.2 Hz, ^3J = 2.5 Hz, 1H, H-6$_b$), 4.01 (ddd, ^3J = 9.3 Hz, ^3J = 5.2 Hz, ^3J = 2.5 Hz, 1H, H-5), 2.47 (t, ^4J = 2.4 Hz, 1H, C*H*), 2.15, 2.09, 2.03, 1.98 (4 × s, 12H, COC*H*$_3$); ^{13}C NMR, HSQC, HMBC (100.6 MHz, $CDCl_3$) δ (ppm) = 170.8, 170.1, 170.0, 169.8 (4 × *C*OCH_3), 96.4 (C-1), 86.0 (*C*≡CH), 75.7 (C≡*C*H), 69.5 (C-2), 69.1 (C-5), 69.1 (C-3), 66.1 (C-4), 62.4 (C-6), 55.1 (*C*H_2), 21.0, 20.9, 20.8, 20.8 (4 × CO*C*H_3).

The spectral data are in accordance with the literature.[3]

Propargyl α-D-mannopyranoside (**4**): Propargyl 2,3,4,6-tetra-*O*-acetyl-α-D-mannopyranoside (**3**, 7.00 g, 18.1 mmol) was dissolved in methanol (70 ml) and sodium methoxide was added until a pH of 9–10 (approx. 60 mg) was reached. The reaction mixture was stirred at room temperature for 16 h. Subsequently, the solution was neutralized using Amberlite 120 H^+ resin. The mixture was filtered over Celite, which was washed thoroughly with methanol. The solvent was removed *in vacuo* to afford the desired 1-propargyl-α-D-mannopyranoside (3.50 g, 16.1 mmol, 89 %) as a highly viscous syrup which solidified soon to an amorphous solid.

R_f = 0.85 (RP-silica gel, acetonitrile/water, 1:9);

^{1}H NMR, COSY (400 MHz, CD_3OD) δ (ppm) = 4.96 (d, ^3J = 1.7 Hz, 1H, H-1), 4.27 (d, 1H, ^4J = 2.4 Hz, C*H*$_2$), 3.84 (dd, ^2J = 11.8 Hz, ^3J = 2.3 Hz, 1H, H-6$_a$), 3.79 (dd, 1H, ^3J = 3.1 Hz, ^3J = 1.7 Hz, H-2), 3.74-3.58 (m, 3H, H-3, H–4, H–6$_b$), 3.54–3.47 (m, 1H, H–5), 2.86 (t, ^4J = 2.4 Hz, C*H*); ^{13}C NMR, HSQC, HMBC (100.6 MHz, MeOD) δ (ppm) = 99.8 (C-1), 80.0 (*C*≡CH), 76.0 (C≡*C*H), 75.1 (C-5), 72.5 (C-3), 72.0 (C-2), 68.5 (C–4), 62.8 (C–6), 54.8 (*C*H$_2$-C≡CH).

The spectral data are in accordance with literature.[3]

Propargyl 2,4-O-di-benzoyl-α-D-mannopyranoside (**5**) *and propargyl 2,6-O-di-benzoyl-α-D-mannopyranoside* (**6**): Trimethyl orthobenzoate (3.1 ml, 18.1 mmol, 2.6 eq.) was added to a mixture of 1-propargyl-α-D-mannopyranoside (**4**, 1.5 g, 6.87 mmol, 1.0 eq.), trifluoroacetic acid (TFA, 45 µl) and camphorsulfonic acid (CSA, 75 mg) in acetonitrile (60 ml) at room temperature. The suspension was stirred for 2 h, until a clear colorless solution was obtained. The solvent was removed *in vacuo* and the residue was redissolved in acetonitrile (45 ml). The solution was treated with 10 % aqueous trifluoroacetic acid (2.6 ml) at room temperature. After stirring for 1 h, the solvent was removed *in vacuo* and the residue was co-evaporated with toluene (4 × 50 ml). The crude product was purified by flash column chromatography (cyclohexane/ethyl acetate, gradient 0 % to 60 % ethyl acetate, Isolera Flash Purification System) to afford the two title compounds (1.61 g, 3.78 mmol, 55 %, 1-propargyl 2,4-*O*-di-benzoyl-α-D-mannopyranoside; 1.11 g, 2.60 mmol, 38 %, 1-propargyl 2,6-*O*-di-benzoyl-α-D-mannopyranoside) as colorless foams.

Propargyl 2,4-O-di-benzoyl-α-D-mannopyranoside (**5**):

R_f = 0.48 (silica gel, cyclohexane/ethyl acetate, 2:1).

^{1}H NMR, COSY (400 MHz, CDCl$_3$) δ (ppm) = 8.12 – 8.05 (m, 4H, H–2–Ar), 7.64 – 7.58 (m, 2H, H–4–Ar), 7.51 – 7.44 (m, 4H, H–3–Ar), 5.52 (pseudo-t, ^3J = 10.0 Hz, 1H, H–4), 5.45 (dd, ^3J = 3.5, ^3J = 1.7 Hz, 1H, H–2), 5.25 (d, ^3J = 1.7 Hz, 1H, H–1), 4.45 (dd, ^3J = 9.8, ^3J = 3.5 Hz, 1H, H–3), 4.33 (d, ^4J = 2.4 Hz, 2H, C*H$_2$*), 4.00 (ddd, ^3J = 10.0, ^3J = 4.1, ^3J = 2.3 Hz, 1H, H–5), 3.82 (dd, ^2J = 12.6, $^3J_{H,H}$ = 2.4 Hz, 1H, H–6$_a$), 3.74 (dd, ^2J = 12.6, ^3J = 4.1 Hz, 1H. H–6$_b$), 2.51 (t, ^4J = 2.4 Hz, 1H, C*H*); ^{13}C NMR, HSQC, HMBC (100.6 MHz, CDCl$_3$) δ (ppm) = 167.4, 166.1 (2 × *C*O–Ar), 133.9, 133.8 (2 × C–4–Ar), 130.1 (2 × C–2–Ar, 2 × C–2’–Ar), 129.3, 129.1 (2 × C$_q$), 128.8, 128.7 (C–3–Ar), 96.7 (C–1, $^1J_{C,H}$ = 173 Hz), 78.4 (*C*≡CH), 75.6 (C≡*C*H), 72.8 (C-2), 71.2 (C-5), 70.3 (C-4), 68.7 (C–3), 61.5 (C–6), 55.4 (*C*H$_2$-C≡CH).

IR (ATR) λ_{max}/cm^{-1} 3465, 3292, 2927, 1715, 1601, 1451, 1317, 1261, 1111, 1059, 1011, 884, 708.

$[\alpha]_D^{22}$ – 11.9° (c = 1.00, CHCl$_3$).

HRMS (ESI): calculated for $[C_{23}H_{22}O_8 + Na]^+$: 449.1212, found: 449.1225.

Propargyl 2,6-di-O-benzoyl-α-D-mannopyranoside (**6**):

R_f = 0.23 (silica gel, cyclohexane/ethyl acetate, 2:1);

^{1}H NMR, COSY (400 MHz, $CDCl_3$) δ (ppm) = 8.14 – 8.09 (m, 2H, H–2–Ar^6), 7.93 – 7.88 (m, 2H, H–2–Ar^2), 7.65 – 7.59 (m, 1H, H–4–Ar^2), 7.53 – 7.48 (m, 1H, H–4–Ar^6), 7.48 – 7.42 (m, 2H, H–3–Ar^6), 7.26 – 7.21 (m, 2H, H–3–Ar^2), 5.41 (dd, ^3J = 3.4, ^3J = 1.7 Hz, 1H, H–2), 5.15 (d, ^3J = 1.7 Hz, 1H, H–1), 4.93–4.87 (m, 1H, H–6$_a$), 4.51 (dd, ^2J = 12.2, ^3J = 1.8 Hz, 1H, H–6$_b$), 4.31 (d, ^4J = 2.4 Hz, 2H, C*H$_2$*), 4.20 (dd, ^3J = 8.7, ^3J = 3.3 Hz, 1H, H–3), 4.22–3.89 (m, 2H, H–4, H–5), 2.47 (t, ^4J = 2.4 Hz, 1H, C*H*); ^{13}C NMR, HSQC, HMBC (100.6 MHz, $CDCl_3$) δ (ppm) = 167.5 (*C*O–Ar^6), 166.1 (*C*O–Ar^2), 133.5, 133.5 (2 × C–4–Ar), 130.0, 129.9 (2 × C–2–Ar), 129.7, 129.4 (2 × C$_q$), 128.7, 128.8 (2 × C–3–Ar), 96.9 (C–1, $^1J_{C,H}$ = 173 Hz), 78.5 (*C*≡CH), 75.5 (C≡*C*H), 72.1 (C-2), 72.1 (C-4), 71.5 (C–5), 70.0 (C-3), 67.8 (C–4), 63.5 (C–6), 55.1 (*C*H$_2$-C≡CH).

IR (ATR) λ_{max}/cm^{-1} 3458, 3345, 3236, 2957, 1717, 1703, 1451, 1317, 1262, 1109, 1053, 977, 706, 648.

$[\alpha]_D^{22}$ – 17.7° (c = 1.00, $CHCl_3$).

HRMS (ESI): calculated for $[C_{23}H_{22}O_8 + H]^+$: 427.1393, found: 427.1404.

1,2,3,4,6-Penta-O-benzoyl-α,β-D-mannopyranose (**7**): Benzoylchloride (70.0 ml, 380 mmol, 6.8 eq.) was added dropwise to a stirred solution of d-mannose (**1**, 10.0 g, 55.6 mmol, 1.0 eq.) and 4-(dimethylamino)-pyridine (DMAP, 30 mg) in pyridine (120 ml) under an argon atmosphere at 0 °C. The reaction mixture was stirred at this temperature for 40 min, then for 36 h at room temperature. The solvent was removed *in vacuo* and the residue was taken up in dichloromethane (400 ml) and water (100 ml), the organic layer was washed with brine (200 ml), saturated $NaHCO_3$ solution (2 × 200 ml) and again with brine (100 ml). The separated organic layer was dried over anhydrous $MgSO_4$ and the solvent was removed *in vacuo*. The residue was dissolved in 100 ml of boiling EtOH, then slowly cooled to room temperature. The precipitate was collected by filtration und dried *in vacuo* to give compound **7** as a colorless powder (36.6 g, 52.3 mmol, 94 %, mixture of both anomers α/β 4.3:1).

α–anomer: R_f = 0.48 (silica gel, toluene/ethyl acetate, 19:1).

β–anomer: R_f = 0.36 (silica gel, toluene/ethyl acetate, 19:1).

Signals assignable to α-anomer: ^{1}H NMR, COSY (400 MHz, $CDCl_3$) δ (ppm) = 8.23–7.84 (m, 10H, H–Ar), 7.71–7.27 (m, 15H, H–Ar), 6.64 (d, ^3J = 2.0 Hz, 1H, H-1), 6.29 (pseudo-t, ^3J = 10.2 Hz, 1H, H-4), 6.08 (dd, ^3J = 10.3, ^3J = 3.3 Hz, 1H, H-3), 5.92 (dd, ^3J = 3.3, ^3J = 2.0 Hz, 1H, H-2), 4.70 (dd, ^3J = 12.2, ^3J = 3.7 Hz, 1H, H-6$_a$), 4.51 (pseudo-dt, ^3J = 10.0, ^3J = 2.9 Hz, 1H, H-5), 4.51 (dd, ^3J = 12.2, ^3J = 3.7 Hz, 1H, H-6$_b$); ^{13}C NMR, HSQC, HMBC (100.6 MHz, $CDCl_3$) δ (ppm) = 166.2, 165.8, 165.4, 165.3, 163.7 (5 × *C*O–Ar), 134.2, 133.8, 133.7, 133.5, 133.2 (5 × C$_q$), 130.3, 130.1, 130.0, 129.9, 129.1, 129.0, 128.9, 128.8, 128.6, 128.6, 128.5 (C–Ar), 91.5 ($^1J_{CH}$ = 180 Hz, C–1), 71.3 (C-5), 70.1 (C-3), 69.6 (C-2), 66.3 (C-4), 62.5 (C-6).

Signals assignable to β-anomer: ^{1}H NMR, COSY (400 MHz, $CDCl_3$) *δ* (ppm) = 8.18–7.84 (m, 10H, H–Ar), 7.67–7.27 (m, 15H, H–Ar), 6.44 (d, ^3J = 1.2 Hz, 1H, H-1), 6.18 (pseudo-t, ^3J = 9.8 Hz, 1H, H-4), 6.11 (dd, ^3J = 3.2, ^3J = 1.1 Hz, 1H, H-2), 5.81 (dd, ^3J = 10.0, ^3J = 3.2 Hz, 1H, H-3), 4.76 (dd, ^3J = 12.4, ^3J = 2.8 Hz, 1H, H-6$_a$), 4.56 (dd, ^3J = 12.3, ^3J = 4.4 Hz, 1H, H-6$_b$), 4.38 (ddd, ^3J = 9.7, ^3J = 4.3, ^3J = 2.8 Hz, 1H, H-5); ^{13}C NMR, HSQC, HMBC (100.6 MHz, $CDCl_3$) *δ* (ppm) = 166.2, 165.7, 165.6, 165.4, 164.3 (5 × *C*O–Ar), 133.9, 133.7, 133.7, 133.6, 133.2 (5 × C$_q$), 130.3, 130.2, 130.0, 130.0, 129.5, 128.9, 128.8, 128.8, 128.6, 128.6, 128.6, 128.5 (C–Ar), 91.4 ($^1J_{CH}$ = 163 Hz, C–1), 73.5 (C-5), 71.7 (C-3), 69.5 (C-2), 66.5 (C-4), 62.8 (C-6).

The spectral data are in accordance with the literature.[4]

2,3,4,6-Tetra-O-benzoyl-α-D-mannopyranosyl bromide (**8**): 1,2,3,4,6-Penta-*O*-benzoyl-α,β-D-mannopyranose (**7**, 5.0 g, 7.14 mmol, 1.0 eq.) was dissolved in dichloromethane (25 ml) and treated with HBr (33 % in acetic acid, 12.3 ml, 71.4 mmol, 10 eq.) at 0 °C. After 2 h, another portion of HBr (1.0 ml, 33 % in acetic acid) was added. TLC (cyclohexane/ethyl acetate 2:1) showed complete conversion after 4 h. The reaction mixture was diluted with dichloromethane (25 ml), washed with water (25 ml), saturated aqueous $NaHCO_3$ solution (4 × 25 ml) and brine (25 ml). The separated organic layer was dried over anhydrous $MgSO_4$ and the solvent was removed *in vacuo* to give compound **8** (4.51 g, 6.85 mmol, 96 %,) as a yellowish, viscous oil.

R_f = 0.60 (silica gel, cyclohexane/ethyl acetate, 2:1).

^{1}H NMR, COSY (400 MHz, $CDCl_3$) *δ* (ppm) = 8.13–7.82 (m, 8H, H–Ar), 7.64–7.27 (m, 12H, H–Ar), 6.59 (d, ^3J = 1.1 Hz, 1H, H-1), 6.32–6.22 (m, 2H, H-3, H-4), 5.91 (dd, ^3J = 2.9, ^3J = 1.7 Hz, 1H, H-2), 4.75 (dd, ^2J = 12.5, ^3J = 2.4 Hz, 1H, H-6$_a$), 4.66 (pseudo-dt, ^3J = 9.4, ^3J = 3.1 Hz, 1H, H-5), 4.51 (dd, ^2J = 12.5, ^3J = 3.7 Hz, 1H, H-6$_b$); ^{13}C NMR, HSQC, HMBC (100.6 MHz, $CDCl_3$) *δ* (ppm) = 166.1, 165.5, 165.4, 165.1 (4 × *C*O–Ar), 133.9, 133.8, 133.5, 133.3 (4 × C$_q$), 130.0, 129.9, 129.9, 129.8, 128.9, 128.8, 128.8, 128.7, 128.6, 128.5 (C–Ar), 83.4 (C–1), 73.3 (C-5), 73.1 (C-2), 69.2 (C-3), 66.1 (C-4), 61.9 (C-6).

The spectral data are in accordance with literature.[5]

2,4-Di-O-benzoyl-3,6-di-O-(2,3,4,6-tetra-O-benzoyl-α-D-mannopyranoside)-1-propargyl-α-D-mannopyranoside (**9**): 1-Propargyl 2,4-*O*-di-benzoyl-α-D-mannopyranoside (**5**, 415 mg, 0.97 mmol, 1.0 eq.) and 2,3,4,6-tetra-*O*-benzoyl-α-D-mannosylpyranosyl bromide (**8**, 1.27 g, 1.94 mmol, 2.0 eq.) were dissolved in dichloromethane (11 ml) in a thoroughly flame dried flask under argon atmosphere. The solution was stirred for 20 min at 0 °C. Silver triflate (AgOTf, 543 mg, 2.11 mmol, 2.4 eq.) in toluene (3 ml) was added dropwise. Immediately, a yellowish precipitate was formed. After 1.5 h the greenish reaction mixture was treated with NEt_3 (500 µl), then filtered over Celite which was washed thoroughly with dichloromethane. The solvent was remove *in vacuo* and the residue was purified by flash column chromatography (cyclohexane/ethyl acetate, gradient 0 % to 50 % ethyl acetate, Isolera Flash Purification System) to afford compound 9 (1.06 g, 0.67 mmol, 69 %) as a colorless foam.

R_f = 0.40 (silica gel, cyclohexane/ethyl acetate, 2:1).

^{1}H NMR, COSY, TOCSY (600 MHz, $CDCl_3$) δ (ppm) = 8.33–8.30 (m, 2H, H–Ar), 8.14–8.10 (m, 4H, H–Ar), 8.09–8.01 (m, 6H, H–Ar), 7.88–7.80 (m, 6H, H–Ar), 7.74–7.70 (m, 2H, H–Ar), 7.64–7.47 (m, 8H, H–Ar), 7.46–7.27 (m, 20H, H–Ar), 7.22–7.19 (m, 2H, H–Ar), 6.14 (t, ^3J = 10.1 Hz, 1H, H–4‘‘), 6.02–5.96 (m, 2H, H–3‘‘, H–4‘), 5.93 (t, ^3J = 10.0 Hz, 1H, H–4), 5.79–5.76 (m, 2H, H–2‘‘, H–2), 5.71 (dd, ^3J = 10.1, ^3J = 2.8 Hz, 1H, H–3‘), 5.37–5.35 (m, 3H, H–1, H–1‘, H–2‘), 5.15 (d, ^3J = 1.8 Hz, 1H, H–1‘‘), 4.68 (dd, ^3J = 9.8, ^3J = 3.5 Hz, 1H, H–3), 4.65–4.52 (m, 4H, H–6$_a$‘‘, H-5‘‘, H–5‘, H–6$_a$‘), 4.47 (dd, ^2J = 16.0, ^4J = 2.4 Hz, 1H, O–C$H_{2,a}$–C≡C), 4.43–4.36 (m, 3H, H–6$_b$‘‘, H–6$_b$‘, O–C$H_{2,b}$–C≡C), 4.33 (ddd, ^3J = 10.3, ^3J = 6.1, ^4J = 2.1 Hz, 1H, H–5), 4.17 (dd, ^2J = 10.8, ^3J = 6.2 Hz, 1H, H–6$_a$), 3.81 (dd, ^2J = 10.9, ^3J = 2.1 Hz, 1H, H–6$_b$), 2.60 (t, ^4J = 2.4 Hz, 1H, –C≡C–*H*); ^{13}C NMR, HSQC, HMBC (151 MHz, $CDCl_3$) δ (ppm) = 166.7, 166.3, 166.2, 165.7, 165.6, 165.4, 165.4, 165.4, 164.8, 164.7 (10 × *C*O), 133.8, 133.6, 133.6, 133.5, 133.4, 133.4, 133.2, 133.1, 133.1, 133.0 (10 × C–4–Ar), 130.4, 130.1, 130.1, 130.0, 130.0, 129.8, 129.8, 129.8, 129.7 (C–Ar), 129.4, 129.3, 129.3, 129.3, 129.3, 129.1, 129.1, 129.1, 129.0, 129.0 (10 × C$_q$–Ar), 128.7, 128.6, 128.5, 128.4, 128.4, 128.3 (C–Ar), 99.6 (C–1‘), 97.6 (C–1‘‘), 96.4 (C–1), 78.3 (–*C*≡C–H), 76.1 (–C≡*C*–H), 76.0 (C–3), 71.7 (C–2‘‘), 70.4 (C–3‘‘), 70.4 (C–2), 70.3 (C–5), 70.3 (C–2‘), 69.7 (C–3‘), 69.4 (C–5‘), 69.0 (C–5‘‘), 68.6 (C–4), 67.1(C–6), 66.7 (C–4‘), 66.7 (C–4‘‘), 62.8 (C–6‘‘), 55.2 (–*C*H$_2$–C≡C).

IR (ATR) λ_{max}/cm^{-1} 3064, 2955, 2926, 1778, 1722, 1642, 1451, 1257, 1066, 1026, 1001, 705, 686, 648.

$[\alpha]_D^{22}$ – 50.7° (c = 1.00, $CHCl_3$).

HRMS (ESI): calculated for $[C_{91}H_{74}O_{26} + Na]^+$: 1605.4366, found: 1605.4390.

1-Methanesulfonyl-2-(2-(2-methanesulfonylethoxy)ethoxy)ethoxy)ethane (11): Methanesulfonyl chloride (Ms-Cl, 4.48 ml, 56.6 mmol, 2.2 eq.) and tetraethylene glycol (10, 5.00 g, 25.7 mmol, 1.0 eq.) were dissolved in dichloromethane (125 ml) at 0 °C. The reaction mixture was treated with NEt_3 (10.7 ml, 77.2 mmol, 3.0 eq.) and stirred for 45 min. Subsequently, water (125 ml) was added and the separated organic layer was washed with ice-cold 2 N HCl (125 ml), saturated aqueous $NaHCO_3$ solution (125 ml) and brine (125 ml). The organic layer was dried over anhydrous Na_2SO_4 and the solvent was removed *in vacuo* to give compound 11 (8.78 g, 25.1 mmol, 98 %) as a yellowish oil.

R_f = 0.20 (silica gel, cyclohexane/ethyl acetate, 1:2).

^{1}H NMR, COSY (300 MHz, $CDCl_3$) δ (ppm) = 4.40–3.35 (m, 4H, 2 × MsO–CH_2), 3.79–3.74 (m, 4H, MsO–CH_2–CH_2), 3.70–3.61 (m, 8H, MsO–Et–O[(CH_2)$_2$–O–]$_2$–Et–OMs), 3.07 (m, 6H, 2 × –CH_3); ^{13}C NMR, HSQC, HMBC (75 MHz, $CDCl_3$) δ (ppm) = 70.8 (2 × CH_2–CH_2–O), 70.7 (2 × CH_2–CH_2–O), 69.3 (2 × MsO–CH_2), 69.2 (2 × MsO–CH_2–CH_2), 37.8 (2 × –CH_3).

The spectral data are in accordance with literature.[6]

1-Azido-2-(2-(2-(2-azidoethoxy)ethoxy)ethoxy)ethane (**12**): 1-Methanesulfonyl-2-(2-(2-(2-methanesulfonylethoxy)ethoxy)ethoxy)ethane (**11**, 2.00 g, 5.71 mmol, 1.0 eq.) was dissolved in a mixture of EtOH (12 ml) and dimethylacetamide (DMAc, 3 ml) and NaN_3 (1.15 g, 17.7 mmol, 3.1 eq.) was added. The reaction mixture was refluxed for 6 h and subsequently slowly poured into a mixture of water (20 ml) and dichloromethane (20 ml). The separated organic layer was washed with water (50 ml) and brine (50 ml). The organic layer was dried over anhydrous Na_2SO_4 and the solvent was removed *in vacuo*. The residue was co-evaporated with toluene (4 × 50 ml) to give compound **12** (1.36 g, 5.57 mmol, 98 %) as a colorless oil.

R_f = 0.60 (silica gel, cyclohexane/ethyl acetate, 4:2).

^{1}H NMR, COSY (300 MHz, $CDCl_3$) δ (ppm) = 3.72–3.62 (m, 12H, 2 × N_3–CH_2–CH_2, 2 × CH_2–CH_2–O), 3.39 (t, ^3J = 5.1 Hz, 4H, N_3–CH_2); ^{13}C NMR, HSQC, HMBC (75 MHz, $CDCl_3$) δ (ppm) = 70.9 (2 × CH_2–CH_2–O), 70.2 (2 × N_3–CH_2–CH_2), 50.8 (2 × N_3–CH_2).

The spectral data are in accordance with the literature.[7]

(1-(2-(2-(2-(2-Azidoethoxy)ethoxy)ethoxy)ethyl)-1H-1,2,3-triazole-4-yl)methoxy)-2,4-di-O-benzoyl-3,6-di-O-(2,3,4,6-tetra-O-benzoyl-α-D-mannopyranosyl)-α-D-mannopyranoside (**13**): DMF (50 ml) was degased by freeze-pump-thaw-cycle three times, then 2,4-di-*O*-benzoyl-3,6-di-*O*-(2,3,4,6-tetra-*O*-benzoyl-α-D-mannopyranoside)-1-propargyl-α-D-mannopyranoside (**9**, 325 mg, 0.21 mmol, 1.0 eq.) and 1-azido-2-(2-(2-(2-azidoethoxy)ethoxy)ethoxy)ethane (**12**, 725 mg, 3.08 mmol, 15 eq.) were dissolved under argon atmosphere. Subsequently, the freeze-pump-thaw-cycle was repeated again for three times. CuBr (15 mg, 0.10 mmol, 50 mol%) and *N*,*N*,*N'*,*N''*,*N''*-pentamethyldiethylenetriamine (PMDTA, 50 µl, 0.24 mmol, 85 mol%) were added and the teal reaction mixture was stirred at 45 °C for 1.5 h. Subsequently, it was diluted with ethyl acetate (40 ml) and washed with aqueous saturated NH_4Cl solution (2 × 40 ml). The aqueous layer was diluted with water so that all salts were dissolved and washed with ethyl acetate (30 ml). The separated organic layer was washed with brine and dried over anhydrous $MgSO_4$. The solvent was removed *in vacuo* and the residue was purified by flash column chromatography (cyclohexane/ethyl acetate, gradient 0 % to 90 % ethyl acetate, Isolera Flash Purification System) to afford compound **13** (302 mg, 0.40 mmol, 81 %) as a colorless oil.

R_f = 0.28 (silica gel, cyclohexane/ethyl acetate, 2:4).

^{1}H NMR, COSY, TOCSY (600 MHz, CDCl$_3$) δ (ppm) = 8.33–8.29 (m, 2H, H–Ar), 8.14–8.00 (m, 10H, H–Ar), 7.89 (s, 1H, H$_{\text{triazole}}$), 7.86–7.82 (m, 4H, H–Ar), 7.78–7.75 (m, 2H, H–Ar), 7.72–7.69 (m, 2H, H–Ar), 7.61–7.35 (m, 20H, H–Ar), 7.31–7.27 (m, 8H, H–Ar), 7.22–7.18 (m, 2H, H–Ar), 6.14 (t, ^3J = 10.1 Hz, 1H, H–4′′), 6.06–5.99 (m, 3H, H–3′′, H–4′, H–4), 5.82–5.81 (m, 1H, H–2′′), 5.76–5.74 (m, 1H, H–2), 5.70 (dd, ^3J = 10.0, ^3J = 2.8 Hz, 1H, H–3′), 5.34–5.32 (m, 2H, H–1′, H–2′), 5.27 (s, 1H, H–1), 5.19 (s, 1H, H–1′′), 5.00 (d, ^2J = 12.2 Hz, 1H, O–CH_{2a}–C=C), 4.84 (d, ^2J = 12.2 Hz, 1H, O–CH_{2b}–C=C), 4.64 (dd, ^3J = 9.8, ^3J = 3.4 Hz , 1H, H–3), 4.61 (dd, ^2J = 12.4, ^3J = 2.5 Hz, 1H, H–6$_a$′), 4.58–4.53 (m, 4H, triazole–CH_2, H–6a′′, H–5′′), 4.47 (dt, ^3J = 10.1, ^3J = 2.9 Hz, 1H, H–5′), 4.42–4.39 (m, 1H, H–5), 4.34 (dd, ^2J = 12.2, ^3J = 4.4 Hz, 1H, H–6$_b$′′), 4.29 (dd, ^2J = 12.4, ^3J = 3.1 Hz, 1H, H–6$_b$′), 4.18 (dd, ^2J = 10.9, ^3J = 5.2 Hz, 1H, H–6$_a$), 3.89 (t, ^3J = 5.0 Hz, 2H, triazole–CH$_2$–CH_2), 3.80 (dd, ^2J = 11.0, ^3J = 2.2 Hz, 1H, H–6$_b$), 3.64 (m, 10H, alkyl CH_2), 3.33 (t, ^3J = 5.0 Hz, 2H, N$_3$–CH_2); ^{13}C NMR, HSQC, HMBC (151 MHz, CDCl$_3$) δ (ppm) = 166.3, 166.2, 166.2, 165.7, 165.6, 165.3, 165.3, 165.3, 164.8, 164.7 (10 × *C*O), 143.3 (C$_q$–in triazole), 133.7, 133.5, 133.5, 133.5, 133.4, 133.4, 133.2, 133.1, 133.1, 133.0 (10 × C–4–Ar), 130.3, 130.1, 130.1, 130.0, 130.0, 129.9, 129.9, 129.9, 129.8, 129.7, 129.7 (C–Ar), 129.4, 129.4, 129.3, 129.3, 129.3, 129.1, 129.1, 129.1, 129.0, 129.0 (10 × C$_q$–Ar), 128.6, 128.6, 128.6, 128.5, 128.5, 128.5, 128.5, 128.4, 128.4 128.2 (C–Ar), 124.6 (triazole-C*H*), 99.7 (C–1′), 97.8 (C–1′′), 97.0 (C–1), 76.9 (C–3), 71.8 (C–2), 70.7 (3 signals, respectively alkyl *C*H$_2$), 70.4 (C–2′), 70.3 (C–3′′), 70.3 (C–2′′), 70.1 (alkyl *C*H$_2$), 69.9 (C–5), 69.6 (C–5′), 69.5 (triazole–CH$_2$–*C*H$_2$), 69.5 (C–3′), 69.0 (C–5′′), 68.4 (C–4), 66.9 (C–6), 66.6 (C–4′), 66.5 (C–4′′), 62.8 (C–6′′), 62.5 (C–6′), 61.0 (O–*C*H$_2$–C=C), 50.7 (N$_3$–*C*H$_2$), 50.3 (triazole–*C*H$_2$).

IR (ATR) λ_{max}/cm^{-1} 2954, 2927, 2876, 2106, 1727, 1602, 1452, 1264, 1108, 1097, 1028, 710.

$[a]_D^{22}$ – 33.7° (c = 1, CHCl$_3$).

HRMS (ESI): calculated for [C$_{99}$H$_{90}$N$_6$O$_{29}$ + Na]$^+$: 1849.5650, found: 1849.5684.

(1-(2-(2-(2-(2-Azidoethoxy)ethoxy)ethoxy)ethyl)-1H-1,2,3-triazole-4-yl)methoxy)-3,6-di-O-α-D-manno-pyranosyl-α-D-mannopyranoside (**14**): (1-(2-(2-(2-(2-Azidoethoxy)ethoxy)ethoxy)ethyl)-1*H*-1,2,3-triazole-4-yl)methoxy)-2,4-di-*O*-benzoyl-3,6-di-*O*-(2,3,4,6-tetra-*O*-benzoyl-α-D-mannopyranosyl)-α-D-mannopyranoside (**13**, 500 mg, 0.27 mmol) was dissolved in a mixture of MeOH (4 ml) and dichloromethane (4 ml) and treated with NaOMe (15 mg, 0.27 mmol, 1 eq.). After stirring for 24 h at room temperature RP-TLC (acetonitrile/water 2:8) showed complete conversion. The reaction mixture was neutralized with concentrated HCl (two drops were required). Subsequently, the solvent was removed *in vacuo* and the residue was coevaporated with toluene (3 × 50 ml). The residue was purified by preparative HPLC (MeOH/H$_2$O, 80:20 for 10 min, then 50:50 for 10 min, flow rate: 37.5 ml/min, R$_t$ 14.7 min) to give the desired unprotected product (**14**, 150 mg, 0.19 mmol, 71 %) as a colorless solid.

R_f = 0.57 (RP-silica gel, acetonitrile/water, 2:8).

^{1}H NMR, COSY (600 MHz, D_2O) δ (ppm) = 8.07 (s, 1H, H–Ar), 5.03 (d, ^3J = 1.7 Hz, 1H, H–1‘), 4.89 (d, ^3J = 1.7 Hz, 1H, H–1), 4.85 (d, ^3J = 1.7 Hz, 1H, H–1‘‘), 4.79–4.78 (m, 1H, O–C*H$_{2a}$*–C=C), 4.69 (d, ^2J = 12.6 Hz, 1H, O–C*H$_{2b}$*–C=C), 4.60 (t, ^3J = 5.0 Hz, 2H, triazole–C*H$_2$*), 4.55 (dd, ^3J = 3.0, ^3J = 1.7 Hz, 1H, H–2), 4.01 (dd, ^3J = 3.3, ^3J = 1.7 Hz, 1H, H–2‘), 3.90–3.56 (m, 26H, all other), 3.45–3.42 (m, 2H, N_3–C*H$_2$*); ^{13}C NMR, HSQC, HMBC (151 MHz, D_2O) δ (ppm) = 143.4 (C_q–triazole), 125.4 (*C*H in triazole), 102.3 (C–1‘), 99.6 (C–1), 99.3 (C–1‘‘), 78.5 (C–3), 73.2, 72.6, 71.2, 70.5, 70.3, 69.9 (C–2‘), 69.8, 69.6 (C–2), 69.5, 69.4, 69.1, 68.7 (triazole–CH$_2$–*C*H$_2$), 66.6, 65.4, 64.9 (C–6), 60.9, 59.9, 50.0, 50.0 (N_3–*C*H$_2$, triazole–*C*H$_2$).

IR (ATR) λ_{max}/cm^{-1} 3355, 2929, 2114, 1642, 1454, 1350, 1302, 1256, 1130, 1048, 1026, 980.

$[a]_D^{22}$ – 63.2° (c = 0.75, MeOH).

HRMS (ESI): calculated for $[C_{29}H_{50}N_6O_{19} + Na]^+$: 809.3028, found: 809.3030.

d. ^1H and ^{13}C NMR spectra

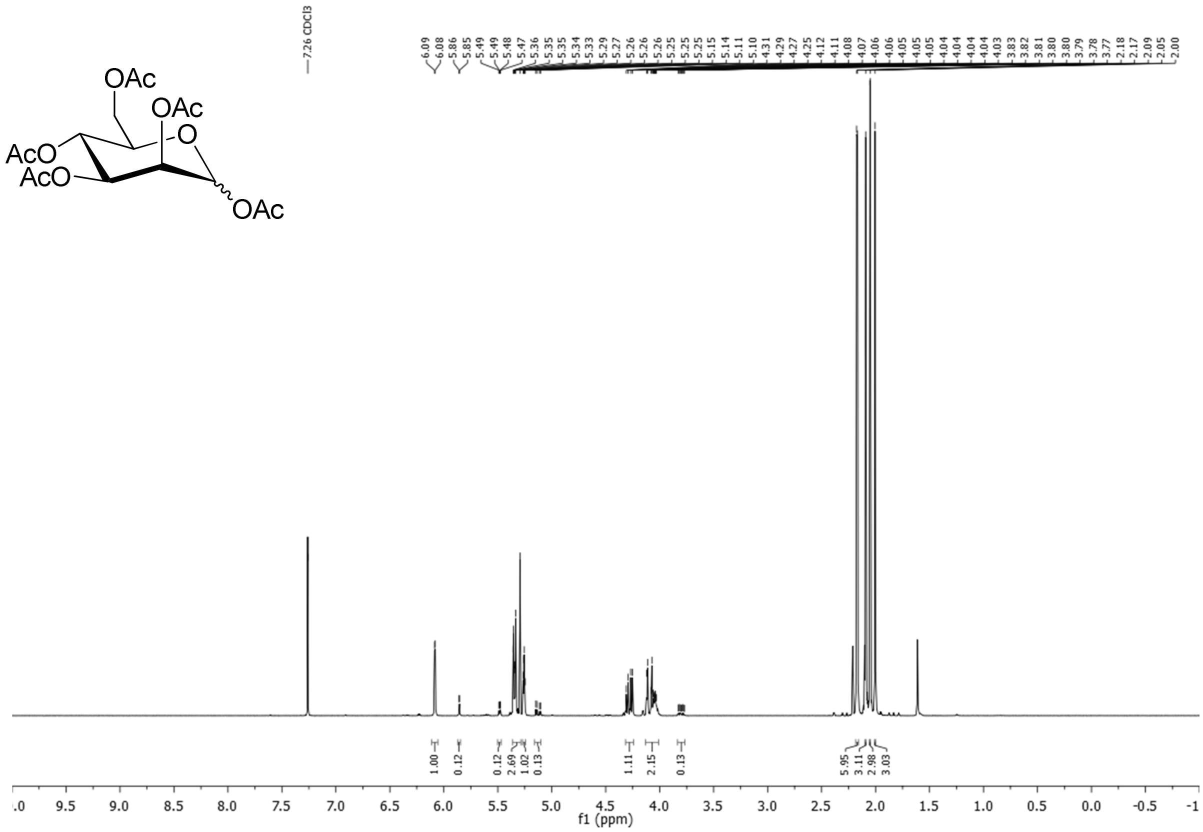

Figure S1. ^1H NMR (600 MHz, $CDCl_3$), compound **2**.

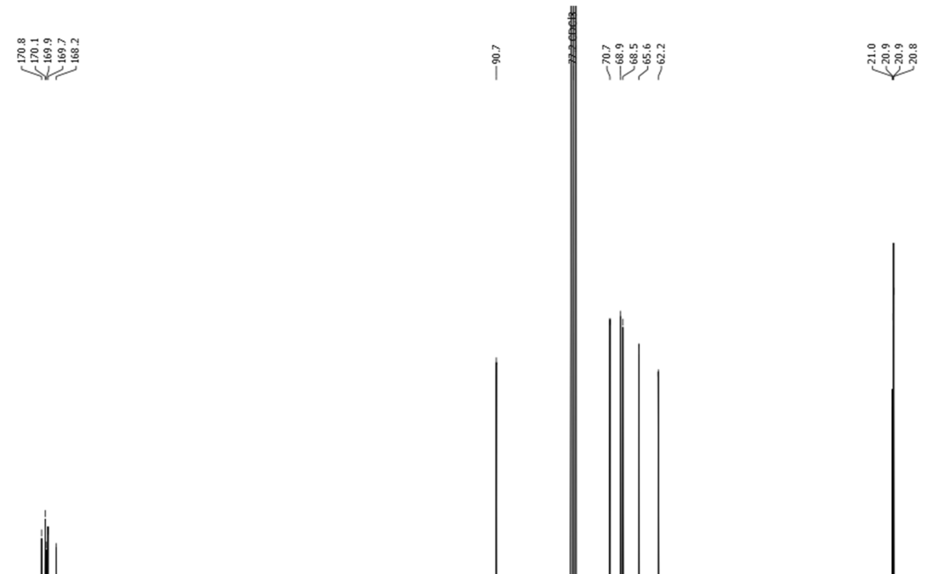

Figure S2. ^{13}C NMR (151 MHz, $CDCl_3$), compound **2**.

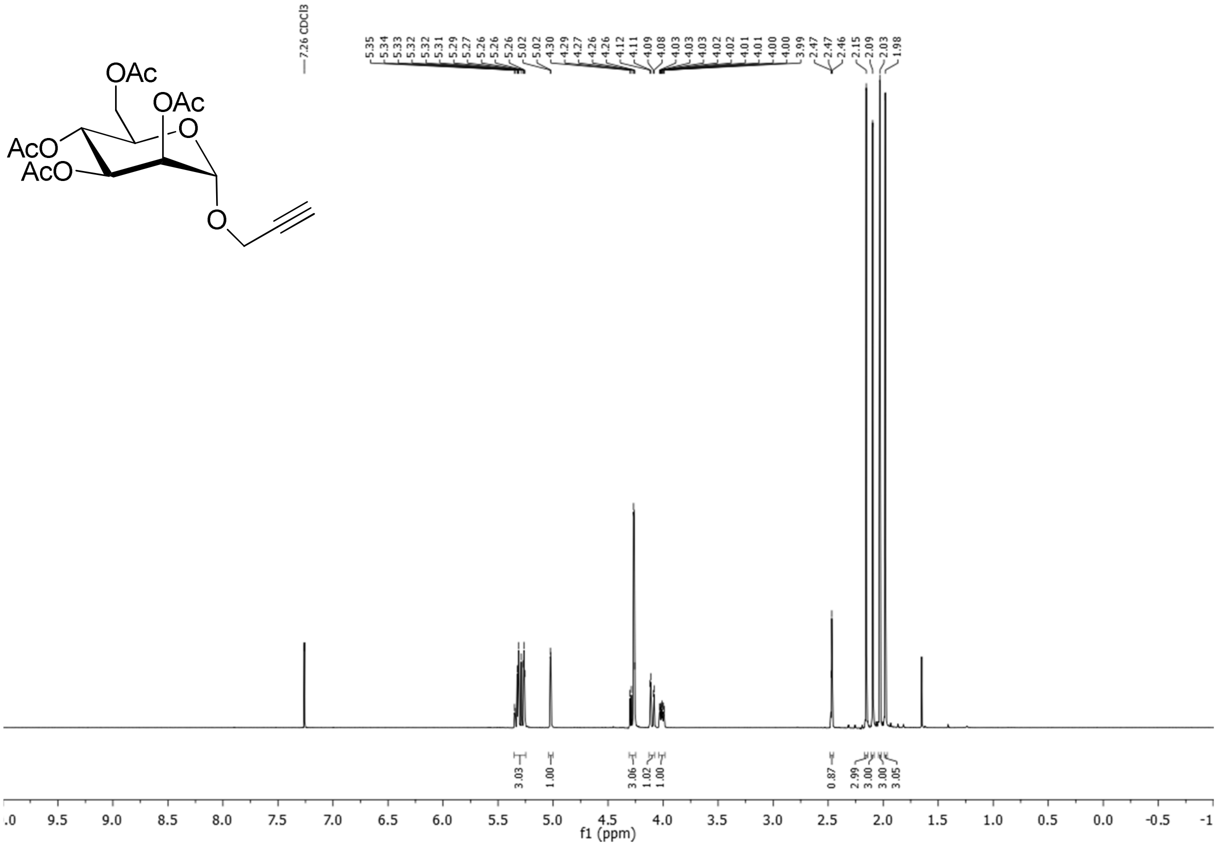

Figure S3. ^{1}H NMR (400 MHz, CDCl$_3$), compound 3.

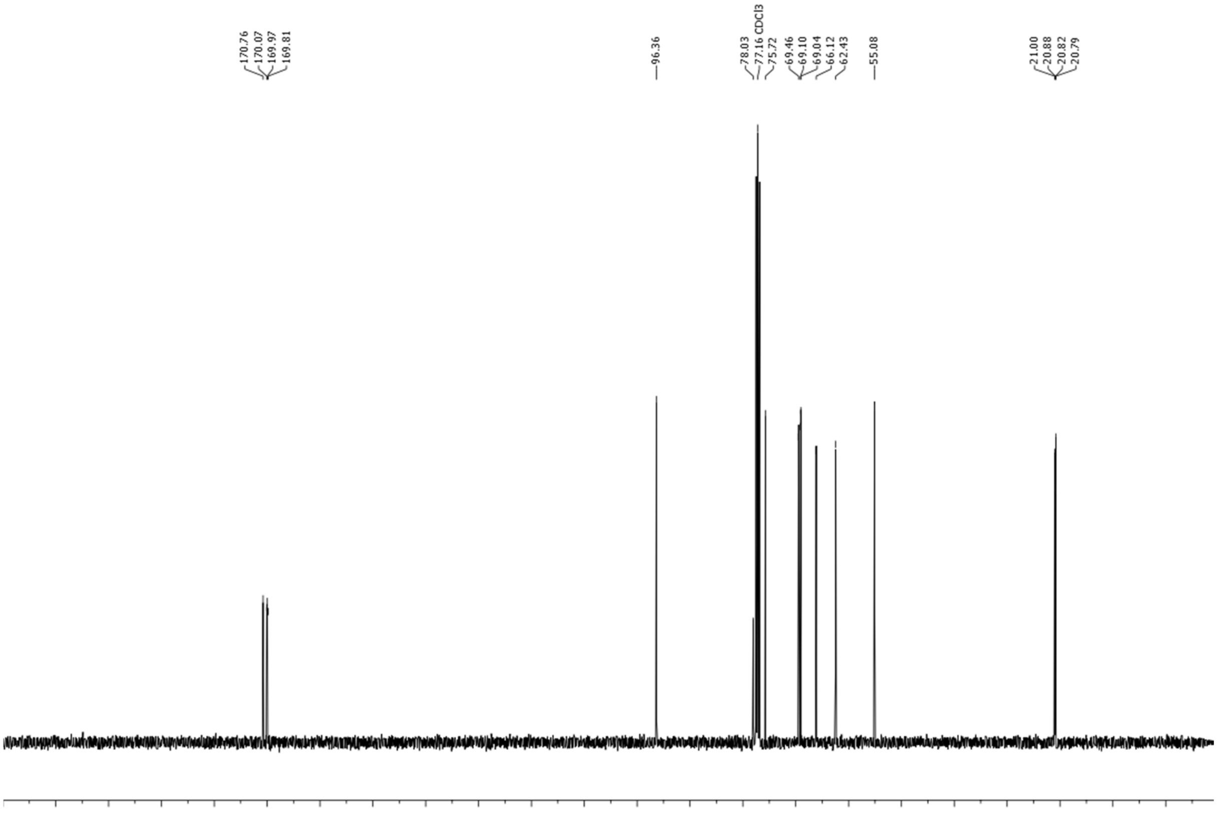

Figure S4. ^{13}C NMR (100.6 MHz, CDCl$_3$), compound 3.

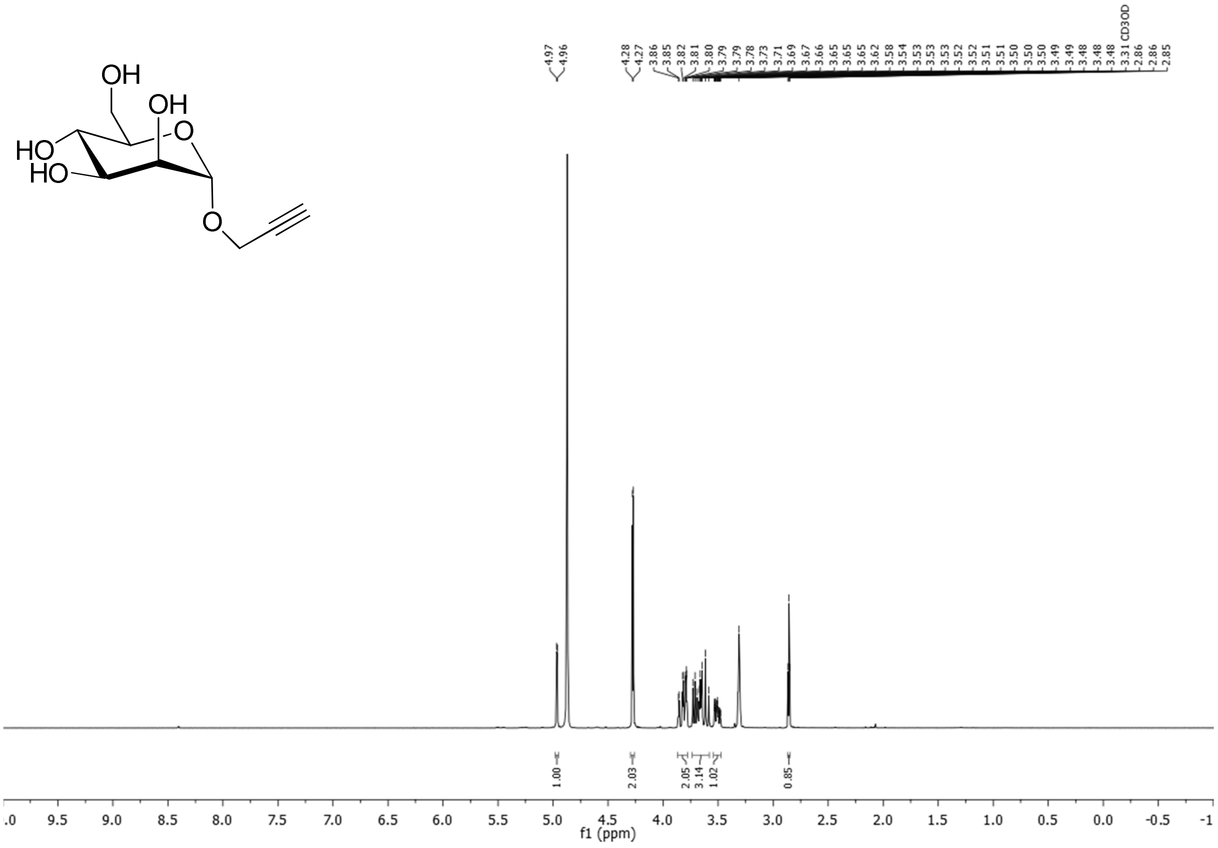

Figure S5. ^1H NMR (400 MHz, CD_3OD), compound **4**.

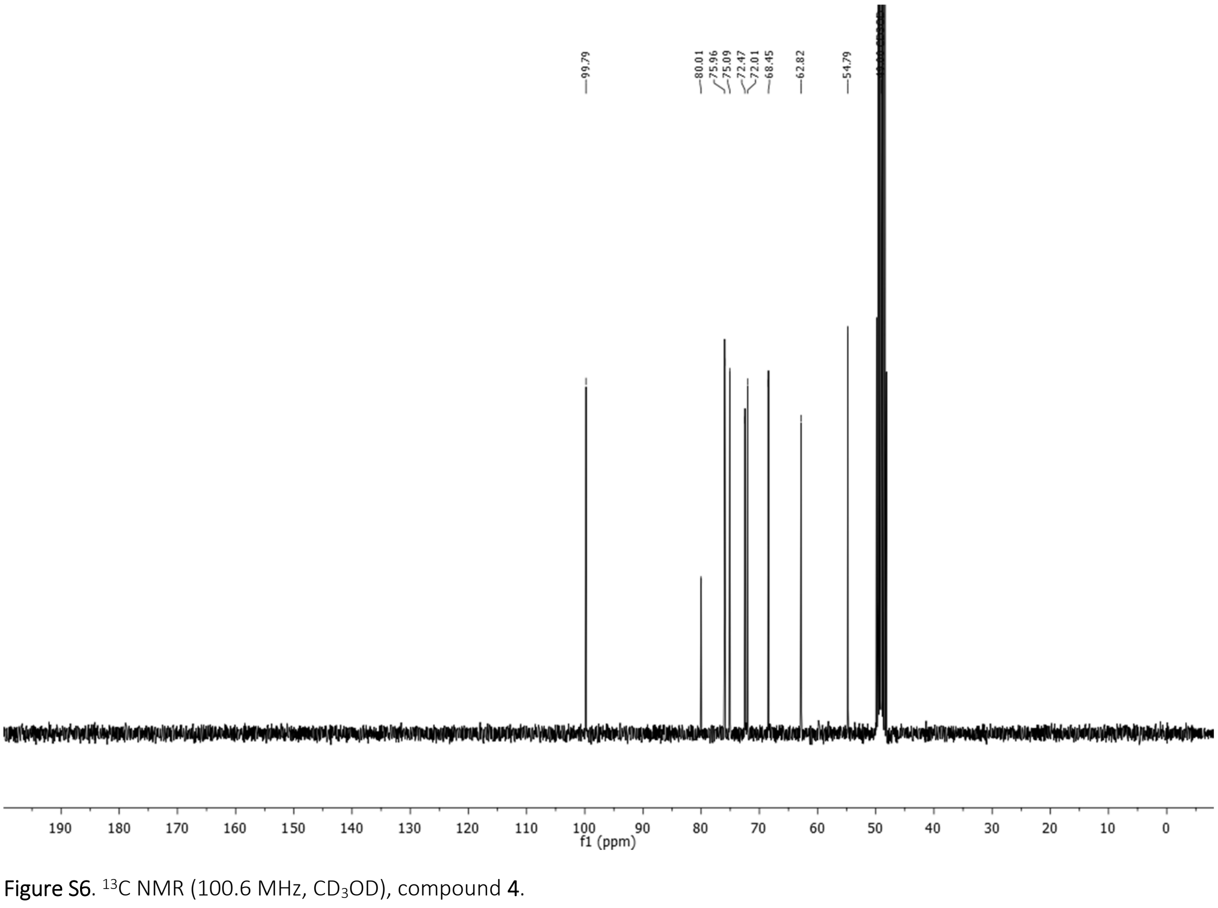

Figure S6. ^{13}C NMR (100.6 MHz, CD_3OD), compound **4**.

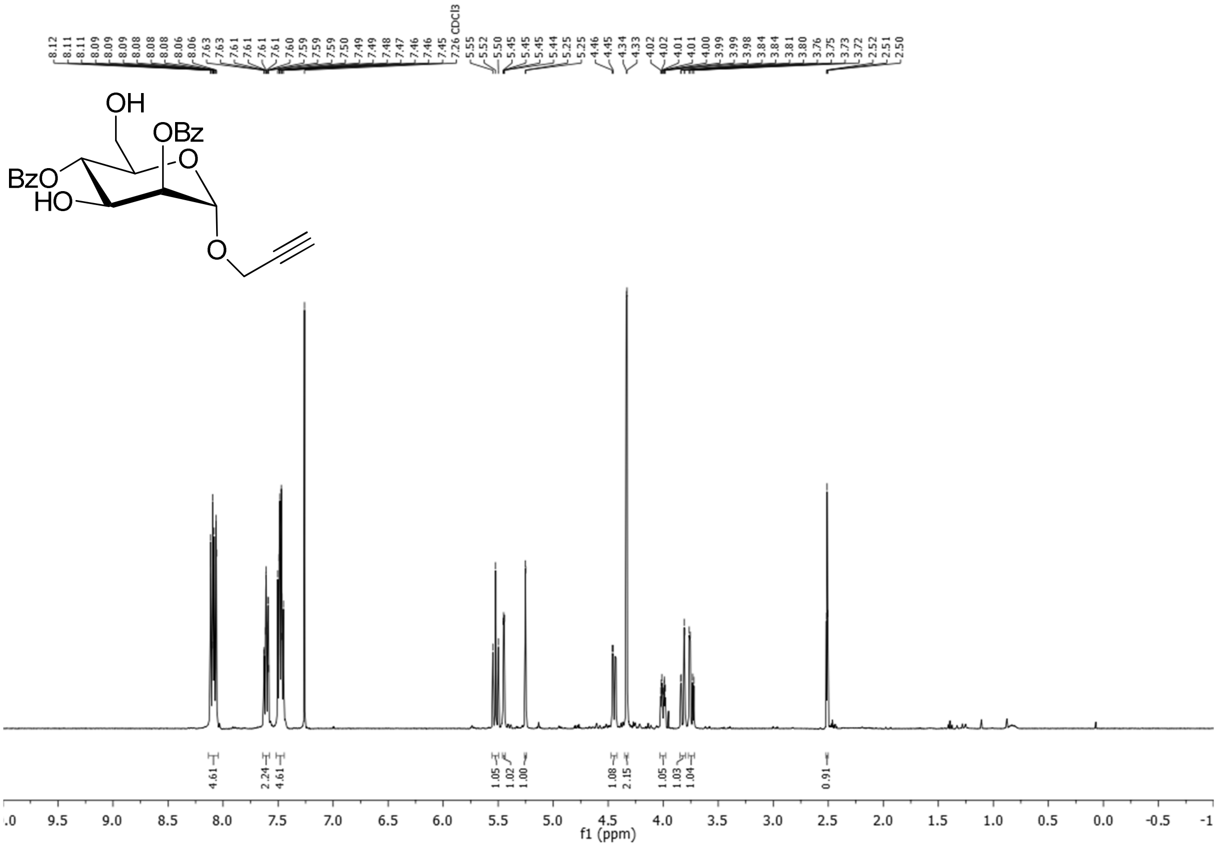

Figure S7. ^{1}H NMR (400 MHz, CDCl$_3$), compound **5**.

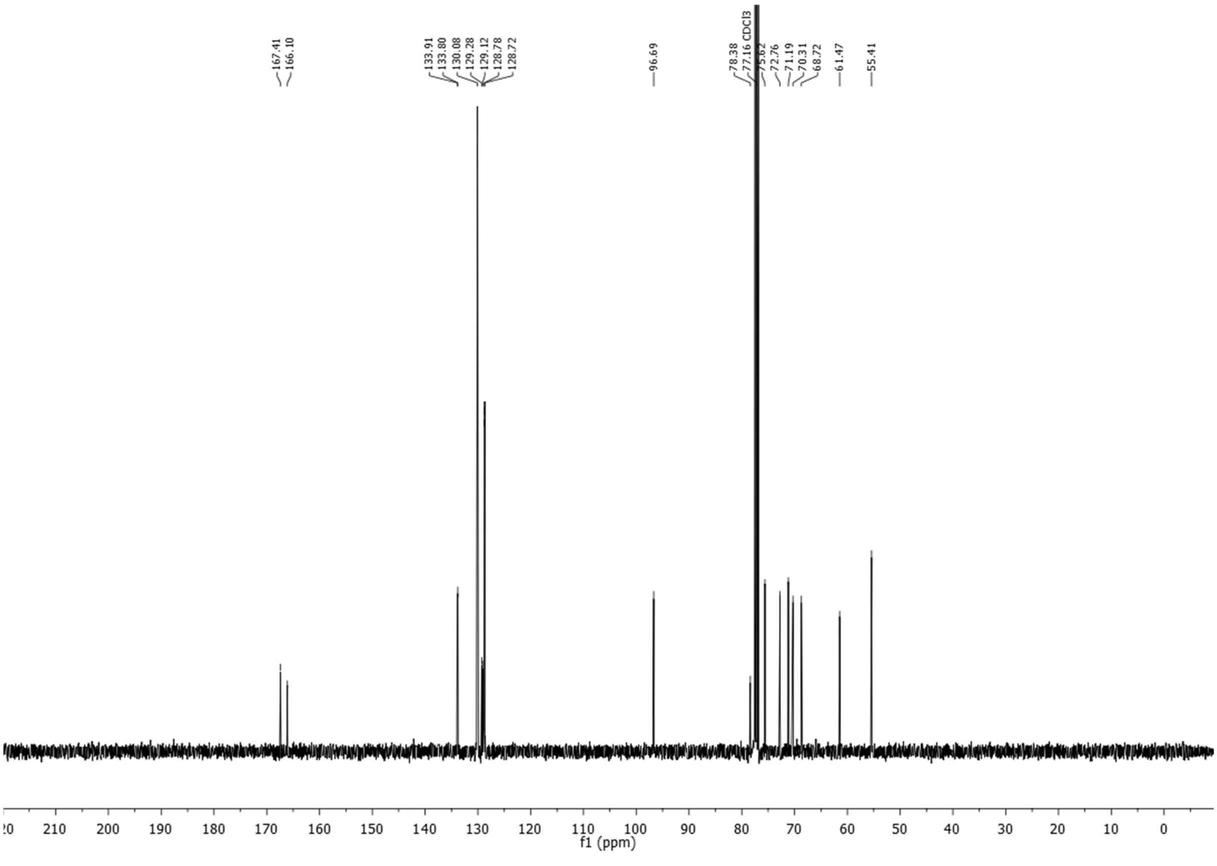

Figure S8. ^{13}C NMR (100.6 MHz, CDCl$_3$), compound **5**.

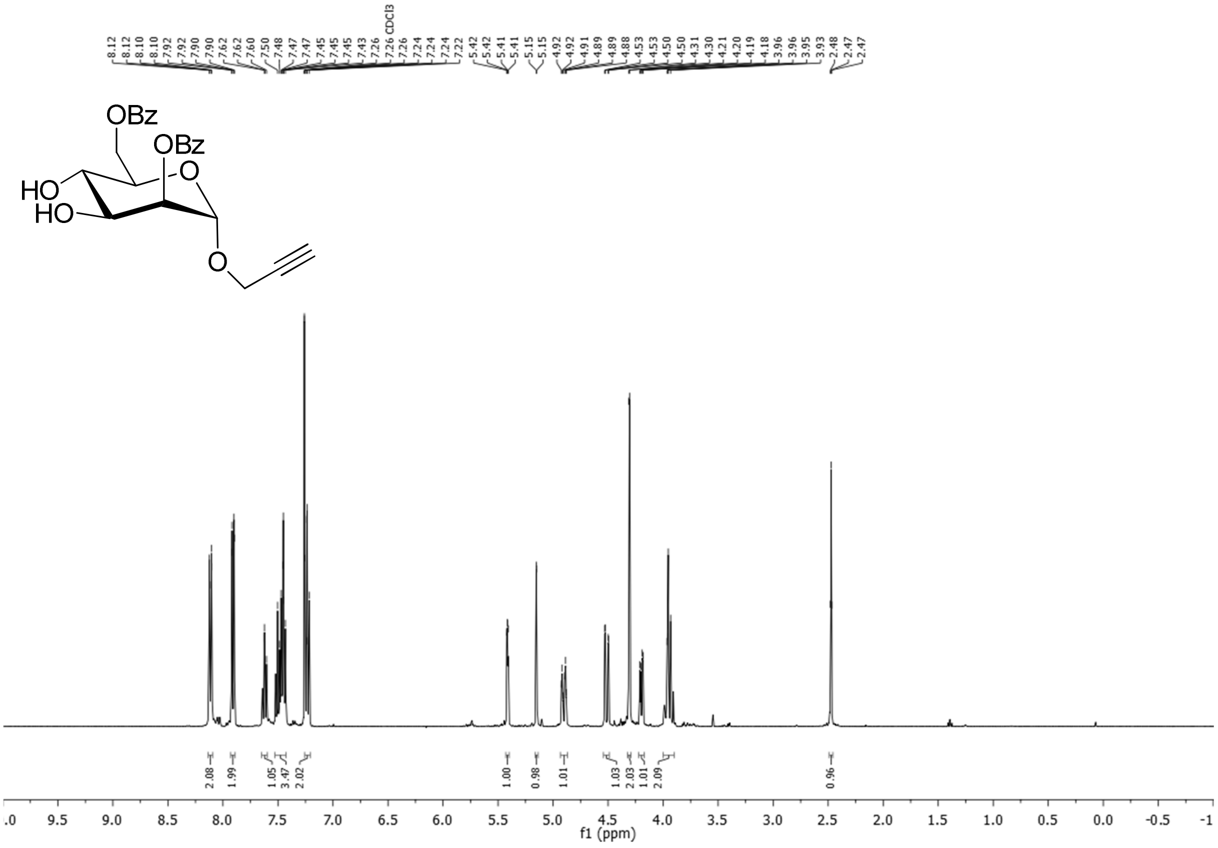

Figure S9. ^{1}H NMR (400 MHz, $CDCl_3$), compound **6**.

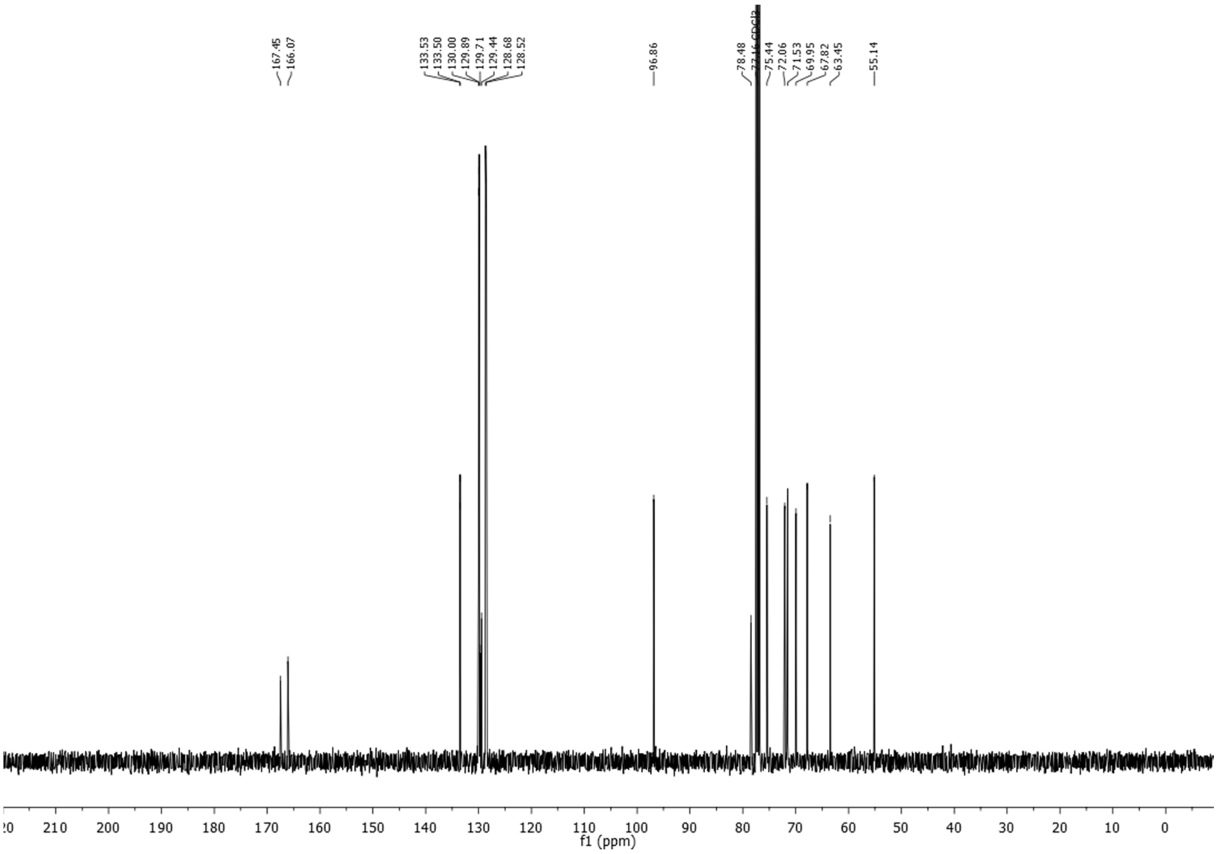

Figure S10. ^{13}C NMR (100.6 MHz, $CDCl_3$), compound **6**.

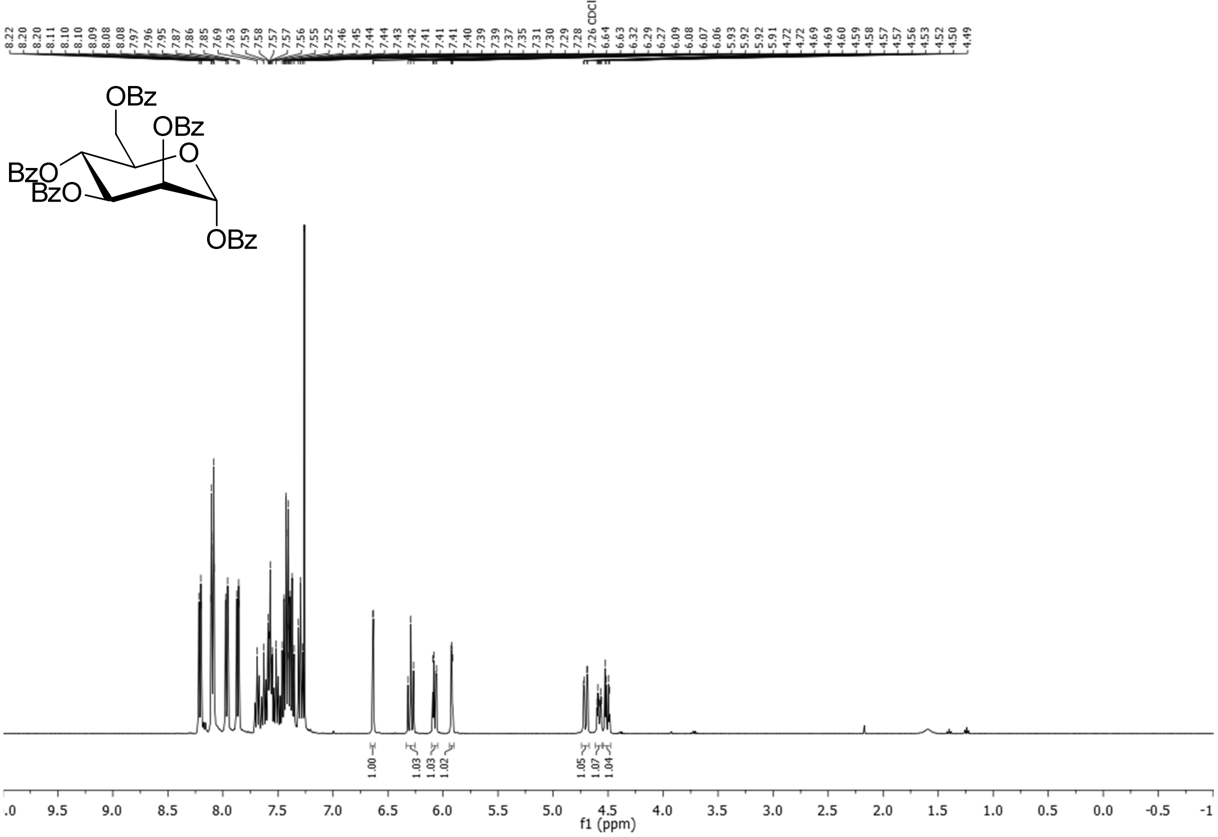

Figure S11. ^1H NMR (400 MHz, $CDCl_3$), compound **7** (α-anomer).

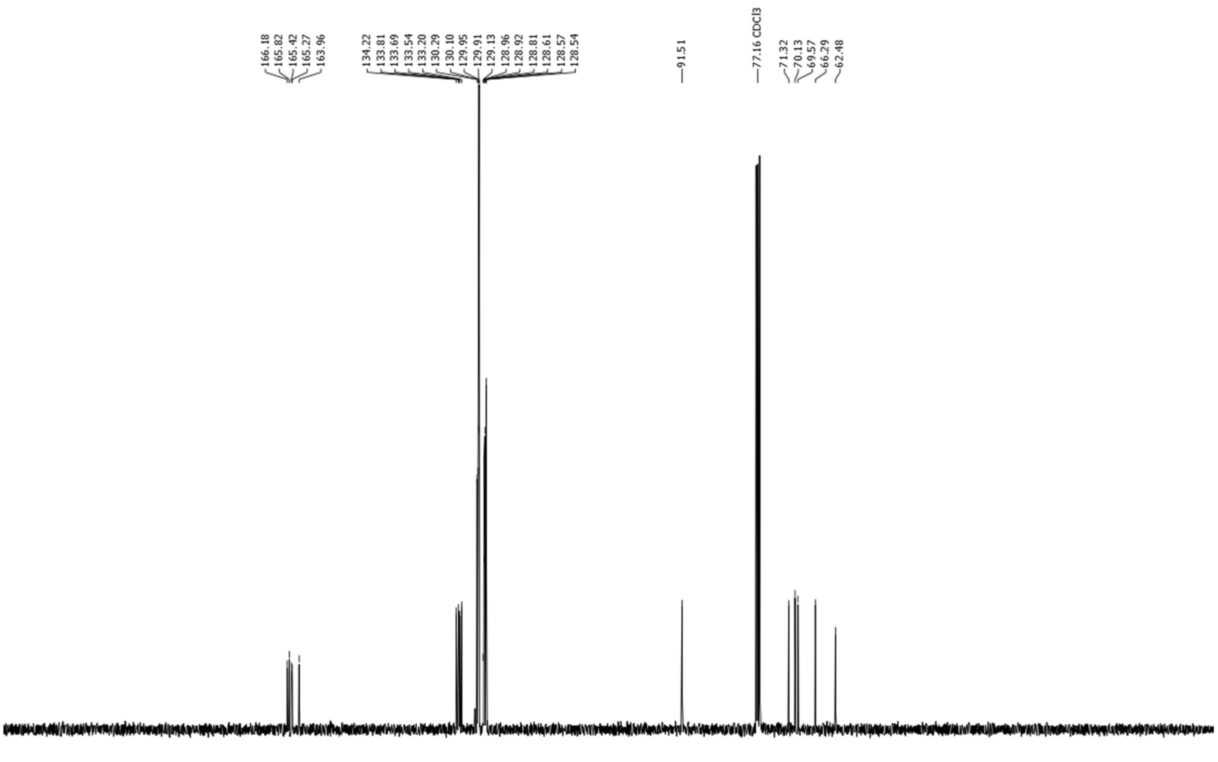

Figure S12. ^{13}C NMR (100.6 MHz, $CDCl_3$), compound **7** (α-anomer).

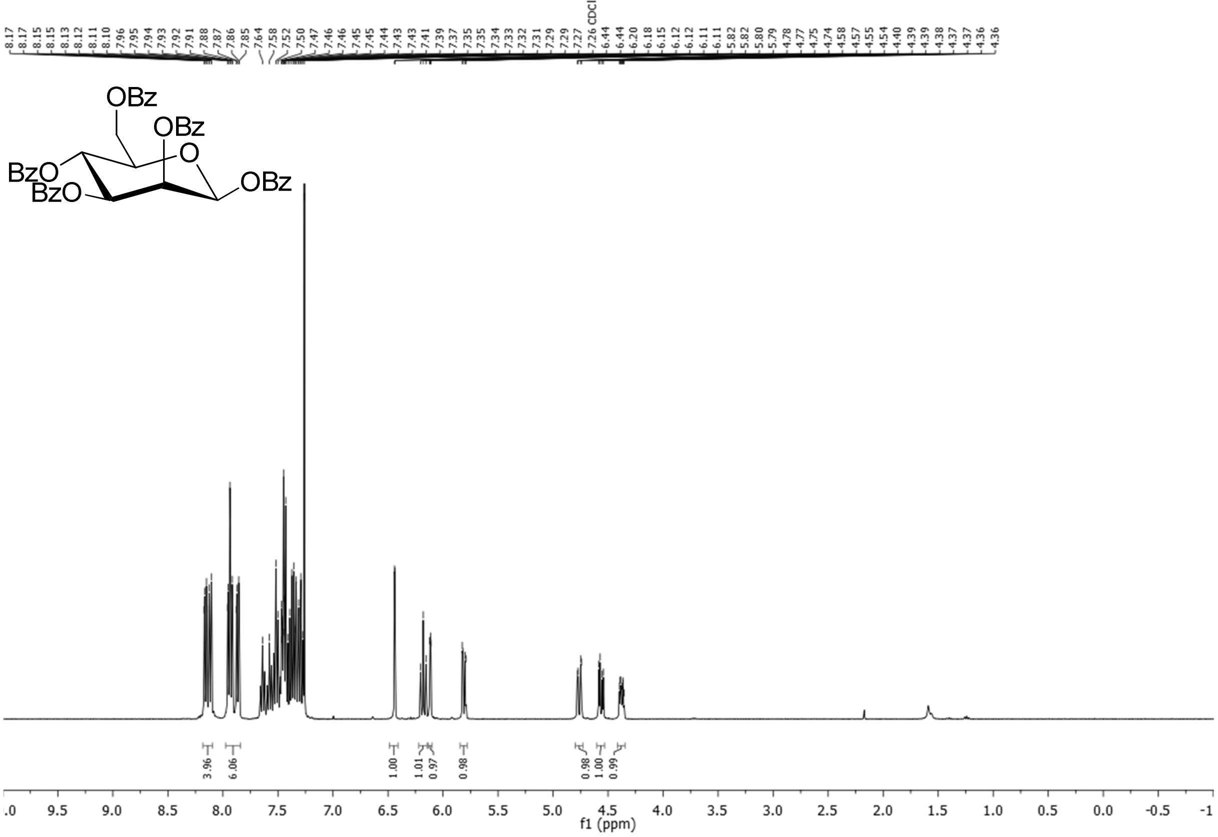

Figure S13. ^{1}H NMR (400 MHz, $CDCl_3$), compound **7** (β-anomer).

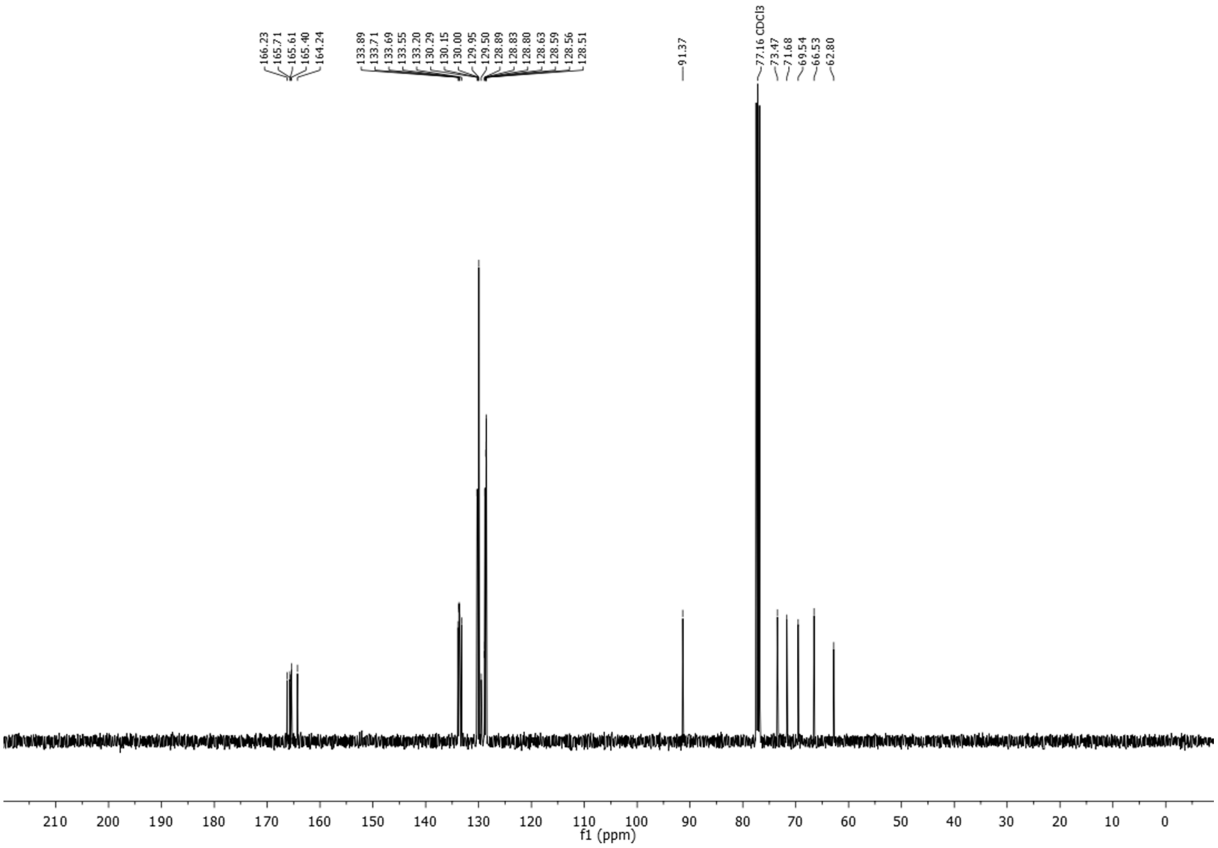

Figure S14. ^{13}C NMR (100.6 MHz, $CDCl_3$), compound **7** (β-anomer).

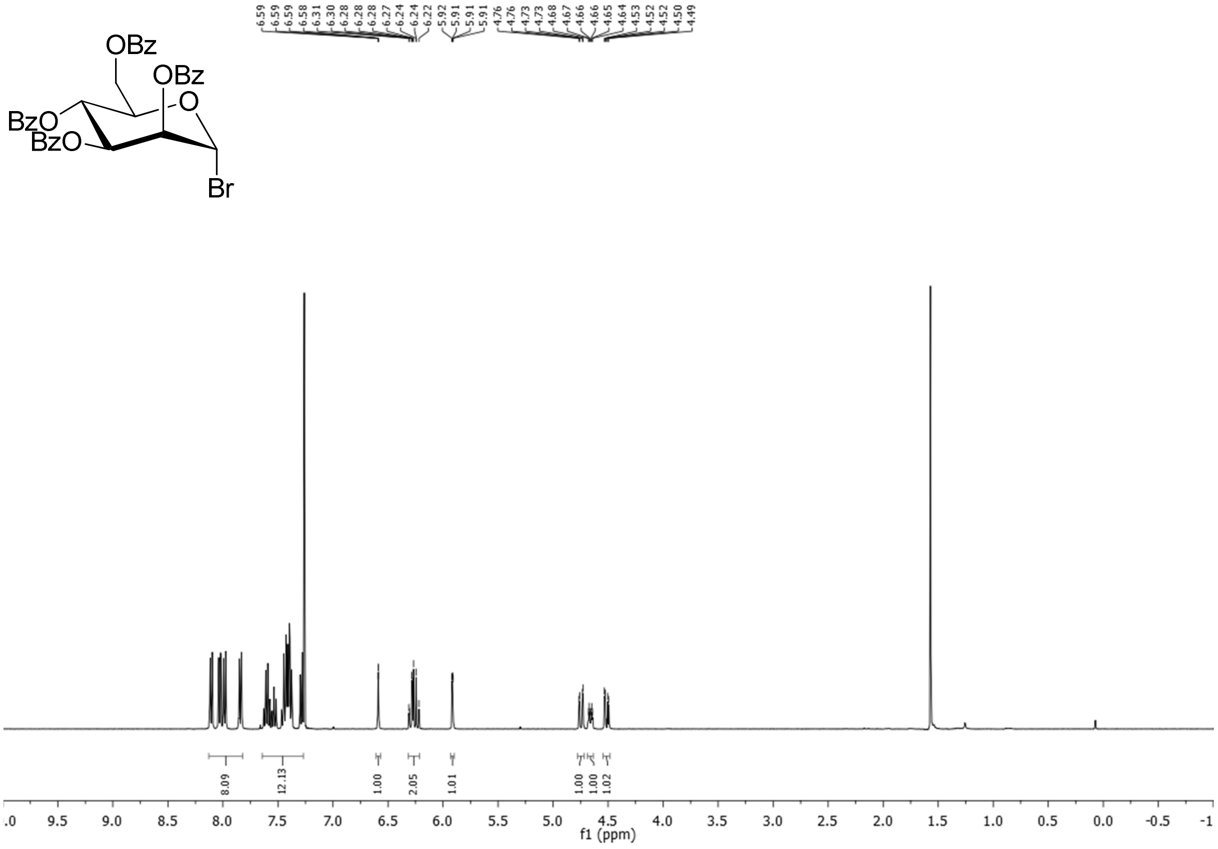

Figure S15. ^{1}H NMR (400 MHz, CDCl$_3$), compound **8**.

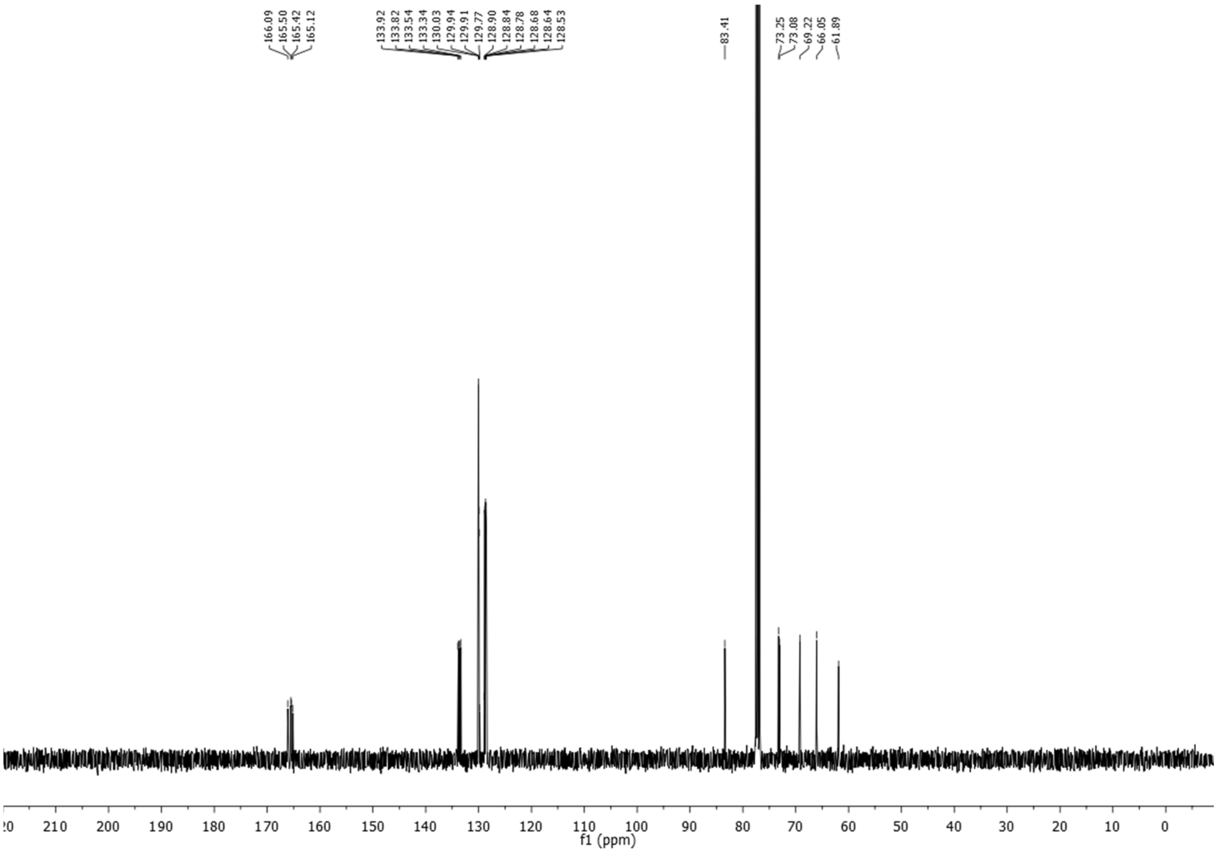

Figure S16. ^{13}C NMR (100.6 MHz, CDCl$_3$), compound **8**.

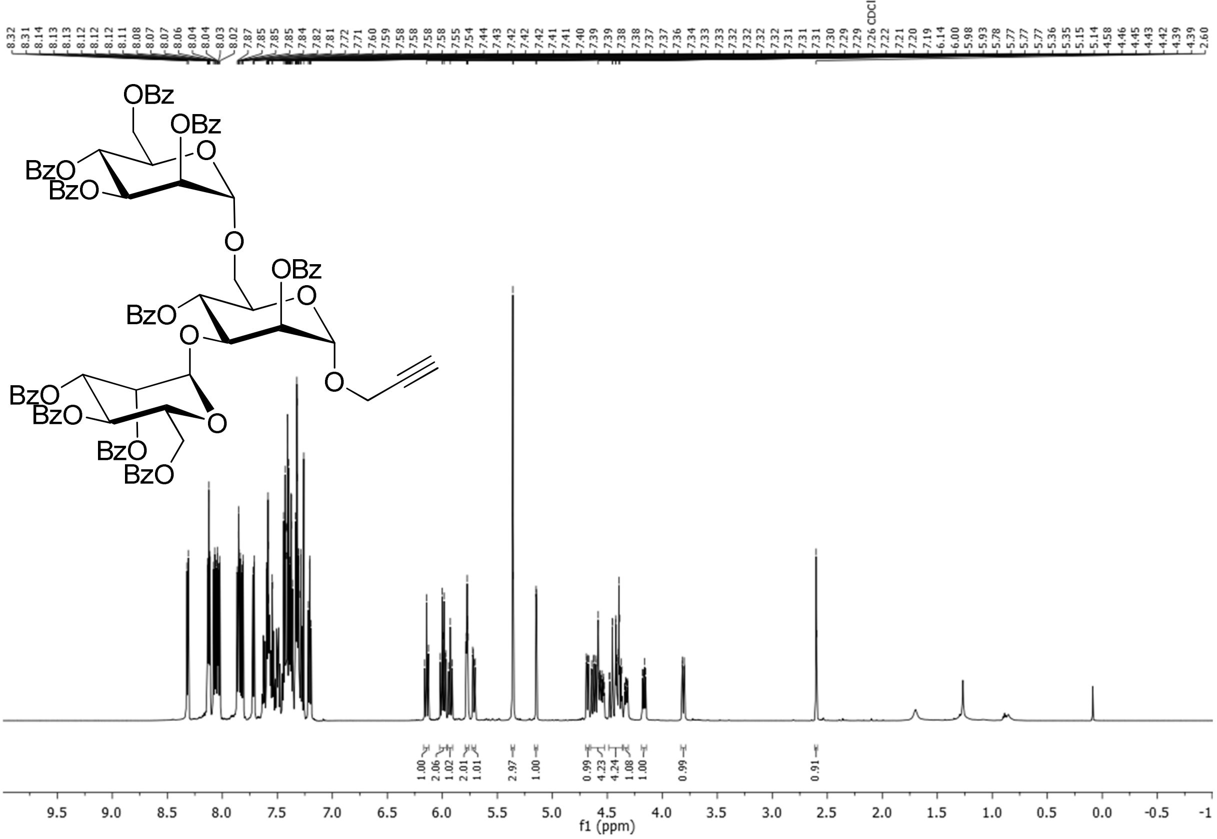

Figure S17. ^{1}H NMR (600 MHz, CDCl$_3$), compound **9**.

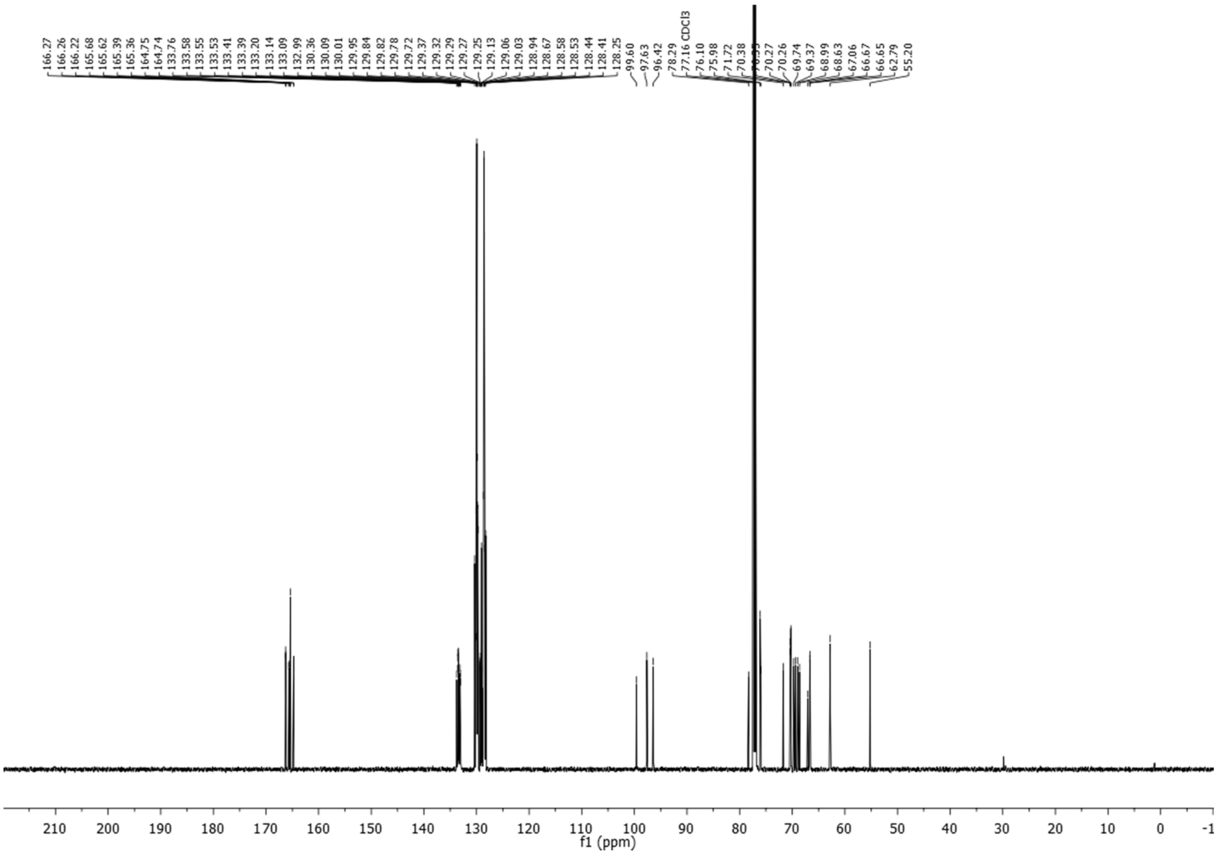

Figure S18. ^{13}C NMR (151 MHz, CDCl$_3$), compound **9**.

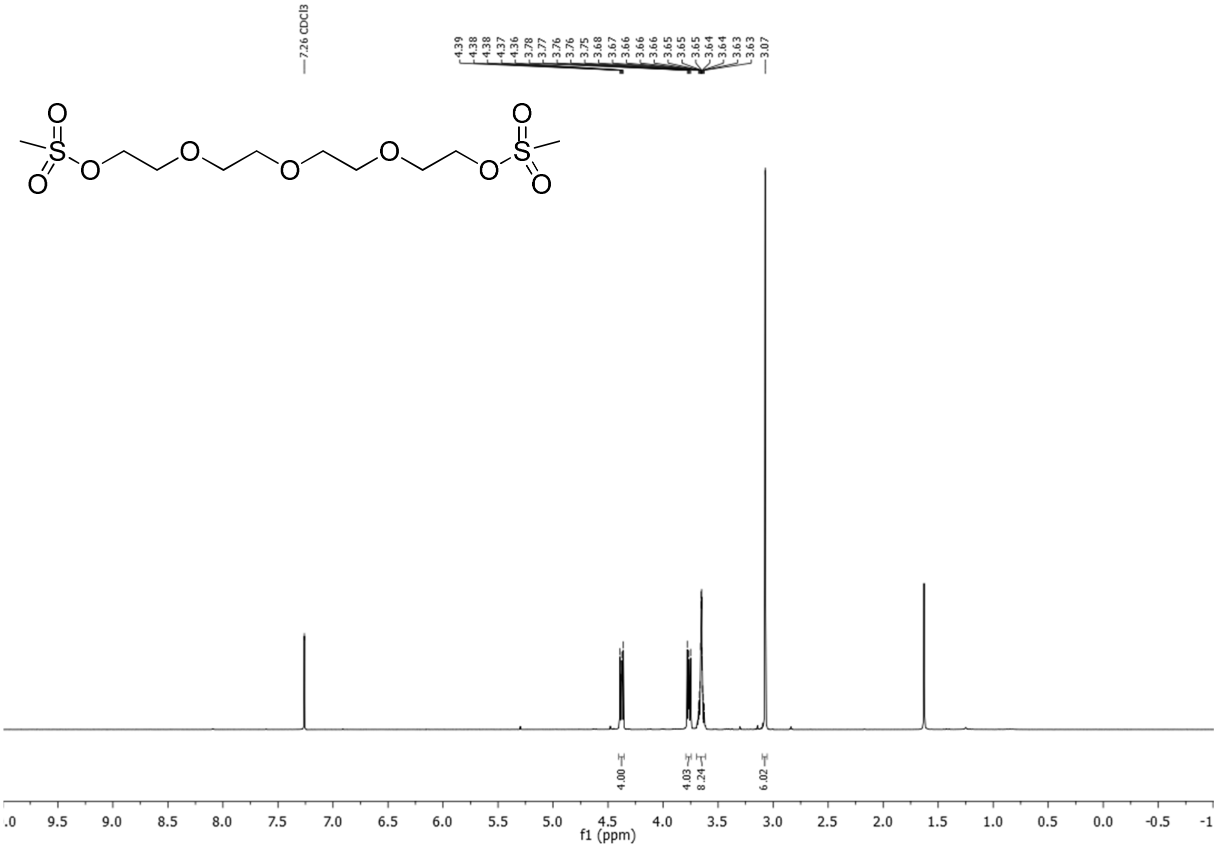

Figure S19. ^{1}H NMR (300 MHz, $CDCl_3$), compound **11**.

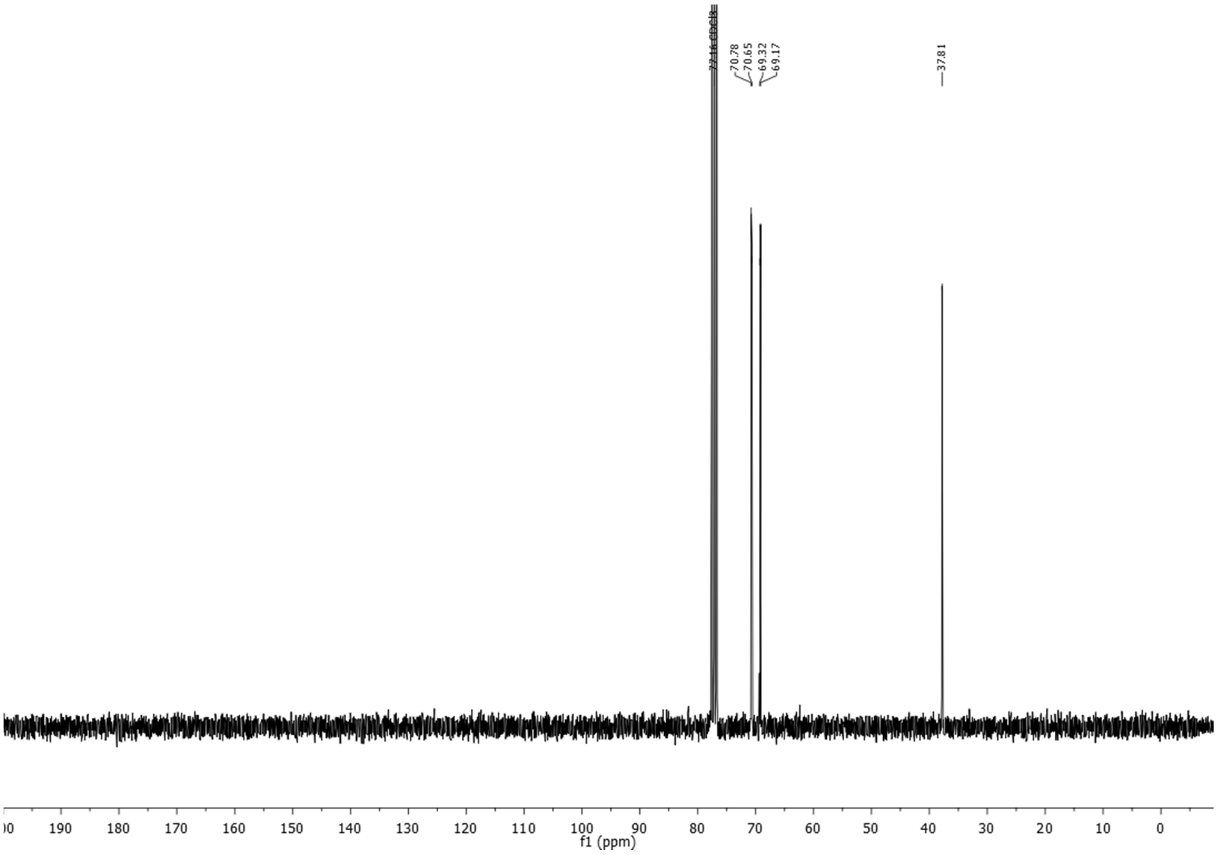

Figure S20. ^{13}C NMR (75 MHz, $CDCl_3$), compound **11**.

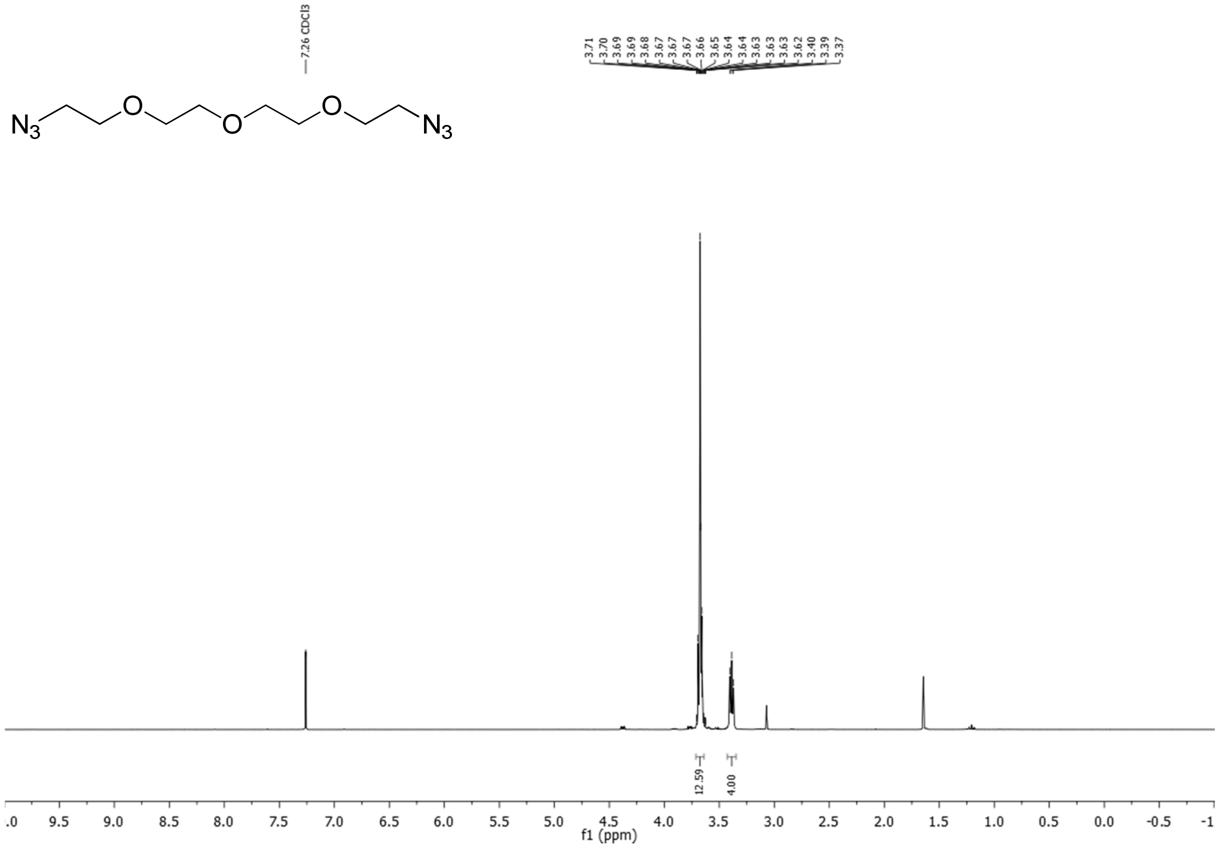

Figure S21. ^{1}H NMR (300 MHz, $CDCl_3$), compound **12**.

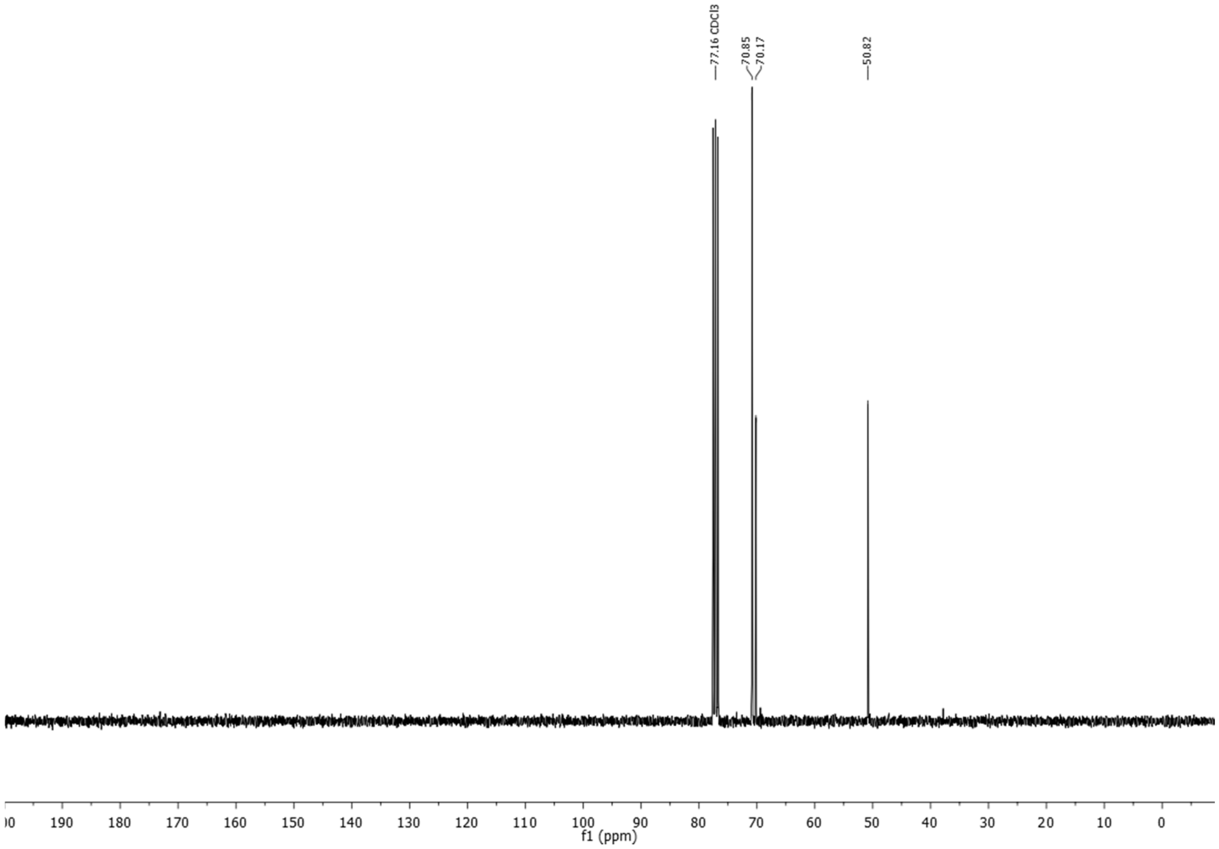

Figure S22. ^{13}C NMR (75 MHz, $CDCl_3$), compound **12**.

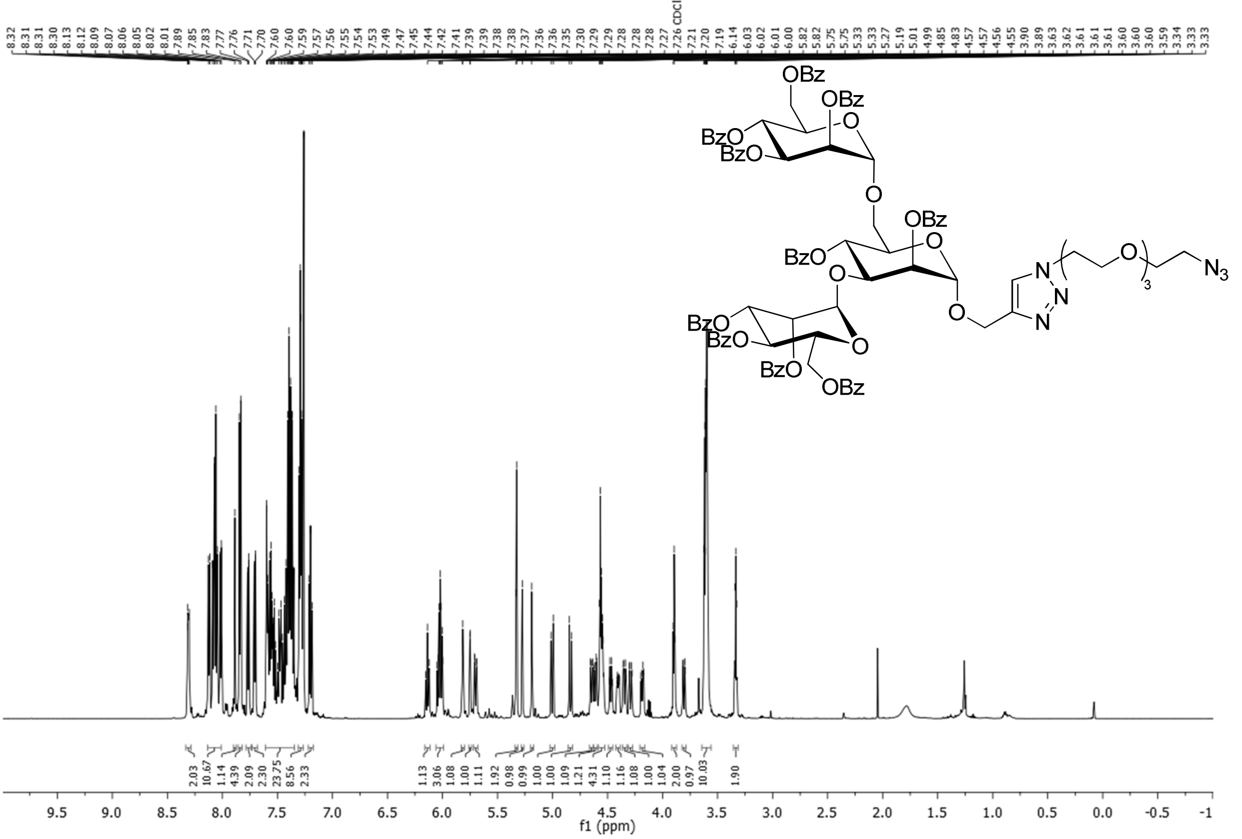

Figure S23. ^1H NMR (600 MHz, $CDCl_3$), compound **13**.

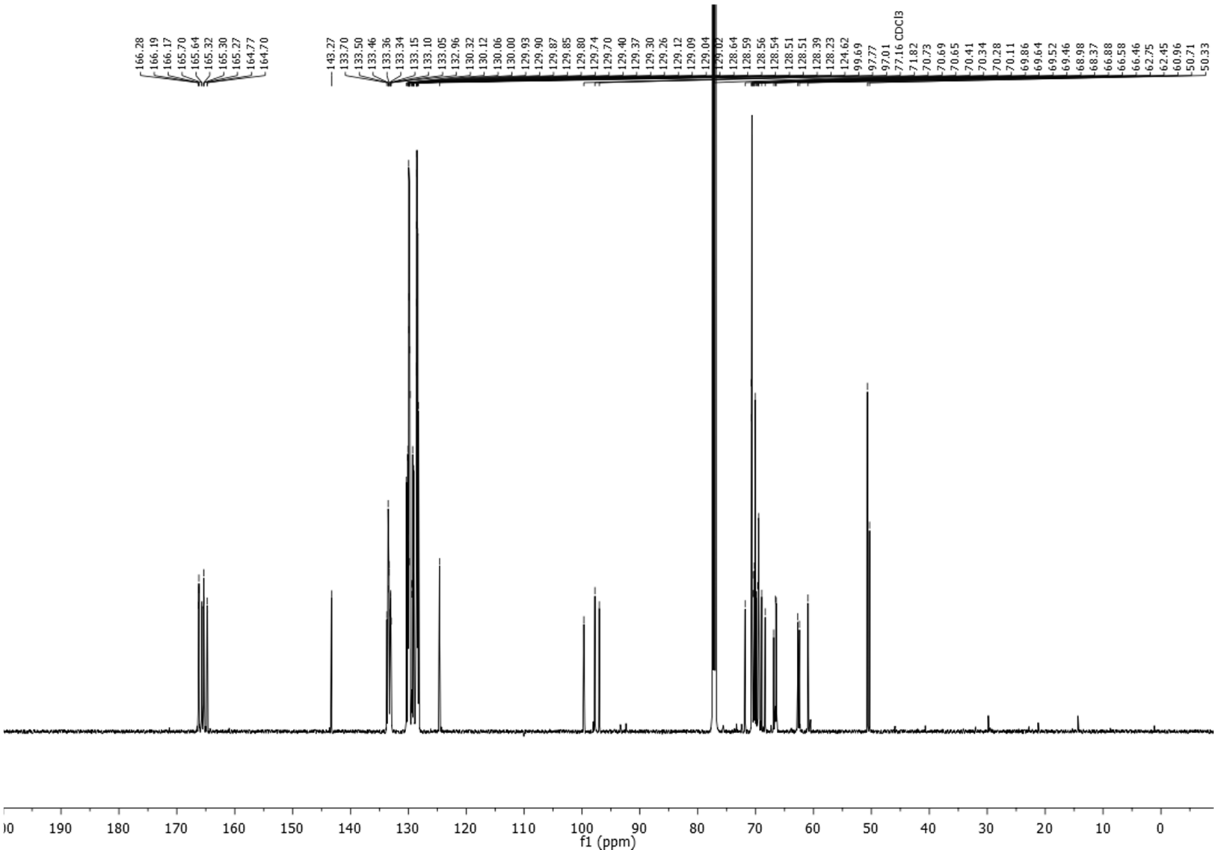

Figure S24. ^{13}C NMR (151 MHz, $CDCl_3$), compound **13**.

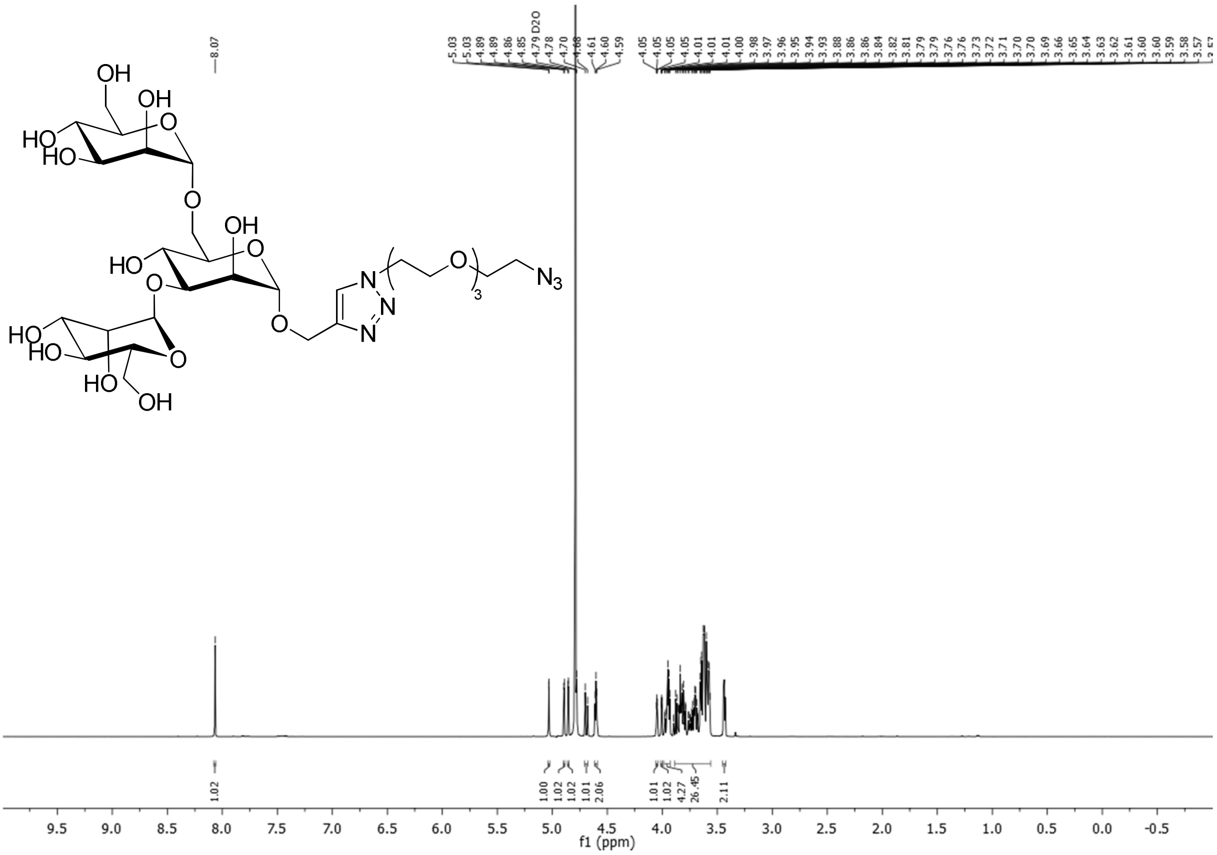

Figure S25. ^{1}H NMR (600 MHz, D_2O), compound **14**.

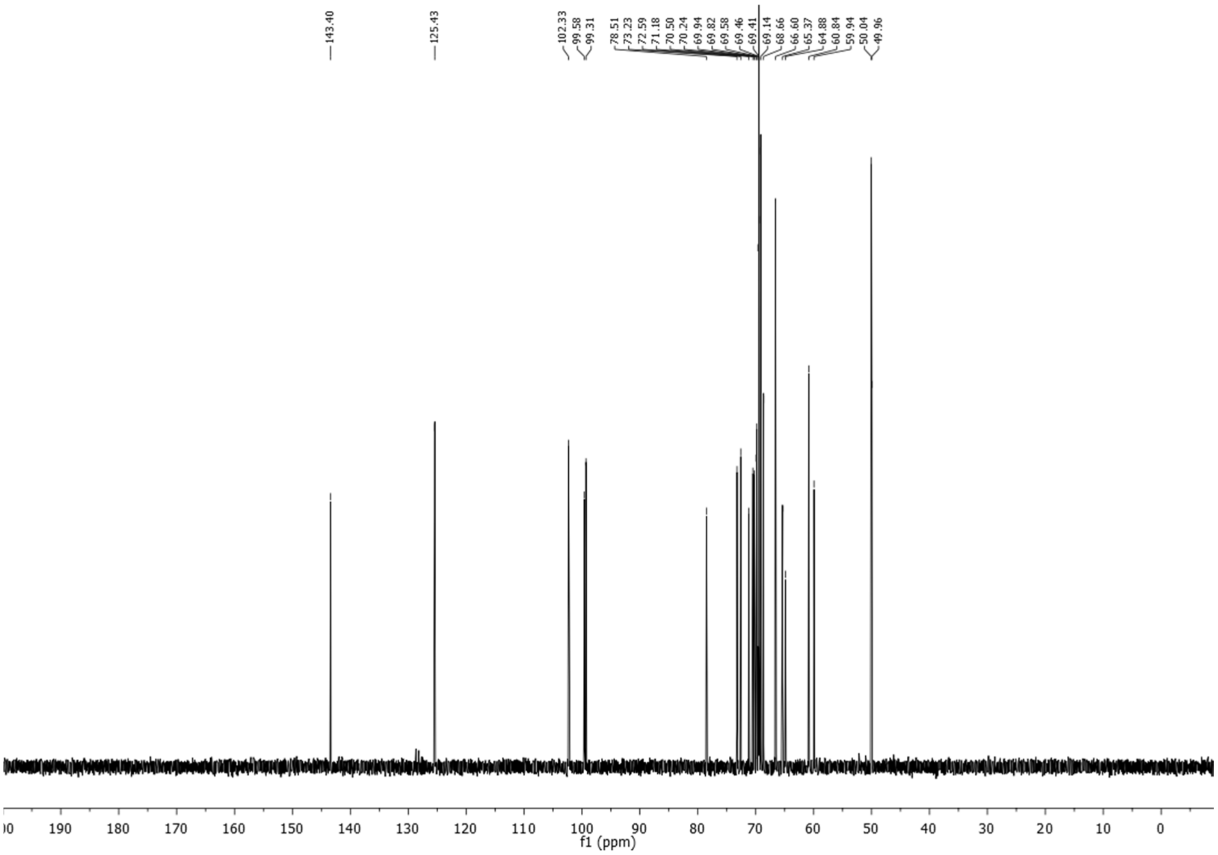

Figure S26. ^{13}C NMR (151 MHz, D_2O), compound **14**.

S2. Characterization of trimannose-alkyne-1,2-bis(hexadecyl)glycerol-*hb*PG$_{63}$

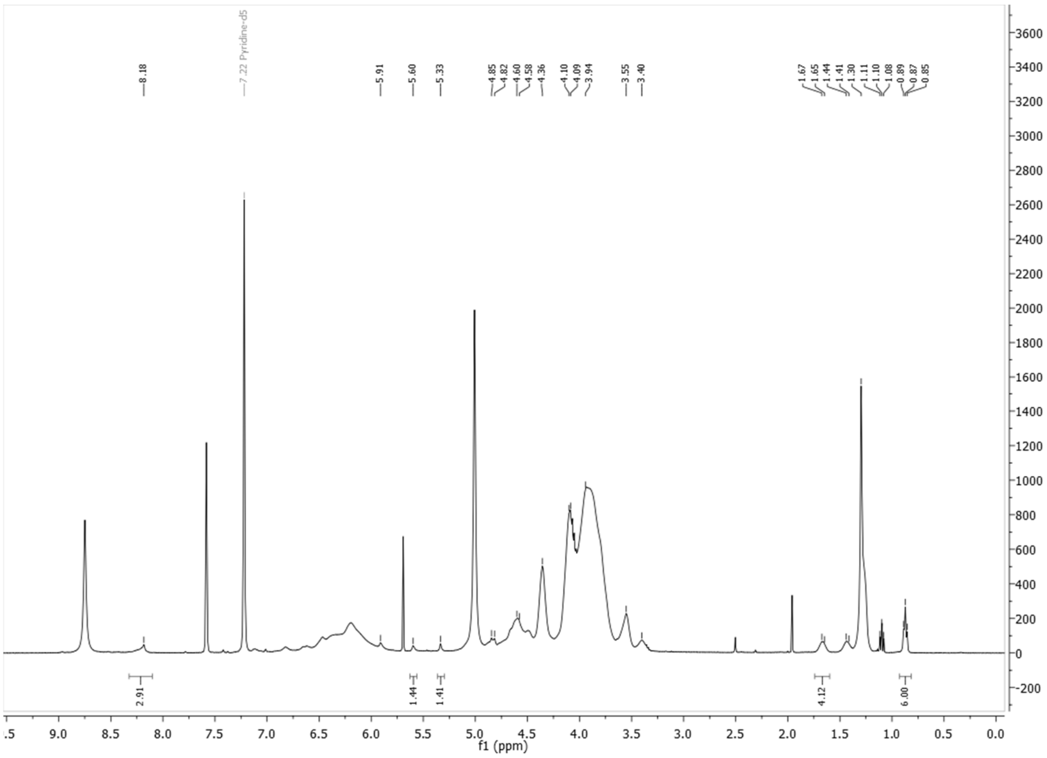

Figure S27. ^{1}H NMR (400 MHz, pyridine-d_5), trimannose-alkyne-BisHD-*hb*PG$_{63}$.

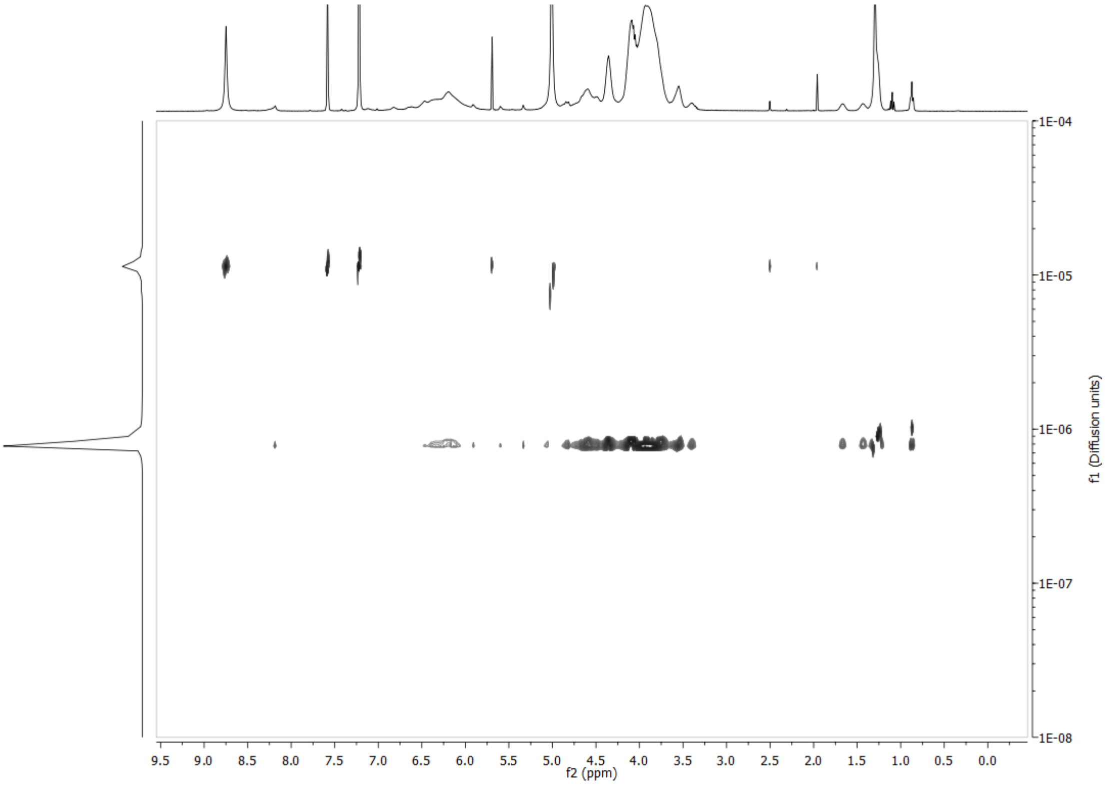

Figure S28. Diffusion-ordered NMR spectrum (DOSY) (400 MHz, pyridine-d_5), trimannose-alkyne-BisHD-*hb*PG$_{63}$.

S3. Fluorescent labeling with Oregon Green 488 (OG 488) azide

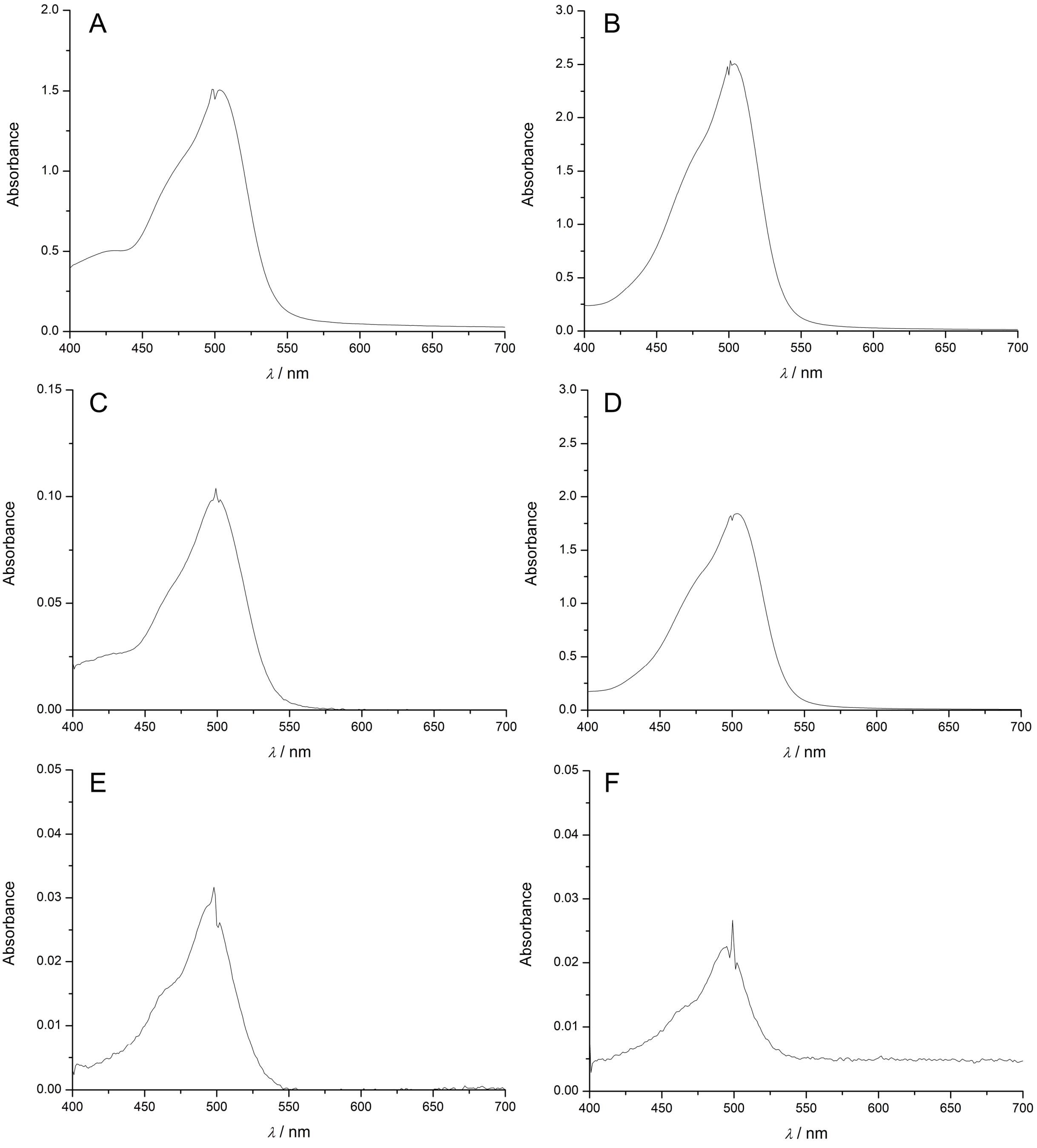

Figure S29. UV-Vis spectra of OG 488-alkyne-BisHD-*hb*PG$_{63}$ after purification (A), of the first (C) and of the 18th (E) filtrate of the spin filtration; UV-Vis spectra of OG 488-trimannose-alkyne-BisHD-*hb*PG$_{63}$ after purification (B), of the first (D) and of the 18th (F) filtrate of the spin filtration.

S4. Radiolabeling

a. Polyether lipids

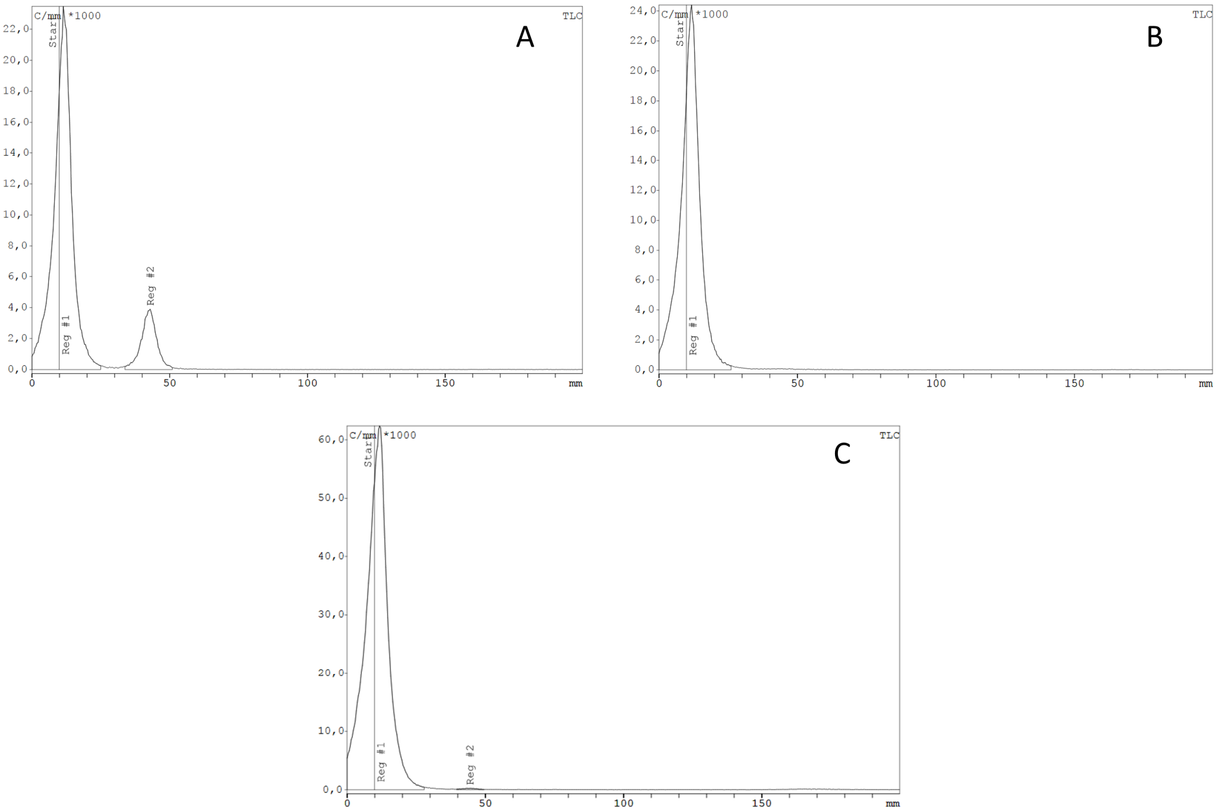

Figure S30. Radio-TLCs of the radiolabeling of alkyne$_4$-BisHD-*hb*PG$_{63}$ (A: reaction time 1 min, RCY 86 %; B: reaction time 10 min, RCY 98 %) and trimannose-alkyne-BisHD-*hb*PG$_{63}$ (C: reaction time 10 min, RCY 98 %) with [^{18}F]F-TEG-N$_3$ via CuAAC. Reg #1 corresponds to the respective polyether lipid, Reg #2 attributes to [^{18}F]F-TEG-N$_3$.

b. Removal of copper

Subsequent to the click reaction, copper was removed using a Chelex 100 resin (BioRad), which (according to the supplier) exhibits uniquely high selectivities for metal ions. In order to investigate the efficiency, we added sodium sulfide to a sample of the purified reaction mixture and to a sample prior to the removal of copper. In the first case, we observed no precipitation of copper sulfide, whereas in the second case we obtained a darkish precipitate of copper sulfide.

S5. Liposome characterization

a. Liposome size

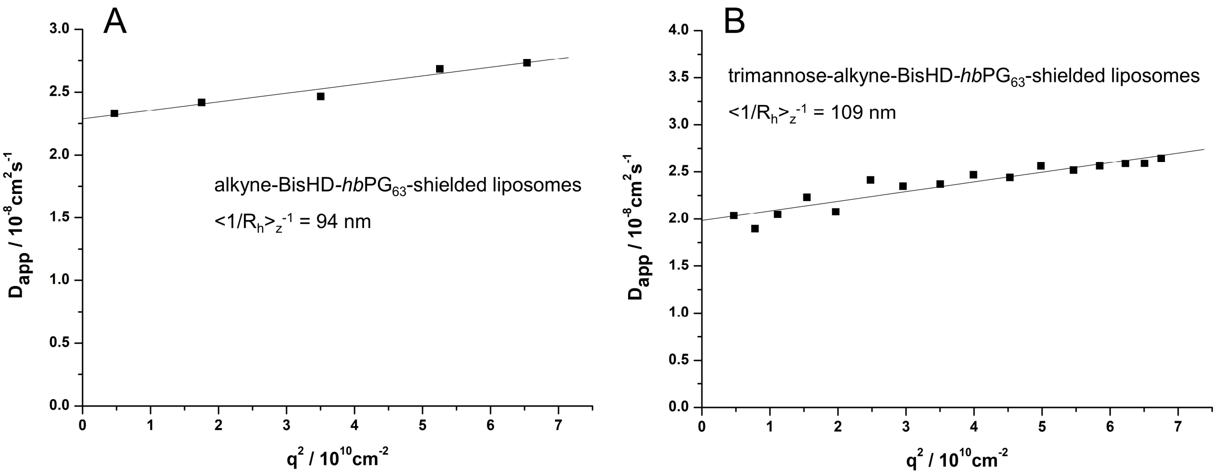

Figures S31. D_{app} plotted against q^2 data and thereof calculated hydrodynamic radii of alkyne-BisHD-*hb*PG$_{63}$-shielded liposomes (A) and trimannose-alkyne-BisHD-*hb*PG$_{63}$-shielded liposomes (B). Experiments were conducted with an aliquot of the liposomes used for the animal experiments after complete disappearance of ^{18}F-radioactivity.

b. Liposome stability

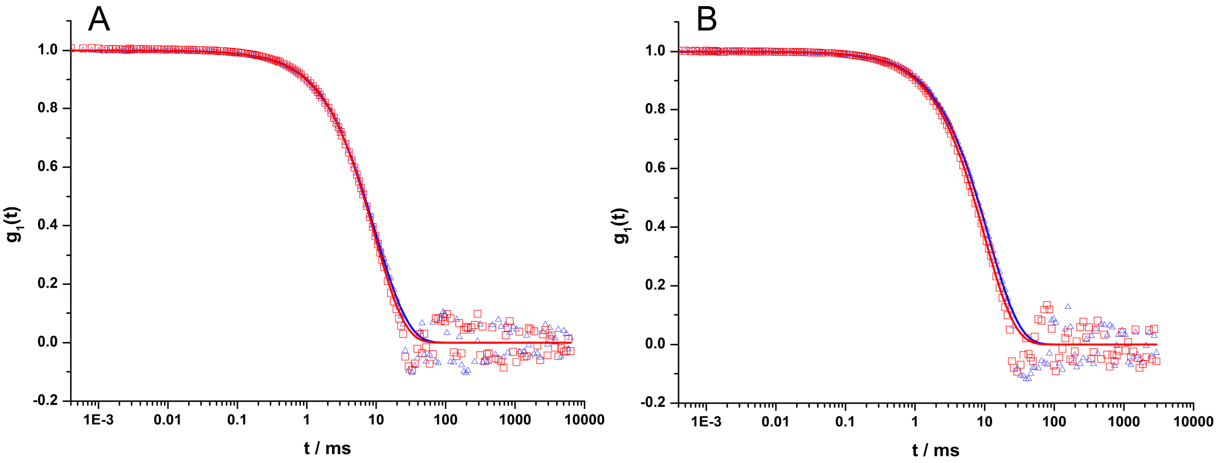

Figure S32. Autocorrelation functions of alkyne-BisHD-*hb*PG$_{63}$-shielded liposomes (A) and trimannose-alkyne-BisHD-*hb*PG$_{63}$-shielded liposomes (B). Blue curves are acquired shortly after the manufacturing of the liposomes. Red curves are acquired at least one month later (A: 1 months later; B: 7 month later).

An aliquot of the liposomes (alkyne-BisHD-*hb*PG$_{63}$-shielded and trimannose-alkyne-BisHD-*hb*PG$_{63}$-shielded) in PBS buffer used for the animal experiments was stored at 4 °C until complete disappearance of radiation. Subsequently, the size of the liposomes was determined via dynamic light scattering (DLS). Following these experiments the samples were stored at 4 °C for at least one month and were then re-measured via DLS. Figure S32 shows overlays of the two measurements of the same liposome sample, each at different time points. Since relating curves differ in position only to a marginal degree and the shape of the curves did not change, this strongly indicates that the liposomes are stable within the respective period of time (A, B: 4 months; C: 1 month).

S6. Animal studies

a. Positron emission tomography (PET) studies

To track the pharmacokinetic profile during the first hour after intravenous administration of the ^{18}F-radiolabeled, polyether-shielded liposomes and the respective non-liposomal polymers, time activity curves were determined by defining volumes of interest (VOIs) around important organs and quantifying the amount of radioactivity inside the VOIs (Figure S33 and S34).

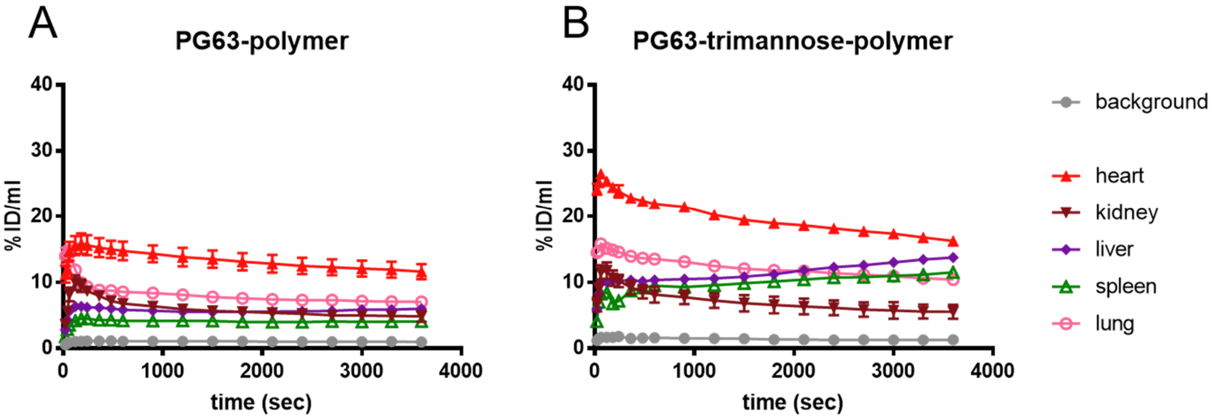

Figure S33. Time activity curves of the accumulation of [^{18}F]FTT-alkyne-BisHD-*hb*PG$_{63}$ (A) and [^{18}F]FTT-trimannose-alkyne-BisHD-*hb*PG$_{63}$ (B) in organs of interest of male C57BL/6 mice.

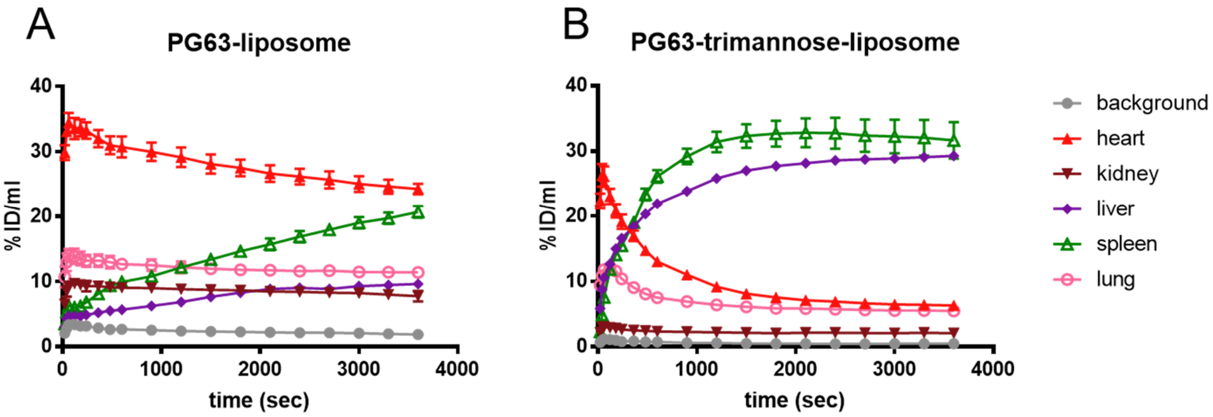

Figure S34. Time activity curves of the accumulation of [^{18}F]FTT-alkyne-BisHD-*hb*PG$_{63}$-shielded liposomes (A) and [^{18}F]FTT-trimannose-alkyne-BisHD-*hb*PG$_{63}$-shielded liposomes (B) in organs of interest of male C57BL/6 mice.

Table S1. *Ex vivo* biodistribution data in percent injected dose per gram tissue (% ID/g tissue) for polyether lipids and liposomal formulations in male C57BL/6 mice.

organ	[^{18}F]FTT-alkyne-BisHD-*hb*PG$_{63}$ (1 h)	[^{18}F]FTT-trimannose-alkyne-BisHD-*hb*PG$_{63}$ (1 h)	[^{18}F]FTT-alkyne-BisHD-*hb*PG$_{63}$ liposomes (1 h)	[^{18}F]FTT-alkyne-BisHD-*hb*PG$_{63}$ liposomes (4 h)	[^{18}F]FTT-trimannose-alkyne-BisHD-*hb*PG$_{63}$ liposomes (1 h)	[^{18}F]FTT-trimannose-alkyne-BisHD-*hb*PG$_{63}$ liposomes (4 h)
lung	10.22±1.28	11.78±1.34	10.96±1.08	7.45±0.58	3.89±2.68	1.73±0.23
blood	29.87±3.85	27.60±2.28	43.86±2.78	19.34±0.86	5.28±2.30	1.98±0.22
liver	12.06±2.25	24.53±2.86	19.61±3.52	42.57±3.24	87.66±20.00	82.74±9.82
spleen	5.94±0.38	23.73±3.48	51.66±4.48	96.90±16.64	128.72±18.66	140.22±12.64
kidney l	8.29±1.26	7.37±0.47	9.95±1.83	8.63±0.91	1.74±0.19	1.31±0.13
kidney r	8.20±1.24	7.39±0.49	10.17±1.94	8.88±0.87	1.87±0.23	1.36±0.12
muscle	0.41±0.06	0.37±0.05	0.44±0.10	0.43±0.06	0.10±0.02	0.10±0.01
heart	4.80±0.45	4.98±1.29	7.90±1.50	4.05±0.56	1.18±0.56	0.68±0.09
urine	35.80±14.59	27.22±8.67	6.76±5.39	2.50±0.27	1.76±0.59	1.08±0.26
intestine	2.50±0.80	2.01±0.24	2.91±1.16	4.21±0.69	0.84±0.70	0.71±0.13
testes	1.12±0.15	0.98±0.09	0.73±0.07	0.83±0.07	0.19±0.06	0.25±0.03
lymph nodes inguinal[a]	1.64±0.18	1.67±0.21	1.95±0.36	3.18±0.76	0.73±0.09	1.62±0.39
bone marrow	0.37±0.19	2.21±0.55	0.55±0.13	0.91±0.23	0.66±0.08	1.50±0.16
femur (without marrow)	0.50±0.11	0.82±0.22	0.58±0.10	0.65±0.23	0.19±0.07	0.38±0.13
skin	0.77±0.11	0.53±0.07	0.68±0.11	1.01±0.23	0.15±0.05	0.27±0.09
	n=5 urine n=5	n=5 urine n=5	n=5 urine n=4	n=5 urine n=4	n=5 urine n=5	n=5 urine n=5

[a] Since liposomes were injected intravenously, the distribution to several lymph nodes should be comparable.

References

(1) Fulmer, G. R.; Miller, A. J. M.; Sherden, N. H.; Gottlieb, H. E.; Nudelman, A.; Stoltz, B. M.; Bercaw, J. E.; Goldberg, K. I. NMR Chemical Shifts of Trace Impurities: Common Laboratory Solvents, Organics, and Gases in Deuterated Solvents Relevant to the Organometallic Chemist. *Organometallics* 2010, *29*, 2176–2179.

(2) Percec, V.; Leowanawat, P.; Sun, H.-J.; Kulikov, O.; Nusbaum, C. D.; Tran, T. M.; Bertin, A.; Wilson, D. A.; Peterca, M.; Zhang, S.; Kamat, N. P.; Vargo, K.; Moock, D.; Johnston, E. D.; Hammer, D. A.; Pochan, D. J.; Chen, Y.; Chabre, Y. M.; Shiao, T. C.; Bergeron-Brlek, M.; André, S.; Roy, R.; Gabius, H.-J.; Heiney, P. A. Modular Synthesis of Amphiphilic Janus Glycodendrimers and Their Self-Assembly into Glycodendrimersomes and Other Complex Architectures with Bioactivity to Biomedically Relevant Lectins. *J. Am. Chem. Soc.* 2013, *135*, 9055–9077.

(3) Daly, R.; Vaz, G.; Davies, A. M.; Senge, M. O.; Scanlan, E. M. Synthesis and Biological Evaluation of a Library of Glycoporphyrin Compounds. *Chem. - Eur. J.* 2012, *18*, 14671–14679.

(4) Morales, C. P.; Catalán, J.; Domingo, V.; González Delgado, J. A.; Dobado, J. A.; Herrador, M. M.; Quílez del Moral, J. F.; Barrero, A. F. Protecting-Group-Free Synthesis of Chokols. *J. Org. Chem.* 2011, *76*, 2494–2501.

(5) Zhao, J.; Wei, S.; Ma, X.; Shao, H. A mild and environmentally benign method for the synthesis of glycals in PEG-600/H_2O. *Green Chem.* 2009, *11*, 1124-1127.

(6) Lill, A.; Scholich, K.; Stark, H. Synthesis of novel dansyl-labeled Celecoxib derivatives. *Tetrahedron Lett.* 2013, *54*, 6682–6686.

(7) Bakleh, M. E.; Sol, V.; Estieu-Gionnet, K.; Granet, R.; Déléris, G.; Krausz, P. An efficient route to VEGF-like peptide porphyrin conjugates via microwave-assisted 'click-chemistry'. *Tetrahedron* 2009, *65*, 7385–7392.

4 Summary and Outlook

4 Summary and Outlook

In the developmental process of novel drug delivery systems (DDSs), *in vivo* tracking is crucial to understand the influence of physicochemical properties of the nanoparticles on their pharmacokinetic profile. For this purpose, positron emission tomography (PET) is a powerful and non-invasive nuclear imaging technique, providing an excellent spatial and temporal resolution combined with the possibility of quantification. In the herein presented work, different nanodimensional DDSs were evaluated via PET and/or biodistribution studies in mice and rats. Figure 13 gives an overview of the cumulated work.

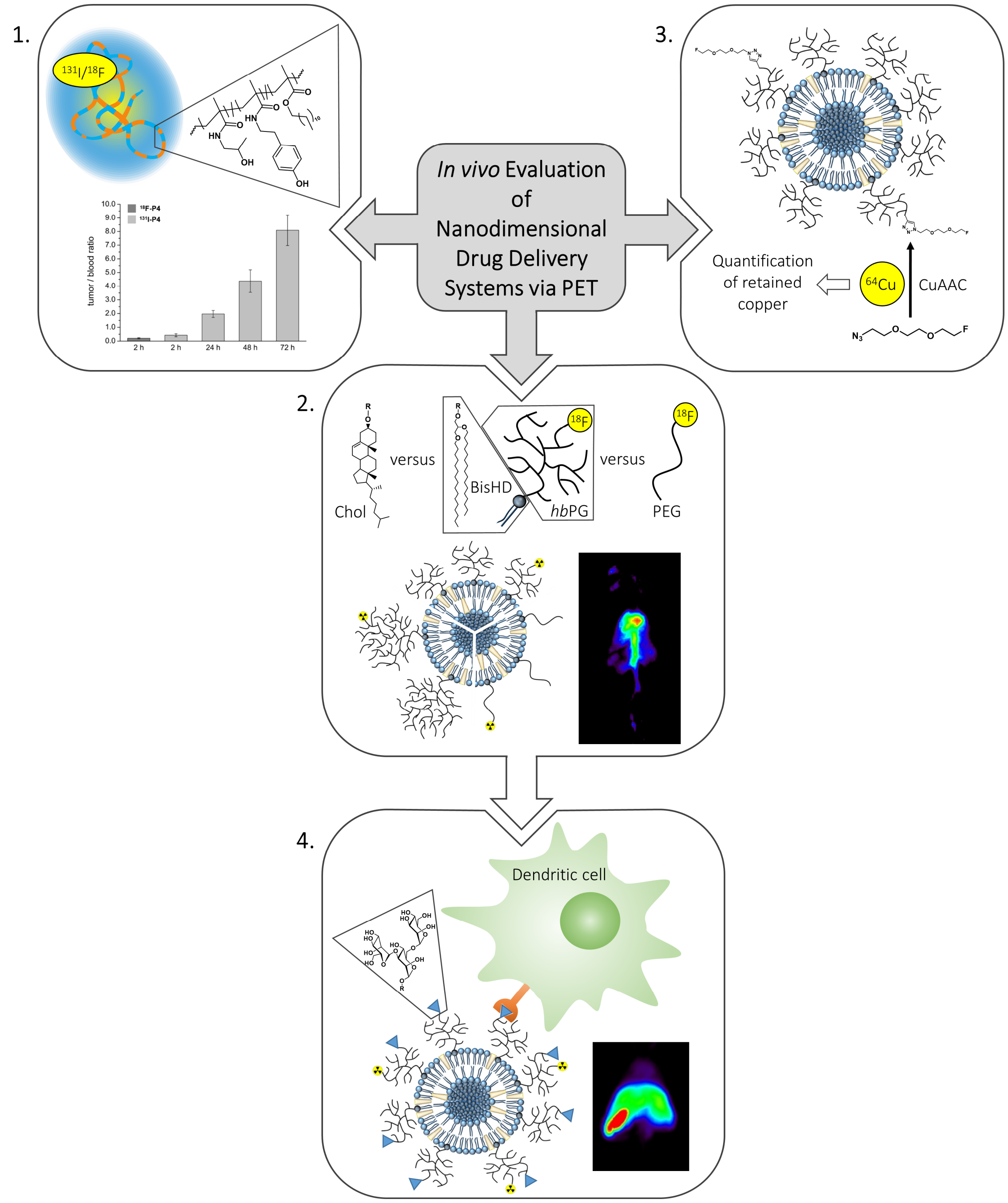
1.
^{131}I/^{18}F
tumor / blood ratio
^{18}F-P4
^{131}I-P4
2 h
2 h
24 h
48 h
72 h
In vivo Evaluation of Nanodimensional Drug Delivery Systems via PET
3.
Quantification of retained copper
^{64}Cu
CuAAC
2.
Chol
versus
BisHD
*hb*PG
^{18}F
versus
PEG
4.
Dendritic cell

Figure 13. Overview of the cumulated work.

Each of the following chapters refers to a box in Figure 13. If adequate, at the end of each chapter, a corresponding outlook is given.

1. From ^{18}F labeled to ^{131}I-labeled HPMA-polymers – short- versus long-term biodistribution

Based on former studies, revealing favorable *in vivo* characteristics for ^{18}F-labeled HPMA-*ran*-LMA copolymers[1,2], such as a prolonged plasma half-life as well as an enhanced tumor accumulation, the *in vivo* fate of a high molecular weight HPMA-ran-LMA copolymer, which had exhibited the most promising properties during short-term evaluation, should be evaluated over a longer period of time.

In this respect, the HPMA-*ran*-LMA copolymer, synthesized by combining reactive ester chemistry with the RAFT polymerization technique, was radiolabeled with [^{131}I]iodide via electrophilic aromatic substitution on tyramine side chains. [^{131}I]radioiodination was accomplished in a mixture of DMSO and phosphate buffered saline (PBS) using chloramine-T (CAT) as oxidizing agent. In this way, 1 mg of polymer precursor could be radiolabeled in radiochemical yields (RCYs) about 50 % in a total synthesis time (including purification via size exclusion chromatography (SEC)) of less than 20 min.

It is worth mentioning, that ^{131}I-incorporation could be accomplished using the same polymer batch, as for the prior ^{18}F-labeling. This provided almost identical polymers. Still, non-radioactive versions of the F-and I-labeled polymer were synthesized in order to enable a direct comparison between their physicochemical properties. Surprisingly, both F-and I-labeled polymers were a bit more hydrophilic (higher critical micelle concentrations) and formed slightly larger micellar aggregates then the non-labeled polymers. However, in direct comparison F-and I-labeled polymers were similar to each other, which allowed for a direct correlation of structure-property relationships between the ^{18}F- and the ^{131}I-labeled HPMA-*ran*-LMA copolymer *in vivo*.

In vivo results were obtained by means of biodistribution and metabolism studies in rats, bearing Walker 256 mammary tumors. Despite the physicochemical similarity between the F- and I-labeled polymers, significant differences between the short-term distribution (2 h) of the ^{18}F-HPMA-*ran*-LMA copolymer and the ^{131}I-labeled analog were observed. For the ^{131}I-labeled polymer, hepatic and splenic uptake was increased, whereas for the ^{18}F-labeled polymer a much higher uptake in the kidneys could be observed after 2 h. Given their physicochemical similarity, this was attributed to different metabolization pathways.

The longer-lived radioisotope ^{131}I enabled tracking of the pharmacokinetics over three days. During this time period the polymer concentration in the blood decreased continuous. Major blood clearance was observed within the first 24 h after injection. In contrast, there was an increase in tumor uptake observable over 24 h, which only slowly decreased thereafter. However, the tumor/blood ratio increased over the complete observation period of 72 h (Figure 13, 1st box). Taken together, these findings strongly emphasizes an EPR-mediated passive tumor accumulation, thus demonstrating the suitability of this HPMA-based copolymer system for anticancer treatment. Although it may have limited potential for a targeted transport of drugs which are just hydrophobically embedded, it might be a promising carrier for covalently bound drugs.

Additionally, the *in vivo* stability of the ^{131}I-label was investigated as well, since deiodination is an issue. This was accomplished via *ex vivo* biodistribution experiments, considering the uptake in the thyroid. Studies revealed a percentage of <1 % of the injected dose being present in the thyroid at all time-points. Together with the percentage of the injected dose in the kidneys which was also <1 % during the whole observation time, that suggests a low deiodination rate of the polymer *in vivo.* Furthermore, the distribution of the polymer in the blood pool was examined. For this purpose, blood samples obtained during the biodistribution studies were separated into different fractions (blood cells, proteins as well as plasma water), whose radioactivity was measured. It was found, that about half of the polymers were present in the plasma water during the whole period of 72 h, whereas the other half interacted with serum proteins and blood cells, which is in accordance with former studies.[3-5]

2. Towards stealth liposomes – from PEG to *hb*PG lipids, from cholesteryl to dialkyl anchorage

A major part of this work focused on the *in vivo* evaluation of stealth liposomes, shielded by multifunctional hyperbranched polyglycerols (*hb*PG) bearing a dialkyl anchor (Figure 13, 2nd box). Different *hb*PG lipids (M_n = 2900, 5200 g mol^{-1}) were examined, regarding their ability to shield the liposomes from being detected by the mononuclear phagocyte system (MPS). A linear bis(hexadecyl)glycerol-PEG lipid (M_n = 3000 g mol^{-1}) was investigated as well, in order to enable a comparison between *hb*PG and PEG with respect to shielding properties. Furthermore, a special focus was set on the performance of the dialkyl anchor, regarding a stable anchorage of the polyether lipids in the lipid bilayer of the liposomes. This was due to the fact that cholesteryl-anchored polyether lipids, investigated in a former study[6], did not provide a stable anchorage, causing, that no stealth effect could be demonstrated.

Well-defined polyether lipids were synthesized via anionic ring-opening polymerization. To enable radioactive labeling of the polyether lipids via copper-catalyzed alkyne-azide cycloaddition (CuAAC), alkyne moieties were introduced in a post-modification step. Radiolabeling of the polymers was carried out using [^{18}F]F-TEG-N_3 via CuAAC with excellent RCYs exceeding 95 % after 10 min.

Subsequent liposome preparation was accomplished by thin-film hydration method followed by repeated extrusion. Performing the extrusion manually led to two major problems: high radiation exposure for the experimentalist and strong fluctuations of the liposomes sizes (determined by dynamic light scattering), even with the same shielding polymer. Therefore an automatic extrusion device was developed, which ensures a reproducible pressure during the extrusion process and has a separate control module. In this way, it is possible to obtain liposomes with reproducible sizes in addition to a remote control of the extrusion process, which considerably reduces the radiation exposure.

To investigate the fate of the polyether lipids and their corresponding liposomal formulations, *in vivo* µPET studies as well as *ex vivo* biodistribution studies were conducted with healthy, male C57BL/6 mice. Dynamic scans over 1 h were started at the time of injection in order to follow the initial distribution. For the liposomal formulations also static scans of 30 min were run 3.5 h after injection to gain information regarding pharmacokinetics at later stages. Organ distribution was examined 1 h after the injection and additionally 4 h after injection for the liposomal formulations. Within 1 h, the non-associated polyether lipids were rapidly cleared via the renal system, which was expected, as their molecular weights were below the renal threshold. In contrast, the corresponding liposomes circulated in the blood stream over a period of 1 h. These findings prove firstly, that the dialkyl anchor provides a stable anchorage of the polyether lipids and secondly, that *hb*PG just like PEG is suitable to shield liposomes from being detected by the MPS. After 4 h, the liver and spleen uptake increased for all three systems (although to varying degrees), hinting at a partly detection of the liposomes by the MPS. However, for all three systems, a fraction of the liposomes was continuously circulating in the blood after 4 h.

It can be concluded, that the three investigated liposomal formulations showed a comparable *in vivo* behavior with remarkable differences in splenic uptake. Liposomes shielded by the lower-weight *hb*PG lipids exhibited the lowest splenic uptake both after 1 and 4 h p.i. and are presumably subjected to the lowest detection by the MPS. Overall, *hb*PG-shielded liposomes showed a favorable biodistribution, rendering them promising novel nanovesicles for drug transport and targeting. In contrast to the PEG-lipids, multifunctional *hb*PG lipids enable the attachment of a variety of structures, such as targeting vectors and radiolabels, facilitating cell-specific drug delivery combined with simultaneous carrier trafficking. With respect to different polymer anchors it can be concluded that a change of the polymer anchor from cholesterol to bis(alkyl)glycerol leads to a significant increase in the stability of the liposomes. Thus, the utilization of bis(alkyl)glycerol *hb*PG lipids enables “stealth” behavior in combination with multifunctionality.

Because of the potential of the *hb*PG-shielded liposomes, they are worth further improvement in the future. For example, the dialkyl anchor could be elongated for an even more stable anchorage of the shielding polymers. Additionally the composition of the liposomes could be altered in order to gain more stability. Here, a switch to phospholipids with a high phase transition temperature might be advantageous, in order to stabilize the lipid bilayer. With the optimized and evaluated systems in hand, a loading of the liposomes with therapeutics could be tested in future work.

3. CuAAC on liposomes – but what about the retention of copper?

As described above, radiolabeling of the polyether lipids via CuAAC was performed prior to the liposome formation. This approach ensured the separation of cytotoxic copper, but entailed a time-consuming radiosynthesis on the other hand. Thus, a direct radiolabeling of preformed liposomes via CuAAC was investigated. Usually, macromolecular structures can easily be purified from light-weighted substances by SEC, unless the substances are retained by the macromolecular structure. In terms of a CuAAC, this would lead to a non-removable fraction of copper, making a usage of the drug delivery systems problematic. Thus, a quantification of the final copper content of the liposomes after purification should be accomplished.

For this purpose, 1 ml of a 1 M Cu(II) nitrate solution was irradiated at the TRIGA Mark II research reactor Mainz to obtain 310 MBq of *c.a.* [^{64}Cu]Cu(II). The irradiated solution was directly used as catalyst for the CuAAC between non-radioactive F-TEG-N_3 and liposomes (Figure 13, 3rd box). Subsequently, liposomes were purified via SEC. Combined liposome containing fractions as well as a sample containing the same amount of [^{64}Cu]Cu(II) nitrate solution that was used for the CuAAC were measured in a gamma detector. Comparison of the resulting values gave the amount of copper still associated with the liposomes after purification. In this way, the final copper content of the liposomes could straightforwardly be quantified, revealing that only 0.018 % of the added radioactivity was still associated with the liposomes after purification. This referred to an absolute amount of copper of 0.17 ng. For humans dietary reference values for Cu range between 0.9 to 2 mg per day in different countries[7], so the residual 0.17 ng of copper are absolutely uncritical in terms of an application *in vivo*. Besides this very application, the experimental methodology may be applied to study many other CuAAC reactions, used for the synthesis of radiolabeled or non-radioactive species, which are intended for human applications. The utilization of a ^{64}Cu-spiked Cu catalyst, in the same amount as for the "normal" CuAAC, allows for an uncomplicated quantification of even very small amounts of copper, which may be hardly to measure by conventional analytical methods and without manipulating or destroying the sample.

After ensuring that copper is retained by the liposomes only to a marginal degree, first attempts to radiolabel the liposomes with [^{18}F]F-TEG-N_3 were accomplished, in order to investigate the yield of the CuAAC. Here, a RCY of 27.4 % was reached after 10 min, which should be improvable by either increasing the liposome concentration in the reaction mixture or increasing the polyether lipid content of the liposomes. An improvement is worth trying, as the possibility to radiolabel liposomes directly, instead of radiolabel components, remove copper and do the liposome formation afterwards, significantly simplifies the radiosynthesis, saves time, enables a higher amount of radioactivity per volume and results in a lesser radiation exposure for the experimentalist.

4. Towards targeted liposomes – addressing dendritic cells with trimannosylated liposomes

In the last part of this work, *hb*PG-shielded liposomes, bearing multiple carbohydratic trimannose molecules on their surface (Figure 13, 4th box), were investigated, regarding their potential to address dendritic cells (DCs) *in vivo*. The results were compared to similar liposomes bearing no trimannose on their surface, which had been evaluated previously.[8]

In this respect, the higher-weight *hb*PG lipid (M_n = 5200 g mol^{-1})[8], bearing four alkyne functionalities, was functionalized with trimannose azide in a CuAAC. The usage of two equivalents trimannose azide resulted in a degree of functionalization of 1.5. This approach left free alkyne functionalities for a subsequent radiolabeling with [^{18}F]F-TEG-N$_3$ or for a fluorescence labeling with Oregon Green 488 (OG 488) azide, both performed via CuAAC. The ^{18}F-label allowed for an *in vivo* tracking of the trimannosylated *hb*PG lipids and respective liposomes, whereas the OG 488-label was introduced for future cell studies.

To investigate the *in vivo* fate of the trimannosylated versus the non-mannosylated polyether lipids and their corresponding liposomal formulations, *in vivo* µPET and *ex vivo* biodistribution studies were conducted in healthy, male C57BL/6 mice. Dynamic scans over 1 h, started at the time of injection, revealed the initial distribution. For the liposomal formulations also static scans of 30 min were run 3.5 h after injection to gain information regarding pharmacokinetics at later stages. Organ distribution was examined 1 h after the injection and additionally 4 h after injection for the liposomal formulations. Within 1 h, a major amount of the non-associated polyether lipids was cleared via the renal system, which was expected, as their molecular weights were below the renal threshold. However, the mannosylated *hb*PG lipids increasingly accumulated in liver, spleen and bone marrow, compared to the non-mannosylated polyether lipids. For the corresponding liposomal formulations, this effect was even more pronounced. The mannosylated liposomes highly accumulated in liver and spleen, compared to their non-mannosylated counterparts. These findings suggest, that the mannosylated liposomes were recognized by DCs, expressed in the mentioned organs.

However, it cannot be excluded that other immune cells, besides DCs, were targeted as well. Future cell studies on murine splenic immune cells have to elucidate which cell types are addressed in particular and to which extent. For this purpose, OG 488-labeled polyether lipids (mannosylated and non-mannosylated) and respective liposomal formulations have already been synthesized. Furthermore, it would be worth testing liposomes bearing other carbohydrate structures, besides trimannose on the surface, regarding their ability to address DCs in cells studies. The most promising candidates could then be evaluated *in vivo*. If successful, a loading with DC-stimulating molecules and antigens could be attempted, in order to come closer to an inducible activation of DCs via DDSs, followed by a targeted immune response.

4.1 References

(1) Allmeroth, M.; Moderegger, D.; Biesalski, B.; Koynov, K.; Rösch, F.; Thews, O.; Zentel, R. Modifying the Body Distribution of HPMA-Based Copolymers by Molecular Weight and Aggregate Formation. *Biomacromolecules* **2011**, *12*, 2841–2849.

(2) Allmeroth, M.; Moderegger, D.; Gündel, D.; Koynov, K.; Buchholz, H.-G.; Mohr, K.; Rösch, F.; Zentel, R.; Thews, O. HPMA-LMA Copolymer Drug Carriers in Oncology: An in Vivo PET Study to Assess the Tumor Line-Specific Polymer Uptake and Body Distribution. *Biomacromolecules* **2013**, *14*, 3091–3101.

(3) Hemmelmann, M.; Metz, V. V.; Koynov, K.; Blank, K.; Postina, R.; Zentel, R. Amphiphilic HPMA–LMA copolymers increase the transport of Rhodamine 123 across a BBB model without harming its barrier integrity. *J. Control. Release* **2012**, *163*, 170–177.

(4) Clemens-Hemmelmann, M.; Kuffner, C.; Metz, V.; Kircher, L.; Schmitt, U.; Hiemke, C.; Postina, R.; Zentel, R. Amphiphilic Copolymers Shuttle Drugs Across the Blood-Brain Barrier. *Macromol. Biosci.* **2016**, *16*, 655–665.

(5) Hemmelmann, M.; Mohr, K.; Fischer, K.; Zentel, R.; Schmidt, M. Interaction of pHPMA-pLMA Copolymers with Human Blood Serum and Its Components. *Mol. Pharm.* **2013**, *10*, 3769–3775.

(6) Reibel, A. T.; Müller, S. S.; Pektor, S.; Bausbacher, N.; Miederer, M.; Frey, H.; Rösch, F. Fate of Linear and Branched Polyether-Lipids In Vivo in Comparison to Their Liposomal Formulations by ^{18}F-Radiolabeling and Positron Emission Tomography. *Biomacromolecules* **2015**, *16*, 842–851.

(7) Bost, M.; Houdart, S.; Oberli, M.; Kalonji, E.; Huneau, J.-F.; Margaritis, I. Dietary copper and human health: Current evidence and unresolved issues. *J. Trace Elem. Med. Biol.* **2016**, *35*, 107–115.

(8) Wagener, K.; Worm, M.; Pektor, S.; Schinnerer, M.; Thiermann, R.; Miederer, M.; Frey, H.; Rösch, F. Comparison of Linear and Hyperbranched Polyether Lipids for Liposome Shielding by ^{18}F-Radiolabeling and Positron Emission Tomography. *Biomacromolecules* **2018**, dx.doi.org/10.1021/acs.biomac.8b00115.

5 Appendix

5 Appendix

5.1 List of abbreviations

% ID/g tissue	percentage of injected dose per gram of tissue	DCM	dichloromethane
$[^{18}F]$FETos	2-$[^{18}F]$fluoroethyl-1-tosylate	DC-SIGN	dendritic cell-specific ICAM-3 grabbing nonintegrin
$[^{18}F]$F-TEG-N_3	1-azido-2-(2-(2-$[^{18}F]$fluoroethoxy)ethoxy)ethane	DDS	drug delivery system
$[^{18}F]$FTT	$[^{18}F]$F-TEG-triazole	DLS	dynamic light scattering
AIBN	2,2'-azo-bis-(isobutyronitrile)	DMF	dimethylformamide
AROP	anionic ring-opening polymerization	DMSO	dimethyl sulfoxide
A_S	specific activity	D^o_{298}	bond dissociation energy at 298 K
ATRP	atom transfer radical polymerization	DOPC	1,2-dioleoyl-*sn*-glycero-3-phosphocholine
BGO	bismuth germanate	DOSY	diffusion-ordered NMR
BisHD	1,2-bis(hexadecyl)glycerol	DPPE	dipalmitoyl phosphatidylethanolamine
Bq	becquerel	DPPG	1,2-dipalmitoyl-*sn*-glycero-3-phosphoglycerol
c.a.	carrier added	DSPC	1,2-distearoyl-*sn*-glycero-3-phosphocholine
c.f.	carrier free	DSPE	1,2-distearoyl-*sn*-glycero-3-phospho-ethanolamine
CAT	chloramine-T	D_z	z-average diffusion coefficient
Ch	cholesterol	E^*	excitation energy
CHCA	α-cyano-4-hydroxy-cinnamonic acid	EA	ethyl acetate
CMC	critical micelle concentration	EC	electron capture
cryo-TEM	cryo-transmission electron microscopy	EEGE	ethoxyethyl glycidyl ether
CSA	camphorsulfonic acid	EO	ethylene oxide
CT	computed tomography	EPR effect	enhanced permeability and retention effect
CTA	chain transfer agent	ETAAS	electrothermal atomic absorption spectrometry
CTP	4-cyano-4-((thiobenzoyl)sulfanyl)pentanoic acid	eV	electronvolt
CuAAC	Cu(I)-catalyzed azide-alkyne cycloaddition	$E_{\beta+,\mathrm{max}}$	maximum β^+-energy
Đ	dispersity	FBP	filtered back projection
D_{app}	apparent diffusion coefficient	FCS	fluorescence correlation spectroscopy
DAST	*N,N*-diethylaminosuflur trifluoride	F-TEG-N_3	1-azido-2-(2-(2-fluoroethoxy)ethoxy)ethane
DC	dendritic cell	GPC	gel permeation chromatography

*hb*PG	hyperbranched polyglycerol
HPGe	high-purity germanium
HPMA	*N*-(2-hydroxypropyl)methacrylamide
HRMS	high-resolution mass
HSAB concept	Pearson acid base concept
i.v.	intravenous
ICP-MS	inductively coupled plasma mass spectrometry
IR	infrared
Kryptofix®222	4,7,13,16,21,24-hexaoxa-1,10-diazabicyclo[8.8.8]hexacosane
KTFA	potassium trifluoroacetate
lin	linear
LMA	lauryl methacrylate
LOR	line of response
LSO	lutetium oxyorthosilicate
Man	mannose
MeCN	acetonitrile
MIP	maximum intensity projection
M_n	number average molecular weight
*m*PEG	methoxyPEG
MPS	mononuclear phagocyte system
MRT	magnetic resonance tomography
M_w	weight average molecular weight
MWCO	molecular weight cut-off
n.c.a.	no carrier added
NCE	new chemical entity
NMP	*N*-methylpyrrolidone
OG 488	Oregon Green 488
OI	optical imaging
OSEM	ordered subsets expectation maximization
p.i.	post injection
PBS	phosphate buffered saline
PDI	polydispersity index
PEG	poly(ethylene glycol)
PET	positron emission tomography
PFPMA	pentafluorophenyl methacrylate
PG	polyglycerol
PMDTA	*N*,*N*,*N*′,*N*′′,*N*′′-pentamethyldiethylenetriamine
PTFE	polytetrafluoroethylene
RAFT	reversible addition-fragmentation chain transfer
ran	random
RCY	radiochemical yield
R_f	retardation factor
R_h	hydrodynamic radius
RI	refractive index
RP	reverse phase
rpm	revolutions per minute
R_t	retention time
r_W	van der Waals radius
SEC	size exclusion chromatography
SEM	standard error of the mean
SM(d18:1/18:0)	*N*-stearoyl sphingomyelin
SPAAC	strain-promoted alkyne-azide cycloaddition
SPE	solid phase extraction
SPECT	single photon emission computed tomography
$t_{1/2}$	half-life
TFA	trifluoroacetic acid
THF	tetrahydrofuran
TI	therapeutic index
TLC	thin-layer chromatography
trimannose azide	(1-(2-(2-(2-(2-azidoethoxy)ethoxy)ethoxy)ethyl)-1*H*-1,2,3-triazole-4-yl)methoxy)-3,6-di-O-α-ᴅ-mannopyranosyl-α-ᴅ-mannopyranoside

Ts-TEG-N_3	2-(2-(2-azidoethoxy)ethoxy)ethyl-*p*-toluenesulfonate
TXRF	total reflection X-ray fluorescence
US	ultrasound
V	ionization potential
VOI	volume of interest
τ	mean lifetime
Δ_O	Ore gap

5.2 List of publications

“Long-term biodistribution study of HPMA-*ran*-LMA copolymers *in vivo* by means of ^{131}I-labeling”

K. Wagener, D. Moderegger, M. Allmeroth, A. Reibel, S. Kramer, B. Biesalski, N. Bausbacher, R. Zentel, O. Thews, F. Rösch, *Nucl. Med. Biol.* **2018**, *58*, 59-66.

“Comparison of Linear and Hyperbranched Polyether Lipids for Liposome Shielding by ^{18}F-Radiolabeling and Positron Emission Tomography”

K. Wagener*, M. Worm*, S. Pektor, M. Schinnerer, R. Thiermann, M. Miederer, H. Frey, F. Rösch, *Biomacromolecules* **2018**, dx.doi.org/10.1021/acs.biomac.8b00115.

* both authors contributed equally

5.3 Acknowledgment

Deleted for privacy reasons.

5.4 Curriculum Vitae

Deleted for privacy reasons.